ISBN 978-82-326-2656-4 (printed ver.)
ISBN 978-82-326-2657-1 (electronic ver.)
ISSN 1503-8181

NTNU
Norwegian University of
Science and Technology

Doctoral thesis

Mariia Stepanova

Doctoral theses at NTNU, 2017:294

NTNU
Norwegian University of Science and Technology
Thesis for the Degree of
Philosophiae Doctor
Faculty of Natural Sciences
Department of Materials Science and
Engineering

NTNU

Doctoral theses at NTNU, 2017:294

Mariia Stepanova

Zinc-rich coatings for improved corrosion resistance of extruded aluminium heat-exchange tubing in acidified chloride solution

NTNU
Norwegian University of
Science and Technology

Mariia Stepanova

Zinc-rich coatings for improved corrosion resistance of extruded aluminium heat-exchange tubing in acidified chloride solution

Thesis for the Degree of Philosophiae Doctor

Trondheim, October 2017

Norwegian University of Science and Technology
Faculty of Natural Sciences
Department of Materials Science and Engineering

NTNU
Norwegian University of
Science and Technology

NTNU
Norwegian University of Science and Technology

Thesis for the Degree of Philosophiae Doctor

Faculty of Natural Sciences
Department of Materials Science and Engineering

ISBN 978-82-326-2656-4 (printed ver.)
ISBN 978-82-326-2657-1 (electronic ver.)
ISSN 1503-8181

Doctoral theses at NTNU, 2017:294

Printed by NTNU Grafisk senter

Acknowledgements

First and foremost I would like to thank my supervisor, Professor Kemal Nisancioglu, for providing me with opportunity to carry out my Ph.D. studies at NTNU and work on the SuperAl project during the last four years. I greatly appreciate your excellent guidance and encouragement throughout my Ph.D. work, as well as support in settling down in Norway. It has been a great pleasure to work with you and I would especially like to thank you for your patience and encouragement during the last year.

I am very grateful to my co-supervisor, Professor Otto Lunder, for his extensive help and interesting discussions during these years. Professor Jan Halvor Nordlien is highly acknowledged for providing me with many new ideas during our phone meetings.

I wish to thank Anita Storsve for her great help with experimental work in the corrosion lab.

Special thanks to my friends Ingrid and Siri for our long lunch breaks and discussions about everything including even work. Belma is also acknowledged for this part, although she has been missed here for the last three years. I would also like to thank all my colleagues at IMA for making my time as a Ph.D. student enjoyable.

Furthermore, I would like to thank my friends outside of NTNU for helping me to adopt to life in Norway smoothly and all the fun evenings we had and will have. I am especially grateful to Svetlana for proving that making new friends can still be easy. My friends back home and in other parts of the world are highly appreciated for their encouragement and our Skype meetings, especially Julia for our naive and sarcastic discussions and Katia for great support and being there when I need it.

Finally, I would like to thank my family for their love and support through all these years. I am deeply grateful to my mother for being there throughout my entire life. I am very thankful to my husband Mihail for his love, never-ending patience and great support in this adventure. I could not have done it without you! You were giving me strength to continue every day. Last but not the least, thanks to our little daughter Anna for her smiles and just being the way she is.

Preface

This thesis work has been carried out at the Department of Materials Science and Engineering, Norwegian University of Science and Technology (NTNU), from June 2013 to August 2017. Financial support by The Research Council of Norway and Sapa AS through the research project *Superior All Aluminium Solutions for the HVAC&R Industry* (SuperAl) is greatly appreciated. The main supervisor has been Professor Kemal Nisancioglu (NTNU), with Professor Otto Lunder (SINTEF Materials and Chemistry and NTNU) and Professor Jan Halvor Nordlien (Sapa AS and NTNU) as co-supervisors.

The author has performed all the experimental work presented in this thesis with the following exceptions: AlZn alloys in chapter 3 were cast by Kurt Sandaunet (SINTEF Materials and Chemistry), sample preparation and scanning electron microscopy (SEM) of cross sections in chapter 3 were performed by Stanislaw Zajac (Sapa AS), sample preparation and SEM of cross sections in chapter 6 were performed by Anders Nordeide (Hydro Karmøy).

Mariia Stepanova

Trondheim, September 1, 2017

Summary

Thin walled multi-port extruded (MPE) heat exchanger Al alloy tubes, with solid-solution Zn-rich surface, are widely used by the automotive industry and considered by the heat, ventilation, air-conditioning and refrigeration market for improved corrosion resistance of Al tubes against pitting. It is well known that alloying Al with Zn causes decrease in the corrosion potential in chloride solution. At the same time self-corrosion rate of Zn itself is quite high in chloride solution. This work aims to improve understanding of mechanisms of protection against pitting provided to the Al alloy substrate by such layers and investigate to which extent the self-corrosion of the Zn-rich layer can be a limiting factor in determining the service life time of the heat exchanger tubes.

Zinc was applied on AlMn alloy extruded tubes by thermal-arc spraying immediately after extrusion. Typical Zn load on the surface was 8 ± 0.2 g/cm^2. The tubes were subsequently subjected to heat treatment at various temperatures (350 °C - 430 °C) and durations (1 - 5 hours) to obtain solid-state AlZn alloy diffusion layer at the surface with varying thickness and Zn concentration profiles in the AlMn substrate. 99.99 % pure Zn sample, AlMn substrates without coating and as coated with Zn were used as reference samples. Zn-rich layers with lower load of Zn (2.7 ± 0.7 g/cm^2) were produced from Zn thermal-arc sprayed AlMn alloy tubes using hot chromic-phosphoric treatment and subsequent heat treatment (4 hours at 430 °C, 470 °C, 510 °C).

Concentration depth profiles were obtained by glow discharge optical emission spectroscopy (GD-OES). Corrosion rate was determined by weight loss resulting from immersion for predetermined times in acidified artificial sea water solution of pH 3 at 25 °C for slight acceleration of the corrosion rate, during which the open circuit potential change was recorded with respect to time. Electrochemical behaviour of pure Zn sample, Zn-rich layer and AlMn substrate was analysed using potentiodynamic polarisation. The morphology and composition of the Zn-rich layer before and after corrosion were examined by scanning electron microscopy (SEM) and energy-dispersive X-ray spectroscopy (EDS).

The as-sprayed Zn coating was found to be highly non-uniform, with some regions remaining not covered. Non-uniformity of the coating resulted in non-uniformity of the Zn-rich layers laterally and in depth. Calibration of GD-OES for Al-Zn system with minor alloying elements and oxygen was successfully performed regardless of a large difference in sputtering rates

of Al and Zn. GD-OES was found to be a useful technique for depth profiling, providing fast analysis, high depth resolution and analytical sensitivity compared to EDS. Thickness of Zn-rich layer increased with heat treatment time and temperature, while Zn concentration at the surface decreased. At the same time, increasing amount of minor alloying elements, such as Fe, Mn, Si and Mg, became incorporated into the layer.

Zn depth profiles of the Zn-rich layers were fitted to a one-dimensional analytical solution of Fick's second law for diffusion from a layer into a semi-infinite region using an effective binary diffusion coefficient for the system, which successfully incorporated lateral non-uniformity of the layers. The activation energy of diffusion was calculated to be 103 kJ/mol, which agrees well with the literature data. A procedure for prediction of Zn concentration profiles of Zn-rich layers on commercial Al alloy substrate for Zn coatings with different loads, Zn concentrations and thicknesses was established.

Pure Zn coating and Zn-rich layer were found capable of protecting the AlMn alloy substrate anodically against pitting by maintaining corrosion potential below repassivation potential of Al, E_{rp} = -0.85 $\mathrm{V_{SCE}}$, at the expense of increased self-corrosion rate. Corrosion potential of samples, as coated with Zn, reached the critical pitting potential, E_c = -0.73 $\mathrm{V_{SCE}}$, of the AlMn substrate in 4 days. After 11 days of immersion the corrosion potential of the samples with Zn load of 8 g/cm^2, heat treated for 2 hours at 350 °C and 4 hours at 430 °C, increased to about 50 mV and 140 mV below E_c, respectively, the latter 20 mV below E_{rp}. The reduction in thickness after 11 days of immersion for these Zn-rich layers was calculated to be 23 µm and 54 µm, respectively.

Lower Zn load coating (2.7 g/cm^2) obtained by heat treatment for 4 hours at 430 °C after 11 days of immersion maintained corrosion potential 10 mV below E_{rp}, while its total reduction in thickness was 38 µm. These results indicate that an optimal Zn concentration in the Zn-rich layer lies at levels much lower than those obtained by Zn thermal-arc spraying if maintaining the corrosion potential at a level lower than E_{rp} is necessary for protection against pitting. At the same time, if there is no danger in exceeding E_c, below which pitting does not initiate, then maintaining the potential below E_c can be sufficient for protection against pitting. In this case Zn coating with 8 g/cm^2 of Zn, heat treated for 2 hours at 350 °C, can be considered as the optimal alternative for the present test solution.

SEM and EDS area analysis of corroded samples after immersion test showed that corrosion of Zn-rich layers was non-uniform due to non-uniformity of the layers themselves. Regions with higher Zn concentration, ρ_{Zn}, corroded first and protected anodically regions with lower ρ_{Zn}. With increasing immersion time in the test solution, ρ_{Zn} of corroded areas decreased and corrosion spread to a larger area. No evidence of enrichment of Al, expected due to dealloying, was observed.

The well-known relationship between the corrosion potential of AlZn alloys and Zn concentration was extended over a wide concentration range

using ρ_{Zn} of corroded areas and related further to the corrosion rate in acidified synthetic seawater. The database thus developed is useful for optimizing the Zn-rich layer thickness and Zn concentration profile in the layer to minimize uniform corrosion, and therefore maximize service lifetime, without reducing the protection against pitting. Zn coating with Zn load of 3.5 g/cm^2, heat treated for 3 hours at 470 °C, was suggested as the optimal in terms of maintaining the potential of the AlMn substrate below E_{rp} to protect against pitting and providing the lowest self-corrosion rate, applicable to continuous immersion in the present test solution. The methodology developed in this work can be used to estimate optimal conditions for data related to other exposure conditions.

Contents

Acknowledgements . . . . **iii**

Preface . . . . **v**

Summary . . . . **vii**

1 Introduction **1**
1.1 Background 1
1.2 Objectives and methods 3
1.3 Structure of the thesis 4

2 Literature review **7**
2.1 Physical properties of Al, Zn and AlZn alloys 7
2.2 Electrochemical properties of Zn in chloride solution 9
2.3 Anodic activation of Al by alloying with Zn 10
2.4 Electrochemical and corrosion properties of AlMn alloys . . . 12
2.5 Zn coatings for corrosion protection of Al 13
2.5.1 Zn and Al-Zn coatings 13
2.5.2 Zn-rich layers 14
2.6 Discussion 16

3 Characterization of zinc-rich layers on aluminium **21**
3.1 Introduction 21
3.2 Experimental 24
3.2.1 Materials 24
3.2.2 GD-OES calibration procedure. 27
3.2.3 Surface morphology and elemental analysis 29
3.3 Results 30
3.3.1 Composition and dendritic structure of AlZn standard alloys 30
3.3.2 GD-OES calibration for AlZn system 33
3.3.3 Zn concentration profiles on coated AlMn substrate . . 38
3.3.4 Profiles for alloying elements and oxygen 42
3.3.5 Surface characterization 57
3.4 Discussion 65
3.4.1 GD-OES calibration 65
3.4.2 Element profiles 67
3.5 Conclusions 68

4 Modelling of Zn diffusion in Al alloy . . . 73
4.1 Introduction . . . 73
4.2 Theory . . . 74
4.3 Experimental . . . 77
4.4 Numerical Procedure . . . 77
4.5 Results . . . 79
4.6 Discussion . . . 89
4.7 Conclusions . . . 92

5 Continuous immersion corrosion testing of zinc-rich layers on aluminium in acidified chloride solution . . . 95
5.1 Introduction . . . 95
5.2 Experimental . . . 97
5.3 Results . . . 101
 5.3.1 Potentiodynamic polarization . . . 101
 5.3.2 Corrosion potential measurements during immersion . 103
 5.3.3 Continuous immersion corrosion test . . . 107
 5.3.4 Corrosion potential measurements in craters produced by GD-OES Ar-sputtering . . . 115
 5.3.5 Correlation between corrosion potential, Zn concentration and reduction in thickness . . . 116
5.4 Discussion . . . 120
5.5 Conclusions . . . 124

6 Characterisation of corrosion morphology and surface chemistry of zinc-rich layers on aluminium in acidified chloride solution . . 129
6.1 Introduction . . . 129
6.2 Experimental . . . 131
6.3 Results . . . 132
 6.3.1 Corrosion morphology . . . 132
 6.3.2 Local elemental analysis after immersion test . . . 148
 6.3.3 Correlation between corrosion potential and Zn concentration . . . 152
 6.3.4 Correlation between corrosion rate and Zn concentration 154
 6.3.5 Comparative summary of corrosion morphology and chemistry of Zn-rich layers . . . 154
 6.3.6 GD-OES of corroded surfaces . . . 158
6.4 Discussion . . . 161
6.5 Conclusions . . . 165

7 Discussion . . . 167
7.1 Anodic protection of Al by Zn . . . 167
7.2 Characterisation of Zn-rich layers on Al . . . 169
7.3 Modelling of corrosion of Zn-rich layers . . . 170
7.4 Improvement of protection of Al alloys . . . 172
7.5 Suggestions for future work . . . 173

8 Conclusions . . . 177

Chapter 1

Introduction

1.1 Background

Aluminium is widely used in the automotive industry, amongst others as a material for heat exchange applications [1], such as radiators, coolers and heat pumps. Aluminium multi-port extruded (MPE) tubes developed for these applications vary significantly in size and tube wall thickness, which can be lower than 1 mm. Examples of the tubes are shown in figure 1.1. As Al is susceptible to pitting corrosion in presence of aggressive ions, such as chlorides, additional corrosion protection is required for future potential applications of Al MPE tubes in heat, ventilation, air-conditioning and refrigeration industry.

FIGURE 1.1: Aluminium MPE tubes. Reproduced with permission from Sapa AS.

Zinc coatings are widely used for corrosion protection of steel [2]. Zn coating, firstly, works as a barrier between steel and environment. It also provides cathodic protection by galvanic action in case the coating is damaged. Zinc corrosion products in the form of zinc hydroxide precipitate on the places where the coating was damaged and serve as a second barrier [3–5]. ZnAl alloy coatings with 5 and 55 wt% Al were developed to provide higher corrosion resistance of steel [6], the latter providing superior corrosion protection. The most common way to deposit Zn coating on steel is hot dip galvanizing [2], while electroplating can also be used [7].

Several studies show that coating of Al with Zn and AlZn alloys [8–11] can successfully protect Al against pitting due to reduction of the corrosion potential into the passive zone. However, self-corrosion rate of Zn coatings and AlZn alloys with high Zn content was found to be significantly higher than that of the Al alloy itself. Therefore, AlZn alloy coatings with the lower Zn content appear to be more beneficial [8, 9]. Another promising approach is to use a diffusion layer of Zn (Zn-rich layer) in Al alloy, obtained by heat treatment of Zn or AlZn coating [12]. It was suggested that the diffusion layer acts as multicladding, where surface layer with higher Zn concentration provides cathodic protection of the rest of diffusion layer with lower Zn concentration. This effect is beneficial due to relatively high corrosion rate of AlZn coatings with low Zn concentration [8, 9].

No scientific literature on hot dip galvanized Al was published. The reason must be high temperature of the Zn molten bath, at which Al is not stable. After dissolution of the aluminium oxide, which is initially present on the surface, the metal itself corrodes too fast in the bath without allowing a possibility to control the process. Electroplating of Zn on Al, as well as electroless Zn plating, or zincating, produce coatings with dendritic structure and poor adhesion [13, 14]. Additives should be used for improvement of the coating structure and adhesion. Zincating without additives by a two-step process has also been reported [15]. However, long immersion time required for this deposition method, as well as electroplating, is also unfavourable, while Zn coatings obtained by electroless immersion are too thin for present purposes. The common way for deposition of Zn on the Al alloy components used by the industry is thermal spraying [10]. The main advantage of this method is fast speed, while the coatings themselves are found to be porous and non-uniform [16].

In order to be able to study influence of Zn concentration profile and Zn-rich layer thickness on corrosion properties, Zn depth profiling of the layers on Al should be performed. Profiling of Zn, as well as minor alloying elements and oxygen, can be done using glow discharge optical emission spectroscopy (GD-OES), which is a fast method with high depth resolution and sensitivity [17]. However, GD-OES is a comparative technique, which requires careful calibration for achievement of quantitative results with good accuracy.

The most common way for corrosion testing of materials for heat exchange application is sea water acidified accelerated test (SWAAT) (ASTM G85). The test includes consecutive cycles of spraying with acidified artificial sea water for 30 minutes and soaking in 98% humidity for 90 minutes of the samples located in a test chamber kept at 49 °C temperature. However, salt spray tests cannot provide information about electrochemical behaviour necessary for scientific research.

1.2 Objectives and methods

This work focuses on improvement of corrosion resistance of Al alloys against pitting by development of Zn-rich coatings. The main objectives are to:

- obtain improved understanding of the mechanisms of formation of the Zn sprayed layer, its diffusion during heat treatment and protection of the obtained Zn-rich layer of the All alloy substrate against pitting by depth profiling, charaterisation of the surface structure and morphology, corrosion testing, and electrochemical characterization,
- develop characterization methods to obtain information about elemental composition, microstructure and corrosion properties of the Zn-rich layers,
- minimize the uniform corrosion by optimizing the Zn concentration profile and thickness of the Zn-rich layer without decreasing the pitting resistance of the underlying substrate,
- study the effect of Zn concentration on the corrosion potential and estimate minimum value required to obtain protection against pitting,
- study the effect of Zn concentration on the self-corrosion rate of the Zn-rich layer,
- investigate the possible heavy-metal contamination of the AlMn alloy surface during extrusion in the form of precipitated intermetallic particles and their effect on the corrosion properties of the Zn-rich layers,
- develop a model for estimation of corrosion rate and service life of Zn-rich layers based on coating parameters, such as Zn concentration and thickness, and heat treatment conditions, ultimately for use in the optimization process.

In order to achieve the objectives stated above, Zn thermal-arc sprayed coating on AlMn alloy, supplied by Sapa AS, was used. Chromic-phosphoric treatment, according to ASTM G1, was used in order to produce Zn coatings with lower Zn load than that possible by thermal-arc spraying. Zn-rich layers, obtained by heat treatment of Zn coatings with different Zn loads, were studied by GD-OES, scanning electron microscopy and X-ray energy dispersive spectroscopy to obtain information about their morphology and chemistry. The samples were further subjected to continuous immersion corrosion testing in acidified artificial sea water solution with pH between 2.9 and 3 at 25 °C, combined with corrosion potential measurements. Corrosion rates were estimated based on weight loss measurements of the samples after the test.

1.3 Structure of the thesis

The thesis consists of a literature review (Chapter 2), technical chapters (Chapters 3 to Chapter 6), overall discussion including suggestions for future work (Chapter 7) and conclusions of the thesis (Chapter 8). Chapter 2 provides a literature review on the influence of Zn on electrochemical properties of Al. The available publications on Zn-rich coating on Al alloys are also discussed with the purpose of justifying the objectives of the present work. In Chapter 3, calibration of GD-OES for Al-Zn system including minor alloying elements and oxygen is thoroughly described. Elemental composition, as well as morphology, of the Zn-rich layers on the AlMn alloy of interest are investigated. Chapter 4 discusses the possibility of modelling of Zn diffusion from a coating into Al by using a solution to the simple one-dimensional form of Fick's second law and an effective binary coefficient for the system. In chapter 5, results of immersion corrosion testing are presented. Chapter 6 presents results of microscopic study of corrosion morphology, as well as elemental analysis of corroded surfaces, and discusses an attempt to correlate corrosion potential and corrosion rate with Zn concentration of corroded regions.

References

1. J. Kaufman, Corrosion of aluminum and aluminum alloys, in ASM Handbook, vol. 13B, Corrosion: Materials, 9th ed., pp. 95–124, ASM International, ASM Handbooks Online (2005).
2. H. E. Townsend, Continuous hot dip coatings, in ASM Handbook, vol. 5, Surface engineering, pp. 339–348, ASM International, in ASM Handbooks Online (1994).
3. K. Ogle, V. Baudu, L. Garrigues, X. Philippe, *Journal of The Electrochemical Society*, **147**, 3654–3660 (2000).
4. K. Ogle, S. Morel, D. Jacquet, *Journal of The Electrochemical Society*, **153**, B1–B5 (2006).
5. F. Thébault, B. Vuillemin, R. Oltra, K. Ogle, C. Allely, *Electrochimica Acta*, **53**, 5226–5234 (2008).
6. X. G. Zhang, Corrosion and electrochemistry of zinc, pp. 259–260, Plenum Press, New York (1996).
7. A. Sato, Zinc plating, in ASM Handbook, vol. 5, Surface Engineering, pp. 227–235, ASM International, in ASM Handbooks Online (1994).
8. H. Campbell, F. Porter, Proceedings of 1st International Congress on Metallic Corrosion, London, 1961, pp. 517–530, Butterworths, London (1962).

9. J. C. S. Fernandes, M. G. S. Ferreira, *Surface and Coatings Technology*, **53**, 99–100 (1992).
10. Y. G. Kweon, C. Coddet, *Corrosion*, **48**, 97–102 (1992).
11. X. Zhang, S. Lo Russo, A. Miotello, L. Guzman, E. Cattaruzza, P. L. Bonora, L. Benedetti, *Surface and Coatings Technology*, **141**, 187–193 (2001).
12. H. Ikeda, *Aluminium*, **58**, 467–471 (1982).
13. S. G. Robertson, I. M. Ritchie, *Journal of Applied Electrochemistry*, **27**, 799–804 (1997).
14. W. G. Zelley, *Journal of The Electrochemical Society*, **100**, 328–333 (1953).
15. M. Suzuki, A. Sugihara, T. Sano, T. Suzuki, Zincating aluminium, Patent No: EP0125352A1, Alcan International Limited, Canada (1984).
16. B. Shaw, A. Leimkuhler, P. Moran, Corrosion performance of aluminum and zinc-aluminum thermal spray coatings in marine environments, Testing of metallic and inorganic coatings, STP20041S, pp. 246-264, ASTM International, West Conshohocken, PA (1987).
17. T. Nelis, R. Payling, Glow discharge optical emission spectroscopy: a practical guide, RCS, Cambridge, UK (2003).

Chapter 2

Literature review

The main topics of this thesis concern influence of zinc depth profile on electrochemical and corrosion properties of Zn-rich coatings on aluminium. The purpose of this chapter is therefore firstly to review physical and electrochemical properties of Al and Zn. Secondly, a short summary on physical and electrochemical properties of AlZn alloys will be given with emphasis on influence of Zn on corrosion behaviour of Al alloys. Finally, available literature on Zn-rich coatings on Al alloys will be reviewed.

2.1 Physical properties of Al, Zn and AlZn alloys

Corrosion properties of Zn-rich coatings on Al alloys will be influenced by physical properties of the pure metals themselves and solid solubility of one in another. Physical properties of Al and Zn are compared in table 2.1. These metals have large differences in crystal structure and atomic radius, while their electronegativity is quite similar. Zn is almost three times denser than Al and has a melting temperature of 420 °C, which is 240 °C lower than that for Al. Diffusion coefficient of Zn in Al is quite high compared to diffusion coefficients of typical alloying elements, such as Fe, Mn [1]. Diffusion coefficient of Mg is slightly lower than that of Zn, while Si has diffusion coefficient similar to Zn in Al. Diffusion coefficients of these elements at different temperatures are summarized in table 2.2.

TABLE 2.1: Physical properties of Al and Zn.

Element	**Al**	**Zn**
Melting point (°C) [2]	660	420
Density (kg/cm^3) [3]	2.7	7.14
Atomic radius (pm) [3]	143	133
Crystal structure [4]	Face-centered cubic (fcc)	Hexagonal close-packed (hcp)
Electronegativity (Pauling scale) (V) [3]	1.61	1.65

TABLE 2.2: Diffusion coefficients (m^2/s) of Mn, Fe, Zn, Mg and Si in Al [1].

Element	Temperature (°C)				
	350	**390**	**430**	**470**	**510**
Mn	2.3×10^{-20}	2.7×10^{-19}	2.4×10^{-18}	1.7×10^{-17}	9.7×10^{-17}
Fe	4.1×10^{-19}	5.0×10^{-18}	4.5×10^{-17}	3.3×10^{-16}	1.9×10^{-15}
Zn	2.2×10^{-15}	8.5×10^{-15}	2.8×10^{-14}	8.2×10^{-14}	2.1×10^{-13}
Mg	1.2×10^{-15}	4.8×10^{-15}	1.7×10^{-14}	5.0×10^{-14}	1.4×10^{-13}
Si	1.9×10^{-15}	7.5×10^{-15}	2.5×10^{-14}	7.4×10^{-14}	2.0×10^{-13}

According to the Al-Zn binary phase diagram shown in figure 2.1 [5], the Al-Zn system has an eutectic point at 381 °C. Zn concentration at the eutectic point is 95 wt%. At the eutectoid point at 277 °C the solid solution contains 77.7 wt% Zn. Al solid solution with fcc structure lies in a wide range between 2 wt% at 20 °C and 83.1 wt% Zn at the eutectic temperature. A miscibility gap exists between 32.4 and 77.7 wt% Zn, with a critical point at 351.5 °C and Zn concentration of 61.3 wt% [5]. The miscibility gap divides Al into two types of solid solutions with Zn, αAl on the Al-rich side and α'Al on the Zn-rich side, although both with fcc structure. The highest solubility of Al in Zn with hcp structure is 1.2 wt% at the eutectic temperature. Solubility of Al in Zn can be increased by rapid solidification [5]. Solubilities of Al and Zn in each other at different temperature points are summarized in table 2.3.

TABLE 2.3: Solubility data of Al-Zn system at different temperatures [5].

Temperature (°C)	**20**	**100**	**200**	**277**	**381**
Solubility of Zn in Al (wt% Zn)	2	5	12.5	32.4 and 77.7	83.1
Solubility of Al in Zn (wt% Al)	0.03	0.08	0.33	0.7	1.2

AlZn alloys possess dendritic microstructure for compositions between about 5 - 90 wt% Zn with Al-rich dendrites and Zn-rich interdendritic regions [6–9]. Alloys with Zn concentration close to the eutectic show lamellar structures [9].

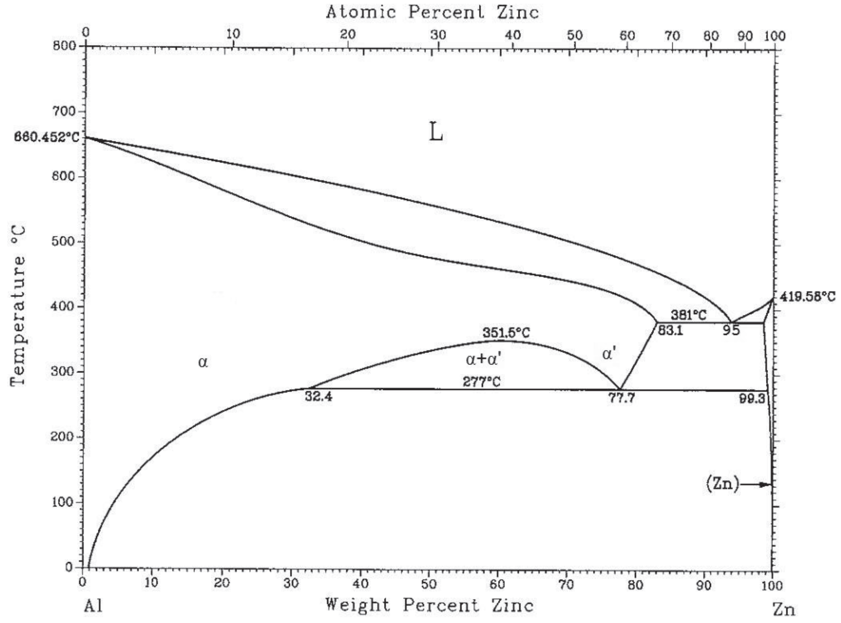

FIGURE 2.1: Al-Zn binary phase diagram [5].

2.2 Electrochemical properties of Zn in chloride solution

According to the Pourbaix diagram [10], oxidation of Zn is thermodynamically possible, with hydrogen evolution as the reduction process, over the entire practical pH range in aqueous solutions. In acidic and neutral solutions dissolution occurs via a charge-transfer reaction [11]

$$Zn \leftrightarrow Zn^{2+} + 2e^{-} \tag{2.1}$$

This oxidation mechanism gives a Tafel slope of 40 mV/decade [11, 12] with hydrogen evolution occurring via proton reduction as the cathodic reaction with the Tafel slope 120 mV/decade [13]. Hydrogen overpotential on Zn is quite large due to small hydrogen exchange current density, which is suggested to originate from weak interaction between zinc and hydrogen and, hence, absence of chemisorbed layer of atomic hydrogen [14]. Hydrogen exchange current density is independent of pH except in concentrated acid and alkaline solutions.

Recent studies [11, 15] suggest that oxygen reduction reaction is the dominating cathodic reaction at pH between 4 and 11, which leads to local alkalization of the surface due to release of HO^{-} ions. The kinetics of the reduction process is nearly independent of pH in this range [11]. Between pH 4 and 6 oxygen reduction is mass-transfer controlled [16]. In NaCl solution of pH 6.5, a very porous corrosion layer is formed on Zn, which consists mostly of zinc hydroxy chloride and carbonate, and is not passivating [15, 17]. Between pH 7 and 10, the formation of ZnO, which is thermodynamically predicted [10], is suggested to be accompanied by release of protons due to formation of $ZnOH^+$ by metal hydrolysis, which destabilizes the ZnO layer [11, 13, 15].

At pH between 10 and 12, formation of $ZnOH^+$ is reduced, and a ZnO/ $Zn(OH)_2$ layer is precipitated, which serves as a barrier to HO^- ions [11, 18]. At pH > 13 soluble zinc-hydroxy complexes, such as $ZnOH_3^-$ and $ZnOH_4^{2-}$, are formed instead, which are less stable [18]. To summarize, it can be concluded that Zn shows passive behavior only between pH 10 and 12.

Corrosion potential of Zn in 1 M NaCl solution is about -1.1 V_{SCE} [13]. Corrosion potential of Zn decreases with increasing concentration of Cl^-, SO_4^{2-}, Br^- and I^- with the same slope [19]. Electrolyte pH has no significant influence on the corrosion potential of Zn for pH < 8 in solutions containing Cl^-, SO_4^{2-}, NO_3^- [20]. In contrast, the corrosion current in chloride solutions is very much dependent on pH [12]. It is lowest between pH 8 and 12 [11, 20]. Corrosion rate of Zn in seawater is higher than for other common metals including Al [21]. With increasing temperature in synthetic sea water, precipitation of corrosion products increases and corrosion rate decreases [22]. This can be attributed to formation of calcium carbonates [22] or zinc hydroxy carbonates, which can inhibit corrosion if they form compact layers [23, 24]. Increasing chloride concentration up to 5 g/l enhances corrosion of Zn, while further increase of chloride concentration inhibits it [21]. This is associated with formation of a film of zinc chloride containing other corrosion products.

2.3 Anodic activation of Al by alloying with Zn

Corrosion behaviour of Al alloyed with Zn has been studied before [25–34]. Redding and Newport [25] were first to report reduction of pitting potential by addition of Zn. Even small additions of Zn (up to 0.12 wt%) were found to increase the passive current and decrease the stability against pitting relative to pure Al [31, 32]. At the same time, alloying with 0.2 wt% Zn was reported to decrease pit density and depth significantly, while a more uniform corrosion occurred [29]. However, contrary to the above, it was suggested that alloying with Zn did not influence pit nucleation frequency, while the dissolution rate was increased [26, 28, 30, 32, 33]. It was also found that pitting potential of AlZn alloys with up to 2 wt% Zn decreased with increasing chloride concentration and was independent of pH [33]. As an explanation, Muller and Galvele [28] suggested that, while the localized acidification is the main reason for pitting of Al, alloying of Al with Zn resulted in increase in the overpotential for hydrogen evolution, causing decrease of the potential inside the pits. However, this mechanism is related more to propagation rather than initiation of pits.

In AlZn alloys with high Zn concentrations, which possess dendritic microstructure, preferential corrosion occurs [27]. In open circuit conditions only phases with pitting potential lower than the corrosion potential of the alloy (for example, Zn-rich interdendritic regions) are preferentially attacked, while phases with higher pitting potential (for example, Al-rich dendritic regions) remain unattacked. Dependence of corrosion potential on coarseness of dendritic structures was also reported [35, 36].

Pitting potential values for high purity binary AlZn alloys measured in references [25, 27, 28, 30, 31, 33, 34] are shown in figure 2.2 with respect to Zn concentration. Table 2.4 summarizes the techniques and electrolytes used for measurement of the pitting potential. Quite good agreement between data from these studies is observed in figure 2.2 with the exception for work [31]. The reason must be too high scan rate, which was reported to result in high errors of pitting potential measurement of Al [37], while potentiostatic techniques were found to be the most reliable. In work [31], as in works [25, 34], the pitting potential decreased with increasing Zn concentration up to about 3-4 wt% Zn, and was not affected by further increase of concentration.

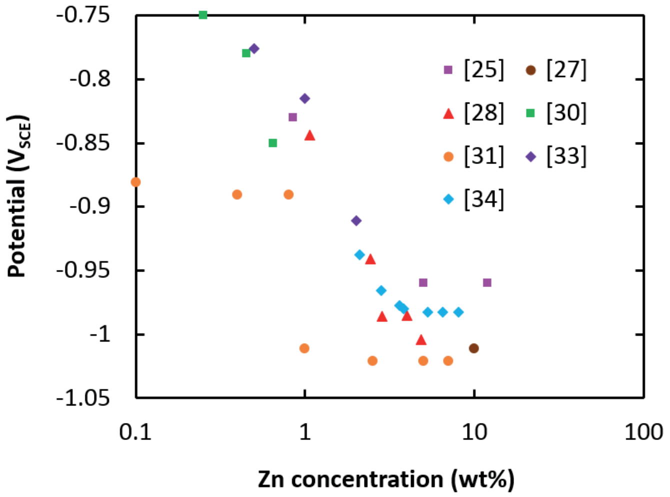

FIGURE 2.2: Pitting potential of high purity binary AlZn alloys [25, 27, 28, 30, 31, 33, 34]. The measurement techniques and electrolytes are summarised in table 2.4.

TABLE 2.4: Summary of measurement techniques and electrolyte properties for measurement of pitting potential of high purity binary AlZn alloys found in literature [25, 27, 28, 30, 31, 33, 34] and shown in figure 2.2.

Reference	**Electrolyte**	**Technique**
[25]	Syntetic sea water	Galvanostatic
[27]	1M NaCl solution, deareated	Galvanostatic and potentiostatic
[28]	1M NaCl solution, deareated, 25 °C	Galvanostatic and potentiodynamic
[30]	1M NaCl, pH = 3, 40 °C, deareated	Potentiodynamic (0.5 mV/s)
[31]	3 wt% NaCl	Potentiodynamic (10 mV/s)
[33]	0.5 M NaCl, room temperature, deareated	Galvanostatic and potentiodynamic (0.5 mV/s)
[34]	53 g/l NaCl + 3 g/l H_2O_2, 25 °C	-

In AlZn alloys most of the Zn is in solid solution with Al [38]. However, in commercial alloys, Zn can precipitate in the form of intermetallic particles $MgZn_2$, Mg_2Zn_{11}, $Mg_3Zn_3Al_2$, Mn_3ZnAl_{24} and $Al_{32}Zn_{49}$ [38, 39]. In reference [39] corrosion potential of $MgZn_2$ and $Al_{32}Zn_{49}$ particles in chloride solution was measured to be slightly lower than that of the pure Zn.

2.4 Electrochemical and corrosion properties of AlMn alloys

Addition of Mn to pure Al increases the pitting potential of Al in chloride solutions by about 50 mV per 1% Mn in solid solution [25, 40]. Most Mn in AlMn commercial alloys precipitate in the form of the primary Al-rich phases $(Fe,Mn)_3Si_2Al_{15}$ and $(Fe,Mn)Al_6$ intermetallic particles [41]. Since Fe is significantly more noble than Al and has very little solubility in Al, it precipitates as cathodic Al_3Fe particles, which increase the pitting susceptibility of the Al matrix [42]. This effect is reduced in AlMn alloys due to formation of forementioned $(Fe,Mn)Al_6$ and $(Fe,Mn)_3Si_2Al_{15}$ particles in the presence of alloyed Mn and Si. Solid solubility of Mn in Al is reduced by addition of Fe and Si [41]. By formation of these phases the cathodic nature of Fe is reduced by decreasing their nobility closer to the potential of the matrix [40, 42–44]. During corrosion, Al, as the less noble component of the particles, oxidizes preferentially and the corrosion potential of the particles increases or decreases depending on the ratio of Fe and Mn concentrations becoming enriched on the surface [42]. It has been shown that thermo-mechanical processing and heat treatment of AlMn alloys can lead to high precipitation of Fe-rich intermetallic particles, while the matrix becomes depleted in noble alloying elements [45–47]. As a result, the difference between potential of the particles and the matrix increases. This deformed layer becomes more susceptible to corrosion than the substrate bulk and can lead to filiform corrosion.

2.5 Zn coatings for corrosion protection of Al

2.5.1 Zn and Al-Zn coatings

Papers available in the open literature about Zn coatings for corrosion protection of aluminium are quite scarce [48–52]. Work on corrosion of 4 µm thick pure Zn coatings on 3103 Al alloy in 0.1 M NaCl solution [51] and thermally sprayed pure Zn and ZnAl alloy (with 85 and 98 wt% Zn) coatings on 5086 Al alloy in synthetic sea water [50] claimed that coatings functioned as sacrificial layers and provided galvanic protection of the substrate. However, the coatings were susceptible to significant general self-corrosion. Corrosion potential of the coated sample in reference [51] was reduced by about 200 mV compared to the uncoated sample, and its corrosion rate was about 10 times higher.

Zn-Mg pigments of 74 wt% and 80 wt% Zn, added to a two-pack epoxy system and sprayed on aluminum alloys AA2024 and AA5754 to form coatings of about 80 µm thickness, were found to provide protection against pitting in NaCl slolution [52]. The results were similar to that shown in references [50, 51]. Corrosion potential of the coated samples was lower than for the uncoated Al alloys, while the self-corrosion rate was higher. The coatings were able protect the substrate against pitting in salt spray tests up to 3000 hours.

AlZn coatings with 3 and 6 wt% of Zn, deposited by physical vapour deposition on 7075 Al alloy, appeared to dissolve very slowly in the presence of 3.5% NaC1 and thus claimed to suit well for corrosion protection [49]. Corrosion potential of the coated samples was reduced compared to the substrate and was lowest for the Zn concentration of 6 wt%. Corrosion rate was higher for the coating with 3 wt% Zn than for the coating with 6 wt% Zn. No explanation was given for this behaviour.

AlZn coatings with even lower Zn concentrations (0.75, 1 and 1.25 wt%) were applied as cladding on AlMn alloy [48]. Immersion testing in various public supply waters for 10 – 12 months showed that 1.25 wt% Zn content was sufficient for protection against pitting as no pits perforating through the cladding were formed. No significant difference in the corrosion rates of the claddings in all of the supplied waters was observed. Corrosion rate in waters with the highest chloride concentration (35 ppm) was about 50 µm/year. 1 wt% Zn clad showed better performance for the substrate alloy with 0.04 wt% Cu compared to the same coating on the substrate alloy with 0.15 wt% Cu. This result was explained in terms of decrease in the absolute value of the slope of the cathodic polarisation curve with increasing copper content. This was attributed to higher electrical conductivity of the surface film. As a result, samples with higher Cu content had higher corrosion potential compared to the samples with lower Cu content for a given Zn concentration in the cladding. The potential provided by cladding with 1 wt% Zn was not sufficient to polarize the substrate with the higher copper content to the potential sufficiently negative for galvanic protection against pitting and, therefore, pits penetrating trough the coating were observed. Increasing the Zn concentration in the cladding to 1.25 wt% reduced the potential of the substrate sufficiently, such that no pits penetrating the cladding were formed, as already mentioned above. Zn content of 0.75 wt% in the cladding was not sufficient to lower the potential for protection of the substrates against pitting and many perforating pits were found on samples with this cladding.

In references [48–52] the type of protection provided by the Zn-rich coatings is called galvanic or cathodic. Zn lowers the potential of the Al substrate into its region of passivity rather than close to its thermodynamic reduction potential, as for conventional cathodic protection of steel, due to the possibility of cathodic corrosion [53]. The phenomenon of passivity is the base for anodic protection [54], hence, such protection should perhaps be called anodic rather than cathodic [55]. In the absence of a clear terminology, the term "galvanic protection" is also used in this thesis to refer to passivation of the surface by use of Zn-rich coatings or layers.

2.5.2 Zn-rich layers

In the literature reviewed above, there is no information about formation of Zn-rich layers by controlled diffusion of Zn coating into the Al substrate by heat treatment and the effect of such Zn-rich layers formed on the corrosion resistance of the underlying Al-alloy substrate. However, heat treatment of Zn coatings on Al, leading to creation of a diffusion layer of Zn, has been used widely by the industry. Enhancement of corrosion resistance of Al against pitting by such layers was claimed in patents [56–60]. The deposition method, Zn load, heat treatment parameters and resulting Zn diffusion layer parameters reported in these patents are summarised in table 2.5. Patents [56–58] describe deposition of Zn via electroless zinc plating, or zincating, while in patents [59, 60] Zn is deposited by thermal spraying. As can be seen from the table, Zn load and heat treatment parameters and the properties of the resulting Zn diffusion layer suitable for protection of Al

TABLE 2.5: Summary of Zn coating properties, heat treatment parameters and resulting Zn diffusion layer properties reported in patents [56–60].

Reference	**Deposition method**	**Zn load (g/m^2)**	**Heat treatment**	**Zn diffusion layer parameters**
[56]	Zincating	1 - 100	400 to 600 °C for 1.5 - 10 h	at least 0.5 wt% Zn at 25 μm distance
[57]	Zincating	5 - 20	590 to 610 °C for 2 min	50 - 150 μm depth, 1 - 7 wt% Zn
[58]	Zincating	3 - 15	400 to 600 °C for 1.5 - 10 h	50 - 150 μm depth, 0.5 - 7 wt% Zn
[59]	Thermal spraying	6 - 12 (7 - 10 preferred)	470 to 620 °C (480 - 590 °C preferred) for 5 min - 10 h	-
[60]	Thermal spraying	2 - 16 (2 - 8 preferred)	580 to 610 °C for 3 - 15 min	at least 0.2 wt% Zn at 60 μm distance

against pitting vary widely, and no conclusion about obtaining an optimal Zn-rich layer can be drawn from these results.

The only scientific work about Zn diffusion layers for protection of Al alloys against pitting was published by Ikeda [61], who produced these layers by heat treatment of AlZn alloy clad coating (with 0.37 - 5 wt% Zn) on 3003 Al alloys and subjected these to different corrosion tests. Higher Zn surface concentrations were reported to lead to higher corrosion rates. Zn surface concentrations of 1.1 to 2.2 wt% were found to be optimal for protection against pitting while the optimal depth of the diffusion layer was assigned to be 50 - 100 μm deeper than the maximum permitted corrosion depth set for the particular application and length of the protection period. It was suggested that Zn diffusion treatment works in the same way as multicladding, meaning that lower Zn regions at depths close to the substrate surface are protected by higher Zn regions closer to the surface.

2.6 Discussion

The reviewed literature on the effect of Zn on corrosion properties of Al alloys discusses mostly decrease of pitting potential of Al with increasing Zn content. The pitting potential should be lowered by addition of Zn sufficient for protection of Al against pitting in chloride solutions. There is no agreement in the literature on which Zn concentration is suitable for this purpose. It can be concluded that at least 0.2 wt% Zn is required to suppress pitting in chloride solutions [29], although, some of the papers report pitting for alloys with higher Zn concentrations [28]. Significantly high self-corrosion rate of Zn and the reported increase of corrosion rate with increasing Zn concentration in AlZn alloys or Zn-rich layers on Al put constrains on the Zn concentration in the Zn- rich layer. In the presence of chloride, difference between 1.25 and 1 wt% Zn was found to be important [48]. At the same time, information about the effect of the alloy type is limited, as most of the studies were performed with binary alloys. Preferential corrosion of Zn from AlZn alloys would be expected due to the difference in their corrosion potentials in the galvanic series for chloride environments. However, no results on the effect of dealloying is available.

Effect of AlZn alloy microstructure, especially Zn-enriched interdendritic regions, can also have impact on corrosion properties of the alloys, as was suggested in reference [27]. If corrosion is localized only on Zn-rich interdendritic regions, a direct correlation of pitting potential with Zn concentration of the alloy is not feasible. This suggestion can explain invariance of pitting potential with Zn concentration after reaching a certain concentration level reported in references [25, 31, 34].

The purpose of the present work is to study the possibility of protection of AlMn alloys against pitting by Zn-rich layers. The available literature seem to indicate that such protection is possible by presence of Zn at concentrations as low as 1 wt% in the coating or as alloying in the aluminium alloy substrate itself. One drawback with Zn in the alloy is that its presence appears to impart a significant self-corrosion rate to the alloy. The cause of this behaviour does not appear to be clear from the available literature. With this property in mind, it may be desirable to apply Zn as a coating rather than alloying it in the Al substrate. The use of plasma arc spraying is probably a convenient in terms of cost (although a significant amount of Zn is wasted in the process) and avoiding significant change in the properties of the substrate alloy by undesirable Zn content and thermal exposure. However, the effect and significance of such high Zn concentration at the surface and feasibility of forming Zn-rich layers near the surface are not well known.

The scientific objective is therefore to improve the understanding of the formation of the layers by plasma arc spraying and subsequent heat treatment and the mechanisms for the type of protection provided to the Al alloy substrate by such layers in acidified synthetic sea water environment. It is also of interest to what extent self-corrosion of the layers can be minimized by optimizing the Zn concentration profile and thickness of the Zn-rich layer without decreasing the pitting resistance. The existing know-how about these matters is limited based on the review above, thereby justifying the stated objectives of this work.

References

1. Y. Du, Y. A. Chang, B. Y. Huang, W. P. Gong, Z. P. Jin, H. H. Xu, Z. H. Yuan, Y. Liu, Y. H. He, F. Y. Xie, *Materials Science and Engineering A*, **363**, 140–151 (2003).
2. C. E. Housecroft, E. C. Constable, Chemistry: an introduction to organic, inorganic and physical chemistry, Prentice Hall, Harlow, 4th ed. (2010).
3. G. H. Aylward, T. J. V. Findlay, SI chemical data, Wiley, Brisbane, Chichester, 4th ed. (1998).
4. W. M. Haynes, D. R. Lide, T. J. Bruno, CRC handbook of chemistry and physics: a ready-reference book of chemical and physical data, CRC, Boca Raton, Fla.; London, 93rd ed. (2012).
5. J. L. Murray, *Journal of Phase Equilibria*, **4**, 55–73 (1983).
6. S. Khireche, D. Boughrara, A. Kadri, L. Hamadou, N. Benbrahim, *Corrosion Science*, **87**, 504–516 (2014).
7. O. M. Suarez, E. G. Estremera, R. Soler, A. Declet, A. J. Hernandez-Maldonado, *Advances in Materials Science and Engineering*, **2014**, Article ID 963042, 6 pages (2014).
8. T. Savaskan, A. Aydiner, *Wear*, **257**, 377–388 (2004).

9. A. P. Hekimoglu, T. Savaskan, *International Journal of Materials Research*, **105**, 1084–1089 (2014).
10. M. Pourbaix, Atlas of electrochemical equilibria in aqueous solutions, National Association of Corrosion Engineers, Huston (1974).
11. S. Thomas, N. Birbilis, M. S. Venkatraman, I. S. Cole, *Corrosion*, **68** (2012).
12. Z. Zembura, L. Burzynska, *Corrosion Science*, **17**, 871–878 (1977).
13. L. M. Baugh, *Electrochimica Acta*, **24**, 657–667 (1979).
14. X. G. Zhang, Corrosion and electrochemistry of zinc, p. 39–48, Plenum Press, New York (1996).
15. M. Mouanga, P. Bercot, *Corrosion Science*, **52**, 3993–4000 (2010).
16. K. G. Boto, L. F. G. Williams, *Journal of Electroanalytical Chemistry*, **77**, 1–20 (1977).
17. M. Mouanga, P. Bercot, J. Y. Rauch, *Corrosion Science*, **52**, 3984–3992 (2010).
18. S. Thomas, I. S. Cole, M. Sridhar, N. Birbilis, *Electrochimica Acta*, **97**, 192–201 (2013).
19. V. K. Gouda, M. G. A. Khedr, A. M. S. Eldin, *Corrosion Science*, **7**, 221–230 (1967).
20. X. G. Zhang, Corrosion and electrochemistry of zinc, pp. 137–139, Plenum Press, New York (1996).
21. X. G. Zhang, Corrosion and electrochemistry of zinc, pp. 291–303, Plenum Press, New York (1996).
22. E. D. Mor, A. M. Beccaria, *Corrosion*, **31**, 275–279 (1975).
23. G. K. Glass, V. Ashworth, *Corrosion Science*, **25**, 971–983 (1985).
24. J. D. Yoo, K. Ogle, P. Volovitch, *Corrosion Science*, **83**, 32–37 (2014).
25. J. T. Reding, J. J. Newport, *Materials Protection*, **5**, 15–18 (1966).
26. R. Ramanathan, K. Raman, *Transactions of SAEST*, **6**, 132–135 (1971).
27. A. M. Zossi, A. Moralestorres, S. M. D. Demicheli, H. Biloni, *Metallurgical Transactions A*, **7**, 1489–1496 (1976).
28. I. L. Muller, J. R. Galvele, *Corrosion Science*, **17**, 995–1007 (1977).
29. K. Tohma, Y. Takeuchi, Proceedings of 7th International Light Metals Congress, Leoben-Vienna, pp. 138–139 (1981).
30. K. Tohma, Y. Takahashi, Y. Takeuchi, *Aluminium*, **61**, 277–279 (1985).
31. I. N. Ganiev, M. S. Shukroev, B. B. Eshov, *Russian Journal of Applied Chemistry*, **68**, 910–912 (1995).
32. F. Sato, R. C. Newman, *Corrosion*, **54**, 955–963 (1998).

33. F. Sato, R. C. Newman, *Corrosion*, **55**, 3–9 (1999).
34. J. Kaufman, Corrosion of Aluminum and Aluminum Alloys, in ASM Handbook, vol. 13B, Corrosion: Materials, 9th ed., pp. 95–124, ASM International, ASM Handbooks Online (2005).
35. W. R. Osorio, C. M. Freire, A. Garcia, *Journal of Alloys and Compounds*, **397**, 179–191 (2005).
36. W. R. Osorio, J. E. Spinelli, N. Cheung, A. Garcia, *Materials Science and Engineering A*, **420**, 179–186 (2006).
37. K. Nisancioglu, H. Holtan, *Corrosion Science*, **18**, 835–849 (1978).
38. L. F. Mondolfo, Aluminium alloys: structure and properties, pp. 842–882, Butterworths, London, Boston (1976).
39. N. Birbilis, R. G. Buchheit, *Journal of The Electrochemical Society*, **152**, B140–B151 (2005).
40. W. A. Anderson, H. C. Stumpf, *Corrosion*, **36**, 212–213 (1980).
41. L. F. Mondolfo, Aluminium alloys: structure and properties, pp. 834–841, Butterworths, London, Boston (1976).
42. O. Lunder, K. Nisancioglu, Proceedings of 8th International Light Metals Congress, Leoben-Vienna, 1987, pp. 706–709, Aluminium–Verlag, Düsseldorf (1988).
43. M. Zamin, *Corrosion*, **37**, 627–632 (1981).
44. K. Nisancioglu, *Journal of the Electrochemical Society*, **137**, 69–77 (1990).
45. A. Afseth, J. H. Nordlien, G. M. Scamans, K. Nisancioglu, *Corrosion Science*, **43**, 2093–2109 (2001).
46. A. Afseth, J. H. Nordlien, G. M. Scamans, K. Nisancioglu, *Corrosion Science*, **43**, 2359–2377 (2001).
47. A. Afseth, J. H. Nordlien, G. M. Scamans, K. Nisancioglu, *Corrosion Science*, **44**, 2491–2506 (2002).
48. H. Campbell, F. Porter, Proceedings of 1st International Congress on Metallic Corrosion, London, 1961, pp. 517–530, Butterworths, London (1962).
49. J. C. S. Fernandes, M. G. S. Ferreira, *Surface and Coatings Technology*, **53**, 99–100 (1992).
50. Y. G. Kweon, C. Coddet, *Corrosion*, **48**, 97–102 (1992).
51. X. Zhang, S. Lo Russo, A. Miotello, L. Guzman, E. Cattaruzza, P. L. Bonora, L. Benedetti, *Surface and Coatings Technology*, **141**, 187–193 (2001).
52. P. Plagemann, J. Weise, A. Zockoll, *Progress in Organic Coatings*, **76**, 616–625 (2013).

53. P. Gimenez, J. J. Rameau, M. C. Reboul, *Corrosion*, **37**, 673–682 (1981).
54. C. Locke, Anodic protection, in ASM Handbook, vol. 13A, Corrosion: fundamentals, testing, and protection, p. 851–854, ASM International, ASM Handbooks Online (2003).
55. K. Nisancioglu, Corrosion and protection of aluminium alloys in seawater, in D. Féron, Corrosion Behaviour and Protection of Copper and Aluminium Alloys in Seawater, pp. 145–155, Woodhead Publishing Limited, Cambridge, England (2007).
56. M. Bothwell, Diffusion cladding, Patent No: 3268358, The Dow Chemical Company, United States (1962).
57. M. Suzuki, A. Sugihara, T. Sano, T. Suzuki, Zincating aluminium, Patent No: EP0125352A1, Alcan International Limited, Canada (1984).
58. M. Suzuki, A. Sugihara, T. Sano, T. Suzuki, Process for applying a zinc coating to an aluminum article, Patent No: 4888218, Alcan international Limited, Canada (1989).
59. T. Morita, Heat exchanger, method for manufacturing the same , and heat exchanging tube, Patent No: WO2005066570, Showa Denko K.K, Japan (2005).
60. T. Morita, Aluminum pipe and process for producing same, Patent No: US20060185168, Showa Denko K.K, Japan (2006).
61. H. Ikeda, *Aluminium*, **58**, 467–471 (1982).

Chapter 3

Characterization of zinc-rich layers on aluminium

Abstract

This chapter first gives a detailed presentation of the calibration procedure for depth profiling of Zn coatings and Zn-rich layers on Al alloys by glow discharge optical emission spectroscopy (GD-OES). Zn thermal-arc sprayed coatings on extruded AlMn alloy tubes were subjected to heat treatment at various temperatures and durations to produce Zn-rich layers which were subsequently examined by GD-OES, scanning electron microscopy and X-ray energy dispersive spectroscopy (EDS). The as-sprayed Zn coating was highly non-uniform. It did not cover the Al surface completely and the non-uniformity remained after heat treatment. At the same time, increasing amounts of the constituent elements Fe, Mn, Si and Mg of the Al alloy substrate became incorporated into the layer. GD-OES was found to be a useful technique to characterize Zn-rich layers on Al despite the high difference in sputtering rates of Al and Zn. It was faster and enabled higher depth resolution and analytical sensitivity than EDS. However, its lateral resolution was large (4 mm) in relation to EDS, limiting its use to obtain laterally averaged depth profiles.

3.1 Introduction

Zn-rich layers on Al alloys are widely used for protection against pitting corrosion [1–6]. Nevertheless, the influence of the Zn concentration profile in depth and layer thickness on the corrosion properties have not been studied thoroughly. Zn composition profiling can be done by X-ray energy dispersive spectroscopy (EDS) via line scans of layer cross sections. However, the depth and spatial resolution obtainable by this method is of the order of several micrometers due to the volume of X-ray production which depends on the accelerating voltage of the incident beam and the type of material investigated [7]. The analytical sensitivity and detection limit are quite poor. This is also a time consuming method. Glow discharge optical emission spectroscopy (GD-OES) is a widely used and rapid method for depth profiling of solid materials and coatings. In GD-OES the sample is sputtered by ionised Ar atoms leading to migration of sample atoms into the negative glow region. Here they are excited by Ar ions and electrons and subsequently become de-excited emitting light with characteristic wavelength. The light is analysed by an optical spectrometer and recorded by photomultipliers. As these processes are separated, GD-OES is considered to be free of matrix effects. The depth resolution in GD-OES can be as low as several nanometers. It has high analytical sensitivity allowing detection of concentrations as low as few ppm [8]. However, GD-OES is a comparative technique, which requires careful calibration to be able to produce quantitative results with such sensitivity.

The Al-Zn system is particularly difficult to calibrate due to a large difference in the sputtering rates of Al and Zn [8]. Such calibration requires a set of AlZn alloys covering the full 0-100 wt% concentration range. Moreover, the large difference in the sputtering rates of Al and Zn makes it impossible to interpret qualitative data without calibration.

The measured intensity of an element i depends on the rate at which this element is removed from the surface (elemental sputtering rate q_i), photon emission, and their detection processes. The elemental sputtering rate depends on the overall sputtering rate of the sample q (grams per second) and elemental mass fraction ω_i (weight percent)

$$q_i = \omega_i q \tag{3.1}$$

The measured intensity is

$$I_i = k_i R_i S_i \omega_i q + b_i \tag{3.2}$$

where k_i is instrumental detection efficiency, R_i is the emission yield, S_i is correction for self-absorption, and b_i is the background signal [8]. The terms k_i, q and b_i are determined by each given set of plasma conditions, which in turn are defined by pressure and power. The term b_i moreover consists of several components including matrix components which vary with sputtering rate [9]. Nevertheless, b_i, R_i and S_i are assumed to be constant for a given element and plasma conditions, such that the relationship between I_i and q_i becomes linear, and equation 3.2 represents a linear analytical calibration equation. However, composition, ω_i, and the sputtering rate, q, of the standards must be known in order to implement the calibration.

Sputtering rate and emission process are directly dependent on the plasma conditions, determined by the Ar discharge power and pressure in the reaction chamber, which need to be adjusted individually for every material. The sputtering rate should be optimal to sustain both good depth resolution and rapid measurement, and to eliminate heating of the sample. Pressure influences the emission yield, the sputtering rate to a less extend than the power, and the shape of the crater formed on the sample, which is an important factor in obtaining high depth resolution.

The theory of relative sputtering rates [10] is commonly used to simplify the calibration process. Relative sputtering rate is the sputtering rate of a standard divided by the sputtering rate of a reference sample, usually pure iron, at the same plasma conditions. Relative sputtering rates are assumed to be independent of plasma conditions. Therefore, once measured for a standard, the value can be used for calibration at different plasma conditions. This also gives the possibility to compare sputtering rates of elements and standards independent of the plasma conditions. The sputtering rate measurements are unfortunately the largest source of error, usually error of 10-15%, in the calibration for compositional depth profiling [8]. This may introduce additional scatter in the calibration curves and errors during quantification, especially for the elements with low concentrations.

Quantification procedure in GD-OES involves estimation of the sputtering rate of the sample at each measurement point by using the analytical calibration curves for all elements,

$$q = \sum_i (I_i - b_i)/(k_i R_i S_i) \tag{3.3}$$

and then calculation of the concentration for each element,

$$\omega_i = (I_i - b_i)/(k_i R_i S_i q) \tag{3.4}$$

where the parameters q and ω_i now apply to the sputtering rate of the actual sample and the composition of species i in the sample.

There is very little literature available on GD-OES calibration of the AlZn system. Calibration for AlZn commercial alloys reported in reference [11] for the whole concentration range is based on the assumption that the concentrations of Al and Zn sum up to 100% for the whole concentration range. It results in errors in the presence of additional alloying elements and does not allow calibration for oxygen. The sputtering rate was not measured. It was estimated from data in reference [12], assuming essentially that it is equal to the sputtering rate of pure AlZn system. Reference [13] describes calibration of ZnAl alloys with Al concentration range restricted to 9.3 wt%, and calibration for only two minor alloying elements was done.

The purpose of the present work is to perform surface characterization and elemental depth profiling of Zn-rich layers on Al alloy substrates, obtained by application of a Zn coating followed by heat treatment at different temperatures and durations. The Al substrates were AlMn multi-port extruded (MPE) tubes for heat-exchange application, provided by Sapa AS. Methods of GD-OES calibration of AlZn system described in reference [13] is not suitable for the present work because it does not cover the entire concentration range of Zn and Al (0-100 wt%) which is needed to examine Zn coatings and Zn-rich layers on Al. Calibration procedure described in reference [11] is not too clear. It gives rise to significant errors related to the assumptions made, and it does not include calibration for oxygen, which is essential for the present work in view of the fact that oxide layers form as a result of application of the Zn coating and subsequent heat treatment.

The calibration of the GD-OES spectrometer described here allows for Al and Zn in the full concentration range along with calibration for other alloying and trace elements which may be present. The calibration is based on the requirement that concentrations of all elements add up to 100%. Calibration curves are based on equation 3.2 and quantification is based on equations 3.3 and 3.4, according to the software provided by the instrument producer. This procedure allows calibration of oxygen signal and more accurate calibration of the relevant alloying elements.

Elemental analysis of the Zn coating and Zn-rich layers was performed also by EDS, and surface morphology was studied by scanning electron microscopy (SEM). The data were used for further studies of corrosion properties of such surfaces in the following chapters.

3.2 Experimental

3.2.1 Materials

Standards for GD-OES calibration. Model binary AlZn alloys were cast from metals with 99.99% purity. The targeted Zn content in the alloys was 7, 25, 50, 70 and 95 wt%. These alloys are designated in this work as AlZn7, AlZn25, AlZn50, AlZn70 and AlZn95, respectively. Three samples of 1x1cm^2 size were cut from different locations of each alloy, embedded in epoxy, ground with SiC paper and polished with diamond paste to 1 μm roughness for verification of their composition by EDS, as described in Section 3.2.3 below.

In addition to 5 model alloys described above, 16 standards, obtained from various sources, were used in the GD-OES calibration. Compositions of these standards were provided by the supplier. Al alloy standards, shown in table 3.1, were selected to cover the concentration ranges of the alloying elements obtained in the depth profiles of the coated AlMn MPE substrates after heat treatment. The alloys designated as Alloy 1-6 in table 3.1 were the uncoated MPE Al tubes supplied by Sapa AS. Their composition was measured at Sapa AS by use of spark optical emission spectroscopy (Spark OES). These data were also used as part of the data base for GD-OES calibration. The certified standards AA8112, 7075AF, 2007AA, 2011AC and 5454AC were supplied by Alcan, and SQ-10WP was supplied by Alcoa. The standard designated as RA18/118 was supplied by SUS Ulrich Nell, Germany. Its composition given in table 3.1 is not certified. Such standards

TABLE 3.1: Composition of the Al alloy standards.

Sample	**Chemical composition (wt%)**									
	Al	**Zn**	**Mn**	**Fe**	**Si**	**Mg**	**Ni**	**Cu**	**Cr**	**Pb**
Alloy1	98.93	0.02	0.69	0.2	0.1	0.01	0.003	0.0016	0.009	0.0006
Alloy2	98.91	0.0015	0.74	0.2	0.08	0.013	0.003	0.0013	0.0011	0.0009
Alloy3	98.9	0.0006	0.93	0.08	0.05	0.001	0.0025	0.0008	0.0002	0.0013
Alloy4	99.08	0.002	0.15	0.17	0.09	0.0025	0.003	0.46	0.0006	0.0008
Alloy5	99.16	0.19	0.33	0.08	0.08	0.12	0.0045	0.001	0	0
Alloy6	99.16	0.003	0.23	0.48	0.06	0.004	0.003	0.003	0.0007	0.0006
AA8112	98.2	0.035	0.11	0.66	0.52	0.014	0.02	0.26	0.024	0.008
7075AF	89.02	5.75	0.031	0.17	0.19	2.66	0.027	1.75	0.22	0.0073
2007AA	92.22	0.071	0.58	0.41	0.46	0.56	0.075	4.24	0.023	1.08
2011AC	92.77	0.047	0.023	0.26	0.12	0.015	0.024	5.62	0.019	0.53
5454AC	95.11	0.03	0.75	0.4	0.25	3.16	0.033	0.1	0.03	0.0035
SQ-10WP	99.99	0.0002	0	0.0004	0.0004	0.0002	0	0.0004	0	0
RA18/118	70.46	0.29	0.32	0.49	16.34	0.24	2.8	8.08	0.002	0.27

are recommended by Horiba-Yvon for periodic drift correction of the spectrometer. Composition of RA18/118 was verified by EDS within the acceptable error range of 5% for major elements and 10-30% for minor elements. It was used in the calibration to cover small Zn concentration ranges.

The ceramic standard CE650, supplied by AB Sandvik Coromant, was used for calibration of the oxygen signal. Low alloyed steel standard 1766-NBS from NIST was used as a reference standard. All measured sputtering rates were divided by the sputtering rate of 1766-NBS to calculate relative sputtering rates. The compositions of these additional standards are shown in table 3.2. Al and Zn samples with 99.99% purity were also used in the calibration process. They are designated in this work as Al99 and Zn99, respectively. All standards were ground with 1000 SiC paper except the standard CE650, which was ground with a 320 diamond disc. The MPE tube samples used in the calibration were only degreased with acetone followed by rinsing in ethanol.

TABLE 3.2: Composition of additional standards.

Standard	**Chemical composition (wt%)**							
CE650	**Al**	**Ti**	**O**	**N**	**C**	**W**		
	38	22	34	0.27	4.9	0.4		
1766-NBS	**Fe**	**Mn**	**Al**	**Si**	**Ni**	**Cu**	**C**	**Cr**
	99.8	0.067	0.012	0.01	0.021	0.015	0.015	0.024

Zn coated AlMn tube samples. The coated MPE tube substrates were provided by Sapa AS. Composition of the substrate alloy, measured by Spark OES, is shown in table 3.3, both in mass fraction and mass concentration. The Zn coating was applied by thermal arc spraying immediately after extrusion. Typical Zn load on the surface, determined by X-ray fluorescence (XRF) spectrometer (CMI 900 from Oxford Instruments) was 8.0 ± 0.2 g/m^2. The tubes were cut, rinsed in distilled water, acetone and ethanol and subsequently heat treated for 1, 2, 3, 4 and 5 hours at 350, 390 and 430 °C to obtain Zn-rich layers with varying thickness and Zn concentration profiles on the surface of the AlMn substrate. Weight of the Zn coated tubes per area was 124.15 ± 0.11 mg/cm^2, based on weight and size measurements of 50 tube samples, including those which were heat-treated. Heat-treatment temperatures were selected based on values of practical significance.

The following procedure was used to produce Zn-rich layers with lower Zn loads than that possible to obtain by thermal-arc spraying. The sprayed Zn layer was thinned by use of standard hot chromic-phosphoric acid solution, conventionally used to remove anodized oxides and corrosion products from Al alloys according to ASTM G1. One liter solution consisted of a mixture of 50 ml phosphoric acid, 20 g chromium trioxide and distilled water. This solution does not attack aluminium. The Zn coated tube samples

TABLE 3.3: Composition of the substrate alloy.

Element	**Al**	**Zn**	**Mn**	**Fe**	**Si**
Content (wt%)	98.92	0.005	0.72	0.21	0.09
Content (g/cm^3)	2.685	0.0001	0.02	0.006	0.002
Element	**Mg**	**Ni**	**Cu**	**Cr**	**Pb**
Content (wt%)	0.019	0.003	0.001	0.0004	0.0006
Content (g/cm^3)	0.0005	0.00008	0.00003	0.00001	0.00002

were immersed in the solution heated to 90 °C for 10 minutes and subsequently thoroughly rinsed in tap and distilled water and dried. The weight loss per area was measured as 0.53 ± 0.07 mg/cm^2 based on 11 samples. The Zn load on such samples was estimated as 2.7 ± 0.7 g/m^2, with the assumption that the underlying Al-alloy substrate was not attacked significantly by the solution. The remaining estimated Zn weight is approximately 35% of the original Zn load (8 ± 0.2 g/m^2). The samples with Zn load of 8 g/m^2 and 2.7 g/m^2 will be designated in this work as samples with high Zn load and low Zn load, respectively. MPE tubes with low Zn load were heat treated for 4 hours at 430, 470 and 510 °C.

3.2.2 GD-OES calibration procedure.

The GD-OES instrument used was a RF glow discharge optical emission spectrometer GD-PROFILER 2 with a 4 mm anode supplied by HORIBA Jobin Yvon. The plasma parameters power and pressure were adjusted to 32 W and 600 Pa, respectively, to produce flat craters on the Zn-rich layers. These settings were used for the calibration and further characterization. The flatness of the crater bottoms was checked by a profilometer (mobile surface measuring unit Mar-Surf M400 supplied by Mahr).

Density ρ of the standards was calculated based on the composition of the alloys and the densities of the pure elements ρ_i using the constant volume approach [14]

$$\frac{1}{\rho} = \sum_i \frac{\omega_i}{\rho_i} \tag{3.5}$$

which was shown to work very satisfactorily for AlZn alloys. This assumption is not accurate for oxides, nitrides and carbides because their atomic volume is reduced due to strong covalent bonding. The empirical method used, and claimed to work well, for calculating the density of the ceramic standard is described in Reference [15]. It is assumed that the material consists of a mixture of pure elements and their compounds, each with known (experimentally measured) density. If the nature of compounds are not known *a priori*, it is assumed that these compounds are likely to form in the order of increasing electronegativity of their elemental components. For standard CE 650, these are TiO_2, Al_2O_3, AlN and Al_4C_3. A mass balance is performed in the following manner. The concentration of the compounds is calculated as a sum of concentrations of the elements required to form this compound according to the stated stoichiometries. The elements which remain free (part of Al and all W in the standard CE 650) are included in the density estimation in their elemental forms. The rest of the elements (part of Al and all W) are considered to be in pure forms. The density is then calculated by use of Equation 3.6, which includes one term on the right for selected compounds and the second one for the remaining free elements with respective calculated concentrations and measured densities.

$$\frac{1}{\rho} = \sum_i \frac{\omega_i'}{\rho_i'} + \sum_i \frac{\omega_i''}{\rho_i''} \tag{3.6}$$

where ω_i' and ρ_i' are the concentration of the metal component i and its density, and ω_i'' and ρ_i'' are the concentration of the compound i and its density, respectively. The required database and the algorithm for the foregoing evaluation are included in the instrument software.

The spectral lines used (available in the GD-OES polychromator) for the measurement of the main elements of interest are shown in table 3.4. The calibration procedure consisted of 40 s continuous measurement at 3 different locations on each standard. The measured intensities at each location were then averaged over 10 s sequential intervals and the average of these numbers was calculated. This is a standard procedure for estimation of variations due to noise, short-term stability of the instrument, inhomogeneity of the standards and variations of the distance between the anode and the sample [8]. After the measurement was done, for each element to be calibrated, standards were chosen considering the elements of interest and their targeted concentration range in the actual Zn coated MPE tube samples. Calibration plots were constructed in the form of product of concentration and relative sputtering rate versus intensity for every element. Points in the plot with concentrations exceeding twice or more of the highest value for a given element expected in the Zn coated MPE tubes, were excluded from the calibration data. Weighted residuals in the form of average difference between the measured values and the values estimated from the calibration curve divided by the standard deviation of this difference at every point, were calculated. Points on the calibration curve, with weighted residuals being ± 2.5 or higher, were also omitted.

TABLE 3.4: Spectral lines used for measurement of elements of interest.

Element	Al	Zn	Mn	Fe	Si	Mg
Line (nm)	396.152	481.053	403.448	371.994	288.158	285.213

3.2.3 Surface morphology and elemental analysis

Surface characterisation of the model AlZn binary alloys and Zn coated AlMn samples (MPE tubes) was performed by Hitachi S-3400N thermionic emission gun SEM equipped with EDS capability supplied by Oxford Instruments. EDS measurements were performed on 1x0.75 mm^2 areas at selected positions on the specimens at an accelerating voltage of 20 kV . Composition of the AlZn alloys was obtained by averaging several such measurements performed on each of three replicate samples cut from the same alloy. Similar procedure was used for Zn coated Al tube samples. The locations of analysis on each sample included areas close to the tube edges to obtain an idea about the uniformity of the Zn-rich layer, as shown in figure 3.1.

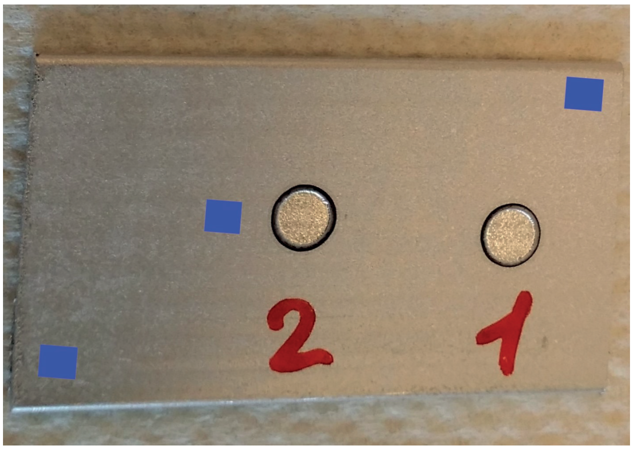

FIGURE 3.1: MPE Al tube with typical locations of analysis by EDS (blue rectangles, size is enlarged) and GD-OES (craters in the centre of the tube).

Cross-sections of selected samples were also studied by SEM to investigate further non-uniformity of the Zn rich layers. The samples were cut from MPE tubes and embedded in epoxy. Active oxide polishing to 0.04 μm roughness was performed. Analysis was performed by use of a high resolution FEG-SEM XL30S equipped with INCA-Energy EDS.

Elemental profiles of Zn coated Al samples were obtained by GD-OES using the calibration procedure described above. All such measurements were made on locations picked close to the centerline of the flat surfaces along the extrusion direction of the tubes, as shown in figure 3.1. At least one measurement was made on the opposite surface of the sample in order to take into account nonuniform Zn distribution. All profiles from different locations on the same sample were statistically smoothed out and averaged, and the curves presented in the next section are based on the average values. Errors were estimated based on relative standard deviations of the concentration due to experimental noise and variations at location of measurement on the sample. Zn coating weight per unit area was calculated by integrating the mass concentration profile of Zn with respect to depth.

GD-OES analysis was performed also on uncoated Al MPE tube sample with known composition, which was designated as Alloy 1 in table 3.1.

3.3 Results

3.3.1 Composition and dendritic structure of AlZn standard alloys

Polished surfaces of alloys AlZn7, AlZn25 and AlZn50 are characterized by large Al-rich dendrites and Zn-rich interdendritic regions (probably coring) as shown in figures 3.2a, b and c, respectively. The average cell size was approximately 150 µm for alloy AlZn7. Dendrite size decreased with increasing Zn content. Dendritic structure of alloys AlZn50 (Figure 3.2c) and AlZn70 (Figure 3.2d) was similar to that on alloy AlZn25 (Figure 3.2b). Alloys AlZn50 and AlZn70 showed in addition eutectoid and eutectic phases, respectively, in the interdendritic region. AlZn95 was an eutectic alloy with a lamellar structure, as indicated in figure 3.2e. Composition of the AlZn alloys obtained by EDS analysis is presented in table 3.5.

TABLE 3.5: Zn concentration of the AlZn binary alloys.

Alloy	**AlZn7**	**AlZn25**	**AlZn50**	**AlZn70**	**AlZn95**
Content (wt%)	6.8±0.5	26.4±1.8	49±1.5	71.6±2.4	94.5±0.8

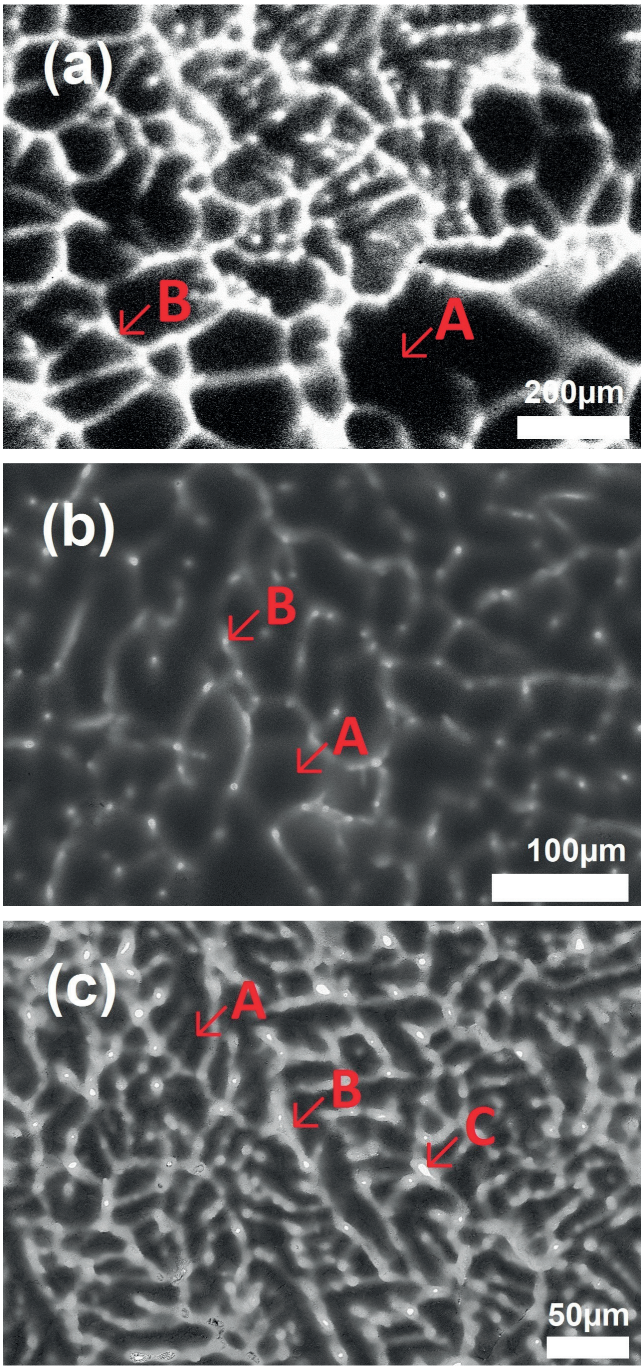
(a)
B
A
200µm
(b)
B
A
100µm
(c)
A
B
C
50µm

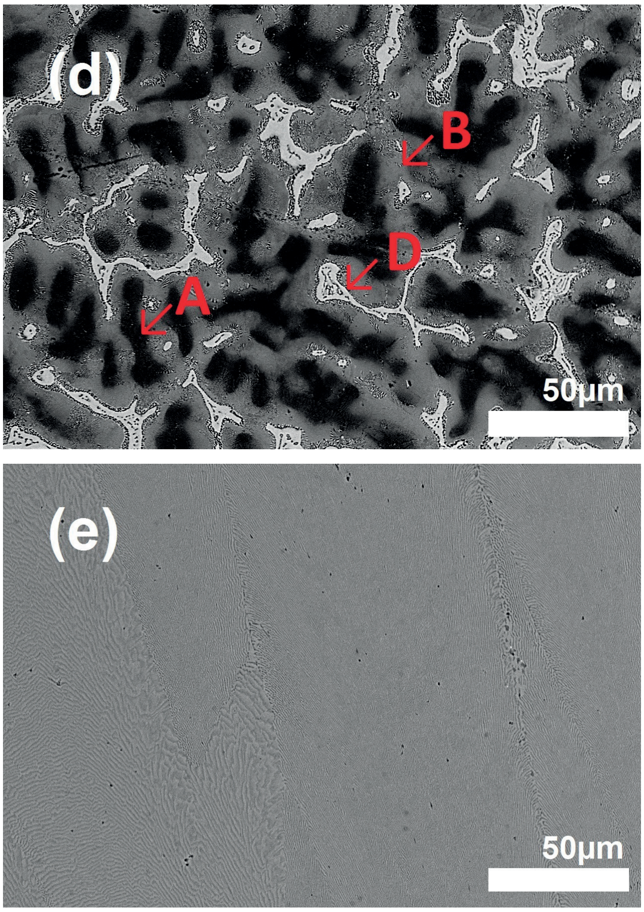

FIGURE 3.2: Backscattered SEM images of the AlZn binary alloys a) AlZn7, b) AlZn 25, c) AlZn50, d) AlZn70, and e) AlZn95. Al-rich dendrites (marked as A), Zn-rich interdendritic regions (B), eutectictoid phase (C) and eutectic phase (D) are observed.

3.3.2 GD-OES calibration for AlZn system

Density, measured sputtering rate and relative sputtering rate of the standards are shown in table 3.6. Sputtering rate measurements were within 3-7% error. Sputtering rate as a function of Zn concentration in the AlZn alloys is shown in figure 3.3. The result demonstrates the large differences between the sputtering rates of aluminium and zinc and their alloys. The sputtering rate increases significantly above 50 wt% Zn in the alloy. The calibration data for high Zn concentration are thus highly important for accurate characterisation of the initially high Zn concentration of the coating on the AlMn substrate before any heat treatment is applied.

TABLE 3.6: Densities and sputtering rates of the standards measured with applied power of 32 W and Ar pressure of 600 Pa.

Standard	**Density (g/cm^3)**	**Sputtering rate (μm/min)**	**Relative sputtering rate**
AlZn7	2.818	3.1	0.32
AlZn25	3.228	3.8	0.46
AlZn50	3.880	5.3	0.78
AlZn70	4.861	7.7	1.4
AlZn95	6.542	12.4	3.03
Alloy1	2.714	2.9	0.3
Alloy2	2.715	2.9	0.3
Alloy3	2.716	2.9	0.3
Alloy4	2.713	2.9	0.3
Alloy5	2.707	2.8	0.28
Alloy6	2.711	2.9	0.3
AA8112	2.718	3.2	0.33
7075AF	2.801	4.0	0.42
2007AA	2.820	4.1	0.44
2011AC	2.838	4.2	0.45
5454AC	2.675	3.4	0.34
SQ-10WP	2.698	2.9	0.3
RA18/118	2.874	-	0.49
CE650	3.719	1.3	0.18
1766-NBS	7.863	3.4	1
Al99	2.698	2.8	0.28
Zn99	7.13	22.1	5.89

Two calibration curves were obtained for Zn. The first one shown in 3.4a was fitted to a second degree polynomial and can be used for Zn concentrations up to 100 wt%. The intensity increases significantly after reaching 50 wt% Zn. For low intensities, the calibration data can be fitted to a straight line, as shown in figure 3.4b. It is expected to give higher accuracy

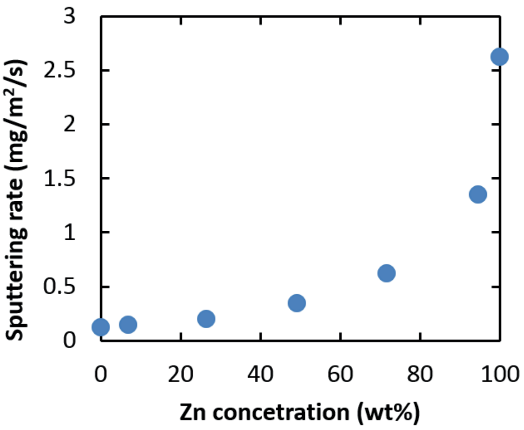

FIGURE 3.3: Sputtering rate as a function of Zn concetration in AlZn binary alloys.

in analysing Zn concentrations below 50 wt%, and it is needed particularly for characterising lower Zn concentration layers formed by heat treatment. The coefficient of determination, R^2, is 0.937 and 0.998 for the calibration curve for Zn concentrations up to 100 wt% and up to 50 wt%, respectively. Higher accuracy in the calibration of Zn composition is expected to improve the accuracy in the calibration of minor alloying elements, as explained in Section 3.1.

Among the standards used, Alloy5 with Zn concentration of 0.19 wt% gave the lowest detectable signal for Zn above the background level. The detection limit was estimated as 0.12 wt% based on the formula $3\sqrt{2}SD$ [16], where SD is the standard deviation in the measurements made on the Zn-free standard SQ-10WP.

The calibration data for the main alloying elements in the AlMn substrate are shown in figure 3.5. These were fitted to straight lines by least-squares regression analysis in the concentration ranges of interest for the elements Mn, Fe and Si, as shown in figure 3.5a, b and c, respectively. Similar analysis of the data for Mg required fitting to a 2nd degree polynomial (figure 3.5d). The reason must be that the 285.213 nm Mg spectral line is a resonance line with a high self-absorption coefficient [8]. The data for Mn and Fe (figure 3.5a and b) showed satisfactory fits to straight lines, while the data for Si (figure 3.5c) gave appreciable scatter. This is probably related to the low sensitivity factor of the spectral line for Si [17] . The errors introduced by sputtering rate measurements become more critical on Si calibration curve, as discussed in Section 3.1.

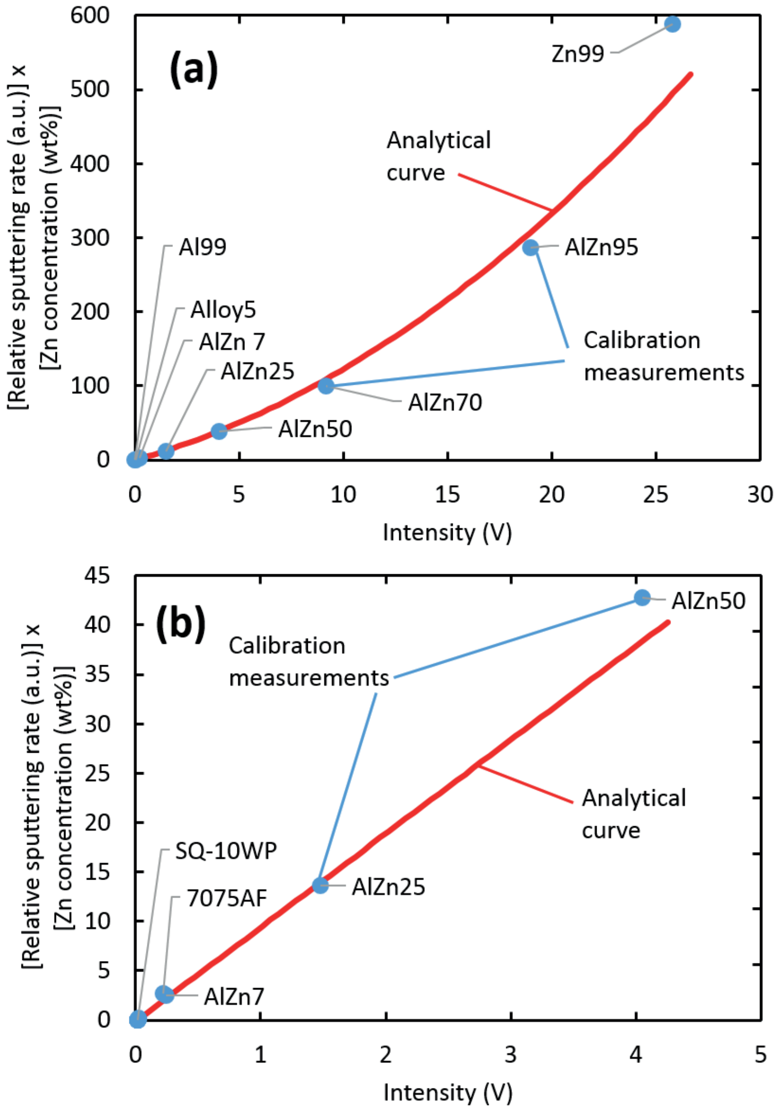

FIGURE 3.4: Calibration curves for Zn with concentration up to a) 100 wt%, b) 50 wt%

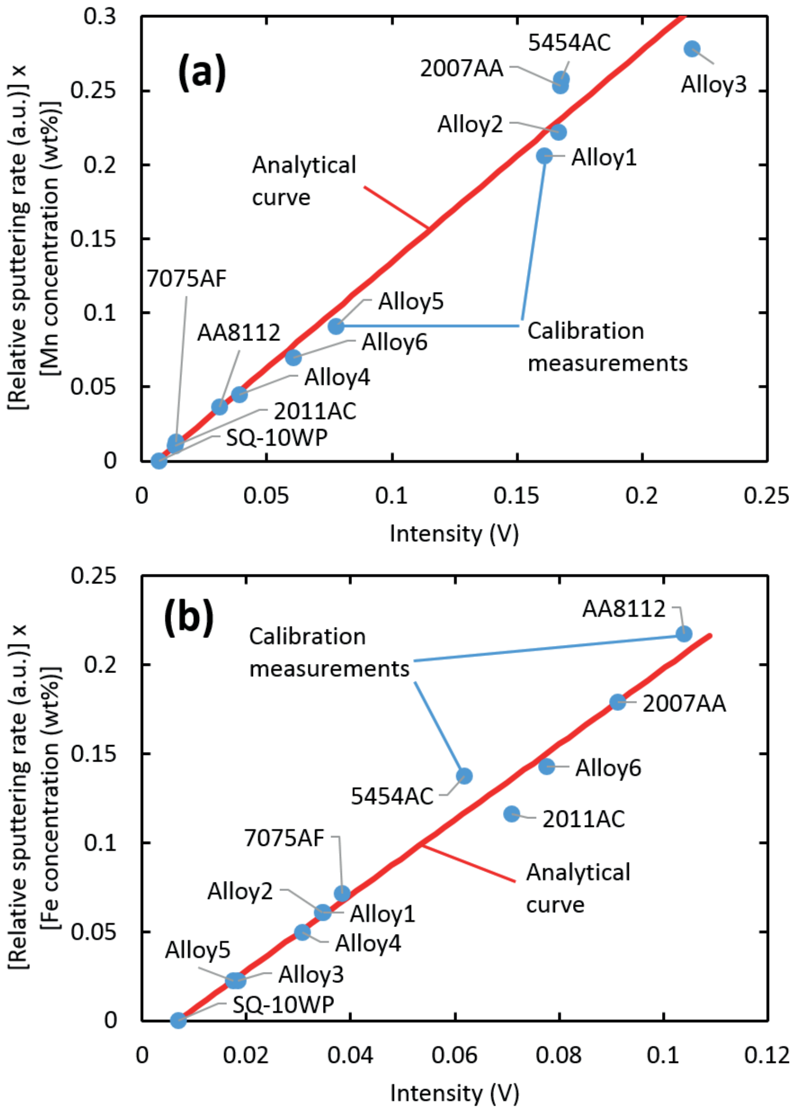
(a)
[Relative sputtering rate (a.u.)] x [Mn concentration (wt%)]
0
0.05
0.1
0.15
0.2
0.25
0.3
Intensity (V)
0
0.05
0.1
0.15
0.2
0.25
5454AC
2007AA
Alloy3
Alloy2
Alloy1
Analytical curve
7075AF
Alloy5
AA8112
Alloy6
Calibration measurements
Alloy4
2011AC
SQ-10WP
(b)
[Relative sputtering rate (a.u.)] x [Fe concentration (wt%)]
0
0.05
0.1
0.15
0.2
0.25
Intensity (V)
0
0.02
0.04
0.06
0.08
0.1
0.12
AA8112
Calibration measurements
2007AA
Alloy6
5454AC
2011AC
7075AF
Analytical curve
Alloy2
Alloy1
Alloy4
Alloy5
Alloy3
SQ-10WP

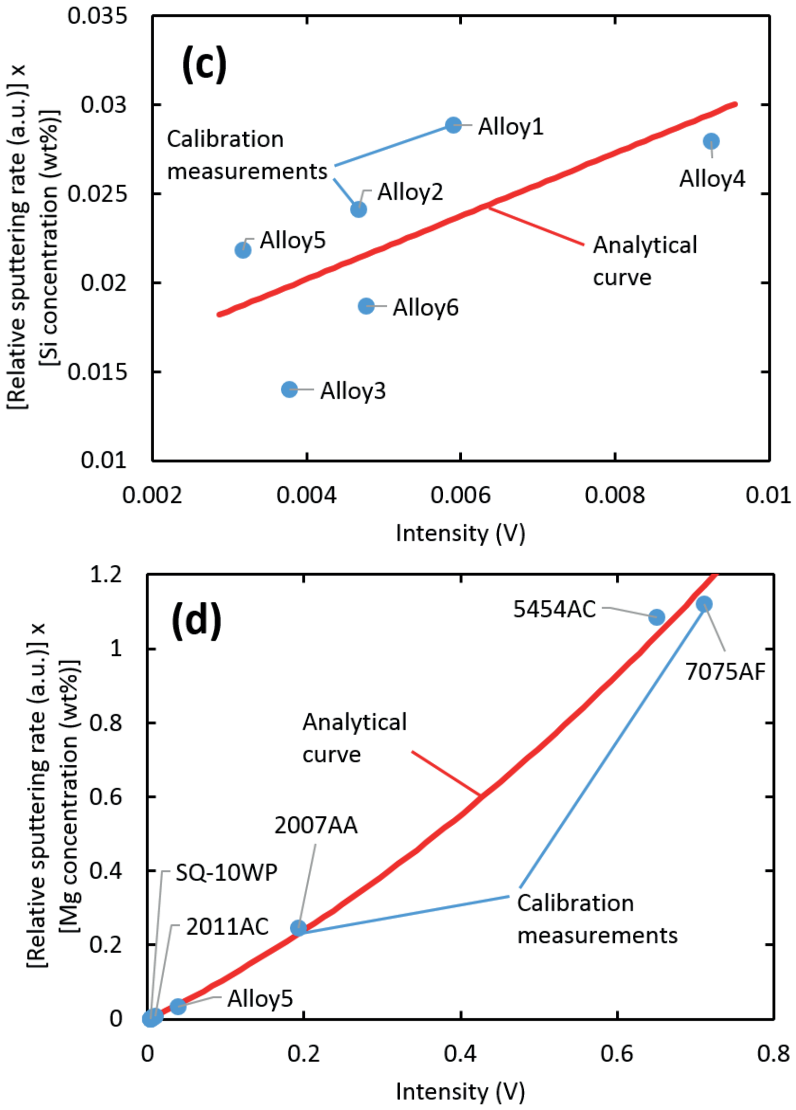

FIGURE 3.5: Calibration curves for a) Mn, b) Fe, c) Si, d) Mg

3.3.3 Zn concentration profiles on coated AlMn substrate

Figures 3.6a-c show depth profiles for Zn on AlMn alloy MPE tubes, which were originally coated with 8 g/m^2 of Zn (high Zn load) and then subjected to heat treatment at 350°C (3.6a), 390°C (3.6b) and 430 °C (3.6c) for selected durations. The profile for the as-coated sample (no heat treatment) is also included in all figures. Zn concentration at the surface of the as-coated sample was about 5 g/cm^3 (90 wt%), i.e., less than the expected 7.14 g/cm^3 (100 wt%), presumably due to the nonuniformity of the thermal-arc sprayed coating. This nonuniformity was indicated also by unexpected high Zn concentration on the outermost surface of the heat treated samples. It was caused by nearly pure zinc islands still remaining on the surface after annealing. Zn concentration profile of as-coated sample decreased monotonically from the surface to 0.2 g/cm^3 (10 wt%) at a distance of 5 μm from the surface, and it dropped below the detection limit of 0.0035 g/cm^3 (0.12 wt%) for Zn estimated above, at a distance of 9.6 μm.

With increasing temperature or time of heat treatment, Zn concentration on the outermost surface decreased, and the depth of the Zn-rich layer increased. The surface concentration ρ_s and concentration at the distance of 1 μm from the surface $\rho_{1\mu m}$ are summarized in table 3.7. The layer thickness L, also reported in table 3.7, was assumed to be the depth at which Zn concentration dropped to 0.0081 g/cm^3 (0.3 wt%), a value selected to be slightly larger than the detection limit 0.12 wt% for Zn. In cases where Zn concentration did not reach this value during the duration of GD-OES measurement, the maximum depth measured is shown. The total weight of zinc W_{Zn} in the layer was calculated by integration of the Zn mass concentration profile with respect to depth and reported in table 3.7. The average total weight of Zn in the heat treated samples was 8.5 ± 0.4 g/m^2, which agrees well with the value for the weight of sprayed Zn in the original coating obtained by XRF (8 ± 0.2 g/m^2).

GD-OES depth profiles of Zn coated MPE tubes with Zn load of 2.7 g/m^2 (low Zn load) are shown in figure 3.6d. Zn concentration at the surface ρ_s and at the distance of 1 μm from the surface $\rho_{1\mu m}$ are also reported in table 3.7. Zn concentration of the sample without heat treatment was about 0.3 g/cm^3 (13 wt%) at the very surface and increased to a maximum of about 1.1 g/cm^3 (32 wt%) at a distance of 0.6 μm. This shows that all metallic Zn was removed from the outermost surface by immersion in chromic-phosphoric acid, such that only Zn alloyed with Al remained. Zn concentration dropped to the detection limit of 0.12 wt% at 8.3 μm. This implies that the thickness of the high-load Zn coating was reduced by about 1 μm in obtaining the low-load layer by chromic-phosphoric acid treatment. Subsequent heat treatment lead to significantly lower Zn concentrations on the surface of the samples, ranging from 0.08 to 0.03 g/cm^3 (3 to 1.2 wt%), while the penetration of Zn into the substrate became significantly large, as expected. In fact, some of the layers became too thick to be effectively detected by GD-OES.

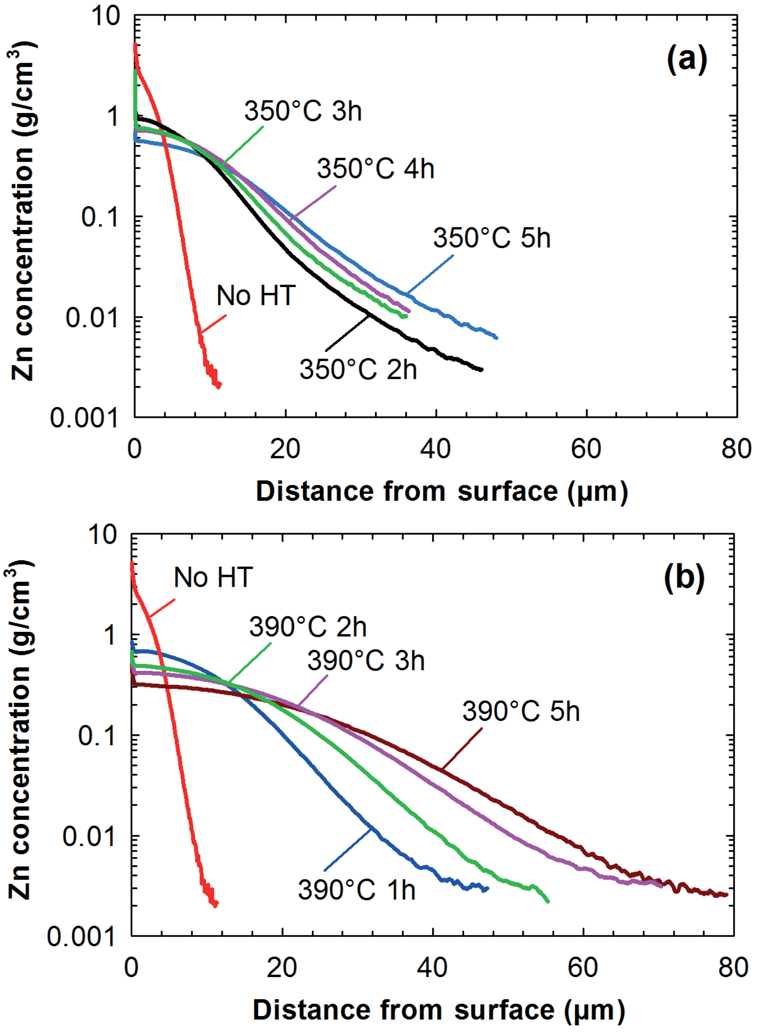
(a)
Zn concentration (g/cm^3)
10
1
0.1
0.01
0.001
0
20
40
60
80
Distance from surface (µm)
350°C 3h
350°C 4h
350°C 5h
No HT
350°C 2h
(b)
Zn concentration (g/cm^3)
10
1
0.1
0.01
0.001
0
20
40
60
80
Distance from surface (µm)
No HT
390°C 2h
390°C 3h
390°C 5h
390°C 1h

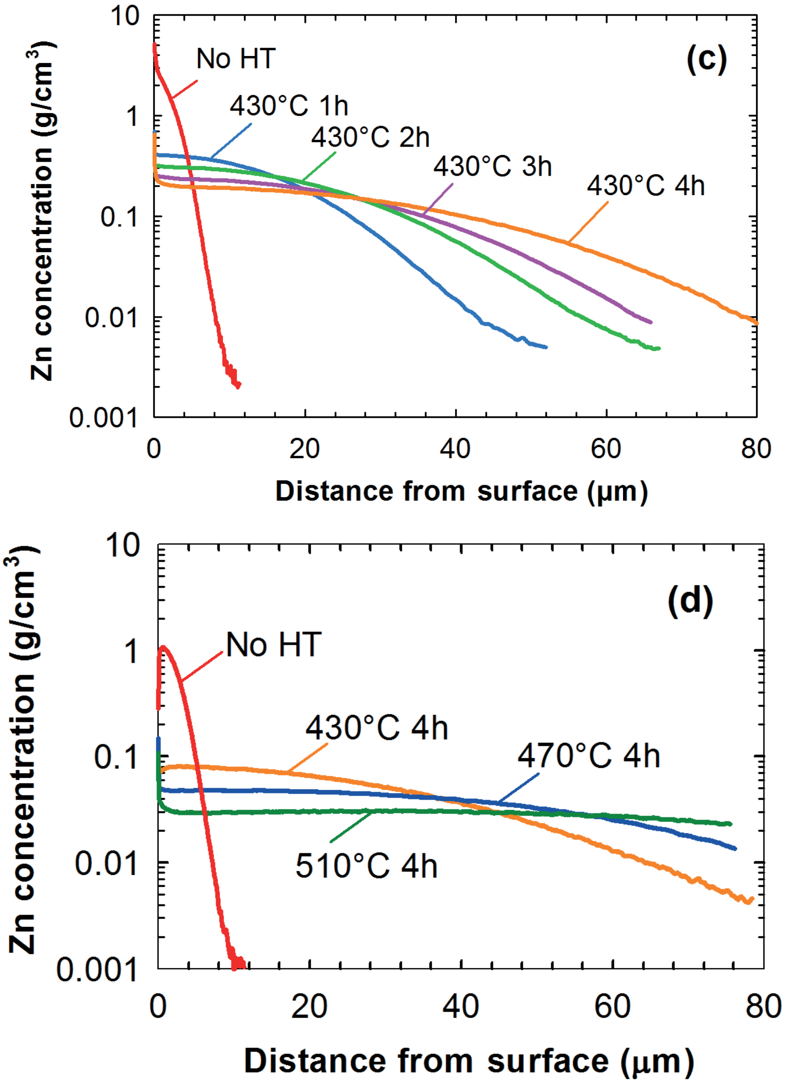

FIGURE 3.6: Effect of heat treatment on Zn concentration profiles of Zn coated AlMn alloy samples with Zn load of 8 g/m^2, heat treated for selected durations at a) 350 °C, b) 390 °C, c) 430 °C, and d) Zn load of 2.7 g/m^2, heat treated for 4 hours at selected temperatures. Curves for untreated samples (No HT) are included.

TABLE 3.7: Zn-rich layer thickness L, Zn coating weight W_{Zn}, Zn surface concentration ρ_s and concentration at the distance of 1 µm from the surface $\rho_{1\mu m}$, estimated by analysis of Zn depth profiles obtained by heat treatment of Zn coated AlMn alloy samples.

Zn load (g/m^2)	**Heat treatment**	L **(**μ**m)**	W_{Zn} **(g/m^2)**	ρ_s **(g/cm^3)**	$\rho_{1\mu m}$ **(g/cm^3)**
8 ± 0.2	No HT		7.5	5.14	2.27
	350 °C 2h	33.5	8.6	1.24	0.92
	350 °C 3h	>36	8.4	1.93	0.74
	350 °C 4h	>36	8.9	1.55	0.71
	350 °C 5h	44.4	8.0	1.31	0.56
	390 °C 1h	34.3	8.9	0.85	0.68
	390 °C 2h	42.2	8.7	0.64	0.49
	390 °C 3h	52.6	9.2	0.67	0.42
	390 °C 5h	58.7	8.3	0.60	0.32
	430 °C 1h	44.8	8.0	0.88	0.41
	430 °C 2h	59.0	8.6	1.19	0.31
	430 °C 3h	>66	7.9	0.56	0.25
	430 °C 4h	80.9	8.4	0.50	0.21
2.7 ± 0.7	No HT		3.1	1.08	1.02
	430 °C 4h	67.9	3.2	0.08	0.08
	470 °C 4h	>76.1	2.8	0.09	0.05
	510 °C 4h	>75.5	2.2	0.08	0.03

The total Zn weight in low Zn load samples, calculated by integration of the Zn mass concentration profiles with respect to depth, is also shown in table 3.7. The total weight of Zn in the sample without heat treatment and the sample heat treated at 430 °C for 4 hours was around 35% of the average Zn coating weight calculated for the heat treated samples with the high Zn load. This agrees well with the data obtained by XRF analysis for high Zn-load samples (8 g/m^2) and weighing of the low Zn-load samples (2.7 g/m^2). Lack of data on layer thickness and lower Zn coating weight for samples heat treated at 470 and 510 °C for 4 hours is due to the interruption of the measurements too early (at Zn concentration of 0.0136 and 0.0232 g/cm^3 (0.5 and 0.85 wt%), respectively).

The estimated average error in GD-OES measurements for Zn was 18%. The error varied in a profile with a trend to increase with decreasing concentration of the element, for example, from 3% to 70% in one of the profiles. This is illustrated in figure 3.7 which shows Zn concentration profiles for some of the samples with error bars at selected points along the curves.

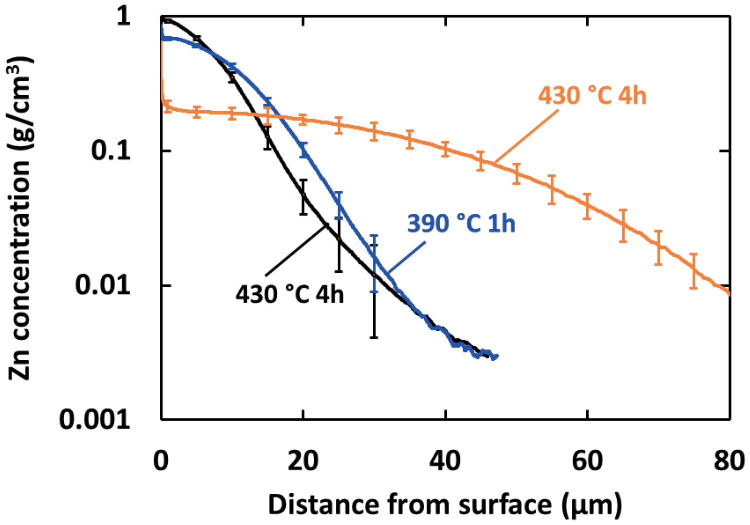

FIGURE 3.7: Selected Zn concentration profiles of Zn coated and heat treated AlMn MPE tubes with high Zn load with error bars indicated at selected points.

3.3.4 Profiles for alloying elements and oxygen

Uncoated samples. Depth profiles of Al, O, Mn, Fe, Si and Mg of Alloy1 (Al MPE tube) are shown in figure 3.8 for the purpose of comparison with the profiles of the same elements on Zn coated MPE tubes although surface roughness will probably not allow a straightforward comparison. The GD-OES profiles, averaged over the analysis area of 4 mm in diameter, are expected to become more evenly distributed in depth than a similar profile over a smaller area. This means that a layer with high concentration gradient and small thickness can appear in a GD-OES profile as a layer with lower concentration gradient spread over a larger depth. Nevertheless it appears from figure 3.8 and figures 3.9b and 3.10b discussed below, that the as extruded Al tube was more oxidized than the coated sample with both Zn loads. Unexpectedly high enrichment of Fe (0.03 g/cm^3) and Cr (0.002 g/cm^3) was observed relative to their bulk values, which are reported in terms of mass concentration in table 3.8. The enrichment is attributed to the contamination from the extrusion dye. Mg and Si were also enriched at the surface relative to their respective bulk values while Mn concentration level was smaller at the surface than in the bulk. Enrichment of Mg is expected to be in the form of an oxide, resulting from thermomechanical processing of the tube, as expected for Mg containing Al alloys [18, 19].

Substrate alloy. Bulk composition of the AlMn alloy substrate measured by GD-OES, after the Zn coating has been sputtered, is compared to the as-received alloy composition measured by SPARK OES in table 3.9, together

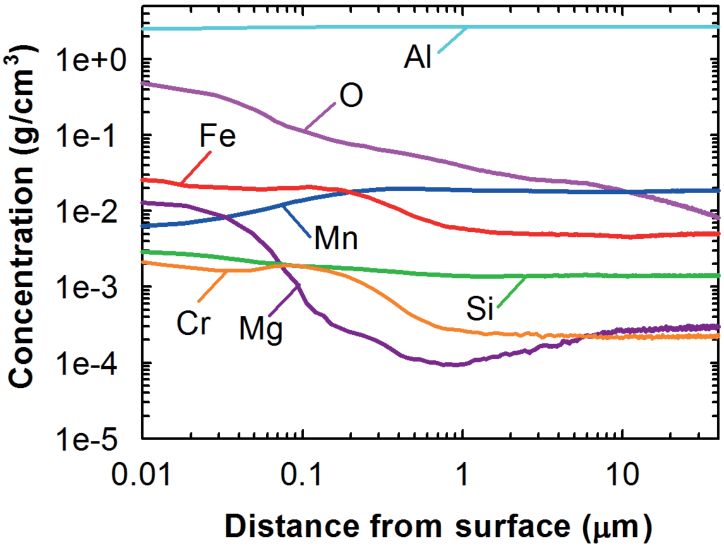

FIGURE 3.8: GD-OES depth profiles for Alloy1.

with the percent deviation between the values obtained by the two measurements. Quantification of the GD-OES data was performed using two different calibration curves for Zn, given in figures 3.4a and b designated as Cal1 and Cal2, respectively. The error was estimated based on GD-OES measurement error and deviation between locations of analysis. Zn concentration in the sample measured by Spark OES is much lower than the detection limit of Zn in the GD-OES calibration obtained, which is 0.12 wt%. Zn concentration measured by GD-OES was an order of magnitude higher than the one measured by Spark OES. Although GD-OES is considered a more accurate technique, in this case the value obtained by Spark OES was more reliable. Zn concentration obtained by GD-OES with Cal2 was 30% less than the one obtained with Cal1. Quantification is based on the condition that all concentrations add up to 100 wt%. As Zn concentration was calculated to be one magnitude higher than expected, all concentrations of the alloying elements were affected. This result was confirmed by the results for the elements other than Zn in table 3.9. All concentrations measured by GD-OES were smaller than the values obtained by Spark OES, the values obtained

TABLE 3.8: Composition of Alloy1 in g/cm^3.

Element	**Al**	**Zn**	**Mn**	**Fe**	**Si**
Content (g/cm^3)	2.685	0.0005	0.019	0.005	0.003
Element	**Mg**	**Ni**	**Cu**	**Cr**	**Pb**
Content (g/cm^3)	0.0003	0.00008	0	0.0003	0.00002

using Cal2 being closer. This implies that the calibration curve for Zn concentration up to only 50 wt% gives better accuracy for the alloying elements. The deviation for Mn and Fe obtained by GD-OES with Cal2 compared to Spark OES results were quite small, while it was higher for Mg and Si. The reasons of poor accuracy of Si due to calibration were noted in section 3.3.2. Moderate error for Mg can be attributed to the fact that the bulk value of of Mg is close to the detection limit of Mg. The results obtained with Cal2 in mass fraction were also calculated in mass concentration (g/cm^3) and reported in table 3.9.

TABLE 3.9: Comparison of the bulk composition of the substrate alloy measured by Spark OES ($\omega_{SparkOES}$) and GD-OES (ω_{GD-OES} and ρ_{GD-OES}) for mass fraction and mass concentration, respectively).

	Elt	$\omega_{SparkOES}$ **(wt%)**	ω_{GD-OES} **(wt%)**	**Deviation (%)**	ρ_{GD-OES} **(g/cm^3)**
Cal1	Mn	0.72	0.65±0.02	10	
	Fe	0.21	0.19 ±0.01	11	
	Si	0.09	0.068 ±0.005	24	
	Mg	0.019	0.015 ±0.002	18	
	Zn	0.005	0.085 ±0.089	large	
Cal2	Mn	0.72	0.69±0.02	4	0.019±0.0005
	Fe	0.21	0.20 ±0.01	6	0.005±0.0003
	Si	0.09	0.072 ±0.006	20	0.002±0.0002
	Mg	0.019	0.016 ±0.002	13	0.0004±0.00005
	Zn	0.005	0.062 ±0.069	large	0.0017±0.0019

High Zn load. GD-OES depth profiles of aluminium, oxygen and alloying elements for samples with high Zn load (8 ± 0.2 g/m^2) before and after heat treatment at various conditions are shown in figure 3.9. Aluminium profiles (figure 3.9a) showed smooth increase of Al concentration with increasing depth, as expected. For the non-heat-treated sample in figure 3.9a, aluminium concentration at the very surface of the Zn coating was appreciable at about 0.7 g/cm^3 (10 wt%), showing incomplete coverage by Zn, as discussed further in Section 3.3.5. The Al concentration at the coating surface increased with increasing heat-treatment temperature and time due to inward diffusion of Zn from the coating into the AlMn alloy substrate, as expected.

The profiles of the other elements reached their maximum plateaus as they attained their bulk values in the AlMn alloy substrate. The distance from the surface at which this occurs corresponded to the thickness of the Zn-rich layer. The thickness of the layer increased with increasing heat-treatment temperature and time, as expected.

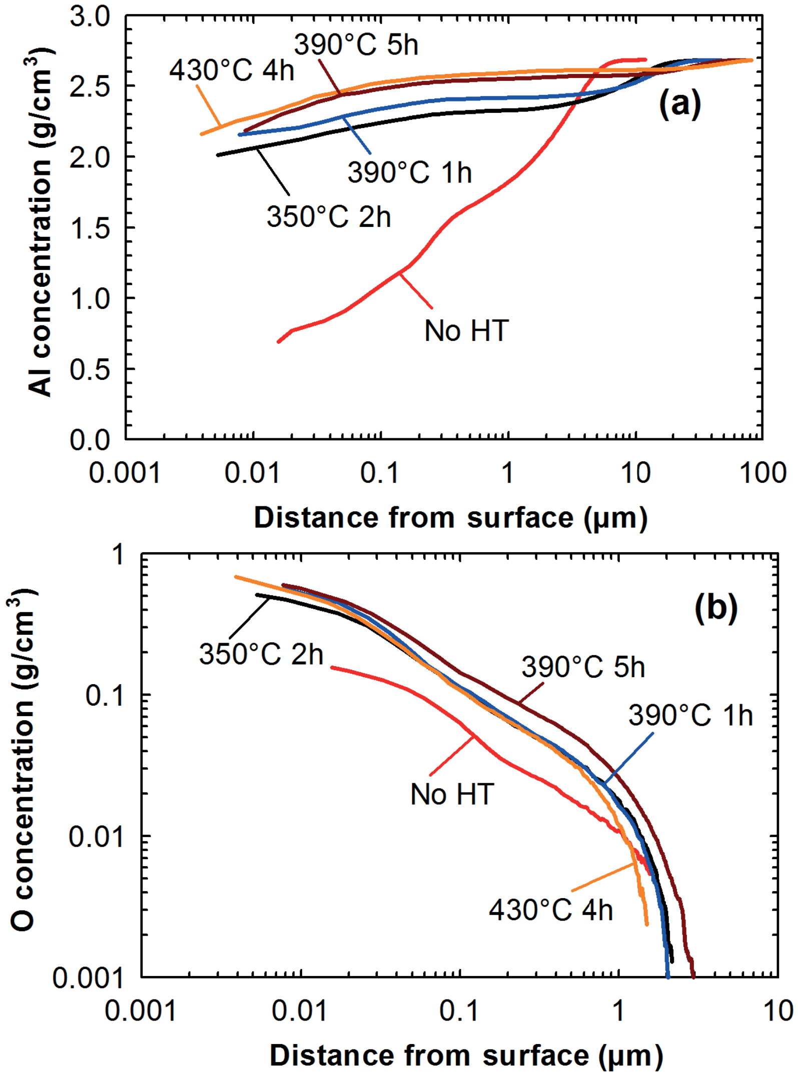
(a)
Al concentration (g/cm^3)
3.0
2.5
2.0
1.5
1.0
0.5
0.0
0.001
0.01
0.1
1
10
100
Distance from surface (µm)
430°C 4h
390°C 5h
390°C 1h
350°C 2h
No HT
(b)
O concentration (g/cm^3)
1
0.1
0.01
0.001
0.001
0.01
0.1
1
10
Distance from surface (µm)
350°C 2h
390°C 5h
390°C 1h
No HT
430°C 4h

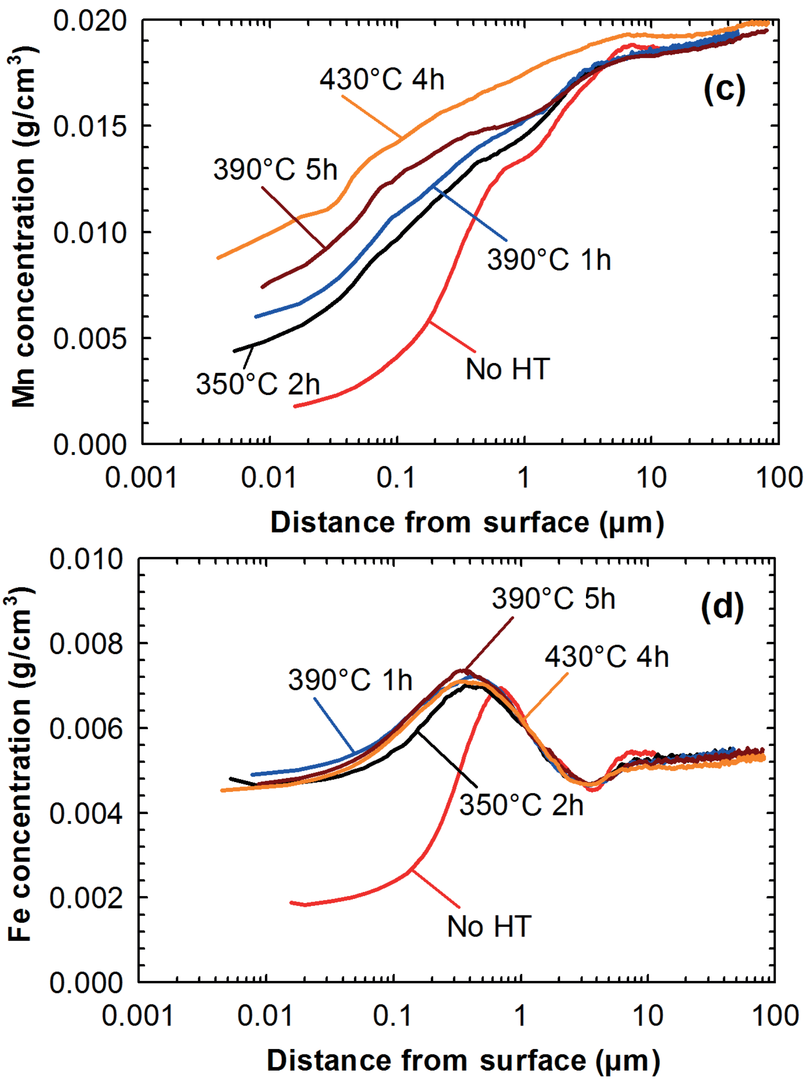
(c)
Mn concentration (g/cm³)
0.020
0.015
0.010
0.005
0.000
430°C 4h
390°C 5h
390°C 1h
350°C 2h
No HT
0.001
0.01
0.1
1
10
100
Distance from surface (µm)
(d)
Fe concentration (g/cm³)
0.010
0.008
0.006
0.004
0.002
0.000
390°C 5h
430°C 4h
390°C 1h
350°C 2h
No HT
0.001
0.01
0.1
1
10
100
Distance from surface (µm)

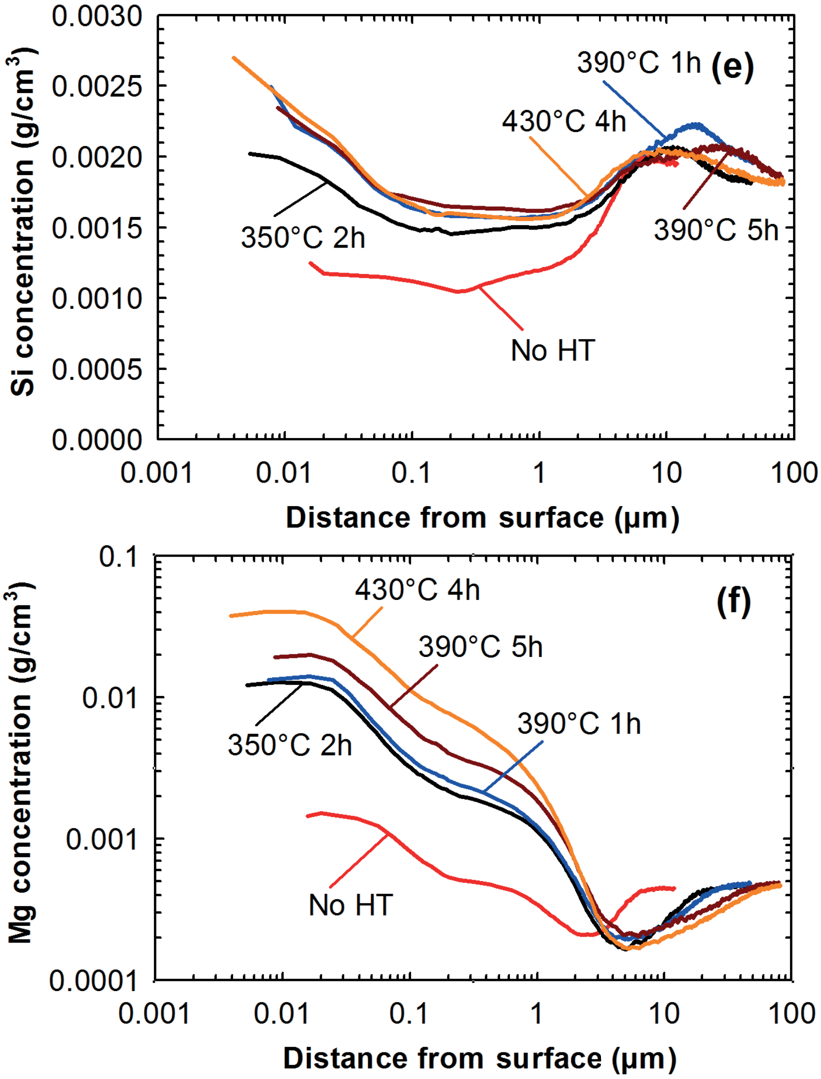

FIGURE 3.9: Effect of heat treatment on concentration profiles of a) Al, b) O, c) Mn, d) Fe, e) Si, f) Mg of samples with Zn load of 8 g/m^2

The changes observed in the oxygen concentration in figure 3.9b occured in the direction opposite to the changes in Al profile with the exception for the sample heat treated for 4 hours at 430 °C. Interpretation of these are not as straightforward as it is for the Al profile because of irreproducible variations in O_2 penetration into a rough and porous surface and its formation of different and mixed oxides with zinc and the alloying elements, as well as with Al. Since even small leakages unavoidable on such a rough surface can lead to appreciable error in the oxygen signal, typical (rather than averaged) oxygen profiles are presented. Therefore, the observed trend may arise from the variations on the surface and errors introduced by leakages into the chamber rather than due to heat treatment.

Mn (figure 3.9c) was present at the coating surface of the non-heat-treated sample and its concentration increased with depth until it reached its bulk value at the depth of 7 μm. The presence of Mn at the surface and in the Zn coating can be explained by incomplete coverage of the surface by the Zn coating. During heat treatment Mn diffused to the surface along with Al, but its concentration remained below its level in the substrate bulk.

Fe (figure 3.9d) profiles differed from Mn due to the presence of a maximum peak, appearing at about 0.7 μm depth from the surface for the non-heat-treated sample. After this maximum, Fe concentration profiles went through minima at about 3.5 μm depth and then increased to their bulk level at about 7 μm. The distance of the minimum from the surface was not affected by the heat-treatment conditions. Fe concentration near the surface increased by heat treatment from non-heat-treated to 2 hours treatment at 350 °C condition. It was not affected by further increase in the degree of heat treatment in the temperature and time ranges of interest. The maximum concentration was larger than the bulk value for Fe for all the samples. The maximum moved closer to the surface to a depth of about 0.35 μm by heat treatment.

Si concentration of the non-heat-treated sample (figure 3.9e) increased from a small value at the surface to the bulk level at the distance of about 7 µm from the surface. Heat treatment caused increase in the Si concentration near the surface. Most of the increase relative to the non-heat-treated case occurred already by the mildest case of heat treatment for 2 hours at 350 °C. Increasing level of heat treatment conditions gave minor increase, as for the other elements. All curves exhibited shallow minima in the range 0.1 – 1 μm away from the surface, followed by maxima for most of the curves at a depth of about 10 μm from the surface.

Mg (figure 3.9f) was enriched at the surface of the non-heat-treated sample and showed a minimum at about 2.5 μm from the surface. After the minimum, Mg concentration profile increased gradually and reached its bulk value at about 7 μm. Heat treatment lead to higher enrichment of Mg up to 0.04 g/cm^3 (1.2 wt%) after heat treatment for 4 hours at 430 °C. Concentration minima moved deeper to about 5-6 μm from the non-heat-treated condition to the mildest level of heat treatment similar to the other elements.

The minima were not much affected by further increase in the heat treatment conditions.

Low Zn load. GD-OES depth profiles of aluminium, oxygen and alloying elements for the samples with low Zn load (2.7 g/m^2) are shown in figures 3.10a-g before and after heat treatment at various conditions. Profiles for high Zn load samples, the non-heat-treated and heat-treated for 4 hours at 430 °C, are included as reference for easier comparison between the two levels of Zn loads in figures 3.10b - f . In figure 3.10a Al profile for high Zn load sample heat treated for 4 hours at 430 °C was included as reference. Al profile of the non-heat-treated sample with low Zn load exhibited a minimum close to the surface and then increased to its level in the bulk of the AlMn substrate. Al profiles of the heat-treated samples did not exhibit such minima. Increase in the Al level near the surface was again significant from non-heat-treated to the heat-treated conditions. Curves for the heat-treated conditions were quite similar to one another and to the heat-treated high Zn-load cases, showing monotonic increase from the surface towards the bulk substrate. Concentration variation from the surface to the bulk was not too significant, e.g., in comparison to variation exhibited by the Zn concentration for comparable experimental conditions (cf. figure 3.6 and tables 3.7, 3.9 and 3.10).

Oxygen profiles (figure 3.10b) were also quite similar to those of the high Zn-load samples. They were high at the very surface, ranging from around 0.3 g/cm^3 (10 wt%) for non-heat-treated sample to 0.7 g/cm^3 (25 wt%) for the sample heat treated at 510 C for 4 hours. O concentration decreased monotonically with increasing depth.

Mn concentration profile of the non-heat treated sample in figure 3.10c exhibited a maximum at around 50-60 nm from the surface and a minimum at around 0.2 μm. After the minimum Mn concentration increased smoothly until it reached its bulk value at around 6 μm. Heat treatment at 430 °C and higher lead to increase of Mn level closer to the surface, and maxima and minima became less pronounced. The curves showed wavy patterns around the bulk value of 0.018 g/cm^3 (0.6 wt%) already starting from 0.4 μm depth from the surface.

Fe concentration profiles (figure 3.10d) showed high enrichment of Fe at the surface ranging from 0.007 g/cm^3 (0.2 wt%) for the non-heat treated sample to 0.018 g/cm^3 (0.55 wt%) for the sample heat treated at 510 °C for 4 hours. In the latter case, this high level of Fe persisted up to about 100 nm depth from the surface. Fe profiles of the other samples showed maxima at about the same depth. Fe profiles of all samples in the figure showed minima at about 3 μm depth before the profiles reached the bulk value of Fe in the AlMn substrate. The level of the minimum was not affected by heat treatment.

Si profiles were quite similar for all heat-treatment conditions and further similar to those of the heat-treated, high Zn-load samples, as shown in figure 3.10e. The curves indicate Si enrichment at the surface, followed by

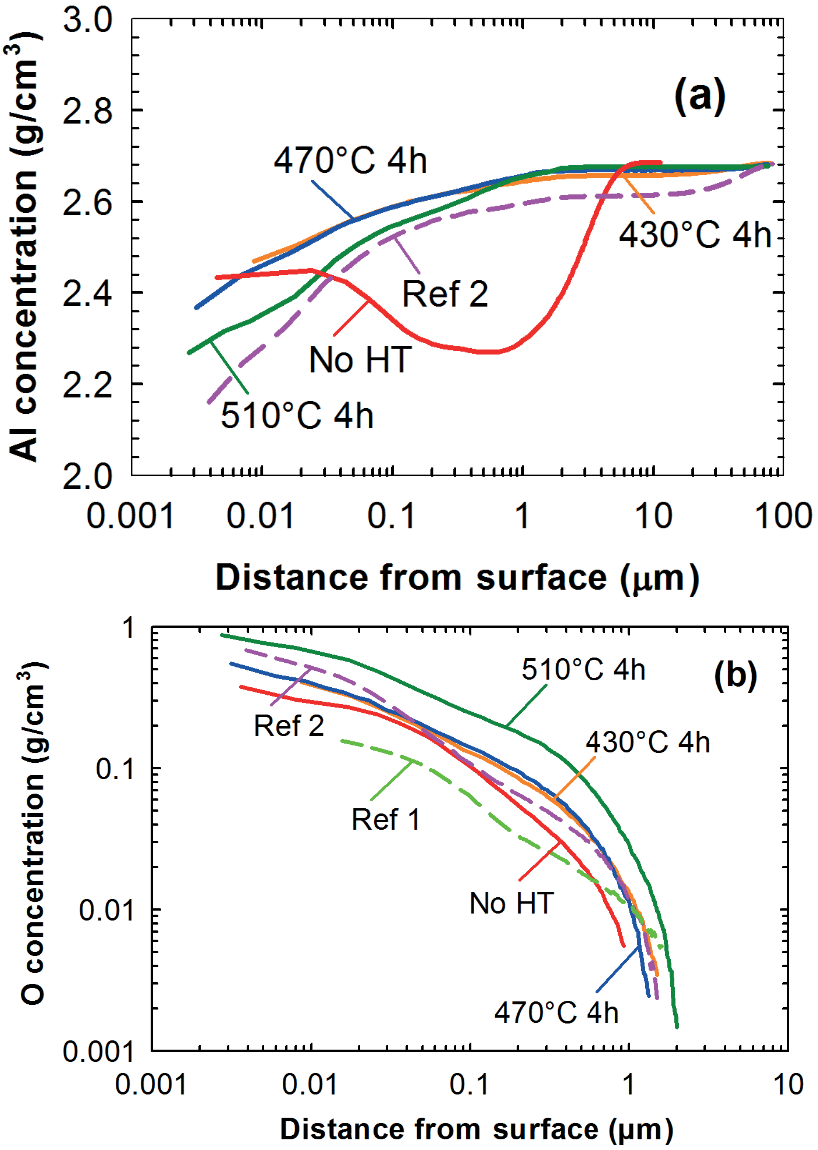
(a)
Al concentration (g/cm^3)
3.0
2.8
2.6
2.4
2.2
2.0
0.001
0.01
0.1
1
10
100
Distance from surface (µm)
470°C 4h
430°C 4h
Ref 2
No HT
510°C 4h
(b)
O concentration (g/cm^3)
1
0.1
0.01
0.001
0.001
0.01
0.1
1
10
Distance from surface (µm)
510°C 4h
430°C 4h
Ref 2
Ref 1
No HT
470°C 4h

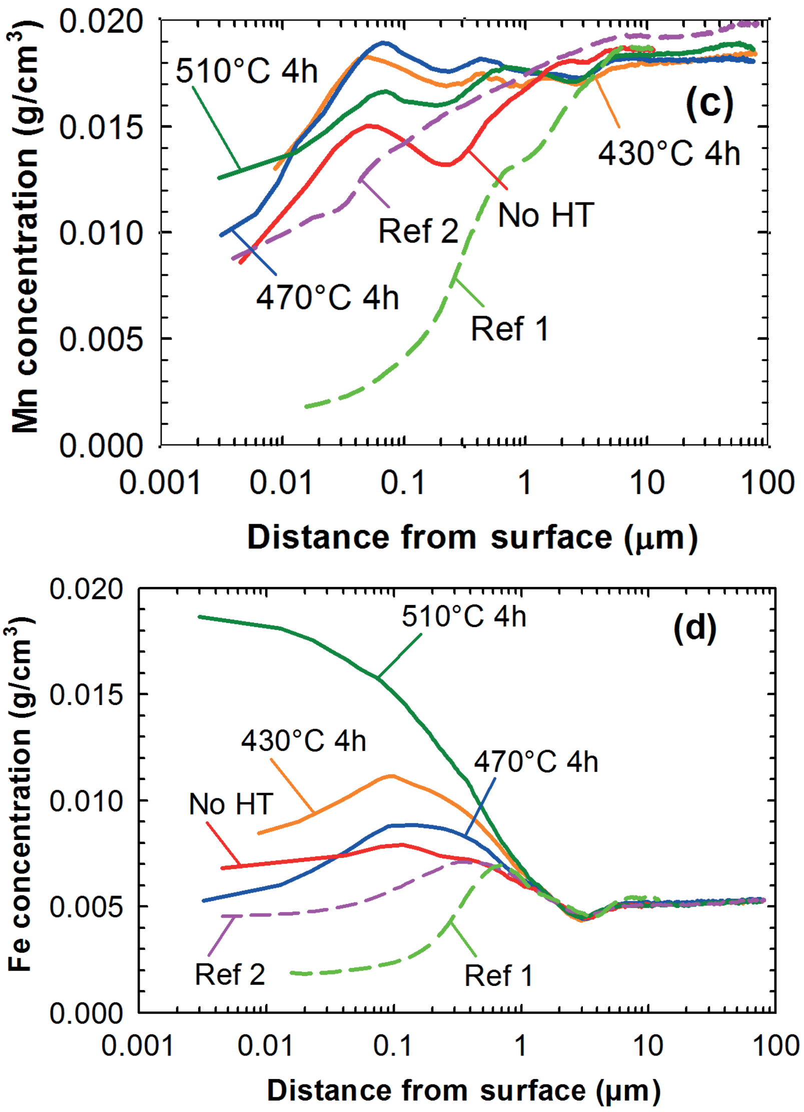
Mn concentration (g/cm³)
0.020
0.015
0.010
0.005
0.000
0.001
0.01
0.1
1
10
100
Distance from surface (µm)
510°C 4h
(c)
430°C 4h
No HT
Ref 2
470°C 4h
Ref 1
Fe concentration (g/cm³)
0.020
0.015
0.010
0.005
0.000
0.001
0.01
0.1
1
10
100
Distance from surface (µm)
510°C 4h
(d)
430°C 4h
470°C 4h
No HT
Ref 2
Ref 1

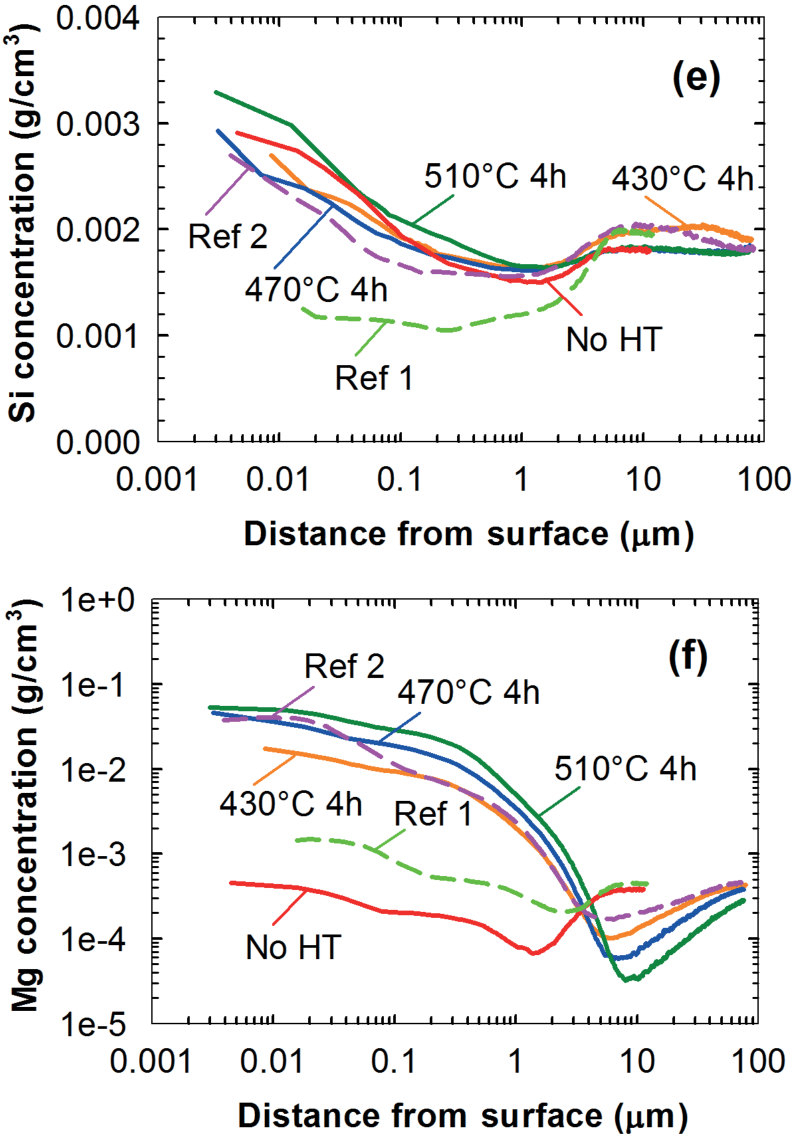
(e)
Si concentration (g/cm^3)
0.004
0.003
0.002
0.001
0.000
0.001
0.01
0.1
1
10
100
Distance from surface (μm)
510°C 4h
430°C 4h
Ref 2
470°C 4h
No HT
Ref 1
(f)
Mg concentration (g/cm^3)
1e+0
1e-1
1e-2
1e-3
1e-4
1e-5
0.001
0.01
0.1
1
10
100
Distance from surface (μm)
Ref 2
470°C 4h
510°C 4h
430°C 4h
Ref 1
No HT

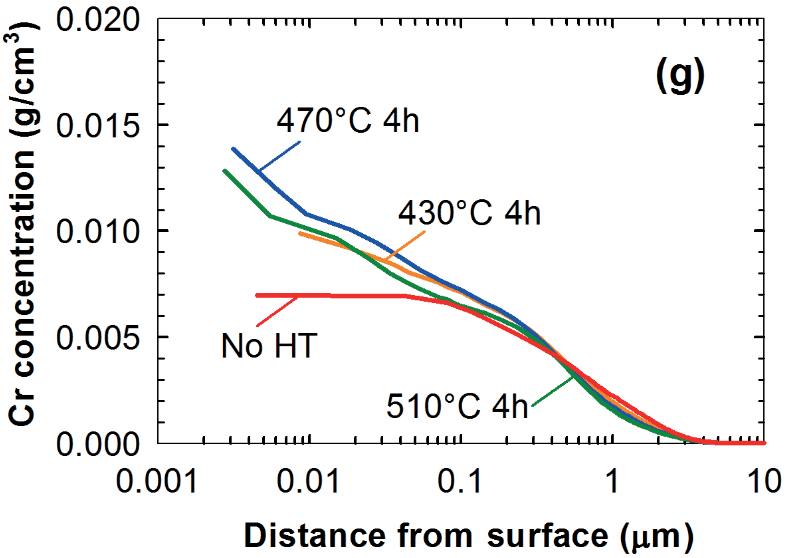

FIGURE 3.10: Effect of heat treatment on concentration profiles of a) Al, b) O, c) Mn, d) Fe, e) Si, f) Mg and g) Cr on samples with Zn load of 2.7 g/m^2. In a)-f) the reference profiles correspond to the non-heat-treated sample with Zn load of 8 ± 0.2 g/m^2 (Ref 1) and to the sample heat-treated for 4 h at 430 °C (Ref 2).

shallow minima with the same concentration level at around 1 μm depth. After the minima, concentrations increased with depth until the bulk level was reached at about 6 μm. The level of enrichment increased slightly with increasing degree of heat treatment.

Mg (figure 3.10f) was enriched at the surface at the level close to the bulk value for the non-heat-treated sample and up to the order of 0.05 g/cm^3 (1.5 wt%) for the heat treated ones. The non-heat-treated sample showed a minimum at a depth of about 1.5 μm from the surface and reached the bulk value at 6 μm. The minima occured at around 6, 7 and 8 μm for samples heat treated for 4 hours at 430, 470 and 510 °C, respectively. Mg concentration at the minima decreased with increasing degree of heat treatment. With increasing depth past the minima, Mg concentration increased gradually to its bulk value.

Significant enrichment of Cr was detected near the surface resulting from the Cr-P treatment, as shown in figure 3.10g. The Cr concentration at the surface was higher for the heat treated samples. Cr level dropped to the bulk level of 0.00001 g/cm^3 (0.0004 wt%) at about 6-7 μm depth from the surface.

Comparison: high and low Zn load. Surface mass concentration ρ_s, depth of the maximum point d_{max}, concentration at the maximum point ρ_{max}, depth of the minimum point d_{min}, and concentration of the minimum point ρ_{min} of Al, O, Mn, Fe, Si, Mg and Cr in the samples with high and low Zn load heat treated at different conditions are summarized in table 3.10. The data for the uncoated sample discussed above in relation to figure 3.8 above is also included. The data for the Zn profiles was reported in table 3.9.

For non-heat-treated samples, low Zn load gave smaller level of oxygen concentration in the depth profile for O than the high Zn load. O-profile for the latter case persisted deeper than the former (cf. figures 3.9b and 3.10b). The depth difference was about 1 μm. For most of the heat-treated samples the O-profiles for low Zn load were at slightly lower concentrations than high Zn load for correponding heat-treatment conditions. Heat treatment of low Zn load samples at 510 °C lead to higher oxidation of the surface than any other due to the highest temperature applied.

For the non-heat treated sample with high Zn load, concentration of all minor alloying elements reached their bulk levels at about 7 μm depth from the surface. This value corresponds approximately to the as-sprayed thickness of the Zn-rich layer, as seen in figure 3.6. Concentration of the minor alloying elements in the samples with low Zn load reached their bulk level at about 6 μm. The difference between these two values corresponded to the difference in the thicknesses of the Zn-rich layers for high and low Zn load, which was estimated to be about 1 μm in section 3.3.3.

Concentration of Mn and Mg increased with the degree of heat treatment close to the surface for both Zn loads. Moreover, Mg, Si and Fe were enriched towards the surface (i.e., with decreasing depth) for all cases, with the exception of Mn (decreased towards the surface for all cases) and Si in the non-heat-treated high Zn load case. Mn concentration was higher for the low Zn load than high Zn load for the comparable tempers at the surface.

Mg concentration profile for the non-heat-treated samples was lower for the low Zn load samples than for the high Zn load ones. Heat treatment caused significant enrichment for both Zn loads commensurate with the degree of heat treatment, except at the minima. The minima attained by the low Zn load samples were appreciably smaller than the minima for the high Zn load samples. Minimum in the Mg profile of the non-heat-treated sample shifted closer to the surface by about 1 μm after chromic phosphoric acid treatment, same value as the shift in the O profile. The position of the minima for the heat-treated samples was significantly deeper from the surface for the low Zn (6 - 8 μm) than for the high Zn (about 5 - 6 μm) samples. For the low Zn load, the depth of the minimum increased with increasing level of heat treatment while for the high Zn load there was no clear trend. After heat treatment Mg concentration profiles at the outermost surface continued to follow O concentration profiles. Both O and Mg surface concentration level increased and both of their concentrations decreased further into the sample with increasing heat treatment.

Fe concentration profiles were significantly higher for the low Zn load than for the high Zn load. Fe was the only alloying element in figures 3.9 and

TABLE 3.10: Summary of the results shown in figures 3.9 and 3.10 in terms of the critical parameters: surface concentration (ρ_s), depth (d_{min}, d_{max}) and concentration (ρ_{min}, ρ_{max}) of the extremum points in Zn depth profiles obtained by heat treatment of Zn coated AlMn alloy samples and the uncoated sample.

Elt	**Zn load (g/m^2)**	**Heat treatment**	ρ_s **(g/cm^3)**	d_{max} (μm)	ρ_{max} **(g/cm^3)**	d_{min} (μm)	ρ_{min} **(g/cm^3)**
Al	8.0 ± 0.2	No HT	0.69				
		350 °C 2h	2.05				
		390 °C 1h	2.16				
		390 °C 5h	2.19				
		430 °C 1h	2.27				
	2.7 ± 0.7	No HT	2.44				
		430 °C 4h	2.47			0.5	2.27
		470 °C 4h	2.45				
		510 °C 4h	2.34				
	0	No HT	2.49				
O	8.0 ± 0.2	No HT	0.16				
		350 °C 2h	0.46				
		390 °C 1h	0.55				
		390 °C 5h	0.58				
		430 °C 1h	0.54				
	2.7 ± 0.7	No HT	0.30				
		430 °C 4h	0.41				
		470 °C 4h	0.42				
		510 °C 4h	0.70				
	0	No HT	0.51				
Mn	8.0 ± 0.2	No HT	0.002				
		350 °C 2h	0.005				
		390 °C 1h	0.006				
		390 °C 5h	0.007				
		430 °C 1h	0.010				
	2.7 ± 0.7	No HT	0.010	0.05	0.015	0.22	0.013
		430 °C 4h	0.013	0.05	0.018	0.22	0.017
		470 °C 4h	0.012	0.06	0.019	0.22	0.018
		510 °C 4h	0.013	0.07	0.017	0.18	0.016
	0	No HT	0.006				
Fe	8.0 ± 0.2	No HT	0.0019	0.70	0.0069	3.6	0.0045
		350 °C 2h	0.0046	0.38	0.0070	3.5	0.0047
		390 °C 1h	0.0049	0.40	0.0072	3.5	0.0046
		390 °C 5h	0.0047	0.36	0.0074	3.5	0.0047
		430 °C 1h	0.0046	0.35	0.0071	3.5	0.0047
	2.7 ± 0.7	No HT	0.0069	0.1	0.0079	3.2	0.0045
		430 °C 4h	0.0085	0.1	0.0111	3.0	0.0043
		470 °C 4h	0.0057	0.1	0.0088	3.2	0.0044
		510 °C 4h	0.0183			3.0	0.0045
	0	No HT	0.0266				

Elt	**Zn load (g/m^2)**	**Heat treatment**	ρ_s **(g/cm^3)**	d_{max} (μm)	ρ_{max} **(g/cm^3)**	d_{min} (μm)	ρ_{min} **(g/cm^3)**
Si	8.0 ± 0.2	No HT	0.0012	7.3	0.0020	0.2	0.0011
		350 °C 2h	0.0020	11.0	0.0020	0.2	0.0014
		390 °C 1h	0.0024	17.0	0.0022	0.7	0.0016
		390 °C 5h	0.0023			1.0	0.0016
		430 °C 1h	0.0025	8.8	0.0020	0.8	0.0016
	2.7 ± 0.7	No HT	0.0028			1.4	0.0015
		430 °C 4h	0.0027			1.1	0.0016
		470 °C 4h	0.0025			1.3	0.0016
		510 °C 4h	0.0031			1.5	0.0016
	0	No HT	0.0029				
Mg	8.0 ± 0.2	No HT	0.0014			2.4	0.00021
		350 °C 2h	0.0128			5.0	0.00017
		390 °C 1h	0.0134			4.9	0.00020
		390 °C 5h	0.0192			6.2	0.00021
		430 °C 1h	0.0403			6.3	0.00017
	2.7 ± 0.7	No HT	0.0004			1.4	0.00007
		430 °C 4h	0.0173			5.9	0.00010
		470 °C 4h	0.0383			7.0	0.00006
		510 °C 4h	0.0509			8.0	0.00003
	0	No HT	0.0139				
Cr	8.0 ± 0.2	No HT	0.007				
		430 °C 4h	0.010				
		470 °C 4h	0.011				
		510 °C 4h	0.010				
	0	No HT	0.002				

3.10 which had maxima in the concentration profiles except for Mn in the non-heat-treated low Zn load sample. Fe maxima shifted much closer to the surface after chromic-phosphoric acid treatment.

Si profile of the non-heat-treated sample with low Zn load was much higher than of the sample with high Zn load. Concentration at the minimum of Si profile was roughly the same for all samples except for high Zn load non-heat-treated sample.

Minima were present in all concentration profiles for Mg, Si and Fe and in the Mn concentration profile of the low Zn load samples. Heat treatment lead to broadening/evening out of both maxima and minima in the Mn profiles.

The average errors in GD-OES profiles were 0.6% for Al, 19% for O, 4% for Mn, 20% for Mg, 8% for Fe, 8% for Si and 27% for Cr. The errors varied in each profile with a trend to increase with decreasing concentration of the element.

3.3.5 Surface characterization

Figure 3.11 shows SEM micrograph of typical morphology and elemental nonuniformity of Zn coated Al MPE tubes with Zn load of 8 g/m^2 (not heat treated). Zn coverage of the surface is non-uniform, with some regions remaining not covered (dark areas). As shown at a higher magnification in figure 3.12a, there are regions with almost 100 wt% Zn (bright areas) as well as regions of Zn alloyed with Al (grey areas) and Zn-free areas (dark areas). This was confirmed by EDS maps of Al and Zn (figures 3.12b and c, respectively) and point analysis (not shown). Intermetallic particles on the top right corner are probably (Fe,Mn)Al_6, as suggested by qualitative EDS analysis (not shown), which are typical for this type of alloy [20]. They can also be $(Fe,Mn)_3Si_2Al_{15}$ particles as Si concentration can be below the detection limit of EDS.

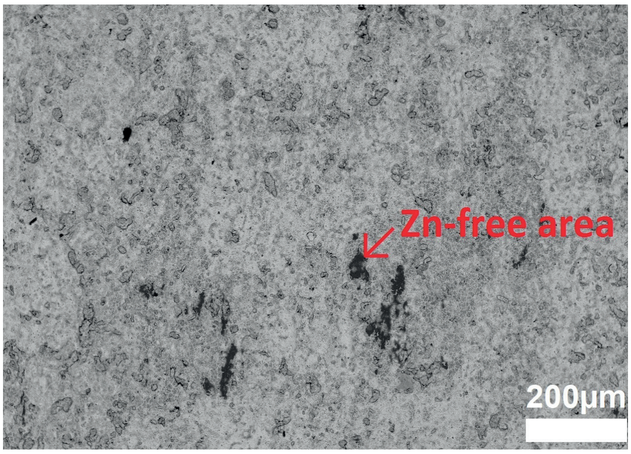

FIGURE 3.11: Backscattered electron image of Zn thermal arc-sprayed coating on Al MPE tube with Zn load of 8 g/m^2.

Figure 3.13a shows that most of the Zn has diffused into the substrate after heat treatment for 2 hours at 350 °C. However, islands with high Zn content and uncoated areas are still observed on the surface. The figure also shows the nonuniformity of Zn concentration on the surface of the Zn-rich layer. After heat treatment for 2 hours at 390 °C (figure 3.13b) high Zn islands and Zn lean areas and variations in the Zn concentration are significantly reduced. As can be seen in figure 3.13c, Zn concentration on the surface appears quite uniform as a result of heat treatment for 4 hours at 430 °C, with Zn islands still present.

EDS elemental analysis of 1 mm x 0.75 mm areas of the heat treated samples was performed at several locations on the samples. The average values and scatter limits are shown in table 3.11. The scatter limits

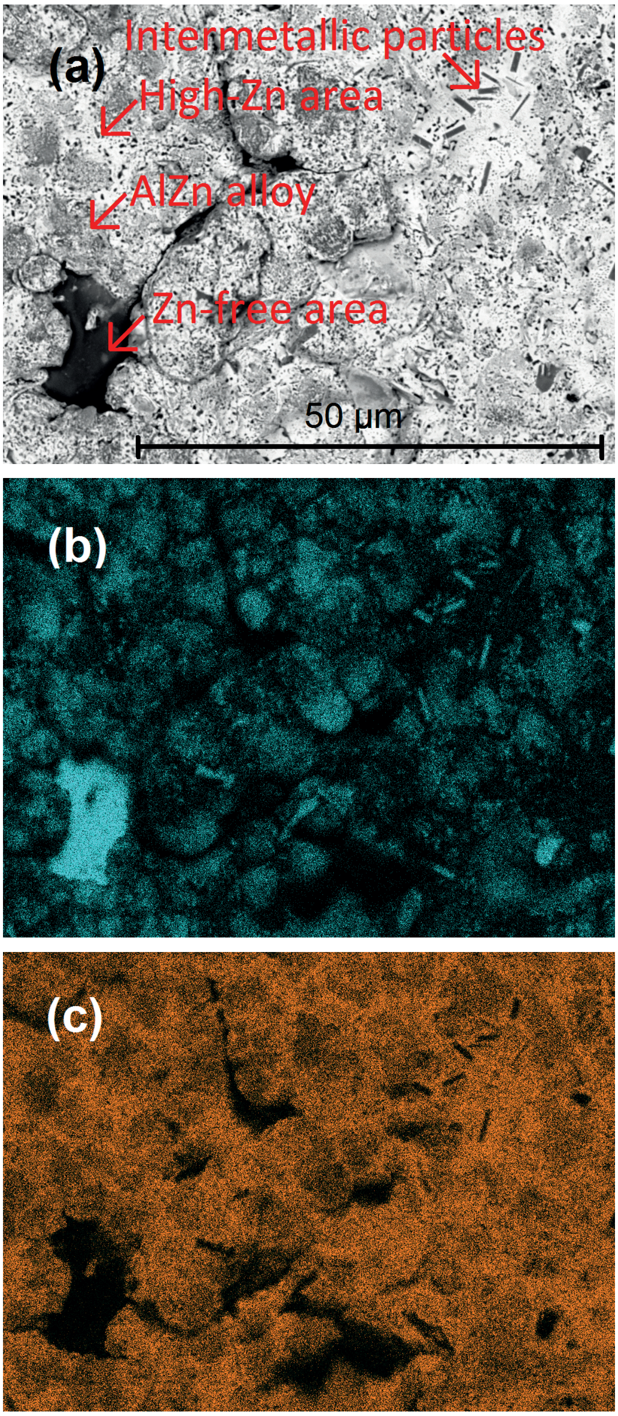

FIGURE 3.12: EDS maps of Zn thermal-arc sprayed coating on Al MPE tube with Zn load of 8 g/m^2. a) Backscattered electron image, b) Al, c) Zn.

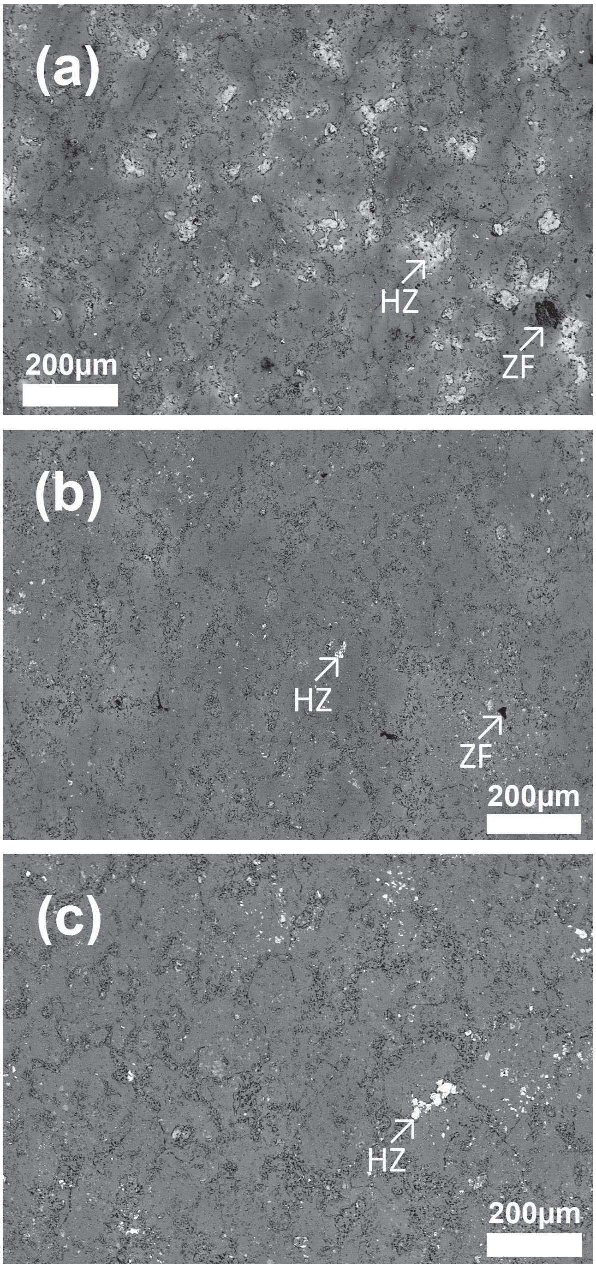

FIGURE 3.13: Backscattered electron images of surfaces of Zn-rich layers obtained by heat treatment of AlMn samples with Zn load of 8 g/m^2 for a)2 hours at 350 °C, b) 2 hours at 390 °C, c) 4 hours at 430 °C. The arrows show the Zn-free (marked as ZF) and high-Zn (HZ) areas.

TABLE 3.11: EDS area analysis of heat treated AlMn samples with Zn load of 8.0 g/m^2.

			Chemical composition (g/cm^3)			
HT	**Al**	**Zn**	**O**	**Mn**	**Fe**	**Mg**
No HT	1.70 ± 0.20	2.54 ± 0.21	0.078 ± 0.017	0.012 ± 0.002	0.004 ± 0.001	0.0043 ± 0.0009
350°C 2h	2.30 ± 0.11	0.95 ± 0.12	0.084 ± 0.003	0.015 ± 0.001	0.007 ± 0.001	0.0044 ± 0.0007
390°C 1h	2.39 ± 0.06	0.70 ± 0.06	0.100 ± 0.006	0.015 ± 0.001	0.007 ± 0.001	0.0048 ± 0.0006
390°C 2h	2.49 ± 0.06	0.45 ± 0.06	0.076 ± 0.003	0.016± 0.002	0.006 ± 0.001	0.0046 ± 0.0006
390°C 3h	2.49 ± 0.08	0.43 ± 0.08	0.085 ± 0.003	0.016 ± 0.001	0.007 ± 0.001	0.0049 ± 0.0003
390°C 5h	2.51 ± 0.01	0.38 ± 0.01	0.087 ± 0.006	0.017 ± 0.001	0.007 ± 0.001	0.0054 ± 0.0006
430°C 4h	2.55 ± 0.02	0.28 ± 0.02	0.085 ± 0.003	0.017 ± 0.001	0.007 ± 0.001	0.0065 ± 0.0009

indicate the nonuniformity of the lateral distribution of element compositions on the Zn-rich layers in as-sprayed and heat-treated conditions. The scatter in Zn and Al concentration is reduced with increasing heat treatment which indicates increasing uniformity of the Zn distribution. The data confirm the increase of Mn and Mg concentration with increasing heat treatment temperature and time, and general enrichment of Fe at the surface. Si concentration was below the detection limit of EDS. Zn concentration at the surface decreased with increasing temperature and time of heat treatment, as expected.

Low magnification back-scattered SEM images of cross sections of Zn coated Al MPE tubes in figure 3.14 confirm the non-uniformity of the as-sprayed Zn thickness (figure 3.14a) and the non-uniformity of lateral Zn distribution (figure 3.14b, c and d) resulting from different degrees of heat treatment. Diffusion of Zn into the substrate due to heat treatment is also observed. With increasing temperature and time of heat treatment, the Zn-rich layer becomes more uniform laterally as it becomes deeper. Nevertheless, figure 3.14d shows that the layer thickness and the lateral Zn concentration are still non-uniform after 4 hours of heat treatment at 430 °C. Higher magnification image in figure 3.15a shows Al-rich dendrites and Zn-rich interdendritic regions. The micrograph indicates that Zn starts to diffuse along the grain boundaries when it is sprayed. It continues to diffuse along the grain boundaries during subsequent heat treatment (figure 3.15b). After heat treatment at higher temperatures and durations this effect becomes less visible (figure 3.15c).

Figure 3.16 shows low magnification back-scattered SEM images of surfaces of Zn coating with Zn load of 2.7 g/m^2 and Zn-rich layers obtained by heat treatment of such samples at 430 C and 510 C for 4 hours.. Zn-free areas were observed on the coating without heat treatment (3.16a) as was the case for the coating with the high Zn load (figure 3.8). Some grain boundaries also became visible. However, no high-Zn islands were visible. These were probably dissolved by immersion in chromic-phosphoric acid. However, lateral variation in Zn concentration existed, indicated qualitatively by the presence of high and low zinc areas in figure 3.16a. These probably correspond to the Zn islands and AlZn alloy areas on the original high Zn load samples (cf. figure 3.9a), with Zn content diluted. After heat treatment at 430 C for 4 hours (figure 3.16b), Zn concentration at the surface became more uniform while small islands with Zn content higher than the average remained. Heat treatment at 510 C for 4 hours has evened out the Zn concentration further, as shown in figure 3.16c. Higher magnification images in figure 3.17 indicate that a large number of intermetallic particles were exposed at the surface after treatment in chromic-phosphoric solution.

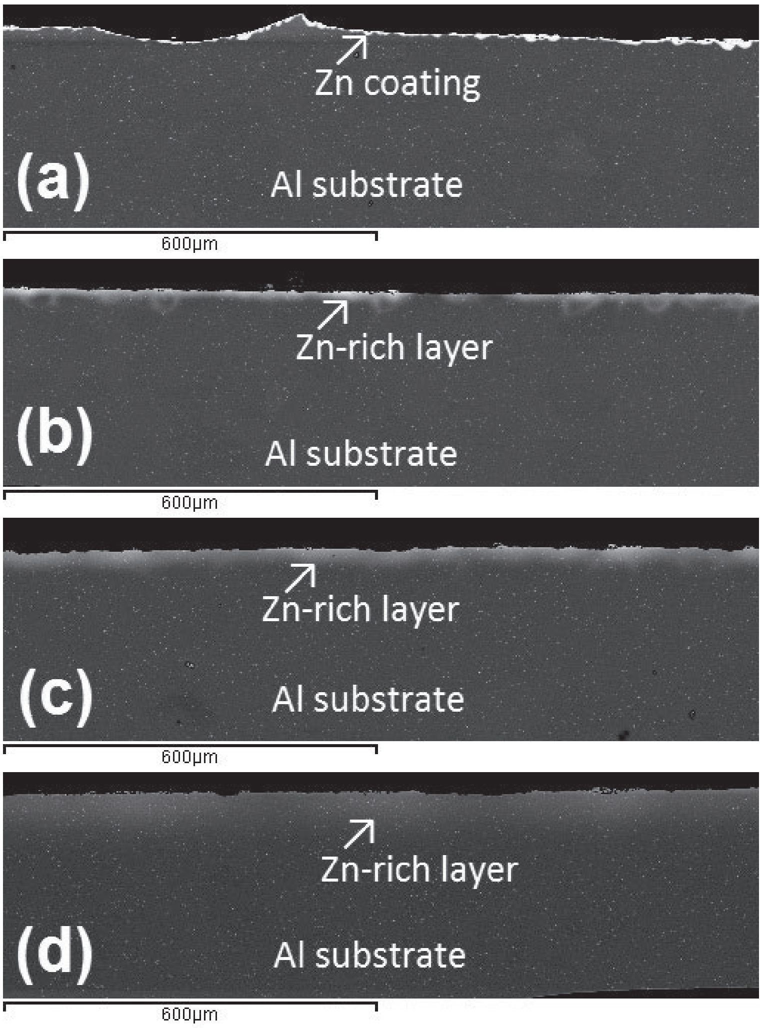

FIGURE 3.14: Backscattered electron images of cross sections of a) Zn coating on Al, and Zn-rich layers obtained by heat treatment for b) 2 hours at 350 °C, c) 2 hours at 390 °C, d) 4 hours at 430 °C for samples with Zn load of 8 g/m^2.

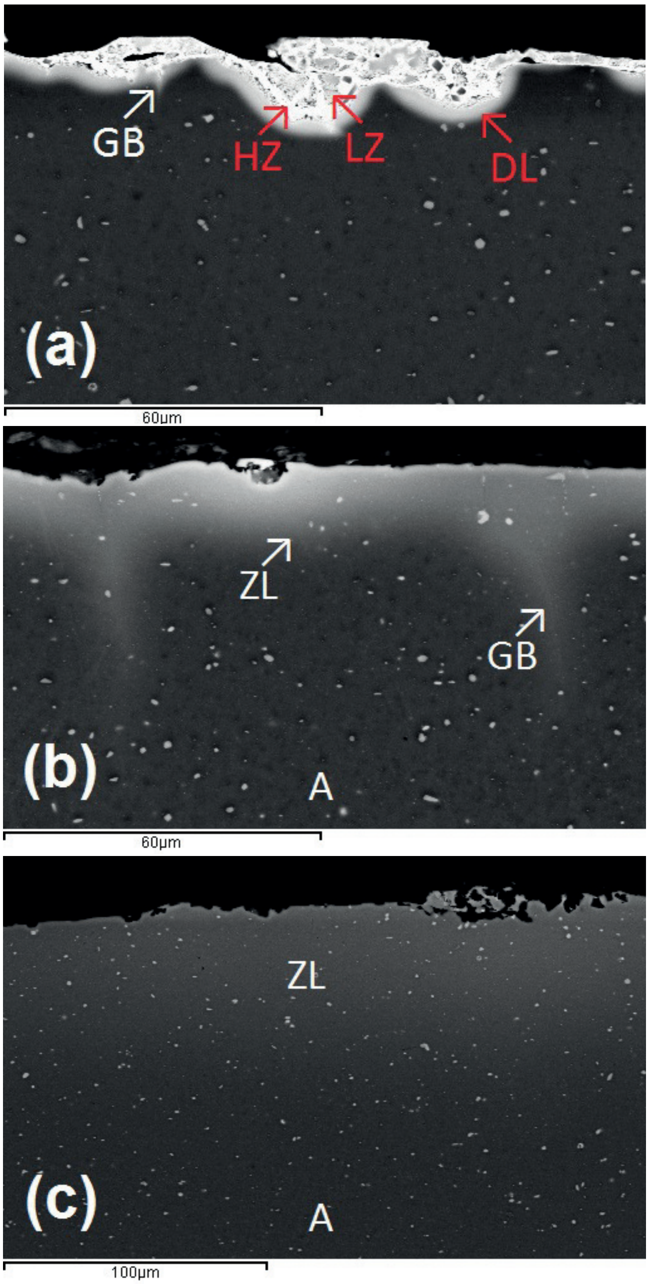

FIGURE 3.15: Higher magnification, backscattered electron images of cross sections of a) Zn coating on Al, and Zn-rich layers obtained by heat treatment for b) 2 hours at 350 °C, c) 4 hours at 430 °C for samples with Zn load of 8 g/m^2. Markings: HZ - high Zn region, LZ - low Zn region, DL - Zn diffusion layer, ZL - Zn-rich layer, A - Al substrate, GB - grain boundaries with Zn diffusing along them.

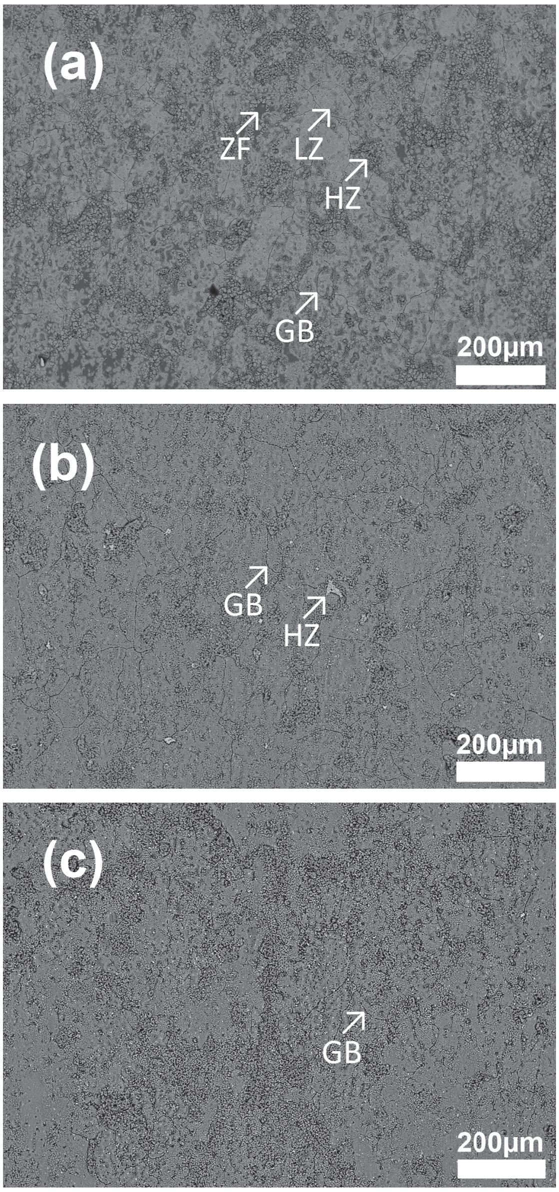

FIGURE 3.16: Backscattered electron images of surfaces of a) Zn coating on Al, and Zn-rich layers obtained by heat treatment for b) 4 hours at 430 °C, c) 4 hours at 510 °C for samples with Zn load of 2.7 g/m^2. Arrows indicate the Zn-free areas (marked as ZF), higher-Zn areas (HZ), lower-Zn areas (LZ) and grain boundaries (GB).

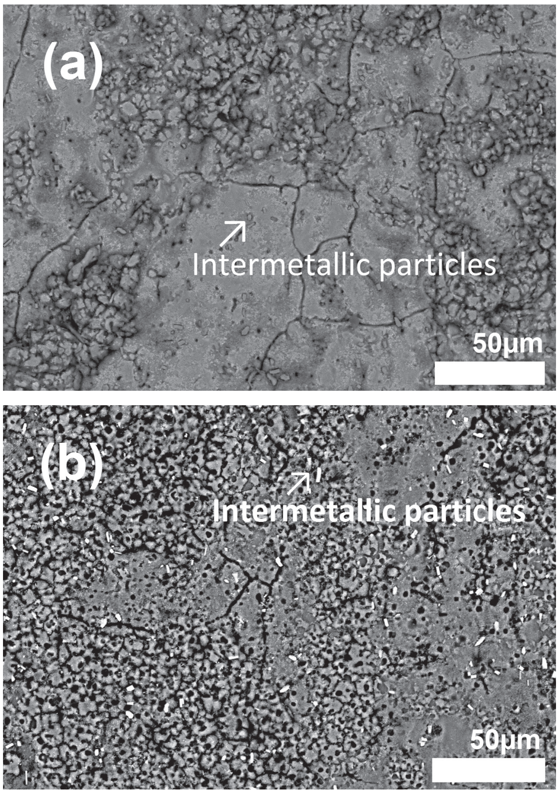

FIGURE 3.17: Higher magnification, backscattered electron images of surfaces of a) Zn coating on Al, and b) Zn-rich layers obtained by heat treatment for 4 hours at 510 °C for samples with Zn load of 2.7 g/m^2. Arrows show intermetallic particles.

3.4 Discussion

3.4.1 GD-OES calibration

Calibration of Zn achieved for 0 to 100% concentration range in Al by use of model binary AlZn standards, which were prepared in the laboratory for the present work, is considered reliable. This is indicated by the good agreement obtained between the weight of Zn coating before heat treatment, calculated by integration of mass concentration profile of Zn, and the value obtained by XRF within the reported error range. The calibration curve developed for up to 50 wt% Zn covers well the range needed for characterisation of Zn-rich layers in the present study. The use of a few AlZn alloys in terms of Zn concentration appears to be sufficient to obtain a satisfactory calibration curve for the present purposes. The detection limit of the 481.053 nm Zn line, estimated from the calibration measurements, is not sufficiently accurate at concentrations below about 0.1%. Selection of another spectral line, which is more sensitive to low concentrations, would be recommended along with a separate calibration curve tailored for small Zn concentrations.

Dendritic structures of the model binary alloys were similar to that reported in references [21–24]. Lamellar structure of AlZn95 eutectic alloy was also observed in [24]. However, the local concentration variations resulting from solidification morphology, are considered to be negligible with respect to the average concentration corresponding to an analysis area of 4 mm in diameter obtained by GD-OES.

The calibration curves for Mn and Fe, obtained from the other available standards listed in table 3.1, also gave good results in measuring the concentration of these elements in the AlMn alloy substrates. The values obtained by GD-OES agreed well with the data obtained by spark OES (table 3.9). The calibration for these elements satisfactorily cover the concentration ranges relevant to the Zn-rich layers and the MPE bulk substrate investigated. Although the calibration data for Si was scattered, the depth-profile results for the AlMn alloy samples show that the changes in Si concentration due to heat treatment are adequately traceable for the present purposes. For Mg, which becomes enriched at the surface at concentrations up to around 50 times higher than in the bulk, the calibration data had to be fitted to a polynomial rather than a straight line, covering both the high surface and low bulk concentrations. This may have lead to reduced accuracy in quantifying the Mg profiles. For higher accuracy, selection of a non-resonant Mg spectral line is recommended. However, since the GD-OES data for Mn, Fe and Mg were confirmed by EDS measurements, the calibration curves presented for these elements are considered to be suitable for the present purposes.

The calibration procedure used in this work improves the methods described in references [11] and [13] for Al-Zn system. It is straight forward, covers full concentration range of Zn and is based on requirement that sum of concentrations of all elements including minor allying ones are equal to 100% (which is not the case in reference [11]). Calibration for O was also achieved.

The sputtering rates measured during calibration are divided by the sputtering rate of the low alloyed iron standard to obtain relative sputtering rates. The effect of Zn concentration on the sputtering rate of AlZn alloys, measured in the present study, compares favourably with the results reported in reference [12]. However, the relative sputtering rates of samples with high Zn and high Al concentrations (nearly pure metals), measured in this work (5.89 and 0.28, respectively), were lower than the results reported in reference [8] (7.8 to 8.6 for Zn and 0.34 to 0.39 for Al). It is known that these values can vary significantly among laboratories due to variation of apparatus for crater depth measurement, method for calculation of the crater depth from the crater profile, including a method of compensation for unevenness of the crater, and the number of replicate measurements done [8]. Therefore, as long as there are no rigid standard procedures available for measurement of the sputtering rates, the reported relative sputtering rates may not be consistent between the laboratories.

In addition to the foregoing, present SEM and GD-OES measurements on the Zn-coated MPE specimens revealed non-uniformity of the Zn coating and Zn-rich layer thicknesses and Zn concentration of the Zn-rich layers laterally and in depth. However, despite all these challenges, GD-OES appears to be well suited for depth profiling of the Zn-rich layers for obtaining information averaged over the analysis area. In depth Zn concentration profiles obtained are reproducible within the 18% error limit, and this confirms the validity of the assumptions related to the present analytical approach. This conclusion seems to be valid despite the roughness of the Zn-rich surface and local variations in the layer thickness. With increasing degree of heat treatment, the Zn concentration in the layer becomes increasingly uniform laterally. Since this applies also to the concentration distribution of Zn on the crater surface during measurement, the depth resolution of the measurement must also improve.

3.4.2 Element profiles

SEM micrographs indicate high roughness of the samples surface, especially in case of low Zn load, which lead to alteration of the concentration profiles and makes it difficult to make comparisons and explain some of the results. Effect of heat treatment on the profiles of the alloying and trace elements originally present in the AlMn base alloy is relatively small when compared between the temperatures applied within the range of interest (350 - 510 °C) in relation to the effect of heat treatment observed compared to the non-heat-treated state. This is especially the case for Al, O and Si. It is true for Fe only for the high Zn-load case. For Al and Si, the changes observed appear as if they are partial recovery of the profiles to their bulk values as the Zn coating diffuses into the material. The concentration difference between the surface and the bulk is not too different for Al and Si in relation to the other elements. Since inward diffusion of Zn causes mutual outward diffusion of Al in a nearly binary system, a significant enrichment of Al toward the surface occurs, rendering a more uniform depth profile not too different from its bulk concentration, even after the mildest heat treatment applied (2 h at 350 °C). Therefore, the diffusion rate of Al appears to become significantly reduced relative to that of Zn for the heat-treated samples, a factor which may facilitate the theoretical treatment of Zn diffusion in Al alloys. These theoretical issues will be discussed further in the next chapter.

Surface enrichment of Fe and Mg on non-heat-treated Al sample is assumed to be related to the areas which did not become covered with Zn. Unexpected high enrichment of Fe near the surface can be attributed to contamination from the extrusion die. $(Fe,Mn)Al_6$ and $(Fe,Mn)_3Si_2Al_{15}$ intermetallic particles [20], which are the most common phases in the AlMn alloy substrate, were possibly enriched closer to the surface of the Zn coating due to the physical processes, such as melting, solidification and deformation, occurring during Zn arc spraying. Some of these could have formed as a result of precipitation of additional Fe-rich phases including contaminants from the extrusion dye, due to extremely small solubility of Fe in Al. Concentration distribution of Fe contained in particles will not be affected by heat treatment. These phases are also known to incorporate Mn and Si, which may be available in solid solution due to their small (but higher than Fe) solubilities, during heat treatment. Increasing Si and Mn concentrations toward the surface can be attributed to the resulting formation of $(Fe,Mn)_3Si_2Al_{15}$ intermetallic particles near the surface. Thus, the depth profiles of the minor elements Fe, Mn and Si will depend partly on the complex dissolution and precipitation mechanisms of intermetallic phases.

High segregation of Mg at the surface of as extruded Al tube is expected because diffusion coefficient of Mg in Al alloy is at least one order of magnitude higher than that for Fe and Mn (table 2.2). Enrichment of Mg, as stated earlier, is mainly due to its enrichment in the form of MgO in the Zn-rich layer. This is enhanced by high diffusion rate of metallic Mg in the substrate and Zn-rich layer during heat treatment and its oxidation in the Zn-rich layer as oxygen becomes increasingly available near the surface. This leads to depletion of Mg on the metal side and its further diffusion closer to the surface during heat treatment.

Comparison of the concentration profiles for Zn, O and alloying elements in the non-heat-treated samples with high and low Zn load indicates thinning of the Zn coating after chromic phosphoric treatment. The Al substrate had enrichment of Fe, Mg and Si at the surface. Removal of metallic Zn by immersion in chromic phosphoric acid lead to a surface with higher enrichment of Fe and Si elements compared to the samples with the original coating. This is confirmed by SEM analysis which shows presence of intermetallic particles on the surface of the samples after chromic-phosphoric treatment. This trend was observed for the heat treated samples also. Mg enriched at the surface of as coated samples, assumed to be in oxide form, was partly removed by the chromic-phosphoric treatment. This was confirmed by lower Mg level in the low Zn load non-heat treated samples and sample heat treated for 4 hours at 430 °C.

3.5 Conclusions

- The sputtering rates of the major components in the AlZn system differ widely with concentration, which seems to be a concern in GD-OES calibration. The present work showed that this is not a drawback in GD-OES calibration, even by using a few standards covering the full concentration range, which makes GD-OES well suited to study such systems.
- Calibration of secondary alloying elements and oxygen in such alloys is also possible and the accuracy depends on the sensitivity and self-absorption of the spectral lines and the errors introduced by measurements of the sputtering rate of the standards.

- Zn depth profiles obtained by GD-OES, using the present calibration curves (up to 100 wt% Zn for the non-heat-treated high Zn load sample and up to 50 wt% Zn for the heat-treated samples), agree well with the Zn content of samples and standards obtained independently by other methods (XRF and SEM), thereby validating the present calibration for the AlZn system with Mg, Fe, Mn and Si as the secondary alloying elements.
- By limiting the calibration curve to 50 wt% Zn, the precision of compositional analysis of alloying elements was improved in terms of reduced variation of the sputtering rate in this range due to Zn.
- Metallic Zn is removed by immersion of Zn-rich surfaces in chromic phosphoric acid. This is an easy and reproducible method to obtain samples with lower Zn load from Zn arc-sprayed MPE Al tubes.
- Exposure of the sample to heat during thermal-arc spraying of AlMn substrates by Zn and subsequent heat treatment of the Zn coated surfaces causes a significant enrichment of Mg in the Zn-rich surface layer, as a result of rapid Mg diffusion to the surface and its subsequent segregation into the layer as MgO.
- The elements Si and Mn, also become enriched in the Zn-rich layer by heat treatment due to inward diffusion of Zn into the AlMn substrate. Enrichment of Fe close to the surface is attributed to contamination of the extruded Al surface by the extrusion die. Due to low solubility in Al, Fe enrichment occurs in the form of Fe-rich intermetallic particles.

References

1. M. Bothwell, Diffusion cladding, Patent No: 3268358, The Dow Chemical Company, United States (1962).
2. H. Ikeda, *Aluminium*, **58**, 467–471 (1982).
3. M. Suzuki, A. Sugihara, T. Sano, T. Suzuki, Zincating aluminium, Patent No: EP0125352A1, Alcan International Limited, Canada (1984).
4. M. Suzuki, A. Sugihara, T. Sano, T. Suzuki, Process for applying a zinc coating to an aluminum article, Patent No: 4888218, Alcan international Limited, Canada (1989).
5. T. Morita, Heat exchanger, method for manufacturing the same , and heat exchanging tube, Patent No: WO2005066570, Showa Denko K.K, Japan (2005).
6. T. Morita, Aluminum pipe and process for producing same, Patent No: US20060185168, Showa Denko K.K, Japan (2006).

7. J. I. Goldstein, D. E. Newbury, P. Echlin, D. C. Joy, C. E. Lyman, E. Lifshin, L. Sawyer, J. R. Michael, Scanning Electron Microscopy and X-ray Microanalysis, Springer US, Boston, MA, 3rd ed. (2003).
8. T. Nelis, R. Payling, Glow discharge optical emission spectroscopy: a practical guide, RCS, Cambridge, UK (2003).
9. R. Payling, in Glow discharge optical emission spectrometry, edited by R. Payling, D. G. Jones, A. Bengtson, pp. 29–31, New York, J. Wiley, Chichester (1997).
10. R. Payling, M. Aeberhard, J. Michler, C. Authier, P. Chapon, T. Nelis, L. Pitchford, *Surface and Interface Analysis*, **35**, 334–339 (2003).
11. M. Marychurch, R. Payling, in Glow discharge optical emission spectrometry, edited by R. Payling, D. G. Jones, A. Bengtson, pp. 524–27, New York, J. Wiley, Chichester (1997).
12. R. Payling, in Glow discharge optical emission spectrometry, edited by R. Payling, D. G. Jones, A. Bengtson, pp. 267–68, New York, J. Wiley, Chichester (1997).
13. A. Ulgen, M. Dogan, *Analytical Letters*, **23**, 1897–1906 (1990).
14. King.V., R. Payling, in Glow discharge optical emission spectrometry, edited by R. Payling, D. G. Jones, A. Bengtson, pp. 289–91, New York, J. Wiley, Chichester (1997).
15. R. Payling, J. Michler, M. Aeberhard, *Surface and Interface Analysis*, **33**, 472–477 (2002).
16. R. K. Marcus, J. A. C. Broekaert, Glow discharge plasmas in analytical spectroscopy, J. Wiley, Chichester, England (2003).
17. R. Payling, D. G. Jones, S. A. Gower, *Surface and Interface Analysis*, **20**, 959–966 (1993).
18. H. Ellingham, *Journal of the Society of Chemical Industry*, **63**, 125–133 (1944).
19. Z. H. Jia, B. Graver, J. C. Walmsley, Y. D. Yu, J. K. Solberg, K. Nisancioglu, *Journal of the Electrochemical Society*, **155**, C1–C7 (2008).
20. L. F. Mondolfo, Aluminium alloys: structure and properties, Butterworths, London, Boston (1976).
21. S. Khireche, D. Boughrara, A. Kadri, L. Hamadou, N. Benbrahim, *Corrosion Science*, **87**, 504–516 (2014).
22. O. M. Suarez, E. G. Estremera, R. Soler, A. Declet, A. J. Hernandez-Maldonado, *Advances in Materials Science and Engineering*, **2014**, Article ID 963042, 6 pages (2014).
23. T. Savaskan, A. Aydiner, *Wear*, **257**, 377–388 (2004).

24. A. P. Hekimoglu, T. Savaskan, *International Journal of Materials Research*, **105**, 1084–1089 (2014).

Chapter 4

Modelling of Zn diffusion in Al alloy

Abstract

The purpose of this work is to study the possibility of modelling of Zn diffusion from a Zn coating into a commercial Al alloy substrate. The rigorous formulation of unsteady-state binary diffusion was reduced to the simple one-dimensional form of Fick's second law by defining an effective binary diffusion coefficient D_{ZnAl}^{eff} for the system. Zn depth profiles of Zn-rich layers, obtained by heat treatment of Zn thermal-arc sprayed coating on AlMn substrate, were fitted to an analytical solution of Fick's second law for diffusion from a layer into a semi-infinite region. The D_{ZnAl}^{eff} values obtained from fitting were reproducible, justifying the assumptions made in the modelling procedure. The activation energy of diffusion was calculated to be 103 kJ/mol based on the D_{ZnAl}^{eff} values obtained in the temperature range 350 – 470 °C. A procedure for prediction of Zn concentration profiles in Zn-rich layers on commercial Al alloy substrate for different Zn loads was established.

4.1 Introduction

Successful development of Zn-rich coatings on Al alloys for protection against corrosion, especially pitting, over a given service period, requires optimization of the layer thickness and composition by optimizing the original Zn load applied to the Al surface and its concentration distribution in depth, obtained by heat treatment. In chapter 3 Zn-rich layers on AlMn alloy multiport extruded (MPE) tubes were characterised by glow discharge optical emission spectroscopy (GD-OES). Zn was deposited by thermal-arc spraying and subsequently subjected to heat treatment, allowing controlled diffusion of Zn into the AlMn substrate. Zn coating with lower Zn load was produced by chromic-phosphoric treatment. Concentration profiles of Zn, Al, O and alloying elements for selected heat treatment conditions were obtained.

The purpose of present work is to study the possibility to model Zn diffusion in such samples. Experimental Zn concentration profiles were fitted to a solution of Fick's second law to obtain an effective diffusion coefficient of Zn in Al as a function of heat treatment temperature in the range 350 - 510 °C. The obtained values of activation energy and pre-exponential factor were used for establishment of a procedure for simulation of such Zn concentration profiles in heat treated Zn coated AlMn samples.

Diffusion of Zn in Al was studied extensively in the past experimentally [1–5] and theoretically [6, 7]. The diffusion coefficients were found to be of the order of 10^{-14} m^2/s for 390 °C and the activation energy was between 100 and 130 kJ/s. In References [1–5] diffusion of Zn in AlZn alloys was also investigated and activation energy was found to depend on Zn concentration [1, 2, 4, 5].

4.2 Theory

Diffusion of a soluble element A, in this case Zn, into a multicomponent commercial alloy is quite complex. The problem can be simplified by neglecting the effect of small concentration secondary elements existing in the alloy, in this case the AlMn alloy, and treating the problem as diffusion of pure A (Zn) into pure B (Al). Fick's first law for such a binary system can be expressed rigorously as [8]

$$\mathbf{n_A} = \omega_A(\mathbf{n_A} + \mathbf{n_B}) - \rho D_{AB}\nabla\omega_A = \mathbf{v}\rho_A - \rho D_{AB}\nabla\omega_A \tag{4.1}$$

where $\mathbf{n_i}$ is mass flux of component i (kg/(m^2s)), ρ_i is the mass concentration of component i (kg/m^3), D_{AB} is the diffusion coefficient of the binary system A and B (m^2/s),

$$\rho = \rho_A + \rho_B \tag{4.2}$$

is the density of the binary alloy (kg/m^3),

$$\omega_i = \rho_i/\rho \tag{4.3}$$

is the mass fraction of species i (wt%),

$$\mathbf{v} = (\rho_A\mathbf{v_A} + \rho_B\mathbf{v_B})/\rho \tag{4.4}$$

is the mass average velocity (m/s), and $\mathbf{v_i}$ is the mass velocity of component i. The bold symbols are vectors.

It is possible to define a reference frame based on the mass average velocity by setting $\mathbf{v} = 0$. If diffusion occurs only in one dimension, perpendicular to the sample surface, then equation 4.1 reduces to

$$j_{Zn} = -\rho D_{ZnAl}\frac{d\omega_{Zn}}{dx} \tag{4.5}$$

where j_{Zn} is the diffusion flux of Zn with respect to the mass average velocity, and the subscripts A and B are replaced with Zn and Al, respectively. Mass balance for component Zn in the x-direction leads to

$$\frac{d\rho_{Zn}}{dt} = -\frac{dj_{Zn}}{dx} = \frac{d}{dx}\rho D_{ZnAl}\frac{d\omega_{Zn}}{dx} \tag{4.6}$$

Diffusion of Zn in a commercial Al alloy with grain boundaries and a non-uniform porous coating is quite complex. It is common in such situations, especially for diffusion in porous media [8], to replace the binary diffusion coefficient by an effective diffusivity D^{eff}, which is vaguely defined and can only be applicable for the present surface morphology and structure of the Zn coating and underlying AlMn substrate. Furthermore, we assume that ρD^{eff} is independent of concentration (constant). This is difficult to justify considering significant change in ρ that can occur with concentration change in the Al-Zn system. With these assumptions equation 4.1 reduces further to

$$\frac{d\rho_{Zn}}{dt} = D^{eff}_{ZnAl}\frac{d^2\rho_{Zn}}{dx^2} \tag{4.7}$$

which is the familiar form of Fick's second law. We went through the derivation to show the assumptions involved in using Fick's second law, some of which are not easily justifiable. In the present case, justification of these will be based on a discussion as to which extent the calculated results are representative of the experimental diffusion data obtained in Chapter 3.

When $\rho_{Zn} << \rho_{Al}$, equation 4.5 can be obtained without defining of reference frame as described above. In this case flux $\mathbf{n_{Zn}} >> \mathbf{n_{Al}}$ and equation 4.1 becomes

$$\mathbf{n_{Zn}} = \omega_{Zn}\mathbf{n_{Zn}} - \rho D^{eff}_{ZnAl}\frac{d\omega_{Zn}}{dx} = -\frac{\rho D^{eff}_{ZnAl}}{1-\omega_{Zn}}\frac{d\omega_{Zn}}{dx} \tag{4.8}$$

for diffusion occurring in one dimension. The term

$$1-\omega_{Zn} \rightarrow 1 \quad \text{for} \quad \rho_{Zn} << \rho_{Al} \tag{4.9}$$

and equation 4.8 reduces to 4.5.

The physical model consists of the Zn coating, which can be represented at the outset (t = 0) as a slab of ZnAl alloy of uniform Zn concentration $\rho_{Zn,0}$ of thickness h, in contact with the semi-infinite AlMn substrate, as shown in figure 4.1. This is another assumption made for simplifying the numerical calculation instead of using the rigorous initial condition $\rho_{Zn,0} = f(x)$, where $f(x)$ would be the actual Zn profile obtained at the surface by thermal-arc spraying of Zn. The practical convenience and possible justification of the assumption will be discussed further in connection with the proposed numerical method.

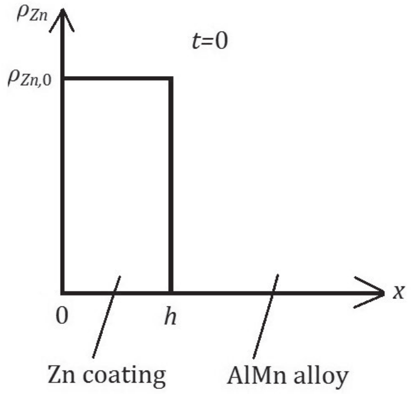

FIGURE 4.1: Approximation for the concentration-depth profile for the Zn coating on the surface of AlMn alloy at $t = 0$.

The boundary conditions for solving equation 4.7 for this system are

$$\frac{\partial \rho_{Zn}}{dx} = 0 \quad \text{at} \quad x = 0 \quad \text{and} \tag{4.10}$$

$$\rho_{Zn} = 0 \quad \text{as} \quad x \to \infty \tag{4.11}$$

In addition, the initial condition,

$$\rho_{Zn} = \rho_{Zn,0} \quad \text{for} \quad 0 \leq x \leq h \quad \text{at} \quad t = 0 \tag{4.12}$$

has to be satisfied.

The solution to equations 4.7 and 4.10 to 4.12 can be expressed as [9]

$$\rho_{Zn} = \frac{1}{2}\rho_{Zn,0}\left\{ erf\frac{h-x}{2\sqrt{(D^{eff}_{ZnAl}t)}} + erf\frac{h+x}{2\sqrt{(D^{eff}_{ZnAl}t)}} \right\} \tag{4.13}$$

The temperature dependence of the diffusion coefficient can be expressed by the Arrhenius equation [10]:

$$D^{eff}_{ZnAl} = D^{eff}_{ZnAl,0} exp\left(\frac{-E_a}{RT}\right) \tag{4.14}$$

where $D^{eff}_{ZnAl,0}$ is the pre-exponential factor (m^2/s), E_a is the activation energy (J/mol), R is the gas constant (J/K/mol) and T is the temperature (K).

4.3 Experimental

Materials. The coated MPE tube substrates were provided by Sapa AS. Composition of the substrate alloy, measured by Spark OES, was shown in table 3.3, both in mass fraction and mass concentration. The Zn coating was applied by thermal-arc spraying immediately after extrusion. Typical Zn load on the surface, determined by X-ray fluorescence (XRF) spectrometer (CMI 900 from Oxford Instruments) was 8.0 ± 0.2 g/m^2. The tubes were cut, rinsed in distilled water, acetone and ethanol and subsequently heat treated for 1, 2, 3, 4 and 5 hours at 350, 390 and 430 °C to obtain Zn-rich layers with varying thickness and Zn concentration profiles on the surface of the AlMn substrate. The procedure used to produce Zn rich layers with lower Zn loads than that possible by thermal-arc spraying was described in the previous chapter. The Zn load on such samples was estimated as 2.7 ± 0.7 g/m^2. The samples with Zn load of 8 g/m^2 and 2.7 g/m^2 will be designated in this work as samples with high Zn load and low Zn load, respectively. MPE tubes with low Zn load were heat treated for 4 hours at 430 °C, 470 °C and 510 °C.

Elemental analysis. Zn concentration profiles of Zn-rich layers on MPE Al substrate were obtained by GD-OES RF glow discharge optical emission spectrometer GD-PROFILER 2 with a 4 mm anode sup- plied by HORIBA Jobin Yvon using the calibration and measurement procedure described in Chapter 3.

4.4 Numerical Procedure

Experimental concentration profiles of Zn-rich layers on AlMn substrate obtained by GD-OES were fitted to equation 4.13 to obtain the parameters D^{eff}_{ZnAl} and h. Concentration profiles in mass per unit volume were used. Zn concentration in the Zn-rich coating before heat treatment $\rho_{Zn,0}$ was set to 100 wt% (7.14 g/cm^3) and 32 wt% (1.09 g/cm^3) for high and low Zn load, respectively, and these values were assumed to be constant within the thickness h, as indicated in the description of the physical (figure 4.1) and mathematical models (equation 4.12) in section 4.2. The value selected for the low-Zn load is the maximum Zn concentration in Zn depth profile for the low Zn load sample, which was at a distance of 0.6 µm from the surface, as reported in Chapter 3. Curve-fitting was performed by least-square regression analysis. The values D^{eff}_{ZnAl} and h were adjusted to maximize the coefficient of determination, R^2. Thus with these assumptions, the parameter h became an effective initial thickness rather than the actual thickness in the present analysis.

The assumptions related to the initial condition are in principle not necessary because solving Fick's law by using any initial concentration distribution $f(x)$ for Zn is tractable [11]. However, the data, which would have to be measured experimentally, to determine $f(x)$ may not be readily available. Such a measurement may not be feasible for pure model calculations for practical design purposes. The proposed assumptions for the initial condition further introduces significant simplifications to the mathematics, first of all in the form of an analytical solution.

The assumption of 100% Zn for this region may be acceptable for the high-load case because of the presence of undisturbed thermally sprayed coating. However, a small fraction of the Zn diffuses into the AlMn substrate already during spraying and before application of further heat treatment. In the case of the low-load case, pure Zn is dissolved by chromic-phosphoric acid treatment. The value 32 wt% selected for this case as the initial condition, and that this value is constant within a depth of h from the surface, is an assumption. Since h could not be measured accurately on surfaces with non-uniform thickness of Zn (or Zn-rich layer), it is suggested to determine h, which became an effective parameter, by curve fitting the experimental data to equation 4.7. This is also one of the assumptions to be justified.

The points in the Zn concentration profiles with high Zn concentration at the outermost surface are due to the non-uniformity of the thermal-arc sprayed coating, as discussed above and in chapter 3. These parts of the curve have non-fickian behavior, *i.e.*, they could not be fitted to the solution to Fick's second law. They are characterized by high slopes, while the slope of the curves calculated from equation 4.13 are required to be zero at $x = 0$. Inspection of figure 3.6 indicates that the depth profiles flatten out, or reach a shallow maxima very close to $x = 0$, nearly satisfying the zero slope boundary condition before the significant anomalous increase in the slope with further decrease in x. The data points giving this anomalous behaviour were not included in the data analysis. It was also discussed in chapter 3 that GD-OES calibration is not reliable for Zn concentrations close to the detection limit of 0.12 wt%. The Zn-rich layer thickness, L, was estimated as the depth at which Zn concentration dropped to 0.3 wt% or 0.008 g/cm^3 in chapter 3. The data measured at depths larger than the Zn-rich layer thickness were also excluded from the data for curve fitting.

The depth of the crater obtained during GD-OES measurement of the low Zn load sample heat treated for 4 hours at 510 °C was much smaller than the Zn rich layer thickness of this sample (as discussed in sections 4.5 and 4.6). Therefore this profile was excluded from further analysis due to inadequate result of fitting. The effective diffusion coefficients obtained by fitting of all the other profiles were plotted in the form of $ln(D_{ZnAl}^{eff}) = f(1/T)$ according to equation 4.14 and fit by least square regression analysis to a straight line. Activation energy and pre-exponential factor were estimated from the slope and y-intercept of this plot.

4.5 Results

The experimental Zn concentration profiles of high Zn load samples (8.0 g/m^2) heat treated for selected durations at 350 °C, 390 °C and 430 °C were shown in chapter 3 in figures 3.6a-c. Zn concentration profiles of Zn rich layers obtained by heat treatment of low Zn load samples (2.7 g/m^2) for 4 hours at 430 °C, 470 °C and 510 °C were shown in chapter 3 in figure 3.6d. These data are reproduced below in each plot of figure 4.2 as red discrete data points. The continuous black curves in the figures are obtained by fitting the data to equation 4.13, in the manner described above. The curves for samples with high Zn load heat treated for 2 hours at 350 °C and 4 hours at 430 °C (figures 4.2a and d, respectively) show satisfactory fits. The fits for the high Zn load samples heat treated for 1 and 5 hours at 390 °C and low Zn load sample heat treated for 4 hours at 430 °C (figures 4.2b, c and e, respectively) are very good. Figures 4.2f and g show satisfactory fits for low Zn load heat treated for 4 hours at 470 °C and 510 °C, respectively, up to a depth of about 60 μm, the fit for 510 °C being worse of the two.

Table 4.1 is a summary of the results, including the (effective) initial Zn coating thickness h, effective diffusion coefficient D^{eff}_{ZnAl} and Zn-rich layer thickness L, obtained by curve fitting. The table reports also the experimental values of L and Zn coating weight W_{Zn}, obtained by GD-OES (chapter 3), and W_{Zn}, given by

$$W_{Zn} = \rho_{Zn,0} h \tag{4.15}$$

In cases where Zn concentration did not reach the values suggested for estimating L during the length of experiment due to limitations of the GD-OES crater depth, the maximum depth measured is indicated.

Thickness of the Zn coating h estimated from curve-fitting is reproducible for different heat treatment procedures with little scatter among the high Zn load samples. The h-values obtained for the low-Zn load samples heat treated for 4 hours at 430 °C and 470 °C are also quite close to one another, while they are much higher for the sample heat treated at 510 °C. The total Zn content in the Zn-rich layers, calculated according to equation 4.15, agree well with the values obtained by GD-OES except for the low Zn-load samples heat treated for 4 hours at 510 °C. The effective diffusion coefficients also agree well with little scatter for each selected temperature of heat treatment, which is expected since D^{eff}_{ZnAl} is a material property and should not be affected by other factors, such as the period of heat treatment at a given temperature and the Zn load, within the stated assumptions. The thickness of the Zn-rich layer L obtained by curve-fitting is much smaller than the L obtained from GD-OES measurements for the low degrees of heat treatment conditions. It is closer to the measured values for the medium degrees of heat treatment and agrees well for the higher degrees of heat treatment.

As indicated above, the Zn depth profile obtained by GD-OES for the low Zn load sample, which was heat treated at 510 °C, was limited to about half

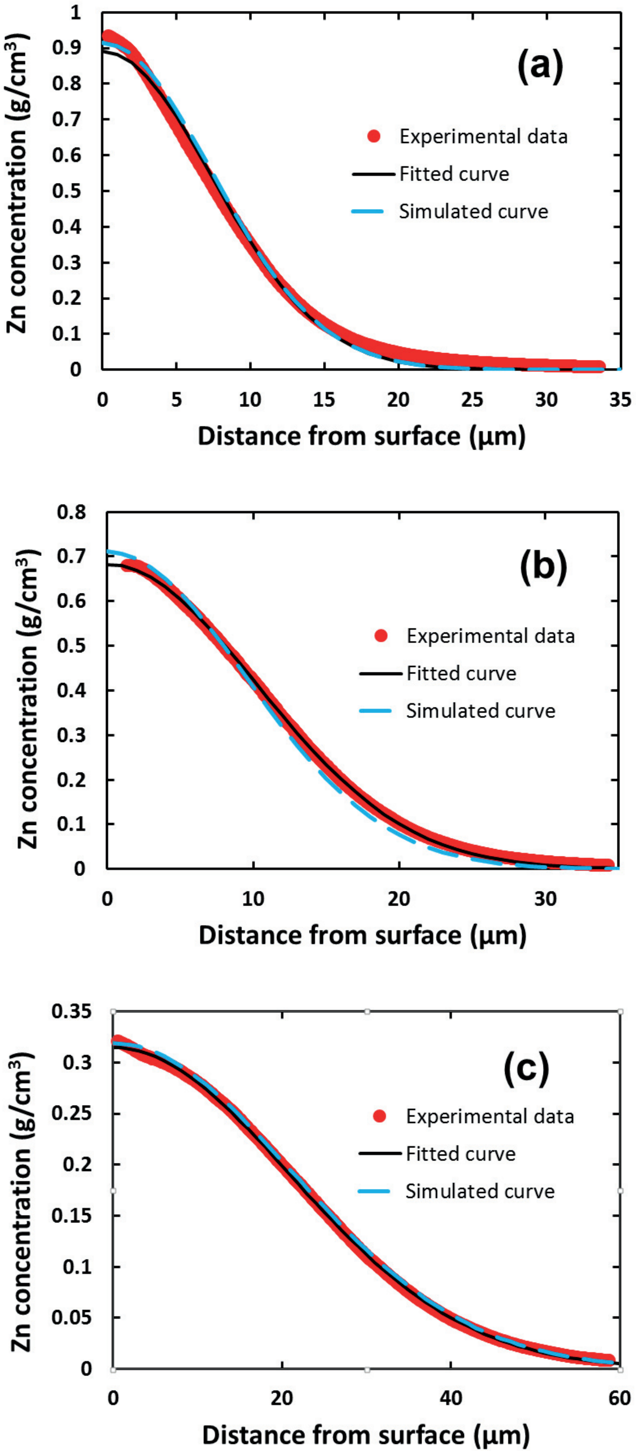
(a)
Zn concentration (g/cm³)
1
0.9
0.8
0.7
0.6
0.5
0.4
0.3
0.2
0.1
0
0
5
10
15
20
25
30
35
Distance from surface (μm)
Experimental data
Fitted curve
Simulated curve
(b)
Zn concentration (g/cm³)
0.8
0.7
0.6
0.5
0.4
0.3
0.2
0.1
0
0
10
20
30
Distance from surface (μm)
Experimental data
Fitted curve
Simulated curve
(c)
Zn concentration (g/cm³)
0.35
0.3
0.25
0.2
0.15
0.1
0.05
0
0
20
40
60
Distance from surface (μm)
Experimental data
Fitted curve
Simulated curve

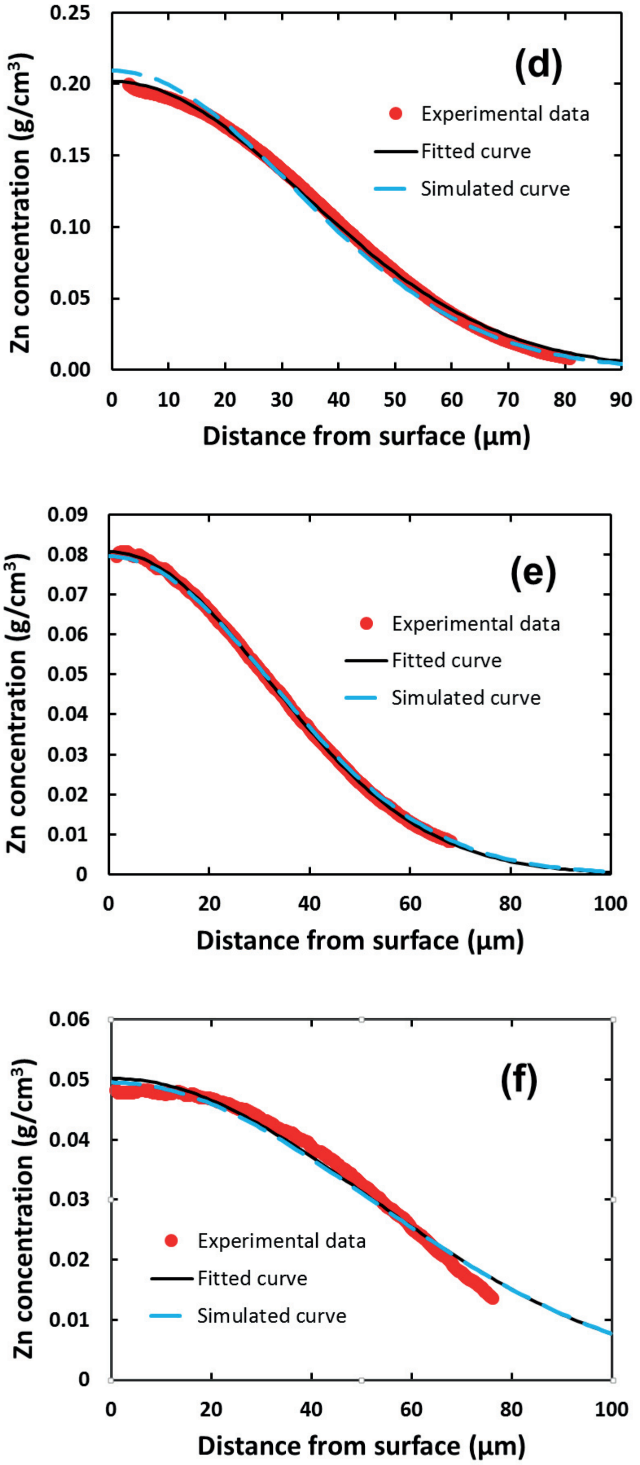
(d)
Experimental data
Fitted curve
Simulated curve
Zn concentration (g/cm^3)
0.25
0.20
0.15
0.10
0.05
0.00
0
10
20
30
40
50
60
70
80
90
Distance from surface (µm)
(e)
Experimental data
Fitted curve
Simulated curve
Zn concentration (g/cm^3)
0.09
0.08
0.07
0.06
0.05
0.04
0.03
0.02
0.01
0
0
20
40
60
80
100
Distance from surface (µm)
(f)
Experimental data
Fitted curve
Simulated curve
Zn concentration (g/cm^3)
0.06
0.05
0.04
0.03
0.02
0.01
0
0
20
40
60
80
100
Distance from surface (µm)

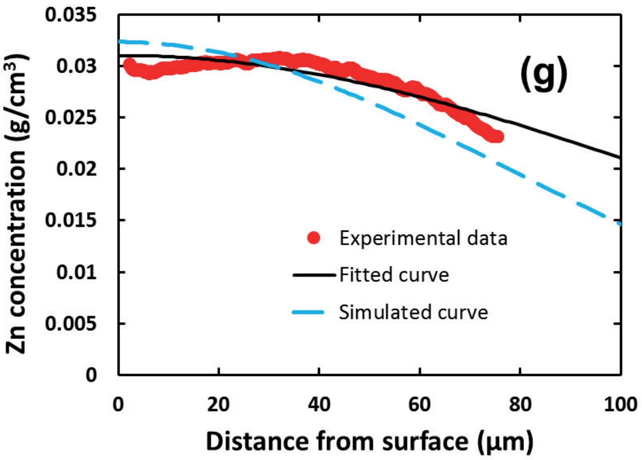

FIGURE 4.2: Zn concentration profiles fitted to the solution of Fick's second law (eq. 4.13) for samples with Zn load of 8 g/m^2 heat treated for: a) 2 hours at 350 °C, b) 1 hour at 390 °C, c) 5 hours at 390 °C, d) 4 hours at 430 °C and 2.7 g/m^2 heat treated for 4 hours at: e) 430 °C, f) 470 °C and g) 510 °C.

of the Zn-rich layer. At the end of the measurement Zn concentration drops by only 15% from the value on the surface. These data did not give a good fit to equation 4.13 (see figure 4.2g). The values obtained for h and W_{Zn} were too high. Therefore, this sample was disregarded in the estimation of the activation energy described below.

In order to check the sensitivity of the assumption related to the initial condition, where the low-Zn load coating is approximated as a layer with fixed concentration and depth, the data for Zn concentration profiles for the low Zn load samples, heat treated for 4 hours at 430 °C and at 510 °C, were analyzed by curve fitting as above to equation 4.13 by using different initial Zn concentrations, selected as $\rho_{Zn,0}$ = 100 wt% (7.14 g/cm^3), and 17 wt% (0.5 g/cm^3) and compared to the results for 32 wt% (1.09 g/cm^3) in table 4.1. The D_{ZnAl}^{eff} and h values obtained are summarized in table 4.2. The estimated weight of Zn coating, diffusion coefficient and thickness of the Zn-rich layer are seen to be nearly the same for all three $\rho_{Zn,0}$ for a given type of sample. It is observed that the D_{ZnAl}^{eff} value obtained for heat treatment at 430 °C is very similar for different heat-treatment periods and Zn-loads given in tables 4.1 and 4.2, as expected along the lines for the material-property argument above. The L values in table 4.2 for each of heat treatments are also similar which implies that the concentration profiles calculated for these cases are similar despite the differences in the initial conditions specified.

Figure 4.3 shows the Zn concentration profiles for the initial conditions and diffusion coefficients given in table 4.2 after different times of heat treatment

TABLE 4.1: Results of fitting of Zn concentration profiles of Zn-rich layers in AlMn substrate to a solution of Fick's second law (eq. 4.13) to obtain thickness of the Zn coating h, Zn coating weight W_{Zn} , effective diffusion coefficient D_{ZnAl}^{eff} and Zn-rich layer thickness L. W_{Zn} and L obtained by GD-OES measurements are included.

Heat treatment	**GD-OES results**		**Fitting results**			
	W_{Zn} **(g/m^2)**	L **(µm)**	h **(µm)**	W_{Zn} **(g/m^2)**	D_{ZnAl}^{eff} **(m^2/s)**	L **(µm)**
High Zn load, $\rho_{Zn,0}$ = 100 wt % (7.14 g/cm^3)						
350°C 2h	8.6	34	1.2	8.2	3.8×10^{-15}	23
350°C 3h	8.4	>36	1.1	8.2	3.6×10^{-15}	27
350°C 4h	8.9	>36	1.2	8.7	3.4×10^{-15}	29
350°C 5h	8.0	44	1.1	7.8	3.6×10^{-15}	33
390°C 1h	8.9	34	1.2	8.8	1.4×10^{-14}	30
390°C 2h	8.7	42	1.2	8.6	1.4×10^{-14}	40
390°C 3h	9.2	53	1.3	9.2	1.4×10^{-14}	49
390°C 5h	8.3	59	1.2	8.2	1.2×10^{-14}	56
430°C 1h	8.0	45	1.1	8.0	3.4×10^{-14}	44
430°C 2h	8.6	59	1.2	8.7	3.3×10^{-14}	59
430°C 3h	7.9	>66	1.1	8.1	3.2×10^{-14}	69
430°C 4h	8.4	81	1.2	8.6	4.0×10^{-14}	86
Low Zn load, $\rho_{Zn,0}$ = 32 wt % (1.09 g/cm^3)						
430°C 4h	3.2	68	2.9	3.2	3.4×10^{-14}	68
470°C 4h	2.8	>76	3.0	3.2	9.2×10^{-14}	98
510°C 4h	2.2	>76	4.0	4.4	4.5×10^{-13}	187

at 430 °C. $\rho_{Zn,0}$, h and D_{ZnAl}^{eff} values from table 4.2 were inserted into the solution of Fick's second law (equation 4.13), and the time of heat treatment was selected as 1, 10 and 60 minutes. The profiles of the initial coating slabs are shown by the dashed lines. After 1 minute of heat treatment Zn concentration profiles vary widely for different initial coatings (figure 4.3a). The difference is reduced significantly after 10 minutes of heat treatment (figure 4.3b) and becomes negligible after 60 minutes (figure 4.3c), *i.e*, the concentration distributions for Zn converge to a common solution with increasing time of heat treatment.

Temperature dependence of the effective diffusion coefficient is shown in figure 4.4. Activation energy and pre-exponential factor were calculated to be E_a = 103 kJ/mol and $D_{ZnAl,0}^{eff}$ = 2 $\times10^{-6}$ m^2/s, respectively.

Zn concentration profiles of Zn-rich layers on Al were simulated by using equation 4.13 and the average h values 1.2 µm and 2.9 µm from table 4.1 for

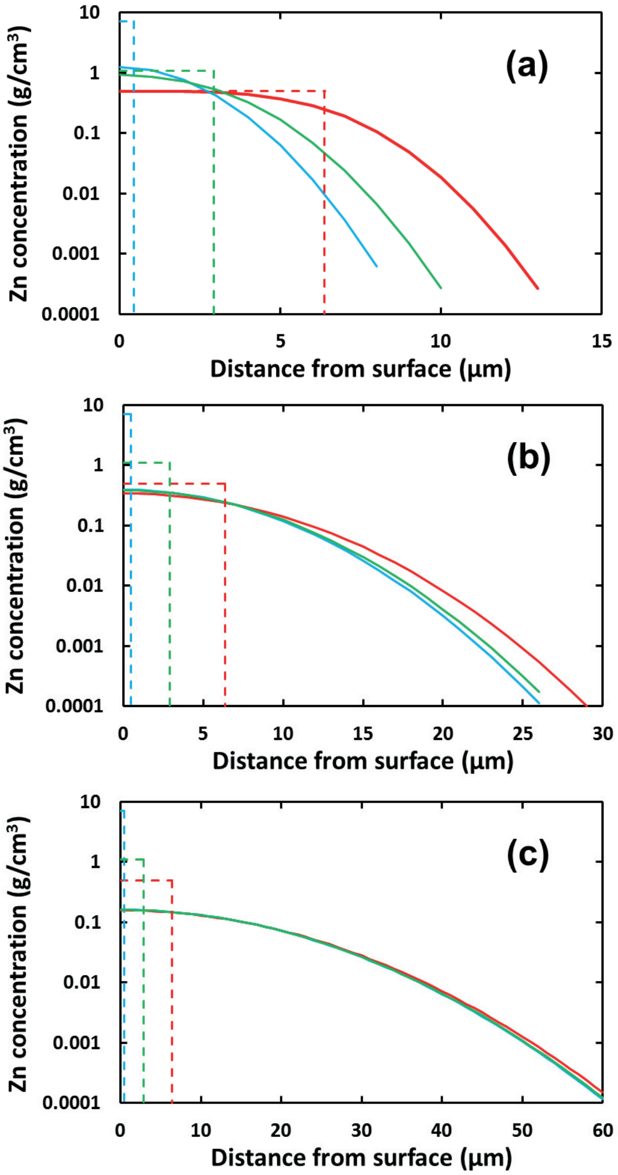

FIGURE 4.3: Calculated Zn depth profiles of heat treated Zn coated AlMn alloy samples with Zn load of 2.7 g/m^2. Simulation was done using equation 4.13, Zn concentration in the initial coating were $\rho_{Zn,0}$ = 0.5 g/cm^3 (red curves), 1.09 g/cm^3 (green curves) and 7.14 g/cm^3 (blue curves). For each $\rho_{Zn,0}$, the corresponding initial coating thickness and effective diffusion coefficient were taken from table 4.2. Dashed lines represent the assumed initial concentration distributions for the coatings. Solid lines represent Zn depth profiles of the samples heat treated for a) 1 minute, b) 10 minutes and c) 60 minutes.

TABLE 4.2: Results of fitting of Zn concentration pro- files of Zn-rich layers in low Zn load samples heat treated for 4 hours at 430 °C and 510 °C to the solution of Fick's second law (eq. 4.13) with different assumed Zn concentrations on the coating $\rho_{Zn,0}$ to obtain thickness of the Zn coating h, Zn coating weight W_{Zn}, effective diffusion coefficient D^{eff}_{ZnAl} and Zn-rich layer thickness L.

Heat treatment	$\rho_{Zn,0}$ **(g/cm^3)**	h **(μm)**	W_{Zn} **(g/m^2)**	D^{eff}_{ZnAl} **(m^2/s)**	L **(μm)**
430°C 4h	7.14	0.4	3.2	3.4×10^{-14}	68
	1.09	2.9	3.2	3.4×10^{-14}	68
	0.50	6.4	3.2	3.4×10^{-13}	68
510°C 4h	7.14	0.6	4.4	4.5×10^{-14}	187
	1.09	4.0	4.4	4.5×10^{-14}	187
	0.50	8.9	4.4	4.5×10^{-13}	187

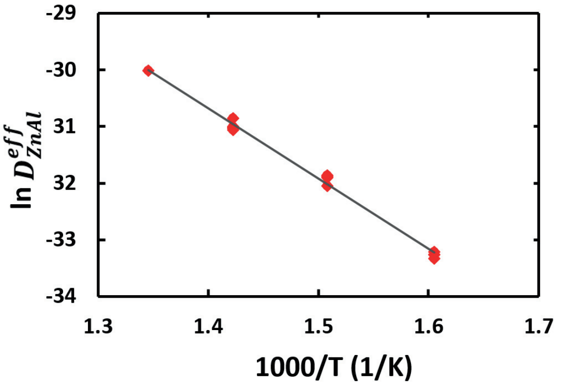

FIGURE 4.4: Arrhenius plot of effective diffusion coefficient (in m^2/s) for Zn-rich layers on AlMn substrate. Symbols represent experimental data, the line represents the least-squares fit of the data to a straight line.

high and low Zn load, respectively. The diffusion coefficient was estimated by equation 4.14 using the calculated activation energy and pre-exponential factor. The initial Zn concentrations for the coating, $\rho_{Zn,0}$, used in the calculation were the same as in the curve fitting procedure described in section 4.4 (100 wt% (7.14 g/cm^3) and 32 wt% (1.09 g/cm^3) for high and low Zn load, respectively). The results are shown as blue dashed lines in figures 4.2a-g. The simulated Zn concentration profiles are quite close to the fitted curves except for the low Zn load sample heat treated for 4 hours at 510 °C.

We would now like to compare the Zn-rich layer thicknesses, L, obtained from the three approaches discussed above, *viz.*, a) measured directly from the experimental GD-OES depth profiles, b) obtained by using the curve-fitting procedure described by using the GD-OES data and equation 4.13 (already reported in table 4.1), and c) estimated analytically from the simulated profiles by direct use of the equations 4.13 and 4.14 together with the reported activation energy and pre-exponential factor. The L values obtained by the three approaches are compared in table 4.3. Table 4.3 includes the values of D_{ZnAl}^{eff}, which were calculated using equation 4.14.

The simulated L-values for all high Zn load samples, heat treated at 350 °C, and the sample heat treated for 5 hours at 390 °C are closer to the directly measured GD-OES values than the L obtained by curve-fitting of the GD-OES data. In case of high Zn load samples heat treated for 1-3 hours at 390 °C, the simulated L is even lower than the values obtained by curve-fitting. For the samples heat treated at 430 °C for both Zn loads, simulated L is higher than the values obtained by both GD-OES and curve-fitting except for the high Zn load sample heat treated for 4 hours, for which it is quite close to the L obtained from GD-OES. The variations in L are generally quite small except for the high Zn load samples heat treated at 350 °C. The simulated profiles are believed to be the most useful of the three high-Zn depth profiles, for which the errors introduced by local variations on the sample and due to GD-OES measurements are minimized.

In an attempt to improve the Zn depth profile for the low Zn load sample heat treated for 4 hours at 510 °C, the following procedure was used. The value of h was fixed at 2.9 µm, which is the average value based on the two lower temperature, low Zn samples reported in table 4.1. The initial Zn concentration in the coating $\rho_{Zn,0}$ was again 1.09 g/cm^3 for the low-Zn samples as in table 4.1. The available GD-OES depth profile data was again fitted to equation 4.13 with these premises. The data-fitting was performed in this case by adjusting D_{ZnAl}^{eff} to maximize the coefficient of determination, R^2 (rather than adjusting both h and D_{ZnAl}^{eff} as in the general case described above). The D_{ZnAl}^{eff} obtained by this approach was 2.2×10^{-13} m^2/s. The same value is calculated by using equation 4.14 and the activation energy and pre-exponential factor obtained from the Arrhenius correlation in figure 4.4 (reported in table 4.3). Similar approach can be used in analyzing GD-OES data to develop or validate an Arrhenius expression for the temperature dependence of D^{eff} for different alloyed metallic coatings.

As an example of generating depth profiles for cases where experimental data are not available, Zn depth profiles for low Zn load samples heat treated for 1-3 hours at 430 °C and 470 °C were simulated by using the procedure described above, as shown in figure 4.5. A hypothetical pure Zn coating with load of 3.9 g/m^2 was also chosen for simulation as an intermediate option between high and low Zn loads. The parameters used were $\rho_{Zn,0}$ = 7.14 g/cm^3, h = 0.55 µm. The diffusion coefficients were obtained using equation 4.14 together with the calculated activation energy and pre-exponential factor. Simulated Zn depth profiles are shown in figure 4.6. Zn-layer thicknesses for all simulated profiles are reported in table 4.4. The

Table 4.3: Comparison of Zn-rich layer thickness L obtained experimentally by GD-OES, by fitting these results to equation 4.13 and from simulation. The effective diffusion coefficients D^{eff}_{ZnAl} calculated using equation 4.14 and used in the simulation are included. $\rho_{Zn,0}$ used in the calculations was 100 wt% (7.14 g/cm^3) and 32 wt% (1.09 g/cm^3) and the h was 1.2 µm and 2.9 µm for high and low Zn load, respectively.

Heat treatment	D^{eff}_{ZnAl} **(m^2/s)**	L (µm)		
		GD-OES	Curve fitting	Simulation
High Zn load				
350°C 2h	3.7×10^{-15}	33	23	23
350°C 3h		>36	26	27
350°C 4h		>36	29	31
350°C 5h		44	33	34
390°C 1h	1.2×10^{-14}	34	30	28
390°C 2h		42	40	38
390°C 3h		53	49	46
390°C 5h		59	56	57
430°C 1h	3.6×10^{-14}	45	44	45
430°C 2h		59	59	61
430°C 3h		>66	69	73
430°C 4h		81	86	82
Low Zn load				
430°C 4h	3.6×10^{-14}	68	68	69
470°C 4h	9.3×10^{-14}	>76	98	99
510°C 4h	2.2×10^{-13}	>76	187	132

profiles presented in figures 4.5 and 4.6 will be discussed in the following chapters considering the optimal Zn concentration profile for reducing the pitting of the Al alloy substrate and minimizing corrosion rate of the Zn-rich layer.

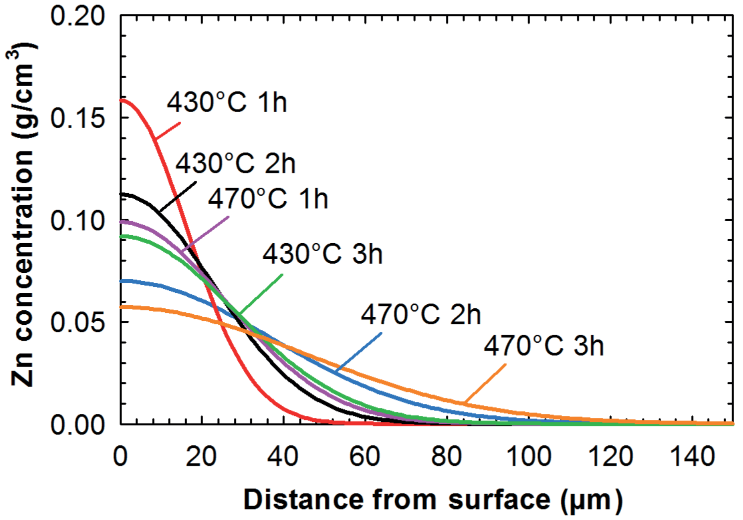

FIGURE 4.5: Simulated Zn depth profiles of heat treated Zn coated AlMn alloy samples with Zn load of 2.7 g/m^2 (low Zn load). Simulation was done using equation 4.13, Zn concentration in the initial coating $\rho_{Zn,0}$ = 1.09 g/cm^3 and initial coating thickness h = 2.9 µm.

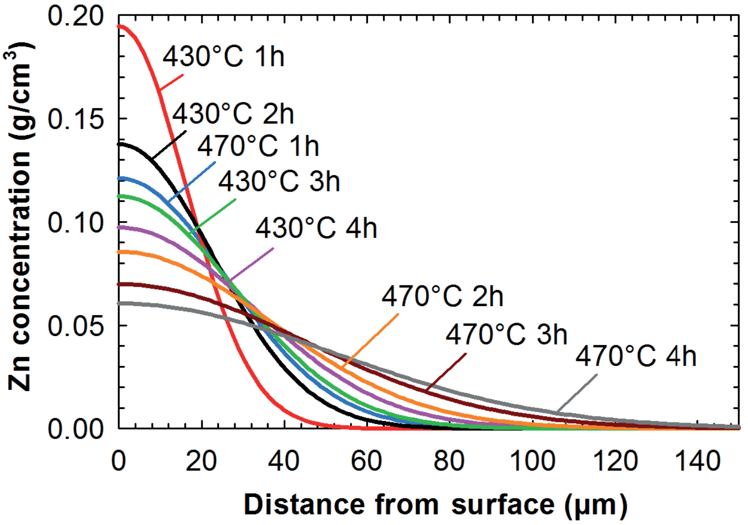

FIGURE 4.6: Simulated Zn depth profiles of Zn coated and heat treated AlMn alloy samples with Zn load of 3.9 g/m^2. Simulation was done using equation 4.13, Zn concentration in the initial coating $\rho_{Zn,0}$ = 7.14 g/cm^3 and initial coating thickness h = 0.6 µm.

TABLE 4.4: Zn-rich layer thickness L obtained from simulation of Zn depth profiles using equation 4.13. Zn concentration in the initial coating $\rho_{Zn,0}$ = 1.09 g/cm^3 and 7.14 g/cm^3, and initial coating thickness h = 2.9 µm and 0.55 µm for Zn loads of 2.7 and 3.9 g/m^2, respectively.

Zn load (g/m^2)	**Heat treatment**	L **(µm)**
2.7	430°C 1h	40
	430°C 2h	52
	430°C 3h	62
	470°C 1h	58
	470°C 2h	76
	470°C 3h	89
3.9	430°C 1h	41
	430°C 2h	54
	430°C 3h	64
	430°C 4h	72
	470°C 1h	60
	470°C 2h	79
	470°C 3h	93
	470°C 4h	104

4.6 Discussion

A methodology is developed for predicting Zn concentration profiles of Zn-rich layers produced by heat treatment of Zn thermal arc-sprayed coating on commercial Al alloy substrate by solution of Fick's second law for binary diffusion from a pure Zn or ZnAl alloy slab with initially uniform concentration into a semi-infinite aluminium alloy. Reducing the equations of mass transfer to the simple form of Fick's first law (equation 4.7) was based on working with respect to a reference frame centered on mass average velocity and using an effective diffusion coefficient for a porous Zn-rich layer of non-uniform thickness. The effective diffusion coefficient was obtained from curve fitting experimental Zn profiles obtained on commercial AlMn alloys coated with different Zn loads and heat treated in the temperature range 350 – 510 °C. The fits of Zn profiles to the solution of Fick's law were satisfactory except for the low Zn load sample heat treated for 4 hours at 510 °C. Initial thickness values obtained in this manner agreed well for samples coated similarly, but subjected to different heat treatments, to give different Zn profiles with the abovementioned exception.

The average total weight of the Zn coating, W_{Zn}, calculated as 8.4 ± 0.4 g/m^2 and 3.2 ± 0.2 g/m^2 for high and low Zn load, respectively, agree well with the data obtained by XRF analysis for the high Zn load samples (8.0 ± 0.2 g/m^2) and weighing of the low Zn load samples (2.7 ± 0.7 g/m^2).

The reproducibility of the effective diffusion coefficient obtained from the replicate specimens analyzed for a given heat-treatment temperature was also satisfactory, despite significant variations in the concentration levels and gradients among the samples. The diffusion coefficient is reproduced even for samples with different Zn loads treated at the same temperature of 430 °C. The obtained diffusion coefficients and calculated activation energy E_a = 104 kJ/mol agree well with the values found in literature [1–7].

The approximation used for the initial thickness and composition of the Zn thermal-arc sprayed coating, which is quite non-uniform both laterally and in depth, as a layer with fixed Zn concentration and thickness for both Zn loads can be questioned. The diffusion coefficient, which is assumed to be constant, may also change with depth near the surface for cases where the Zn concentration is high. Nevertheless, the arguments in the previous paragraph suggest that these assumptions seem to work quite well for obtaining reliable data for the effective diffusion coefficients and the Arrhenius-law parameters (activation energy and the pre-exponential factor). An accuracy within two significant digits is not very common in the measurement of solid-state diffusion coefficients.

The fact that the parameters obtained by curve fitting the depth profile data do not depend much on the initial Zn concentration $\rho_{Zn,0}$ selected for the coating in the example shown in table 4.2 indicate that the assumptions made in formulating the mathematical model, in particular in reducing the basic equation for the flux (equation 4.1) to the simple form of Fick's 1st law (equation 4.5) and further to Fick's 2nd law, and the assumptions involved in obtaining the analytical solution for the Zn concentration (equation 4.13) are justified. The variation in $\rho_{Zn,0}$ naturally requires corresponding variation in h to satisfy the macroscopic mass balance. The fact that the D_{ZnAl}^{eff} obtained by curve fitting does not vary with $\rho_{Zn,0}$ justifies the assumption that it is independent of concentration at a given temperature. Although it does not seem to affect the depth profiles under the heat treatment temperatures and durations of interest, $\rho_{Zn,0}$ and h do not correspond to the actual Zn concentration and thickness. These are the "effective" values obtained for the initial concentration and coating thickness, respectively, during curve fitting by maximizing the coefficient R^2 during the least-squares analysis.

This study has shown by practical examples and mathematical arguments, that the exact values of these parameters are not important in estimating the Zn depth profile for a given Zn load and heat treatment temperature and duration in the range of values important for the present purposes, as long as the macroscopic mass balance for Zn content of the Zn-rich layer, equation 4.15, is satisfied. A mathematical proof of independence of Zn concentration profiles on $\rho_{Zn,0}$ and h for large heat treatment times, as long as the macroscopic mass balance is satisfied, is described in the Appendix to this chapter.

The observed apparent independence of the depth profiles on the details of the initial Zn profile may be related to relatively high diffusion coefficients at the temperatures investigated, together with long heat treatment times. The initial conditions would be expected to become increasingly important with decreasing heat-treatment temperature and time, as shown in figure 4.3 and the Appendix. However, such conditions are neither compatible with each other nor feasible in practice since lower heat-treatment temperatures would require longer heat treatment times, and higher heat-treatment temperatures could affect the microstructure and deteriorate the mechanical properties of the aluminium alloy substrate.

A possible example to the above was the behavior of the low Zn-load samples heat treated at 510 °C. This heat treatment leads to quite small Zn concentrations in the Zn-rich layer, which are comparable with concentration of minor alloying elements in the Al substrate (Mn, Fe, Si and Mg). The diffusion process can no longer be assumed to be binary. At this temperature the alloying elements attain higher solubilities [12] and higher diffusion coefficients in Al [6]. The diffusion coefficient of Al also increases [7]. However, at such small concentrations the alloy can be considered dilute. The concentrations of Zn as well as alloying elements are so small that Zn atoms do not interact with other solute atoms [10]. Therefore, theoretical model described in section 4.2 can still be valid. It was also shown in section 4.2 that at small concentrations the model can be more easily justified.

It can be concluded from the foregoing arguments that the modelling procedure described here can be used to simulate Zn concentration profiles with different Zn loads on Al within the range 3 – 8 g/m^2 due to heat treatment in the range 350 °C - 510 °C. The modelling procedure is the following:

1. Estimate the effective diffusion coefficient for a given temperature from the Arrhenius equation

   $$D_{ZnAl}^{eff} = 2 \times 10^{-6} exp\left(\frac{-103 \times 10^3}{RT}\right) \tag{4.16}$$

   which is equation 4.14 with the presently determined values 103 kJ/mol and 2×10^{-6} m^2/s for the activation energy and the pre-exponential term substituted.

2. Specify/determine the values of the average coating thickness h and initial concentration of Zn in the coating $\rho_{Zn,0}$. If the coating is pure Zn, $\rho_{Zn,0}$ = 7.14 g/cm^3. If it is a ZnAl alloy, the $\rho_{Zn,0}$ value should be corrected for the density of the alloy. h can be obtained from the equation

   $$h = W_{Zn}\rho_{Zn,0} \tag{4.15}$$

   where W_{Zn} is the Zn load.

3. Calculate the Zn distribution ρ_{Zn} from equation 4.13 as a function of x.

4.7 Conclusions

- Zn concentration profiles of Zn rich layers on commercial Al alloy substrate, obtained by heat treatment in the temperature range 350 - 510 °C and heat-treatment time range 1 - 5 hours, were successfully fitted to a solution of Fick's second law for binary diffusion from an initial Zn-rich layer, representing the initial coating, into a semi-infinite region representing the Al alloy. The assumptions made by using a uniform average thickness for the initial Zn thermal arc-sprayed coating and use of a constant effective, rather than a well-defined binary, diffusion coefficient, worked well for the stated heat-treatment conditions.
- The temperature dependence of the effective diffusion coefficient was also described satisfactorily by use of an Arrhenius-type expression with the values for activation energy and pre-exponential factor determined as 103 kJ/mol and 2×10^{-6} m^2/s, respectively. This value of the activation energy agrees well with the literature data.
- The described procedure for modelling of Zn concentration profiles can be employed for estimation of the necessary heat treatment parameters for obtaining the desired Zn concentration profile by heat treatment of Zn coated Al alloy MPE tubes within the specified heat-treatment limits.

Appendix

For $z < 1$, the error function can be expressed by the Taylor series expansion [10]

$$erf(z) = \frac{2}{\sqrt{\pi}}\left\{z - \frac{z^3}{3\times 1!} + \frac{z^5}{5\times 2!} - \frac{z^7}{7\times 3!} + ...\right\} \tag{4.17}$$

or, in a closed form

$$erf(z) = \frac{2}{\sqrt{\pi}}\sum_{n=0}^{\infty}\left\{\frac{(-1)^n z^{2n+1}}{n!(2n+1)}\right\} \tag{4.18}$$

The expansion of equation 4.13 by using equation 4.17 gives

$$\rho_{Zn} = \frac{\rho_{Zn,0}h}{\sqrt{\pi}}\left\{\frac{1}{\sqrt{(D^{eff}_{ZnAl}t)}} - \frac{2h(h^2+3x^2)}{(3\times 1!)\left(2\sqrt{(D^{eff}_{ZnAl}t)}\right)^3} + \right. \\ \left. + \frac{2h(h^4+10h^2x^2+5x^4)}{(5\times 2!)\left(2\sqrt{(D^{eff}_{ZnAl}t)}\right)^5} - ...\right\} \tag{4.19}$$

For large x and since $\rho_{Zn,0}h = W_{Zn}$ (= Zn coating load = constant), equation 4.19 reduces to

$$\begin{aligned}\rho_{Zn} = \frac{2W_{Zn}}{\sqrt{\pi}}\Bigg\{ & \frac{1}{\sqrt{(D^{eff}_{ZnAl}t)}} - \frac{3x^2}{(3\times 1!)\left(2\sqrt{(D^{eff}_{ZnAl}t)}\right)^3} + \\ & + \frac{5x^4}{(5\times 2!)\left(2\sqrt{(D^{eff}_{ZnAl}t)}\right)^5} - ...\Bigg\} \\ = \frac{W_{Zn}}{\sqrt{\pi(D^{eff}_{ZnAl}t)}} & \sum_{n=0}^{\infty}\frac{(-1)^n}{n!}\left(\frac{x}{2\sqrt{(D^{eff}_{ZnAl}t}}\right)^{2n} = \frac{W_{Zn}}{\sqrt{\pi(D^{eff}_{ZnAl}t)}}e^{-z^2}\end{aligned} \tag{4.20}$$

where

$$z = \frac{x}{2\sqrt{(D^{eff}_{ZnAl}t}} \tag{4.21}$$

which is the well-known "thin-film solution" to Fick's 2nd law [10]. Thus, for constant W_{Zn} and $h << x$, the depth profile becomes a function of x and t only (no explicit h dependence). For small x, equation 4.13 reduces to

$$\rho_{Zn} = \rho_{Zn,0}erf\frac{h}{2\sqrt{(D^{eff}_{ZnAl}t}} \tag{4.22}$$

For large t equations 4.20 and 4.22 reduce to the simple well-known solution expression for the surface concentration for diffusion from a thin film [10]

$$\rho_{Zn} = \frac{W_{Zn}}{\pi\sqrt{(D^{eff}_{ZnAl}t}} \tag{4.23}$$

applicable at x = 0.

References

1. J. E. Hilliard, B. L. Averbach, M. Cohen, *Acta Metallurgica*, **7**, 86–92 (1959).

2. I. Godeny, D. Beke, F. J. Kedves, G. Groma, *Physica Status Solidi A*, **32**, 195–202 (1975).

3. S. Fujikawa, K. I. Hirano, *Transactions of the Japan Institute of Metals*, **17**, 808–818 (1976).

4. D. Beke, I. Godeny, F. J. Kedves, G. Groma, *Acta Metallurgica*, **25**, 539–550 (1977).

5. J. Cermak, K. Ciha, J. Kucera, *Physica Status Solidi a-Applied Research*, **62**, 467–474 (1980).

6. Y. Du, Y. A. Chang, B. Y. Huang, W. P. Gong, Z. P. Jin, H. H. Xu, Z. H. Yuan, Y. Liu, Y. H. He, F. Y. Xie, *Materials Science and Engineering A*, **363**, 140–151 (2003).
7. D. Simonovic, M. H. F. Sluiter, *Physical Review B*, **79** (2009).
8. R. B. Bird, W. E. Stewart, E. N. Lightfoot, Transport phenomena, J. Wiley, New York, 2nd ed. (2002).
9. J. Crank, The mathematics of diffusion, Clarendon Press, Oxford, England (1975).
10. H. Mehrer, Diffusion in solids: fundamentals, methods, materials, diffusion-controlled processes, Springer series in solid state science, Springer, Berlin (2007).
11. R. M. Barrer, Diffusion in and through solids, The University press, Cambridge, England (1941).
12. L. F. Mondolfo, Aluminium alloys: structure and properties, Butterworths, London (1976).

Chapter 5

Continuous immersion corrosion testing of zinc-rich layers on aluminium in acidified chloride solution

Abstract

This chapter investigates electrochemical and corrosion behaviour of Zn-rich layers on AlMn alloy, obtained by heat treatment of thermal-arc sprayed Zn coating, with reference to 99.99% purity Zn and bare AlMn alloy substrate in acidified artificial sea water solution of pH 3. Pure Zn, bare AlMn alloy, and AlMn alloy with the Zn-rich layer were potentiodynamically polarized, and their electrochemical parameters were analysed. It was found that AlMn alloy can be protected anodically against pitting by both the pure Zn coating and Zn-rich layer at the expense of high self-corrosion rate of the Zn coating and Zn-rich layer. During continuous immersion test the potential of Al was maintained far below the repassivation potential by both types of layers. High self-corrosion rate of Zn-rich layers during immersion can be decreased by reducing the Zn load of the initial thermal-arc sprayed coating and, subsequently, Zn concentration in the layer to a level which is still sufficient for protection of the substrate against pitting.

5.1 Introduction

Zn-rich layers are believed to improve resistance of Al alloys to pitting corrosion [1–6]. However, the effect of the Zn depth profile and layer thickness on the corrosion properties have not been much investigated. In chloride environment above the critical pitting potential E_c Al oxide becomes unstable and Al undergoes pitting corrosion [7]. Pitting can then propagate further at potentials lower than E_c due to local acidification of the environment in the pit. In order to protect Al from further pitting the corrosion potential is suggested to be reduced below the repassivation potential E_{rp}. E_{rp} of about

-0.85 V_{SCE} is supposed to be sufficient for protection of Al against pitting [8, 9] by maintaining the surface stably in the passive condition. However, this may still be considered as a conservative value if the potential does not exceed the critical pitting potential E_c, which is about -0.75 V_{SCE}, during exposure to chloride environment. Al alloys cannot be protected cathodically in the conventional sense [8, 9], as in the case of more noble alloys, such as steel, by reducing its potential close to its reduction potential, due to the danger for cathodic corrosion [10]. The protection potential has therefore to be maintained between E_{rp} and the cathodic corrosion potential to obtain stable passivity [9].

Zn is more active than Al [11]. ZnAl alloys are also more active, the activity decreasing with increasing amount of Al in the alloy [12–14]. Coatings of pure Zn and AlZn alloys on a number of other types of Al alloys, such as AlMn, are therefore expected to reduce the corrosion potential sufficiently below the critical pitting potential of the substrate alloy to provide protection against pitting in chloride environment [1–3, 15–17]. However, determination of the optimum amount of Zn in the coating and the optimal in-depth concentration distribution and thickness of the Zn-rich layer formed by heat treatment for effective protection and optimal service life of the substrate alloy is not well clarified in the available literature. Another challenge in this respect is the possibility of high self-corrosion imparted to the Zn-rich layer by the Zn component in acidified chloride solutions [2, 11, 18], reducing the current efficiency of the layer in protecting the substrate against pitting. Based on limited literature available, corrosion rate is expected to increase with increasing Zn content in the Al alloy [2, 11, 13]. Possible mechanisms of dealloying in this process and its added effect on the electrochemical properties of the layer have not been investigated.

In chapter 3 Zn rich layers on AlMn alloy multi-port extruded (MPE) tubes were characterised by glow discharge optical emission spectroscopy (GD-OES). Zn was deposited by thermal-arc spraying and subsequently subjected to heat treatment, allowing controlled diffusion of Zn into the AlMn substrate. Zn coating with lower Zn load was produced by controlled etching of excess zinc by hot chromic-phosphoric acid treatment. Zn concentration profiles were obtained for selected heat treatment conditions.

The purpose of the present work is to study the electrochemical and corrosion behaviour of such samples relative to that of pure Zn and bare AlMn alloy substrate immersed in acidified chloride solution. The effectiveness of the sacrificial Zn-rich layers in reducing pitting corrosion of Al will be investigated by monitoring the development of their corrosion potential over time, in comparison to the thinning of the samples by increased self corrosion of the layer due to the Zn component. Possibility of minimizing self-corrosion of the Zn-rich layer by optimizing the Zn concentration profile and thickness of the Zn-rich layer, without decreasing the pitting resistance, will be studied.

It will be attempted to correlate the corrosion potential of the samples with

Zn concentration of the corroding surface. It will be investigated, furthermore, whether such a correlation can be combined with the Zn-depth profiles of the uncorroded sample to estimate the corrosion rate of the samples from measured corrosion potential during exposure to the same solution.

5.2 Experimental

Materials. AlMn alloy MPE tube samples were provided in bare and coated form by Sapa AS. Composition of the bare alloy, designated as Alloy1, was measured by spark optical emission spectroscopy (Spark OES). The results were shown in chapter 3 in table 3.1. Zn samples were 99.99% purity thin Zn plates.

The Zn coating was applied by thermal-arc spraying at the plant immediately after extrusion. Typical Zn load on the surface, determined by X-ray fluorescence (XRF) spectrometer (CMI 900 from Oxford Instruments), was 8.0 ± 0.2 g/m^2. Composition of the tube alloy, which was later coated with Zn, measured separately by Spark OES, was shown in chapter 3 in table 3.3, both in mass fraction and mass concentration. The tubes were cut, rinsed in distilled water, acetone and ethanol and subsequently heat treated for 1, 2, 3, 4 and 5 hours at 350, 390 and 430 °C to obtain Zn-rich layers with varying thickness and Zn concentration profiles on the surface of the AlMn substrate.

The procedure which involved the use of hot chromic-phosphoric acid treatment to produce Zn-rich layers with lower Zn loads than that possible by thermal-arc spraying was described in chapter 3. The Zn load on such samples was estimated as 2.7 ± 0.7 g/m^2. The samples with Zn load of 8 g/m^2 and 2.7 g/m^2 will be designated in this work as samples with high Zn load and low Zn load, respectively. MPE tubes with low Zn load were heat treated for 4 hours at 430, 470 and 510 °C.

Potentiodynamic polarization. The sample area to be exposed to the solution was covered with tape. The samples were then immersed into beeswax heated to about 60 °C with one edge of the sample remaining free of beeswax for connecting the sample to the potentiostat. The beeswax around the tape was cut with a scalpel and the tape was removed, exposing the predetermined metal surface to the test solution, as shown in figure 5.1. The area exposed to the solution was 2.2, 2.8 and 3.3 cm^2 for Al alloy, Zn and high Zn load sample, respectively, depending on the dimensions of samples made available by the supplier. The high Zn-load sample was heat treated for 2 hours at 390 °C.

The samples were immersed in acidified artificial sea water solution prepared according to ASTM D1141 with pH between 2.9 and 3 and constant temperature of 25 °C. This is the same solution used for the corrosion potential measurements to be discussed below. The cell geometry, stirring and the solution volume were the same for all samples.

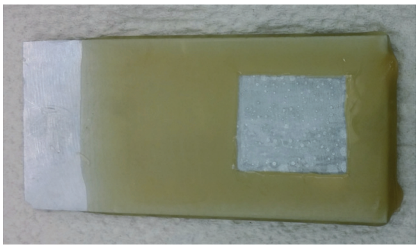

FIGURE 5.1: Zn sample masked with beeswax for potentiodynamic polarization test. The length and width of the sample was 6.5 and 2.9 cm, respectively.

The corrosion potential was measured with respect to a saturated calomel electrode (SCE) until it stabilized. Stabilization time was 75 and 2 minutes for Al and Zn samples, respectively. Cathodic polarization curves were measured for these samples starting from the corrosion potential with the sweep rate of 0.1 mV/s until the potential reached -1.4 V_{SCE}. Subsequently back at open circuit again, the corrosion potential stabilized to the same value as in the beginning after 10 minutes. Anodic polarization curves were then measured starting from the corrosion potential with the same sweep rate until the potential reached -0.48 V_{SCE} and -0.85 V_{SCE} for Al and Zn, respectively.

A slightly different procedure was used for the heat treated high Zn load sample. After 5 minutes of stabilization at the corrosion potential, the sample was polarized to 20 mV below the corrosion potential. The anodic polarisation curve was then measured with the sweep rate of 0.1 mV/s until the potential reached -0.7 V_{SCE}.

Continuous immersion corrosion test combined with corrosion potential measurements. In order to prevent concentration cells and crevice corrosion at the solution-air interface and internal corrosion by solution ingress into the tubes, the samples were coated with beeswax as shown in figure 5.2 to expose an average sample area of 23 ± 4 cm^2. The samples were immersed in solution, such that the solution air interface corresponded to the coated area on the left (upper edge). The coating sealed the tube openings at the edge on the right hand side (figure 5.2). A small area of beeswax at the upper edge of the samples (left edge in figure 5.2) was removed to obtain electrical contact to the multimeter or potentiostat. The same cell geometry and solution volume were used for all samples.

The samples were immersed in acidified artificial sea water solution prepared according to ASTM D1141 at pH between 2.9 and 3 and constant temperature of 25 °C. This is the solution specified for the standardized SWAAT test (ASTM G85) normally used to rank aluminium components to be used in automotive applications. However, electrochemical behaviour is difficult to investigate during a salt-spray test. Immersion tests in the same solution

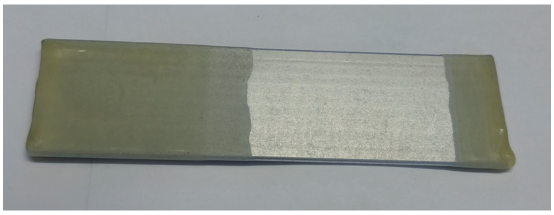

FIGURE 5.2: Zn coated MPE tube sample masked with beeswax for corrosion potential measurement. The length and width of the sample was 9.6 and 2.6 cm, respectively.

were suggested in earlier work [19, 20] to enable electrochemical monitoring and characterising in a similar environment. Selection of the solution for corrosion potential measurements was also based on earlier practice in this laboratory to observe the change in this parameter with respect to time as layers, whose electrochemical properties varied with depth, were corroded off the surface in an accelerated manner. The temperature of the SWAAT test is 49 °C. However, acid solution at elevated temperature is very aggressive and in immersed conditions corrosion could be too accelerated. Long immersion tests at elevated temperatures require building of additional equipment to eliminate fast evaporation of solution. Therefore, solution temperature of 25 °C was chosen instead, which is more likely to be the temperature in real applications.

Test durations were 4 and 11 days for AlMn alloy MPE sample. High Zn load heat treated samples were immersed for predetermined intervals between 10 hours and 11 days. High Zn load non-heat-treated samples were immersed for the same durations with additional tests of 2, 3 and 8 hours. Low Zn load samples were immersed for 3, 6 and 11 days. 3 replicate test were performed for each sample and immersion interval. Immersion tests of the non-heat-treated sample for durations less than 10 hours were not repeated. For selected samples, rapid potential transients at short times after immersion were recorded by a potentiostat every 10 seconds for the first several hours of the measurement and every 2 minutes for the rest of the experiment. For most samples the corrosion potential was measured by a multimeter every 24 hours or right before the test was finished for durations less than 24 hours. Distilled water was added every 2 days to the solution to compensate for the evaporated water.

The corroded samples were removed from the solution, rinsed and cleaned by a wiper tissue in tap and distilled water, and the parts covered with beeswax were finely cut, as shown in figure 5.3. The corrosion morphology will be discussed in chapter 6. The corrosion products were removed by immersion in standard hot chromic-phosphoric acid solution for 10 minutes at 90 °C according to ASTM G1 and subsequently thoroughly rinsed in tap and distilled water. The samples were dried in a furnace for 3 hours at 90 °C. Their weight and size were measured and weight loss per area was calculated. There was no effect of chromic-phosphoric acid treatment on weight loss of the Zn coated and heat treated samples, and this step was skipped for some of these.

FIGURE 5.3: Zn coated MPE tube sample after continuous immersion in acidified artificial sea water solution followed by cutting the edges covered with beeswax. The length and width of the sample was 3.7 and 2.6 cm, respectively.

Average values for weight loss were calculated based on three replicate measurements and errors in the form of standard deviations were calculated. The standard deviation of the initial weight per unit area (237.2 ± 0.2 mg/cm^2 for the uncoated samples and 124.1 ± 0.1 mg/cm^2 for the Zn coated samples) was taken into account.

Reduction in thickness d was estimated from the measured weight loss ΔW and the density profiles $\rho(x)$ calculated from the GD-OES measurements (figure 3.6) by numerical solution of the integral

$$\Delta W = \int_0^d \rho(x)dx \tag{5.1}$$

Standard deviation in d was based on standard deviation of weight loss. For the uncoated samples, reduction in thickness was calculated by dividing the weight loss with the density of the alloy.

Zn concentration on the surface ρ_{Zn} after corrosion was estimated next by using the Zn concentration profiles in which the x-axis (distance from the surface) was replaced by the values of reduction in thickness, d, obtained above. This is shown in figure 5.4. In performing these transformations, the error margins (standard deviation) based on the weight loss data were also transformed over to the calculated parameters, as also sketched in figure 5.4. For this purpose profiles calculated as described in chapter 4 were used. For the non-heat-treated sample GD-OES profile shown in figure 3.6 was used. The estimated value of ρ_{Zn} in this manner is the average for the whole sample surface. Local non-uniformity of ρ_{Zn} is expected to occur due to non-uniform corrosion originating from the non-uniformity of the Zn-rich layer. Corrosion rate was calculated from reduction in thickness between two subsequent measurements divided by the corresponding time interval.

Corrosion potential measurements in GD-OES craters. Selected Zn coated and heat treated AlMn samples with high Zn load were sputtered by Ar ions

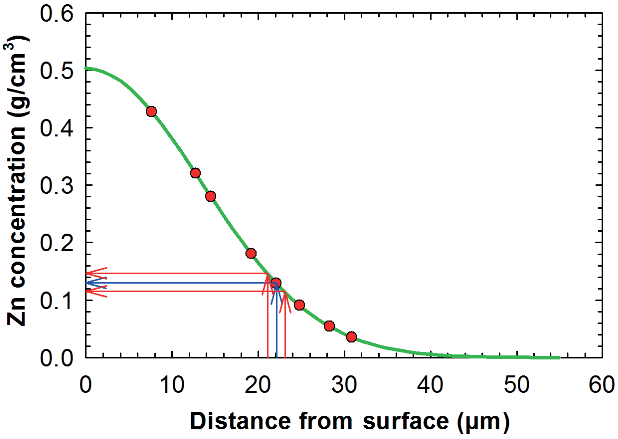

FIGURE 5.4: Example for estimation of surface Zn concentration during corrosion using Zn concentration profiles (green curve), simulated as described in chapter 4, in this case for high Zn load sample heat treated for 2 hours at 390 °C . The blue arrows show the process of correlating reduction in thickness, d, with Zn concentration at the surface. This is done simply by substituting d for the distance from surface on the x-axis to obtain the red circles on the green curve and reading off the corresponding Zn concentration on the y-axis. The red arrows show the analogous process of transforming the error in reduction in thickness into error in the estimated Zn concentration on the corroding surface.

using GD-OES RF glow discharge optical emission spectrometer (HORIBA Jobin Yvon GD-Profiler 2) to form craters with 4 mm diameter and varying depths, using the plasma parameters of 32 W power and 600 Pa pressure. During this process, Zn concentration profiles were obtained using the procedure and calibration described in chapter 3. A drop of an acidified artificial sea water as above was placed on the surface of the craters and corrosion potential was measured by a capillary Luggin probe attached to a SCE reference electrode, as an attempt to establish a correlation between the corrosion potential and Zn concentration in the Zn-rich layer.

5.3 Results

5.3.1 Potentiodynamic polarization

Potentiodynamic polarization curves for Al alloy substrate, pure Zn sample and AlMn alloy coated with 8 g/m^2 of Zn heat treated for 2 hours at 390 °C in acidified artificial sea water solution are shown in figure 5.5. The Al substrate, pure Zn and the heat treated high Zn load sample are designated in this section as Al, Zn and ZAS, respectively. The curves indicate that Zn was much more active than Al, while ZAS was less active than Zn but more active than Al, as expected.

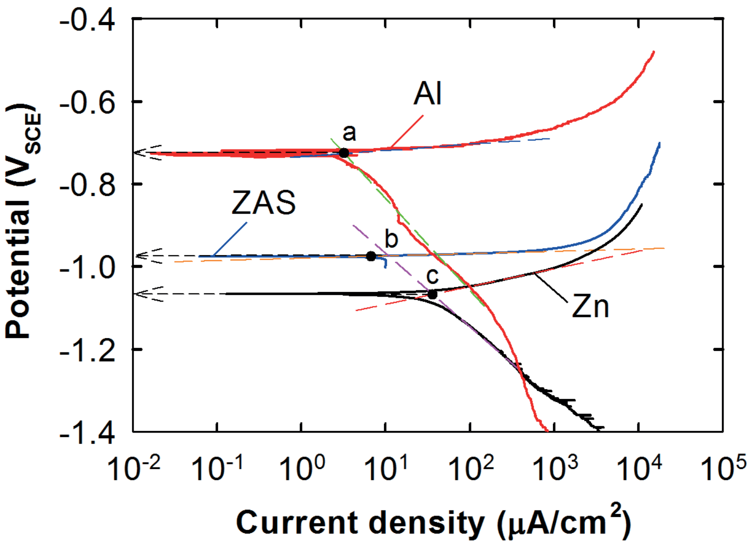

FIGURE 5.5: Potentiodynamic polarization curves for Al alloy substrate (Al), pure Zn sample (Zn) and AlMn alloy tube coated with 8 g/m^2 of Zn heat treated for 2 hours at 390 °C (ZAS) in acidified artificial sea water solution at 25 °C. The dashed lines represent dissolution of Al (blue), ZAS (orange), Zn (red) and reduction of Al (green) and Zn (purple) curves. Points (a), (b) and (c) indicate corrosion rate of Al, ZAS and Zn, respectively, at the corrosion potentials which are indicated by dashed arrows.

Partial current densities for the reduction and oxidation reactions of the samples were estimated by fitting the parts of the polarization curves near the corrosion potential on a semi-logarithmic scale to straight lines in the conventional manner. The reduction curves appear to fit approximately straight lines by this empirical approach, with slopes of 189 mV/decade and 178 mV/decade for Al and Zn samples, respectively. These values suggest that water reduction dominates at higher overpotentials by alkalization of the solution at the electrode surface [21, 22]. The fact that the anodic part of the polarization curves for Al and ZAS were nearly horizontal, indicated non-polarizability of the anodic process, therefore a pitting-type of mechanism [23]. The corrosion potentials of pure Al and Zn-rich layer can therefore considered equal to their corresponding critical pitting potentials [7]. The anodic part of the Zn curve suggests a Tafel-type of oxidation mechanism. The Tafel slope of 43 mV/decade agrees well with other work for pure Zn in acidified chloride solutions [24, 25].

Corrosion rate i_{corr} and corrosion potential E_{corr} were estimated in the conventional manner by use of the mixed potential theory [26]. Due to the absence of the cathodic part of polarization curve for ZAS (the data only for 20 mV below the corrosion potential was available), the corrosion rate was estimated as the current density corresponding to the straight-line fit of the oxidation curve at the corrosion potential, which could easily be obtained from figure 5.5 because of a nearly horizontal anodic polarization curve, as discussed above. These results are summarized in table 5.1.

$E_{corr(ZAS)}$ after polarisation test increased to -0.95 V_{SCE}, which implies that Zn concentration at the surface became smaller due to corrosion during the test, as the Zn concentration decreased with depth.

TABLE 5.1: Corrosion potentials $E_{corr(i)}$, corrosion currents $i_{corr(i)}$, Tafel slopes for anodic $b_{a(i)}$ and cathodic $b_{c(i)}$ part of the polarization curves for AlMn alloy substrate (AlMn), pure Zn sample (Zn), AlMn alloy tube coated with 8 g/m^2 of Zn heat treated for 2 hours at 390 °C (ZAS) in acidified artificial sea water solution. The results were obtained from the analysis of the potentiodynamic data, as shown in figure 5.5.

Sample	$E_{corr(i)}$ **(V_{SCE})**	$i_{corr(i)}$ **(μA/cm^2)**	$b_{a(i)}$ (mV/decade)	$b_{c(i)}$ (mV/decade)
Al	-0.73	3	small	189
Zn	-1.07	36	43	178
ZAS	-0.98	7	small	not measured

5.3.2 Corrosion potential measurements during immersion

Picture of a sample after immersion in acidified artificial sea water for 96 hours and removal of beeswax in figure 5.6 illustrates that the beeswax provided good protection against crevice corrosion. Surface darkening was due to roughening of the corroded surface. Corrosion morphology will be discussed in the next chapter.

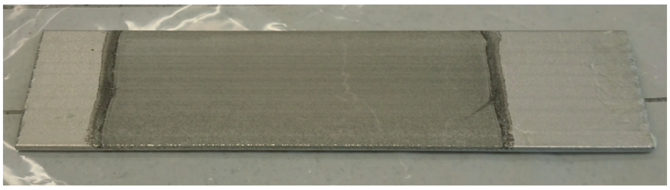

FIGURE 5.6: Zn coated MPE tube sample heat treated for 2 hours at 390 °C after continuous immersion in acidified artificial sea water solution for 96 hours and removal of beeswax. The length and width of the sample was 11.8 and 2.6 cm, respectively.

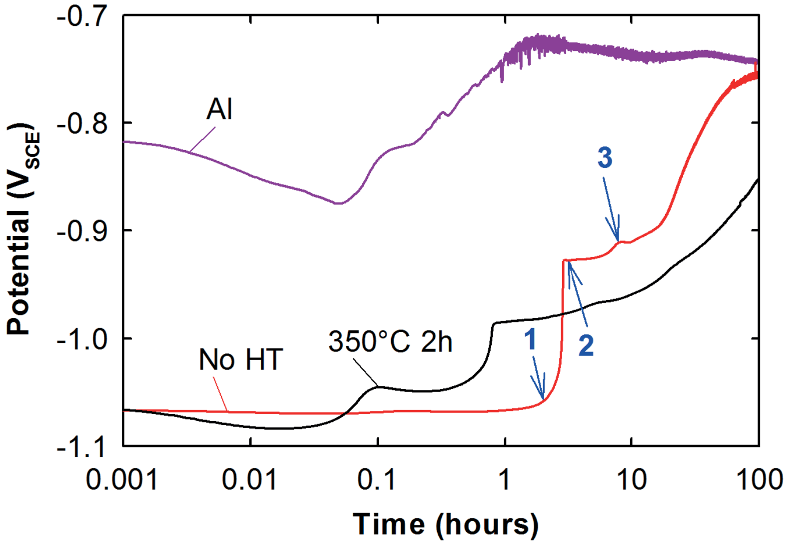

FIGURE 5.7: Typical corrosion potential curves of uncoated Al alloy MPE tube (Al), as coated AlMn alloy MPE tubes with 8 g/m^2 of Zn (No HT) and Zn coated sample heat treated for 2 hours at 350 °C in acidified artificial sea water solution. Blue arrows indicate test durations of (1) 2 hours, (2) 3 hours and (3) 8 hours for the as coated sample.

Figure 5.7 shows typical corrosion potential - time curves for uncoated AlMn alloy MPE tube and Zn coated AlMn alloy MPE tubes, in acidified artificial sea water solution, for the first 4 days of immersion. The coated tubes had high Zn load (8 g/m^2) and the heat treated sample was subjected to temperature of 350 °C for 2 hours. The time scale is logarithmic to emphasize the short-time behaviour. Corrosion potential of the uncoated sample stabilized at around -0.73 V_{SCE} after 70 minutes and decreased to -0.74 V_{SCE} after 4 days of immersion. The potential of -0.73 V_{SCE} is considered to be the critical pitting potential $E_{corr(Al)}$ according to [7] and the potentiodynamic results presented above.

The initial corrosion potential of the non-heat-treated high Zn load sample was around the potential of pure Zn according to data in table 5.1, which confirms that the metallic Zn coating was corroding at the outset. Within two to three hours of immersion (points (1) and (2) in figure 5.7), the potential surged up to a plateau at -0.93 V_{SCE},indicating that, while pure Zn became depleted, the AlZn alloy layer underneath started to corrode. Subsequently, the potential continued to increase slowly, with a small peak at 8 hours (point (3) in figure 5.7), up to a value of around 30 mV more negative than $E_{corr(Al)}$. The initial corrosion potential for the high Zn load sample heat treated for 2 hours at 350 °C was also close to the potential of pure Zn. After 6 minutes the potential stabilized around -1.045 V_{SCE} and then rapidly increased to -0.98 V_{SCE} after 45 minutes of immersion. This indicates that the pure metallic Zn, whose presence on the surface of heat treated samples was confirmed by GD-OES and SEM in chapter 3, was removed, and the Zn-rich layer began to corrode. After 4 days of immersion the potential was about -0.85 V_{SCE}.

Corrosion potential in acidified artificial sea water solution, measured at selected intervals of immersion time based on at least three replicates for high Zn load non-heat treated and heat treated samples are shown in figure 5.8 with error bars indicating standard deviations. The corrosion potential after 10 hours of immersion was roughly the same for the heat treated samples and was about 40 mV higher for the non-heat-treated sample. The potential of the untreated sample increased rapidly to about -0.8 V_{SCE} during the first 2 days of immersion and stabilized at about -0.75 V_{SCE} after 4 days, which it maintained for the subsequent 7 days. The corrosion potential of the heat treated samples increased monotonically. The potential of the samples heat treated for 2 hours at 350 °C increased more rapidly than those of the others presumably due to faster decrease of Zn concentration at the surface during corrosion for such low heat treatment temperature. After 11 days the corrosion potential was in the range from -0.785 V_{SCE} (heat treatment for 2 hours at 350 °C) to -0.87 V_{SCE} (heat treatment for 4 hours at 430 °C). Corrosion potential of the samples heat treated for 5 hours at 390 °C and 4 hours at 430 °C stayed below -0.85 V_{SCE}, which is considered to be sufficiently negative for protection of the Al substrate against pitting. The samples heat treated for 2 hours at 350 °C and 1, 2 and 3 hours at 390 °C exceeded this value after about 3, 7, 10 and 11 days of immersion, respectively.

Typical corrosion potential change with time for heat treated Zn coated AlMn alloy MPE tubes with Zn load of 2.7 g/m^2 (low Zn load) is shown in figure 5.9 for the first 4 days of exposure in acidified artificial sea water solution. The time scale is logarithmic to emphasize the short-time behaviour. The initial corrosion potentials of the sample heat treated for 4 hours at 430 °C and 510 °C were about -0.95 V_{SCE} and -0.91 V_{SCE}, respectively. Thus, no pure Zn was present at the surface, which was confirmed by SEM in chapter 3, and the Zn-rich layer formed by heat treatment of the AlZn alloy remaining after pretreatment of the surface in chromic-phosphoric acid solution was corroding from the beginning of the immersion test. The potential transients for the samples heat treated at 430 °C, 470 °C (not shown) and 510 °C exhibited a maximum and a minimum during first 30 minutes of immersion. The 510 °C sample showed a second maximum and minimum at about 13 and 28 hours of immersion, respectively. After these extrema points, which were reproducible, the potential increased monotonically above the -0.85 V_{SCE} limit.

Figure 5.10 shows the corrosion potentials of Zn coated and heat treated MPE tubes with low Zn load. All three curves, for samples heat treated for 4 hours at different temperatures, show slow increase of the potential after 2 days of immersion compared to more rapid change in the potential between first and second days. Corrosion potential curve for the samples heat treated at 430 °C lies around 10 mV lower than for the samples heat

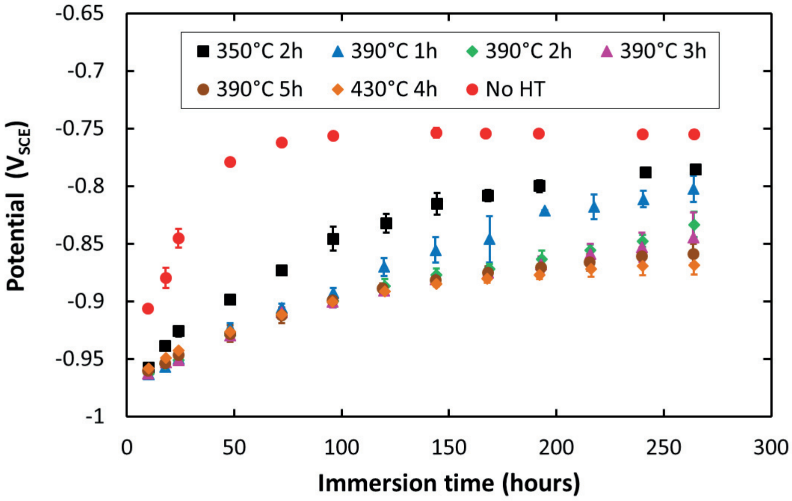

FIGURE 5.8: Effect of heat treatment on the corrosion potential of Zn coated and heat treated AlMn alloy MPE tubes with 8 g/m^2 of Zn during immersion in acidified artificial sea water solution. The data for the non- heat-treated sample (No HT) is included. The symbols correspond to the average for at least three replicate specimens, with scatter bars included.

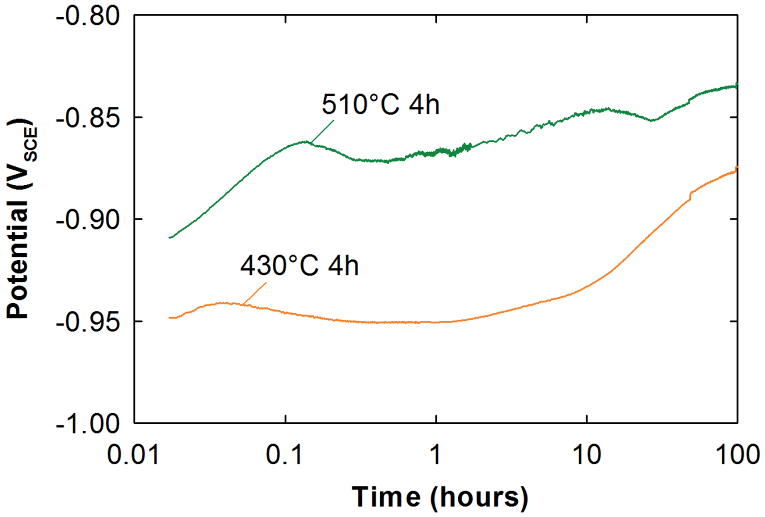

FIGURE 5.9: Typical corrosion potential curves of heat treated Zn coated AlMn alloy MPE tubes with 2.7 g/m^2 of Zn in acidified artificial sea water solution.

treated at 470 °C, which, in turn, is around 30 mV lower than the samples heat treated at 510 °C. After 11 days of immersion the samples heat treated at 430 °C and 470 °C did not exceed -0.85 V_{SCE}. The sample heat treated at 510 °C exceeded this value already after 10 hours of immersion.

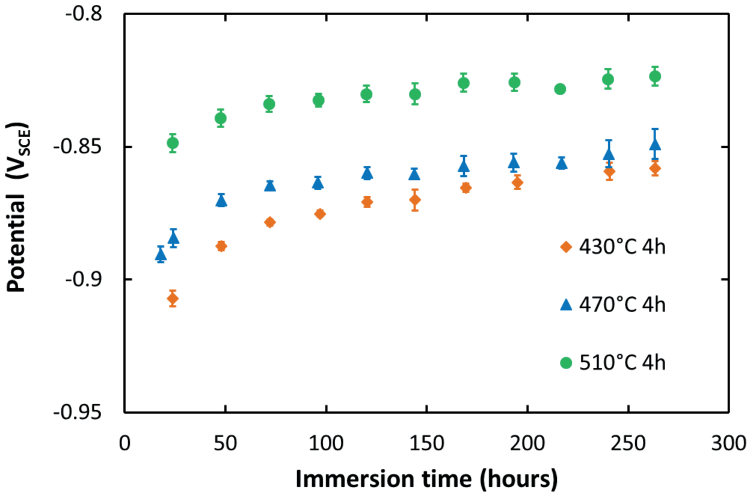

FIGURE 5.10: Effect of heat treatment on the corrosion potential of Zn coated AlMn alloy MPE tubes with 2.7 g/m^2 of Zn during immersion in acidified artificial sea water solution. The symbols correspond to the average for at least three replicate specimens, with scatter bars included.

5.3.3 Continuous immersion corrosion test

High Zn load samples. Results for the immersion corrosion test of the non-heat-treated and heat treated AlMn alloy MPE tubes, which were originally coated with 8 g/m^2 of Zn (high Zn load), in acidified artificial sea water solution are shown in figures 5.11a-c. Corrosion rate is plotted in figure 5.12 with respect to the middle of the time interval.

The weight loss after two hours of immersion of the untreated alloy (point (1) in figures 5.7 and 5.11) corresponded roughly to the weight loss measured after chromic-phosphoric acid treatment (0.5 mg/cm^2) of identical samples, which is believed to be due to the dissolution of the pure Zn constituent of the Zn thermal-arc sprayed coating. The average thickness of the pure Zn layer was thus roughly estimated as the reduction in thickness after two hours of immersion, which was 1.3 ± 0.3 µm. The weight loss after three hours of immersion (point (2) in figures 5.7 and 5.11) was higher than the total weight of Zn in the coating (0.80 ± 0.02 mg/cm^2), and the Zn concentration on the surface was 1.4 ± 0.2 g/cm^3 (40 wt%) according to figure 5.11c. This indicates that the AlZn alloy layer was corroding at this stage. 8

hours of immersion (point (3) in figures 5.7 and 5.11) corresponded to doubling of reduction in thickness with respect to the value after 3 hours. Zn concentration at this point was 0.45 ± 0.09 g/cm^3 (16 wt%) on the surface.

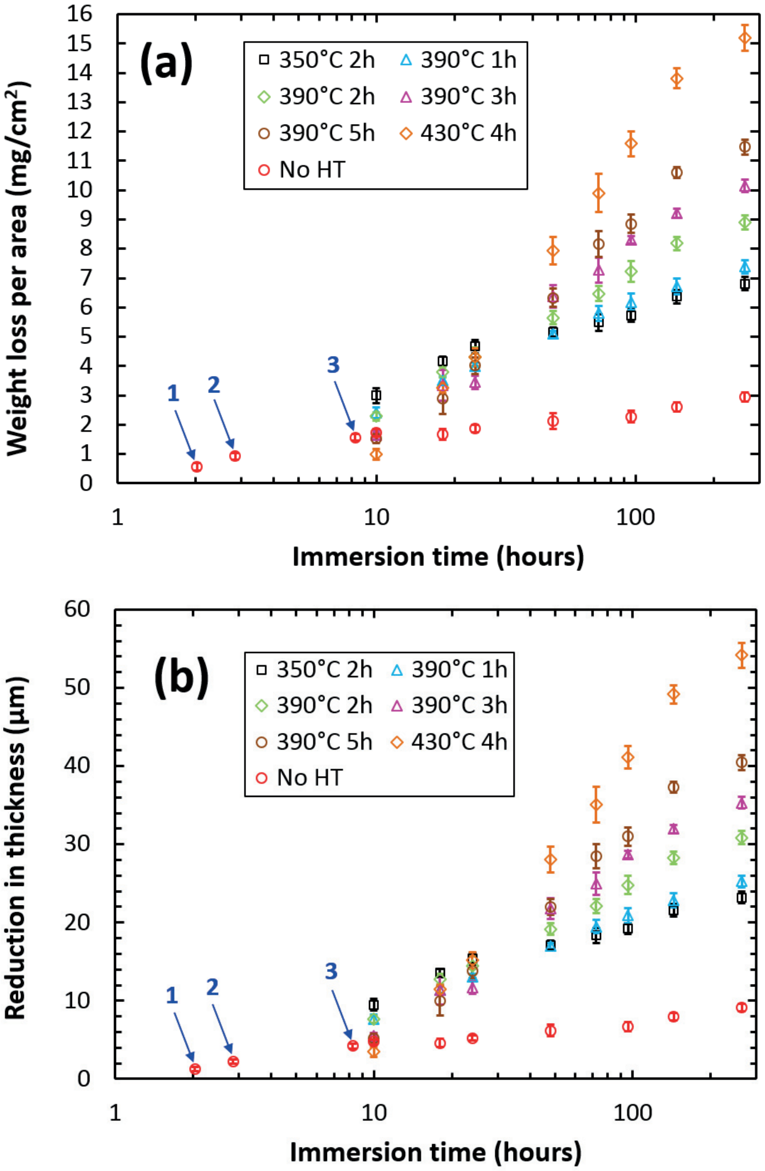

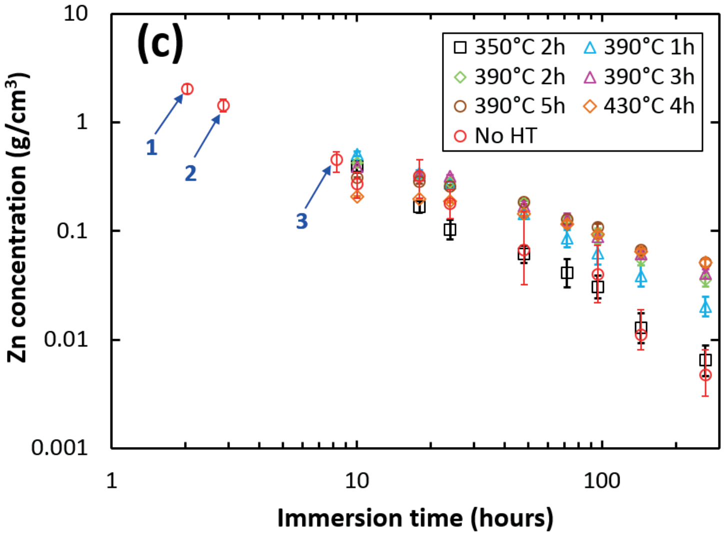

FIGURE 5.11: Results of immersion corrosion testing in the test solution for AlMn alloy tubes as coated with 8 g/m^2 of Zn and heat treated at different temperatures and durations: a) weight loss data, b) reduction in thickness, c) Zn concentration. Blue arrows indicate test durations of (1) 2 hours, (2) 3 hours and (3) 8 hours for the as coated sample.

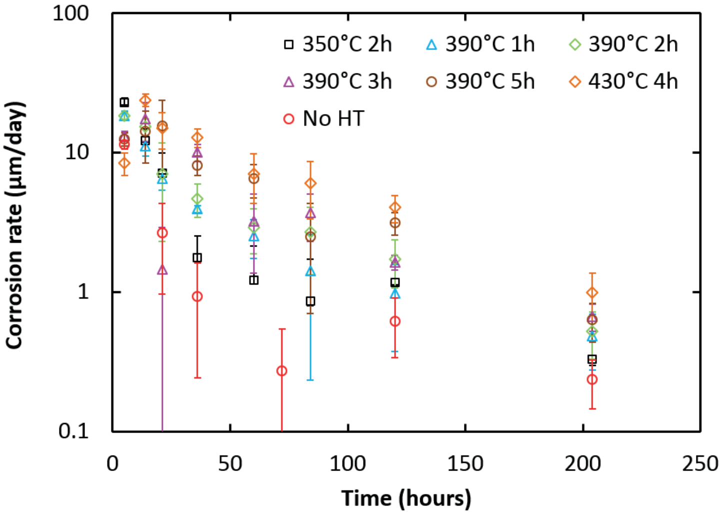

FIGURE 5.12: Corrosion rate of AlMn alloy MPE tubes as coated with 8 g/m^2 of Zn and heat treated at different temperatures and durations in the test solution.

After 4 days, overall reduction in thickness was 6.7 ± 0.6 µm. Zn concentration corresponding to this depth was 0.04 ± 0.03 g/cm^3. The corrosion potential stabilized at a value 30 mV more negative than the critical pitting potential of the AlMn alloy (-0.73 V_{SCE}, as reported in table 5.1). This indicates that most of the Zn coating, including the pure Zn and Zn-rich Al layers, had corroded after 4 days, and the depth of 6.7 µm appears to be the approximate thickness of the Zn coating. Increase in the thickness reduction and corrosion rate (figure 5.12) between 4 and 11 days of immersion was quite small and is considered to be negligible in relation to the reduction in thickness due to the corrosion of the entire Zn and Zn-rich layers.

For most of the heat treated samples, weight loss, ΔW, and reduction in thickness, d, were higher than those for the untreated samples after 10 hours of immersion (figures 5.11a and b). Among the heat treated samples, ΔW was higher for lower degrees of heat treatment. Between 10 and 24 hours of immersion, a shift occurred in ΔW and d. The lowest values were attained by the untreated sample while the highest values corresponded to the sample heat treated for 2 hours at 350 °C. ΔW and d for the other heat treated samples showed no trend based on the degree of heat treatment during this period. The values were close to one another and slightly lower than for the sample heat treated for 2 hours at 350 °C. After two days of immersion a new shift occurred. ΔW and d became much lower for the untreated sample. Among the heat-treated samples, these parameters became increasingly larger with immersion time and with increasing degree of heat treatment.

Zn concentration ρ_{Zn}, shown in figure 5.11c, decreased monotonically during immersion of the heat treated samples on a log-log scale. After 10 hours of immersion, ρ_{Zn} was not easily distinguishable between the heat treated and untreated samples within the scatter limits. ρ_{Zn} was highest for the sample treated for 1 hour at 390 °C and lowest for that treated for 4 hours at 430 °C. Zn concentration of the latter remained at the same level during the first 24 hours of immersion. ρ_{Zn} for the sample heat treated for 2 hours at 350 °C dropped to the same level as the sample heat treated for 4 hours at 430 °C after 18 hours of immersion and decreased below it after 24 hours. The other heat treated samples attained roughly the same concentration level, which was higher than for the sample heat treated for 4 hours at 430 °C. During longer times of immersion ρ_{Zn} of the heat treated samples decreased monotonically. For the sample heat treated for 2 hours at 350 °C it remained lowest. The sample heat treated for 1 hour at 390 °C attained a higher ρ_{Zn} than the latter. ρ_{Zn} of the other heat treated samples were quite close to each other, the samples with lower degrees of heat treatment having lower ρ_{Zn}, which was again higher than for sample heat treated for 1 hour at 390 °C.

The changes in ρ_{Zn} described above during immersion in acidified artificial sea water solution can be analysed based on the Zn depth profiles of the Zn-rich layers shown in figure 3.6. High ρ_{Zn} measured on the lower-degree treated samples during the first 10 hours of immersion can be attributed to the higher Zn concentrations of these samples close to the surface in the depth profiles (figure 3.6) in relation to the higher-degree samples, with the exception of the sample heat treated for 2 hours at 350 °C. In this latter case, which had the lowest degree of heat treatment and the highest reduction in thickness during the first 18 hours of immersion (figure 5.11b), ρ_{Zn} underwent a significant decrease from its surface value on the uncorroded sample (figure 3.6a). With further increase in immersion time, ρ_{Zn} for the same sample decreased at a slower rate. For higher degrees of heat treatment Zn diffused deeper into the surface and ρ_{Zn} was higher for these after long immersion times compared to the lower degrees of heat treatment (2 hours at 350 °C and 1 hour at 390 °C).

Figure 5.12 shows that the corrosion rate of non-heat-treated samples was lower than of the other samples except for the first 10 hours of immersion. Among the heat treated samples, corrosion rate was higher for the lower degrees of heat treatment during this period in general. The sample heat treated for 2 hours at 350 °C showed the highest corrosion rate (22.8 ± 1.9 µm/day) among all samples after 10 hours of immersion time. Corrosion rate of the untreated sample was slightly higher than for the sample heat treated for 4 hours at 430 °C. Corrosion rate of the lower heat-treated samples (2 hours at 350 °C, 1 hour at 390 °C and 2 hours at 390 °C) decreased with immersion time from the start of the experiment. The rates of the higher level heat-treated samples (3 hours at 390 °C, 5 hours at 390 °C and 4 hours at 430 °C) increased up to 18 hours of immersion. Corrosion rate of the sample heat treated for 4 hours at 430 °C, which was the highest level of heat treatment used, became the highest of all types of samples after 18 hours of immersion (23.9 ± 2.4 µm). Further immersion lead to monotonic decrease of log (corrosion rate) with immersion time for most of the samples within the error limits. At any selected immersion time during this period, the corrosion rate decreased with the decreasing level of heat treatment.

Higher degrees of heat treatment lead to more uniform depth profiles for Zn, as was reported in chapter 3 in figure 3.6. As a result, corrosion rate during the first 10 hours of immersion was lower for higher degrees of heat treatment. The increase in the corrosion rate between 10 and 18 hours of immersion for samples heat-treated for 3 hours at 390 °C and higher temperatures cannot be explained by the Zn concentration alone, as it continued to decrease during gradual consumption of the Zn-rich layer. This increase can be attributed to increasing active area as a more passive oxide layer, resulting from higher degree heat treatment, dissolved from the surface at a slower rate. Enrichment of Fe-rich intermetallic particles at the surface, attributed to contamination from the extrusion die (discussed in chapter 3), could also increase the corrosion rate.

Between 6 to 11 days of immersion, corrosion rate of the untreated sample and the sample heat treated for 2 hours at 350 °C was about 0.2 ± 0.1 µm/day. Corrosion rate of the higher-treated samples was significantly higher, varying from 0.5 ± 0.2 µm/day for the sample heat-treated for 1 hour at 390 °C to 1.0 ± 0.4 µm/day for that treated for 4 hours at 430 °C. Higher corrosion rates for the higher-treated samples at this interval corresponded to higher Zn concentrations at the surface in relation to the lower-treated samples, according to figure 5.11c. This suggests that the Zn coating on the untreated sample and most of the Zn-rich layer on the sample heat-treated for 2 hours at 350 °C corroded before 6 days, and the Zn concentration on the surface of these samples became significantly reduced, in agreement with the corrosion potential results in figure 5.8. In general, the Zn concentration on samples with lower degrees of heat treatment decreased faster, indicating that most of the Zn-rich layer corroded away sooner, compared to the samples with higher degrees of heat treatment. Corrosion rate of the latter group did not decrease as fast as the former due to the lower gradient of the Zn depth profile, which lead to higher weight loss and reduction in thickness.

Low Zn load samples. Weight loss, reduction in thickness and Zn concentration of heat treated AlMn alloy MPE tubes coated with 2.7 g/cm^2 of Zn (low Zn load) during the immersion corrosion test are shown in figures 5.13a-c, respectively, for the samples heat treated for 4 hours at 430 °C, 470 °C and 510 °C. Corrosion rate is shown in figure 5.14. Weight loss and reduction in thickness (figures 5.13a and b, respectively) for low Zn load samples were lower for higher degrees of heat treatment, attributed to correspondingly lower Zn concentration of these samples (figure 5.13c). Zn concentration of the samples heat treated at 430 °C decreased faster with immersion time than those heat treated at 470 °C, and decreased to the same level after 11 days of immersion. Zn concentration of the samples heat treated at 510 °C remained nearly constant and lower than that for the other samples during the test period of 11 days. Corrosion rate (figure 5.14) during the first three days was also lower for the samples with higher degrees of heat treatment. It became of the same order of magnitude for all variants with increasing time of immersion. Weight loss and reduction in thickness (13.7 ± 1.8 μm) of the samples heat treated at 510 °C after 11 days of immersion was much smaller than for the other low Zn load samples and smaller than for all heat treated high Zn load samples.

Uncoated samples. Weight loss and reduction in thickness data for immersion of the bare AlMn substrate in acidified artificial sea water solution for 4 and 11 days are reported in table 5.2. Results show that uniform corrosion of AlMn alloy in such solution was very small in relation to Zn and Zn-rich coating, reported above.

TABLE 5.2: Results of immersion corrosion test for AlMn alloy MPE tubes in the test solution: weight loss ΔW, reduction in thickness d and corrosion rate (CR).

Time (days)	**ΔW (mg/cm^2)**	**d (μm)**	**CR (μm/day)**
4	0.4 ± 0.2	1.4 ± 0.8	0.4± 0.2
11	0.7 ± 0.2	2.5 ± 0.9	0.2 ± 0.1

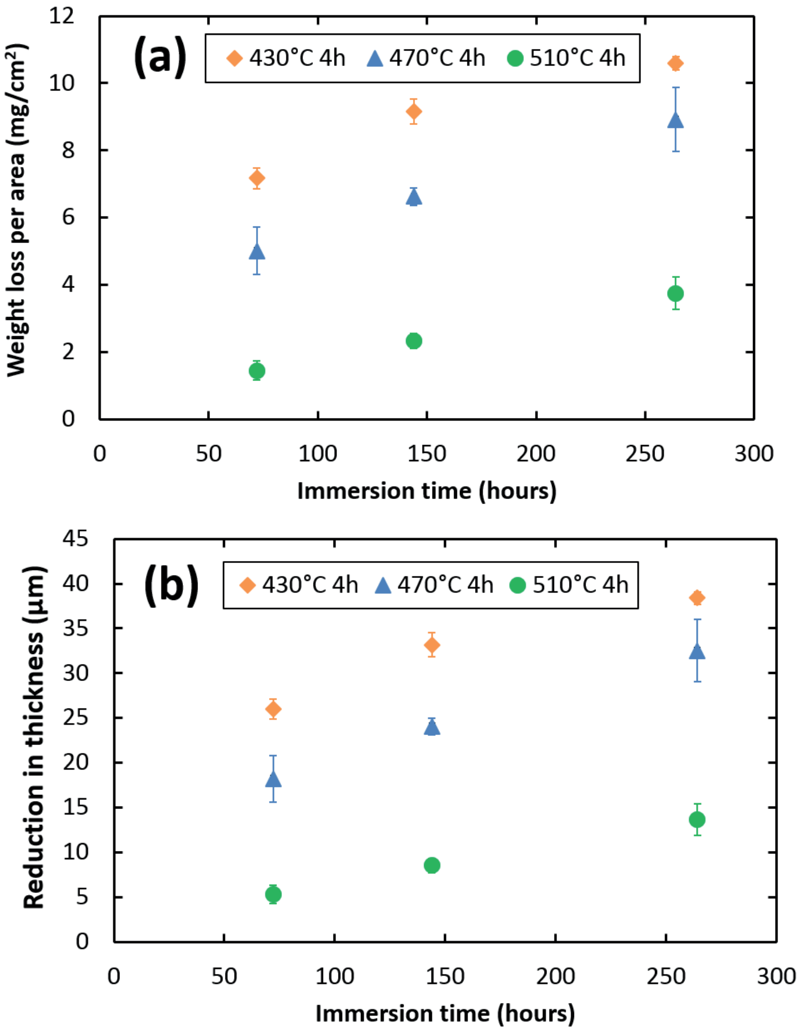
(a)
◆ 430°C 4h
▲ 470°C 4h
● 510°C 4h
Weight loss per area (mg/cm²)
0
2
4
6
8
10
12
0
50
100
150
200
250
300
Immersion time (hours)
(b)
◆ 430°C 4h
▲ 470°C 4h
● 510°C 4h
Reduction in thickness (µm)
0
5
10
15
20
25
30
35
40
45
0
50
100
150
200
250
300
Immersion time (hours)

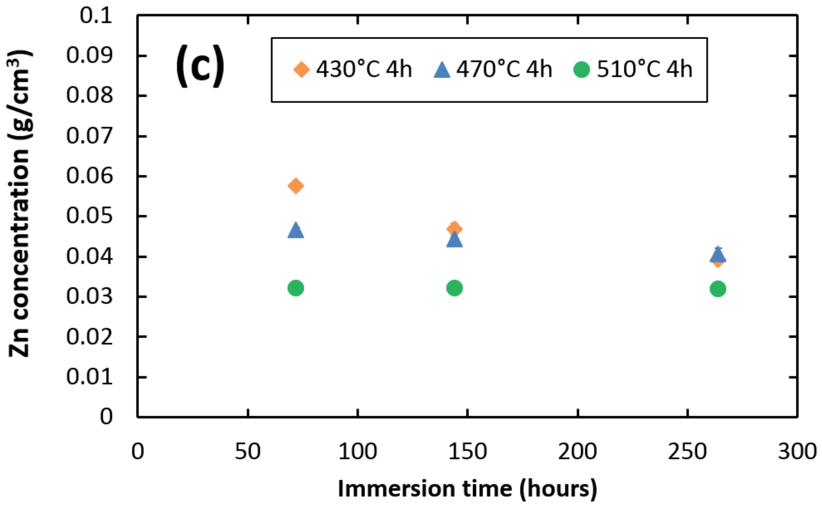

FIGURE 5.13: Results of immersion corrosion testing in the test solution of AlMn tubes coated with 2.7 g/m^2 of Zn and heat treated at different temperatures: a) weight loss data, b) reduction in thickness, c) Zn concentration.

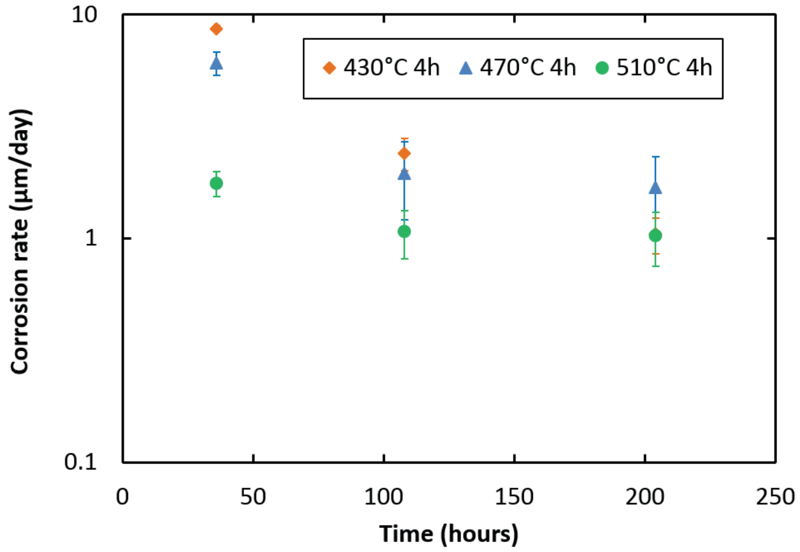

FIGURE 5.14: Corrosion rate of AlMn tubes coated with 2.7 g/m^2 of Zn and heat treated at different temperatures in the test solution.

The corrosion rate for the AlMn substrate can be compared to that obtained by potentiodynamic data shown in figure 5.5 (about 3 μA/cm^2, table 5.1), which would be about 0.86 μm/day when converted to thickness loss. This would then correspond to the corrosion rate of the AlMn alloy after a few hours of exposure to the test solution. In any event, these results show that uniform corrosion of AlMn alloy in such solution was much smaller than those of the Zn-rich layers.

5.3.4 Corrosion potential measurements in craters produced by GD-OES Ar-sputtering

Zn coated AlMn alloy MPE tubes with 8 g/m^2 of Zn and heat treated for 1 hour at 350 °C and 3 hours at 390 °C were used for corrosion potential measurements in craters produced by GD-OES Ar-sputtering. Figure 5.15 shows the depth of these craters and Zn concentration on their surface, obtained by GD-OES analysis during sputtering. Corrosion potential measured by a capillary electrode in a drop of acidified artificial sea water solution in these craters and averaged over 60 seconds is shown in figure 5.16 with respect to Zn concentration in the craters. The results are compared to data from references [12, 14] for high purity binary AlZn alloys and the agreement is quite good for Zn concentrations higher than 2 wt%. At lower Zn concentrations corrosion potential measured in this work was somewhat lower compared to the literature data. It can be concluded that there is an exponential relationship between the corrosion potential and Zn concentration. However, for the data obtained in this work, there was a valley between 3 and 10 wt% Zn where the corrosion potential did not seem to depend on concentration.

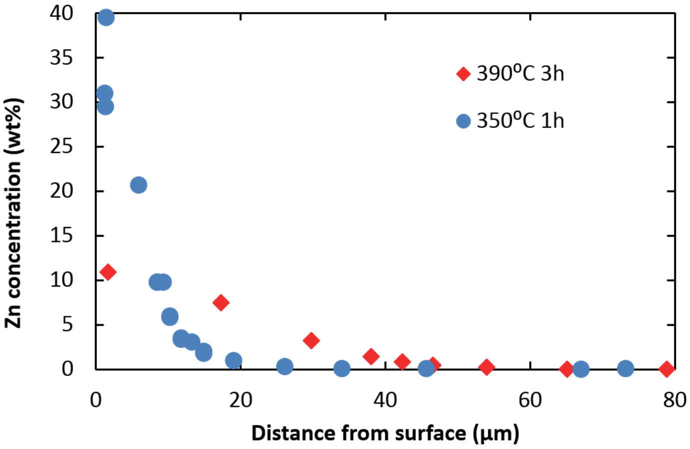

FIGURE 5.15: Zn concentration as a function of depth of the craters produced by GD-OES Ar-sputtering in Zn coated and heat treated AlMn alloy MPE tubes with 8 g/m^2 of Zn.

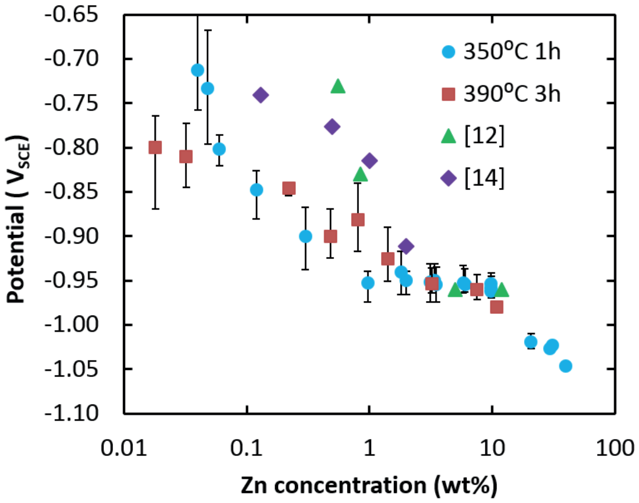

FIGURE 5.16: Effect of Zn concentration on corrosion potential of Zn-rich layers in AlMn alloy MPE tubes with 8 g/m^2 of Zn at selected depths measured by a capillary electrode in a droplet of acidified artificial sea water solution. The data for high purity AlZn binary alloys from references [12] in synthetic sea water and [14] in deaerated 0.5 M NaCl solution are included.

5.3.5 Correlation between corrosion potential, Zn concentration and reduction in thickness

As an attempt to estimate Zn concentration, ρ_{Zn},of the corroding surface and reduction in thickness from the measured corrosion potential, E_{corr}, the corrosion potential data measured on the crater surfaces with respect to the Zn concentration of the surface measured by GD-OES (figure 5.16) were fitted to an exponential function by least squares regression analysis in the form of $\rho_{Zn} = f(E_{corr})$ (figure 5.17). It was thought that such relationship should allow calculation of Zn concentration on the corroding surface based on the measured corrosion potential, if the Zn concentration can be assumed to be uniformly distributed at the surface. Zn mass fraction used in figure 5.16 was converted to mass concentration in plotting figure 5.17 in order to correlate the result later with Zn concentration profiles.

The $\rho_{Zn} = f(E_{corr})$ correlation was used to convert the corrosion potential during the continuous immersion experiments above into ρ_{Zn} – immersion time curves. These curves were in turn combined with the corresponding ρ_{Zn} - depth profiles, measured by GD-OES, to estimate the reduction in thickness during immersion. This conversion assumes also uniform distribution of Zn concentration at the surface. The procedure for these calculations was the following:

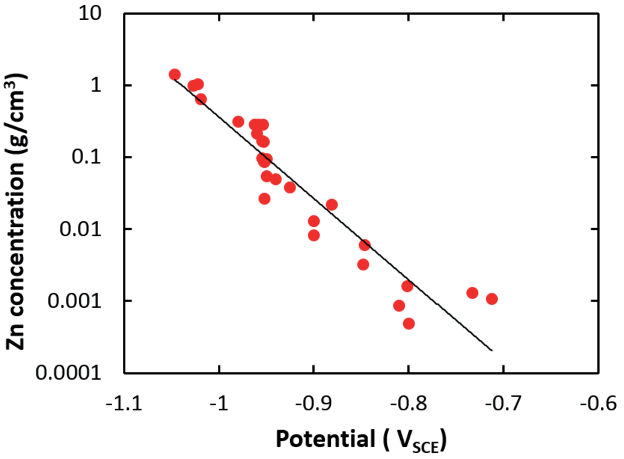

FIGURE 5.17: Zn concentration in Zn-rich layers in AlMn alloy MPE tubes with 8 g/m^2 of Zn at selected depths as a function of corrosion potential in the test solution. Red circles represent experimental data, black line is the fitted curve.

1. Corrosion potential, E_{corr}, vs. immersion time measured during continuous immersion tests, shown in figures 5.8 and 5.10, were correlated with the Zn concentration, ρ_{Zn}, at the surface, using the fitted curve $\rho_{Zn} = f(E_{corr})$ in figure 5.17. This resulted in calculated surface ρ_{Zn} vs. immersion time curves as plotted in figures 5.18a and b for high and low Zn load, respectively.
2. Surface ρ_{Zn} was converted into reduction in thickness by using ρ_{Zn} -depth profiles from figure 3.6, similar to the sketch in figure 5.4 with conversion in the opposite direction. Knowledge of ρ_{Zn} at the corroding surface was assumed to allow estimation of the depth of attack using the GD-OES profiles. The assumption involved in this step was uniform corrosion of the surface.
3. Calculated reduction in thickness was plotted as a function of immersion time, as shown in figures 5.19a and b for high and low Zn load, respectively.

The points with ρ_{Zn} below the GD-OES detection limit of 0.0035 g/cm^3 (calculated in chapter 3) were excluded from the ρ_{Zn} data for estimation of reduction in thickness. For some of the samples, the sputtering depths required for the conversion step 2, involving small ρ_{Zn}, could not be obtained due to limitation of the measurement depth by GD-OES. Therefore, the results for the low Zn load sample heat treated at 470 °C are incomplete, and none of the data for the low Zn load samples heat treated at 510 °C were reliable for the present calculations.

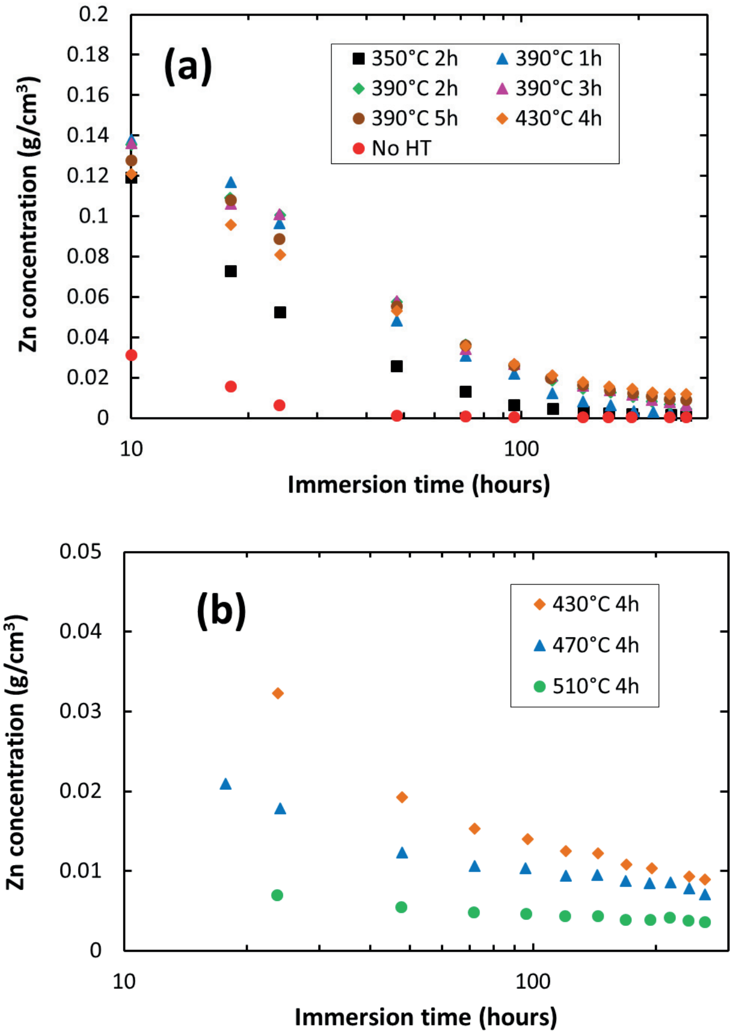

FIGURE 5.18: Surface Zn concentration of Zn-rich layers in AlMn alloy MPE tubes with a) 8 g/m^2 and b) 2.7 g/m^2 during corrosion in the test solution calculated based on the relationship between corrosion potential and Zn concentration shown in figure 5.17.

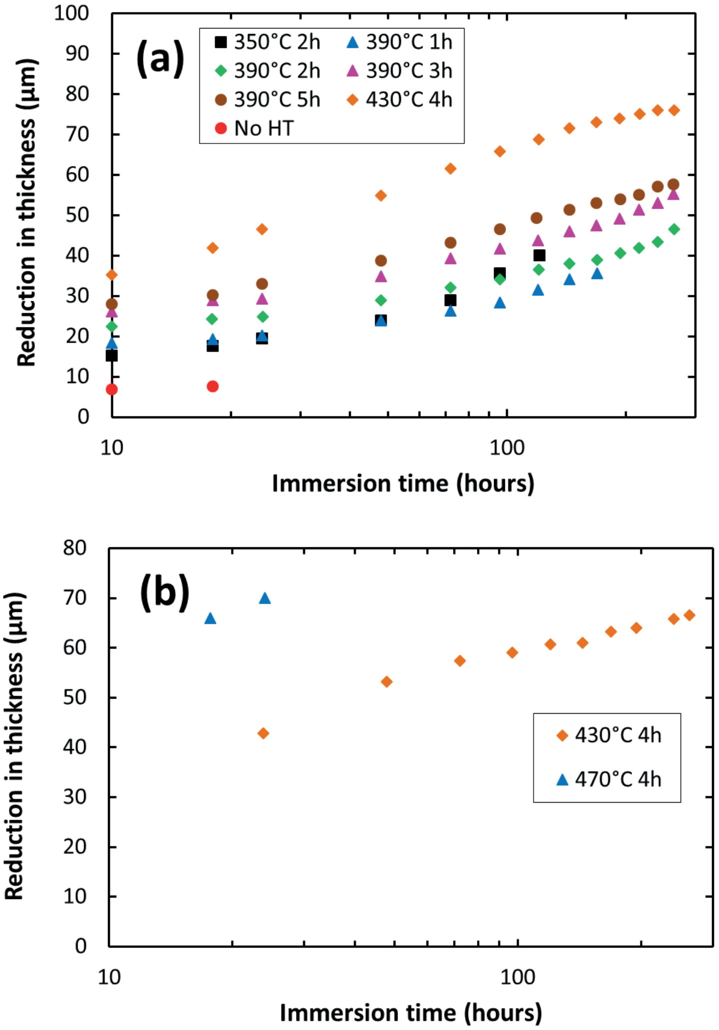

FIGURE 5.19: Reduction in thickness of Zn-rich layers in AlMn alloy MPE tubes with a) 8 g/m^2 and b) 2.7 g/m^2 during corrosion in the test solution estimated from Zn concentration in 5.18 using GD-OES depth profiles, as described above.

The calculated results for ρ_{Zn} and reduction in thickness, d, as a function of immersion time in figures 5.18 and 5.19, respectively, differ significantly from the corresponding data obtained from weight loss measurements in figures 5.11 and 5.13. According to figures 5.18a and b ρ_{Zn} drops at a fast rate during first two days of immersion for both Zn loads and then continues to decrease monotonically at a much lower rate. Figure 5.19a suggests that d of the high Zn load samples was quite high already after 10 hours of immersion, and then it showed a decreasing rate with time. This is in contradiction with d-values calculated based on the measured weight loss, which are 1.5-30 times lower. Moreover, while d after 10 hours of immersion was lower for higher degrees of heat treatment, the trend according to figure 5.19a was the opposite. These results disagree with the premise that corrosion rate should decrease with decreasing ρ_{Zn} in the AlZn alloy resulting from higher degrees of heat treatment.

Based on figure 5.19a, the calculated d for high Zn load samples was 1.5-2 times higher than that based on weight loss measurements after 11 days of immersion. In case of low Zn load samples heat treated at 430 °C and 470 °C, calculated d according to figure 5.19b was also much higher than that based on weight loss measurements. The data for the low Zn load samples heat treated at 510 °C indicates that the whole Zn-rich layer (assumed to be more than 100 µm in chapter 4) was corroded already during first 24 hours of immersion. However according to figure 5.13, d was only 5.3 µm after 3 days of immersion. These results indicate that the procedure suggested for estimating the surface concentration and corrosion rate of the Zn-rich layer on Al, based on E_{corr} measurements by use of the $\rho_{Zn} = f(E_{corr})$ correlation obtained by potential measurements in craters produced by Ar-sputtering, fail to satisfy the experimental data obtained by direct measurement of weight loss of samples exposed to the standard continuous immersion test.

5.4 Discussion

The present results confirm that Zn-rich layers on Al effectively maintain the corrosion potential at values more negative than the critical pitting potential of the AlMn substrate E_c and further below the repassivation potential E_{rp}, which is considered as an important factor for preventing formation of deep pits on the AlMn substrate [8, 9]. This is a critical factor in the design and use of thin-walled AlMn heat exchangers. At this potential AlMn alloy does not become immune, but passivates, and this type of protection can be called anodic rather than cathodic. However, uniform corrosion rate of the alloy increases significantly with increasing Zn concentration, such that it may become more important than pitting in practice.

Potentiodynamic polarization confirmed that both pure Zn and AlMn alloy sample with Zn-rich layer are electrochemically more active than the uncoated AlMn alloy substrate at the temperature investigated in this work (25 °C). Corrosion rates of Zn and Zn-rich Al were also found to be higher than that of the AlMn substrate. Anodic part of the polarization curve for Zn shows Tafel-type behavior with Tafel slope of about 40 mV/decade, which agrees well with other work for pure Zn in acidified chloride solutions [24, 25]. On the contrary, corrosion mechanism of the Zn-rich layer, as well as AlMn alloy substrate, was indicated to be of pitting type by the shape of the anodic polarization curve in figure 5.5 [23], as discussed in section 5.3.1. Anodic polarisation of AlZn binary alloys with Zn concentration varying from 1 to 4.85 wt% was also reported to show pitting type of corrosion [13]. However, deep pits were not observed on the AlZn layer surface in acidified chloride solution (figures 5.3 and 5.6). The corrosion morphology can be described as uniform etching with certain roughening of the surface. The mechanism can still be similar to that of dense pitting rather than formation of discrete deep pits, which is the common pit morphology on aluminium alloys in acidified chloride solution [20, 27]. This behaviour may suggest that the anodic dissolution kinetics is influenced by the aluminium component in terms of pitting-type of behaviour, with the reservations discussed below.

The reduction kinetics of both Al and Zn appeared to be dominated by hydrogen evolution in alkaline environment [21, 22], as inferred from the Tafel slopes reported above as about -180 mV/decade, discussed also in section 5.3.1. Alkaline environment may be created locally at the surface by hydrogen evolution in unbuffered solution, although the bulk solution is acidic. Heavy-metal containing Al-based intermetallics of the substrate AlMn alloy are expected to become exposed to the solution through the Zn-rich layer as a result of corrosion. These will be functioning as the localized cathodes, until they themselves may corrode, as fresh particles of the same type become exposed. Oxygen reduction can occur although not clearly evident from the cathodic part of the polarization curves. This is restricted by mass transfer to the small area fraction of the cathodic intermetallic particles. Oxygen reduction can further become restricted by deposition of calcareous scale on the cathodic sites, while the hydrogen evolution reaction will become enhanced [28].

From polarization curves in figure 5.5 it can be assumed further that hydrogen evolution kinetics on the AlZn surface is similar to that on pure Zn, indicating that it appears to be controlled by the Zn component of the Zn-rich layer. The figure shows also that the rate of hydrogen evolution at a given potential is smaller on Zn and AlZn alloy relative to the AlMn substrate. This is one possible factor in causing apparently more active behavour of the AlZn alloy surface relative to the AlMn substrate. Reduction of the rate of hydrogen evolution on aluminium by alloying with Zn is well known [13]. The surface analysis, which will be discussed in detail in chapter 6, did not indicate a significant enrichment of Zn or Al at the surface of the AlZn layers either. This observation contradicts also the presumption that aluminium should become enriched at the surface due to dealloying of the Zn component. This would be expected to cause a more passive electrochemical behaviour in the course of corrosion in acidified chloride solution. Corrosion and surface-analytical data do not suggest such a specific effect due to Al enrichment. On the contrary, the surface appears to be activated even by quite small Zn concentration in the Zn-rich layer (of the order 1 wt%), as deduced from the corrosion potential and self-corrosion rate during immersion in acidified chloride solution, as will be discussed further below. The mechanism behind these unexpected results cannot be explained presently other than its possible implications in practice.

Open circuit potential of the uncoated AlMn alloy showed typical behaviour for an Al alloy [29] with pit initiation and propagation stages observed. Thin Zn layers obtained by thermal-arc spraying, without heat treatment, effectively protect AlMn alloy substrate against pitting. However, the Zn layer is consumed by self-corrosion quite fast, after which self-corrosion is significantly reduced, but the exposed AlMn substrate becomes susceptible to pitting. In contrast to the untreated coating, deep Zn-rich layers with low Zn content, obtained by heat treatment, give both decreasing self-corrosion rate and protection against pitting. Self-corrosion rate was found to be proportional to the Zn concentration. However, it remains significant even at Zn concentrations as low as 1 wt% (0.03 g/cm^3), such that significant thickness reduction can still occur, which may become undesirable for a thin-walled tube. At the same time, there is a danger of the corrosion potential rising above E_{rp} for Al (-0.85 $_{\text{SCE}}$) with decreasing Zn concentration and thereby increasing the danger for pitting corrosion. Therefore, the use of Zn coatings combined with heat treatment does not appear to be straightforward for effective protection of thin-walled AlMn extrusions in acidified artificial seawater solutions at 25 °C, investigated in the present study.

To be able to obtain sufficiently low self-corrosion rate of the AlMn alloy, as well as sufficiently low E_{corr} for protection against pitting, optimization of the Zn depth profile, taking into account the reduction in the effective thickness of the Zn-free substrate, due inward diffusion of Zn, will be required. This is seen as a difficult task because of the difficulty in scaling up the results from laboratory testing to real practice. Based on the results of the immersion test, Zn load in the thermal-arc sprayed coating should be reduced to decrease self-corrosion of the Zn-rich layer. Among the low Zn load samples, heat treatment for 4 hours at 430 °C gave the lowest total reduction in thickness and corrosion rate while its potential remained 10 mV lower than E_{rp}.

The high Zn load sample heat treated for 4 hours at 430 °C showed the highest corrosion rate among all samples between 10 and 24 hours of immersion. This can be attributed to enrichment of Fe-rich intermetallic particles close to the surface due to contamination from the extrusion die, as discussed in chapter 3, section 3.4.2. Heat treatment is expected to enhance precipitation of Fe in the form of AlMnFeSi-particles by heat treatment [30, 31]. These particles are expected to behave as local cathodes and enhance the corrosion rate [27, 32]. Therefore, higher degrees of heat treatment are unfavourable for corrosion properties of the Zn-rich layers obtained by heat treatment as long as the die contamination cannot be prevented. However, if one considers E_c as the potential below which the substrate is protected against pitting, all heat treated samples examined would be acceptable for the present purpose, since E_c was not exceeded for any of these sample during the immersion tests. In this case the high Zn load coating with the lowest degree of heat treatment (2 hours at 350 °C) can be considered as the optimal alternative. This sample showed lowest total reduction in thickness after 11 days of immersion and lowest corrosion rate between 6 and 11 days, which was approximately the same as that of the AlMn substrate. Optimization of the Zn-rich layers, which takes these issues into consideration, will be discussed further in chapter 6.

The failure of the method proposed in section 5.3.5 for estimating the corrosion rate of Zn-rich protective layers on AlMn substrate needs to be critically analyzed in view of the assumptions made and possibly revised to develop an improved approach. First of all, the assumption of lateral uniformity can be questioned. This is determined by the interrelated factors, viz., surface metallurgy and composition of the coated surface, local corrosion and reduction rates, and solution chemistry.

The apparent success of diffusion modelling, based on Fick's second law, with the assumption of lateral uniformity of Zn concentration, in predicting depth profiles of Zn in the Zn-rich layer, suggested the use of similar assumptions in developing the method. Corrosion potential of simple Al alloys in chloride solutions has often been correlated with the type and concentration of the alloying elements [12, 13]. However, the corrosion potential is a mixed potential determined by the rates and distribution of each oxidation and reduction reaction occurring on the surface, often locally down to microscopic dimensions. These in turn are affected by the surface morphology and microstructure, which were shown to be highly complex in chapter 4. The original Zn coating has a non-uniform thickness. As a result, the AlZn alloy formed by heat treatment has laterally non-uniform concentration, as shown in chapter 3. Both pure Zn islands and Zn-free areas on the AlMn alloy are also expected to be present.

In addition to the above, surface concentration of the heat treated samples was altered during corrosion, which was detected by increase in the corrosion potential. This is related to the increase of Al concentration at the surface as a result of decreasing Zn concentration with depth and possible higher rate of selective corrosion of the more active Zn component. Localized chemistry of the solution can be quite different between these areas of varying Zn concentration and intermetallic particle type and distribution. The same is true in experiments involving restricted volume of a droplet of electrolyte and a larger area sample in a larger volume electrolyte. These factors will affect further the passivity of the surface and the degree of localization of the corrosion process.

The corrosion potential can thus be affected by a large number of parameters, suggesting that the corrosion potential measured in a 4 mm diameter crater can be determined by factors quite different from that measured on a larger surface immersed in a much larger volume of electrolyte. However, non-uniformity of the corrosion process does not imply non-uniformity of the potential distribution at the sample surface. The measured potential corresponds to a uniform potential characteristic of the entire surface. Development of a non-uniform potential distribution is not possible during free corrosion of the present electrode geometries without applied current, due to high conductivities of the solution and the metallic sample exposed to it, unless significantly occluded deep pits develop. It is more likely that localization of the anodic attack and existence of passivated areas will be shifting continuously at the surface, giving the observed nearly uniform corrosion at macroscopic scale, at the same time drifting from a more active, high-Zn area, to a more passive high-Al surface as the Zn-rich layer corrodes. This continuous shift during exposure is reflected in a highly negative corrosion potential for the high-Zn surface ("cathodic control") at the outset, drifting to more positive potentials as the Zn concentration decreases with increasing reduction in thickness and possibly increased passivity due to increasing concentration of Al ("anodic control") [13]. During this process, the corrosion potential is believed to be controlled by the localized active sights. This is more likely to be the case if the oxidation process can be described as a pitting type of mechanism, characterised by a pitting potential, above which polarization of the surface becomes kinetically restricted, although deep pits do not form in the present experiments using an acidified chloride solution [27]. This means that the surface concentration of the localized corrosion site must be determining the corrosion potential, which would be expected also to correspond to the critical pitting potential of the AlZn alloy. This hypothesis is further tested in Chapter 6.

5.5 Conclusions

- Zn-rich layers formed by thermal-arc spraying, followed by heat treatment for diffusing Zn into the surface of AlMn alloy MPE tubes in a controlled manner, maintain the corrosion potential of Al below the pitting potential at the expense of increased self-corrosion.
- Non-uniformity of the Zn-rich layers laterally and in depth lead to galvanic corrosion in which pure Zn islands corrode first, followed by corrosion of the underlying AlZn alloy layer, while the areas of uncoated Al alloy substrate remain protected from pitting.
- Zn load in the Zn thermal-arc sprayed coating should be reduced to minimize self-corrosion of the Zn-rich layer, which was found to decrease with decreasing Zn concentration.

- The optimal Zn-rich layer should have lowest self-corrosion rate and at the same time maintain the corrosion potential below -0.85 V_{SCE} sufficiently long. The best option among the Zn-rich layers studied was the one produced by heat treatment of Zn coating with low Zn load (2.7 ± 0.1 g/cm^2) for 4 hours at 430 °C.
- The sample heat treated for 2 hours at 350 °C had lowest total reduction in thickness and corrosion rate during 11 days of immersion test. Its corrosion potential increased above -0.85 V_{SCE} during the test but maintained at about 50 mV below the critical pitting potential E_c. As long as there is no danger for exceeding E_c, the Zn-rich layer obtained in this manner would be optimal.
- The presence of Zn activates the AlZn layer electrochemically by reducing its corrosion potential, while increasing its self-corrosion rate, even in quite small amounts (of order 1 wt%). The Al component transforms uniform corrosion kinetics of pure Zn, which is electrochemicaly active, to pitting-type of kinetics in the acidified chloride solution. These observations could not be unified in a specific mechanism for the corrosion of AlZn alloys, requiring further work in this direction.
- Non-uniformity of concentration distribution of Zn and Al in the craters produced by GD-OES Ar-sputtering and their galvanic coupling did not allow a straightforward correlation of the corrosion potential measured in these craters in chloride solution with the Zn concentration of AlZn alloys for estimation of corrosion rates from corrosion potential measurements.
- Empirical correlations of the corrosion potential, which is a mixed potential, with respect to bulk composition of an alloying element for aluminium alloys should be used with care since the surface chemistry and structure are expected to change significantly in relation to the bulk properties during corrosion, influencing the corrosion kinetics in a complex manner.

References

1. M. Bothwell, Diffusion cladding, Patent No: 3268358, The Dow Chemical Company, United States (1962).
2. H. Ikeda, *Aluminium*, **58**, 467–471 (1982).
3. M. Suzuki, A. Sugihara, T. Sano, T. Suzuki, Zincating aluminium, Patent No: EP0125352A1, Alcan International Limited, Canada (1984).
4. M. Suzuki, A. Sugihara, T. Sano, T. Suzuki, Process for applying a zinc coating to an aluminum article, Patent No: 4888218, Alcan international Limited, Canada (1989).

5. T. Morita, Heat exchanger, method for manufacturing the same, and heat exchanging tube, Patent No: WO2005066570, Showa Denko K.K, Japan (2005).
6. T. Morita, Aluminum pipe and process for producing same, patent No: US20060185168, Showa Denko K.K, Japan (2006).
7. K. Nisancioglu, H. Holtan, *Corrosion Science*, **18**, 835–849 (1978).
8. K. Nisancioglu, H. Holtan, *Corrosion Science*, **18**, 1011–1023 (1978).
9. K. Nisancioglu, Corrosion and protection of aluminium alloys in seawater, in D. Féron, Corrosion Behaviour and Protection of Copper and Aluminium Alloys in Seawater, pp. 145–155, Woodhead Publishing Limited, Cambridge, England (2007).
10. P. Gimenez, J. J. Rameau, M. C. Reboul, *Corrosion*, **37**, 673–682 (1981).
11. X. G. Zhang, Corrosion and electrochemistry of zinc, Plenum Press, New York (1996).
12. J. T. Reding, J. J. Newport, *Materials Protection*, **5**, 15–18 (1966).
13. I. L. Muller, J. R. Galvele, *Corrosion Science*, **17**, 995–1007 (1977).
14. F. Sato, R. C. Newman, *Corrosion*, **55**, 3–9 (1999).
15. H. Campbell, F. Porter, Proceedings of 1st International Congress on Metallic Corrosion, London, 1961, pp. 517–530, Butterworths, London (1962).
16. J. C. S. Fernandes, M. G. S. Ferreira, *Surface and Coatings Technology*, **53**, 99–100 (1992).
17. X. Zhang, S. Lo Russo, A. Miotello, L. Guzman, E. Cattaruzza, P. L. Bonora, L. Benedetti, *Surface and Coatings Technology*, **141**, 187–193 (2001).
18. O. Lunder, J. Nordlien, J. Lein, Proceedings of the 230th Meeting of the Electrochemical Society, 2016, Honolulu, USA, p. 1354 (2016).
19. J. T. B. Gundersen, A. Aytac, J. H. Nordlien, K. Nisancioglu, *Corrosion Science*, **46**, 697–714 (2004).
20. J. T. B. Gundersen, A. Aytac, S. Ono, J. H. Nordlien, K. Nisancioglu, *Corrosion Science*, **46**, 265–283 (2004).
21. M. Stern, *Journal of the Electrochemical Society*, **102**, 609–616 (1955).
22. R. Andresen, P. Gartland, E. Bardal, Proceedings of 8th International Congress on Met. Corrosion, Mainz, vol. 2, pp. 1333–1339 (1981).
23. G. Frankel, Pitting Corrosion, in ASM Handbook, vol. 13A, Corrosion: Fundamentals, Testing, and Protection, pp. 236–241, ASM International, in ASM Handbooks Online (2003).
24. L. M. Baugh, *Electrochimica Acta*, **24**, 657–667 (1979).

25. G. W. Walter, *Corrosion Science*, **16**, 573–586 (1976).
26. C. Wagner, W. Traud, *Corrosion*, **62**, 844–855 (2006).
27. O. Lunder, K. Nisancioglu, Proceedings of 8th International Light Metals Congress, Leoben-Vienna, 1987, pp. 706–709, Aluminium–Verlag, Düsseldorf (1988).
28. S. H. Salleh, S. Thomas, J. A. Yuwono, K. Venkatesan, N. Birbilis, *Electrochimica Acta*, **161**, 144–152 (2015).
29. K. Nisancioglu, H. Holtan, *Werkstoffe Und Korrosion*, **30**, 105–113 (1979).
30. A. Afseth, J. H. Nordlien, G. M. Scamans, K. Nisancioglu, *Corrosion Science*, **43**, 2093–2109 (2001).
31. A. Afseth, J. H. Nordlien, G. M. Scamans, K. Nisancioglu, *Corrosion Science*, **44**, 2491–2506 (2002).
32. K. Nisancioglu, *Journal of the Electrochemical Society*, **137**, 69–77 (1990).

Chapter 6

Characterisation of corrosion morphology and surface chemistry of zinc-rich layers on aluminium in acidified chloride solution

Abstract

The purpose of this chapter is to make a new attempt at correlating corrosion potential with mass concentration of Zn, ρ_{Zn}, of Zn-rich layers on AlMn alloy multi-port extruded tubes in acidified artificial sea water solution, this time taking into account localized nature of corrosion morphology and surface chemistry by use of SEM and EDS area analysis. Regions with higher ρ_{Zn} ccorroded first and protected galvanically regions with lower ρ_{Zn}. With increasing immersion time in the test solution, ρ_{Zn} in corroding regions decreased and corrosion spread to a larger area. Corrosion morphology of high ρ_{Zn} regions was highly porous and had a finer topography than low ρ_{Zn} corroded regions. The approach was successful in obtaining a correlation between the corrosion potential and ρ_{Zn} of the corroded areas. This allowed determination of the effect of ρ_{Zn} on the corrosion rate of the Zn-rich layers. No evidence of enrichment of either Al or Zn was observed. Zn coating with Zn load of 3.5 $\mathrm{g/m^2}$ heat treated for 3 hours at 470 °C was suggested as the optimal in terms of maintaining the potential of the AlMn substrate below its repassivation potential to protect against pitting and providing the lowest self-corrosion rate.

6.1 Introduction

In chapter 3, Zn-rich layers on AlMn alloy multi-port extruded (MPE) tubes were characterised by glow discharge optical emission spectroscopy (GD-OES), scanning electron microscopy (SEM) and X-ray energy dispersive spectroscopy (EDS). Zn was deposited by thermal-arc spraying and subsequently subjected to heat treatment, allowing controlled diffusion of Zn into the

AlMn substrate. Elemental depth profiles were obtained for different Zn loads and selected heat treatment conditions. In chapter 5 these tubes were subjected to continuous immersion corrosion testing in acidified artificial sea water solution combined with corrosion potential measurements. Corrosion rate decreased significantly with increasing time of immersion, which was correlated to decreasing Zn concentration, questioning the need for high Zn-loads.

In chapter 5, 4 mm diameter craters with different Zn concentrations, ρ_{Zn}, were obtained by GD-OES Ar-sputtering of Zn coated and heat treated AlMn alloy tubes to predetermined depths. Corrosion potential was measured in a drop of electrolyte on these by use of a capillary Luggin probe, in attempt to correlate ρ_{Zn} with the corrosion potential. It was further attempted to correlate these results with the purpose of estimating reduction in thickness on Zn coated samples during immersion in the acidified chloride solution based on corrosion potential measurements. Failure of this approach was attributed to lateral non-uniformity of the Zn-rich layers reported in chapter 3. It was suspected that the anodic attack was localized on areas with high ρ_{Zn}, and therefore, the measured corrosion potential corresponded to ρ_{Zn} of the corroded areas rather than the average ρ_{Zn} measured by GD-OES.

The purpose of the present work is to make another attempt to correlate ρ_{Zn} with the corrosion potential, this time focusing on the ρ_{Zn} of the locally corroding areas unlike chapter 5, where correlation of average ρ_{Zn} of the surface with the corrosion potential was considered. Corrosion type, morphology and chemistry of the Zn coating and Zn-rich layers on AlMn alloy MPE tube samples after immersion in acidified artificial sea water solution and their change with immersion time will be examined by SEM and EDS. These methods are expected to allow local area measurements of corroded and uncorroded regions, which is not possible with GD-OES. It will be furthermore attempted to correlate Zn concentration of the corroded areas with corrosion morphology and corrosion rate calculated in chapter 5. Optimization of the Zn-rich layer properties for minimizing its self-corrosion rate while maintaining the corrosion potential sufficiently low for protection against pitting will be discussed.

In order to understand the mechanism of protection of Al by alloying with Zn, the mechanism of dealloying of Al or Zn from Zn-rich layers on Al need to be investigated. Dealloying results in a highly porous surface morphology if a sufficient difference in the potentials of the pure components exist, and the concentration of the less noble metal component exceeds the minimum partial limit [1–3]. Formation of a porous surface morphology can thus be used as an indication of dealloying, although it cannot serve as a proof. Partial limit is, for example, 20 at% of Zn in Zn-Cu system. However, it is not known for the Zn-Al system. The porosity decreases with increasing concentration of the more noble metal [3]. Another condition is the homogeneity of the alloy [4].

Dealloying of AlZn system is not much discussed in the literature. Selective dissolution of Zn from 55 wt% Al-Zn coating on steel is reported to occur in chloride solution [5–7] without much information about the type of surface microstructure and morphology formed. Localized selective corrosion of Zn-rich interdendritic phases was reported to initiate at sites with higher Zn concentration, and this was attributed to poor passivity of these sites relative to the Al-rich denrites [5]. Selective dissolution of Zn from AlZn alloys in HNO_3 at open-circuit conditions did not cause the formation of a nanoporous morphology [8]. Corrosion under applied potential in the same solution lead to appearance of nanopores on the Al-rich regions in addition to macroporosity due to removal of Zn-rich phases. X- ray diffraction analysis of corroded 15 at% Zn alloy indicated selective removal of Zn from the alloy.

The necessity of creation of Zn diffusion layer with Zn concentration decreasing with depth for improved corrosion protection compared to Zn-rich coatings with fixed concentration, suggested in reference [9], has to be verified. Such layers were considered to work in the same way as multicladding, meaning that higher Zn regions at the surface protect the rest of the diffusion layer due to its lower Zn concentration. Corrosion attack is claimed to spread laterally this way, and localized pitting is prevented.

6.2 Experimental

Materials. AlMn alloy MPE tube samples were provided in bare and coated form by Sapa AS. Composition of the bare alloy, designated as Alloy1, was measured by spark optical emission spectroscopy (Spark OES). The results were shown in chapter 3 in table 3.1. The Zn coating was applied by thermal-arc spraying at the plant immediately after extrusion. Typical Zn load on the surface, determined by X-ray fluorescence (XRF) spectrometer (CMI 900 from Oxford Instruments), was 8.0 ± 0.2 g/m^2. Composition of the substrate, which was later coated with Zn, measured separately by Spark OES, was shown in chapter 3 in table 3.3, both in mass fraction and mass concentration. The tubes were cut, rinsed in distilled water, acetone and ethanol. Zn coated tubes were subsequently heat treated for 1, 2, 3, 4 and 5 hours at 350 °C, 390 °C and 430 °C to obtain Zn-rich layers with varying thickness and Zn concentration profiles on the surface of the AlMn substrate.

The procedure which involved the use of hot chromic-phosphoric acid treatment to produce Zn-rich layers with lower Zn loads than that possible by thermal-arc spraying was described in chapter 3. The Zn load on such samples was estimated as 2.7 ± 0.1 g/m^2. The samples with Zn load of 8 g/m^2 and 2.7 g/m^2 will be designated in this work as samples with high Zn load and low Zn load, respectively. MPE tubes with low Zn load were heat treated for 4 hours at 430, 470 and 510 °C.

Corrosion testing. The samples were immersed in acidified artificial sea water solution for various periods. After removal from the test solution, corrosion products were removed in chromic-phosphoric solution according to the procedures described in chapter 5.

Surface charecterization. Surface characterisation of the Zn coated AlMn samples at low magnification was performed by Hitachi S-3400N thermionic emission gun SEM equipped with EDS capability supplied by Oxford Instruments. EDS measurements were performed at an accelerating voltage of 20 kV. The EDS area analysis of corroded regions was performed on 0.20 - 0.04 mm^2 areas at positions on the specimens indicated in figure 3.1. The size of area analysed was limited by the size of corroded regions and grain size. Composition was obtained by averaging several such measurements performed on each of three locations of analysis on each sample. High magnification images of the corroded samples were obtained using field emission electron microscope Zeiss Supra 55VP (FEG-SEM).

Cross sections of selected corroded samples were also studied by SEM for further investigation of corrosion morphology. The samples were cut from corroded MPE tubes, embedded in epoxy and polished with diamond paste to 0.25 μm roughness. Analysis was performed by use of a JEOL JSM-7000 F FEG SEM.

Concentration depth profiling of the corroded samples was performed by HORIBA Jobin Yvon RF glow discharge optical emission spectrometer (GD-PROFILER 2) with a 4 mm anode. The plasma parameters power and pressure were adjusted to 32 W and 600 Pa, respectively. Calibration described in chapter 3 was used. Due to absence of calibration curves for H and Cl, the profiles for these elements were reported in terms of intensity (V).

6.3 Results

6.3.1 Corrosion morphology

Uncoated samples. Corrosion morphology on uncoated AlMn alloy MPE tube sample after 11 days of immersion in acidified artificial sea water solution is shown in figure 6.1. A backscattered SEM image of uncorroded surface is included (figure 6.1a). The surface of the Al MPE tubes before corrosion showed distinct horizontal extrusion lines and a significant amount of intermetallic particles (bright spots). After 11 days of immersion, the surface of the Al sample was slightly non-uniformly etched (figure 6.1b). The extrusion lines were still observed (vertical lines in figure 6.1b). Surface etching had crystallographic nature and crystallocraphic micropits were also observed, as shown at higher magnification in figure 6.1c.

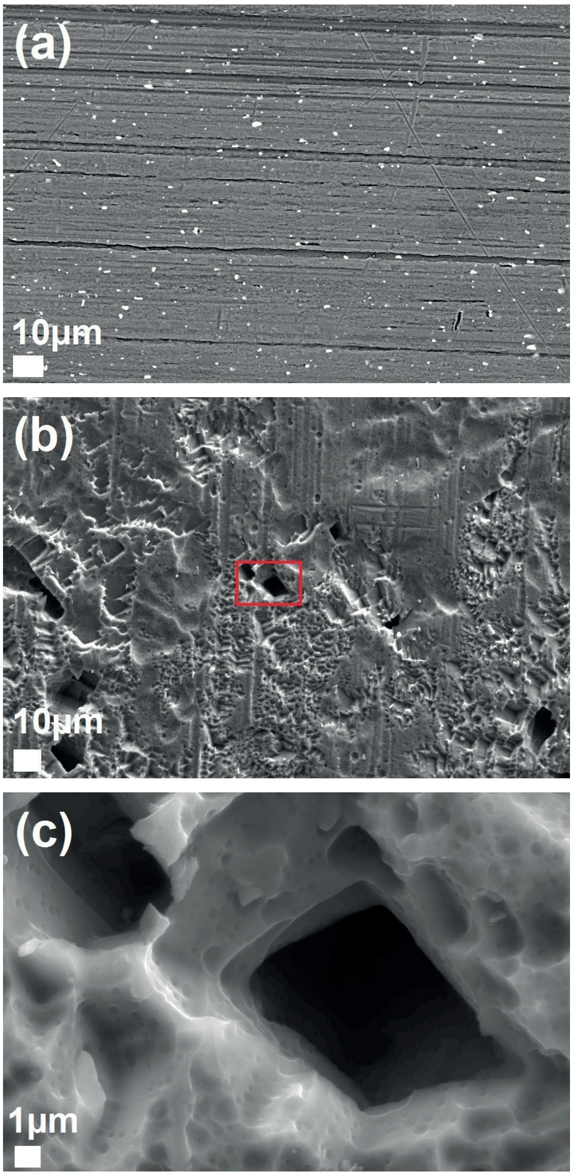

FIGURE 6.1: SEM micrographs of uncoated AlMn alloy MPE tube sample: a) backscattered SEM image before corrosion, b) secondary electron image after immersion in acidified artificial sea water solution for 11 days, c) area marked with a red square in (b).

As coated samples with high Zn load. Figure 6.2 shows EDS maps of elements Al and Zn of as coated sample with 8 g/m^2 of Zn (high Zn load) after immersion in acidified artificial sea water solution for three hours. Smooth uncorroded regions in the backscattered image (marked as ZF in figure 6.2a) correspond to light-green areas in Al map (figure 6.2b) and black areas in Zn map (figure 6.2c), which implies that these regions are Zn-free. Black channels around bright areas in the electron image in figure 6.2a (marked as ZC), which resemble dendritic structure, correspond to black channels in Zn map (6.2c). The same concerns the grain boundaries, marked as GB in figures 6.2a and 6.2c. Zn concentration of the bright regions in figure 6.2a was about 40 wt% Zn (marked as HZ) while grey regions had about 30 wt% Zn (marked as LZ) according to EDS point analysis (not shown). Such variation of Zn concentration was observed also on the Zn map in figure 6.2c. EDS maps of elements Al and Zn on Zn coated AlMn alloy MPE tube sample with high Zn load before corrosion were shown in chapter 3 in figure 3.12. Comparison of EDS maps in figures 3.12 and 6.2 shows that all pure Zn part of the coating corroded after three hours.

The fact that pure Zn corrodes quickly after immersion of the samples in the test solution, according to the results shown in figure 6.2, is supported also by the corrosion potential transients and weight loss data in chapter 5 (point (2) in figures 5.7 and 5.11, respectively). It was reported in chapter 3 that Zn diffused into the grain boundaries already during thermal-arc spraying (figure 3.15a). EDS map in figure 6.2 shows that after immersion for three hours corrosion propagated into these Zn-rich grain boundaries.

Figure 6.3 shows SEM micrographs of non-heat-treated high Zn load samples corroded for 8 hours (figure 6.3a) and 11 days (figures 6.3b and c) in the test solution. During rinsing of the sample immersed for 8 hours, a dark coating (light contrast on the right in figure 6.3a) began to flake off the surface revealing a lighter surface (dark contrast on the left in figure 6.3b) of the sample, as illustrated in the optical macro-image, figure 6.4a. After thorough cleaning a small part of the coating remained on the surface, as shown in figure 6.4b. Corrosion at the grain boundaries was observed on both coating and exposed substrate (figure 6.3a). EDS area analysis (not shown) revealed that the Zn concentration was about 30 wt% and 1.5 wt% on the coating and substrate surfaces, respectively.

According to these results, most of the pure Zn layer appeared to corrode during the first three hours of immersion, exposing the AlZn alloy dendrites formed on the surface and underneath the pure Zn layer during solidification of the thermally sprayed coating. Existence of pure Zn and AlZn alloy dendrites was shown in figure 3.15a. It appears that AlZn alloy dendrite layer was undermined during the next stage of corrosion and the Zn diffusion layer (marked as DL in figure 3.15a) was exposed to the solution. After 8 hours of exposure, corrosion of the Zn diffusion layer propagated significantly and the AlMn alloy surface, containing about 1.5 wt% Zn, was exposed. At the same time, uncorroded Zn-free regions were also observed on the left side of the micrograph in figure 6.3a. Such areas were detected by

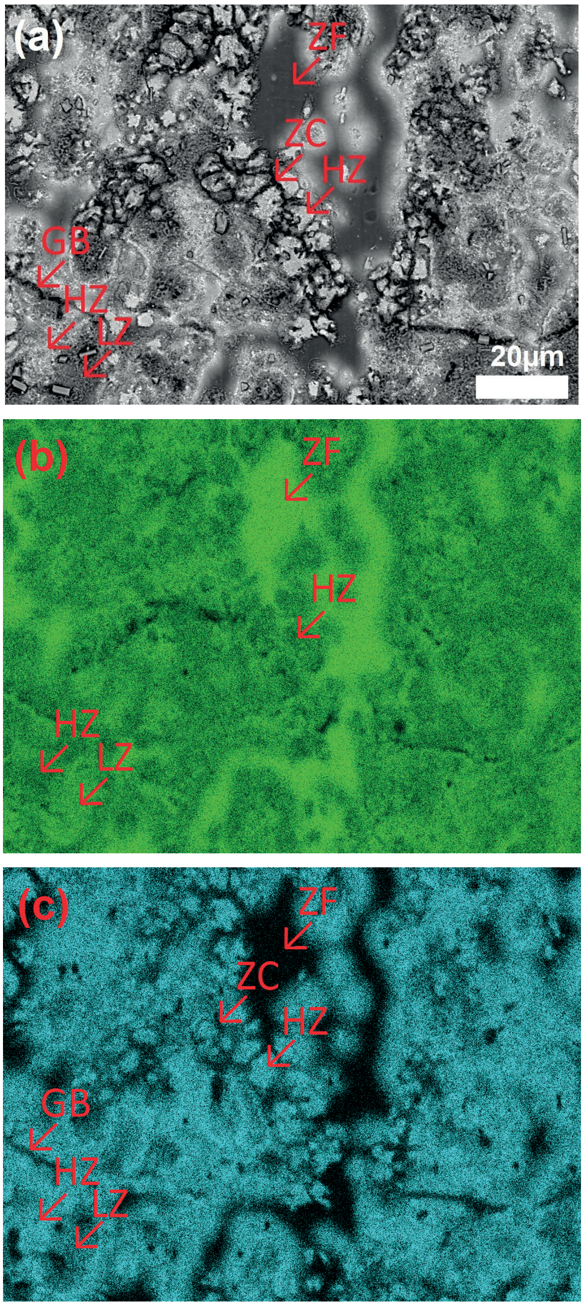

FIGURE 6.2: EDS map of AlMn alloy coated with 8 g/m^2 of Zn (not heat treated), after corrosion in the test solution for 3 hours. a) Backscattered electron image, b) Al map, and c) Zn map. Markings: ZF – Zn-free uncorroded region, ZC – Zn-rich interdendritic channels (corroded), GB – corroded grain boundaries, HZ – higher Zn regions, LZ – lower Zn regions.

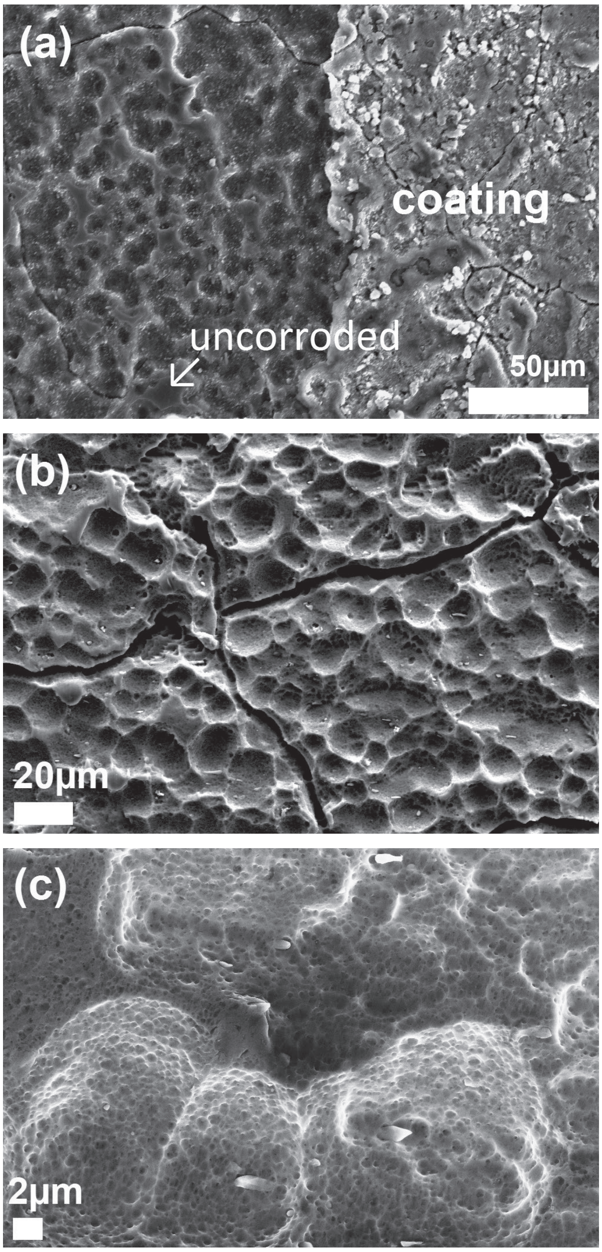

FIGURE 6.3: Corrosion morphology of AlMn alloy MPE tube sample coated with 8 g/m^2 of Zn (not heat treated) after immersion in the test solution for a) 8 hours, b) and c) 11 days. Intermetallic particles are visible in (c) as white spots.

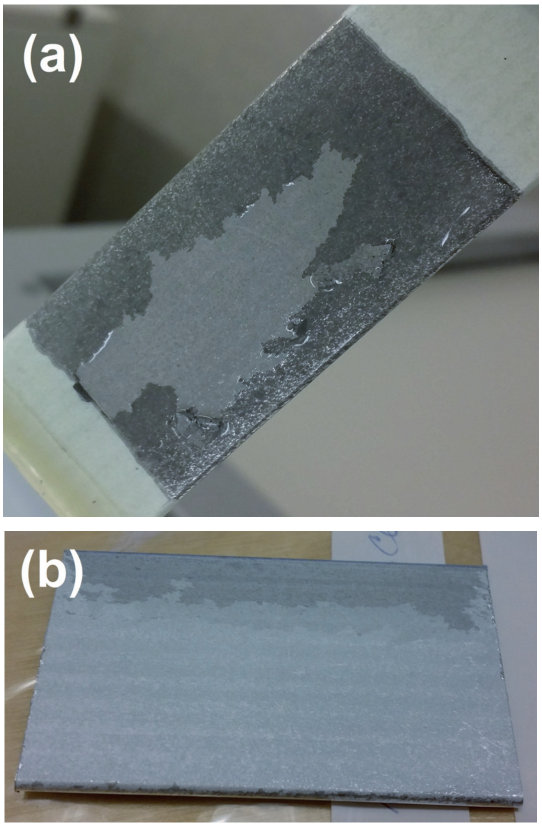

FIGURE 6.4: Zn coated AlMn alloy MPE tube sample after corrosion in the test solution for 8 hours. a) shows a high Zn coating flaking off the surface sample, b) shows sample surface after rinsing. The length and width of the sample in (b) was 4.4 and 2.6 cm, respectively.

use of EDS maps of Zn and Al (not shown for figure 6.3a), similar to those in figure 6.2.

Corrosion morphology after 11 days of immersion in figure 6.3b showed etching with a cellular structure. A higher magnification image (figure 6.3c) revealed that the cell surface had a fine scalloped structure. The region in the top left corner of figure 6.3c showed less corrosion than the rest of the surface in the micrograph, indicating that it was corroding for a shorter period of time than the rest of the surface.

Heat treated high Zn load samples. In the macroscopic images of the corroded, Zn-coated AlMn samples, presented below, the samples lie horizontally with respect to the direction of extrusion. During the corrosion test, the samples were immersed vertically in the direction of extrusion. The top and bottom edges were the cut edges. Therefore, in the macroscopic images, the samples lie perpendicular to their position during immersion.

Figure 6.5 shows macrograph of a high-Zn load sample, heat treated for 2 hours at 350 °C and immersed for 10 hours in the test solution. Most of the surface (the dark-contrast area), which was originally Zn-rich, was attacked. The small, bright areas spread over surface are localized uncorroded regions, characterized as Zn-lean regions by EDS analysis as discussed above in connection with figures 6.2 and 6.3. The figure demonstrates lateral non-uniformity of corrosion of the Zn-rich layer on a macroscopic level. The bright areas corrode slowly as the lateral distribution of Zn concentration evens out. Corrosion of these Zn-lean spots took several days. After 4 days of immersion the entire surface was corroded except several such areas still remaining near one edge (not shown; see below (figure 6.9) for analogous, more detailed macrographs).

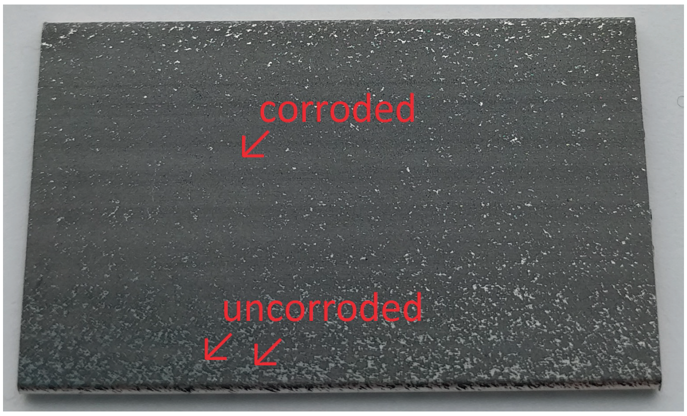

FIGURE 6.5: AlMn alloy sample coated with 8 g/m^2 of Zn and heat treated for 2 hours at 350 °C, after immersion in the test solution for 10 hours. The sample dimensions were 2.6 x 4.2 cm.

SEM micrograph in figure 6.6a confirms that most of the surface of the high Zn load sample, heat treated for 2 hours at 350 °C, was corroded after 10 hours of immersion. Several uncorroded regions are observed (the protruding dark regions in figure 6.6a). Figure 6.6a shows further that the grain boundaries started to corrode due to diffusion of Zn (figure fig:CSHMb). After 4 days of immersion (figure 6.6b), almost entire surface was attacked. Corrosion along the grain boundaries propagated significantly, causing detachment of some of the grains (figure 6.6c).

Changes in the morphology and structure of this sample due to corrosion are illustrated further by high magnification images in figure 6.7. A highly porous surface with fine structure of crystallographic nature was formed after 18 hours of immersion (figure 6.7a). This developed further into a coarser and significantly less porous structure with crystallographic features after 4 days of immersion (figure 6.7b). Corrosion resulting from 11 days of immersion (figure 6.7c) showed an even coarser corrosion morphology with more distinct crystallographic features. No porosity was observed.

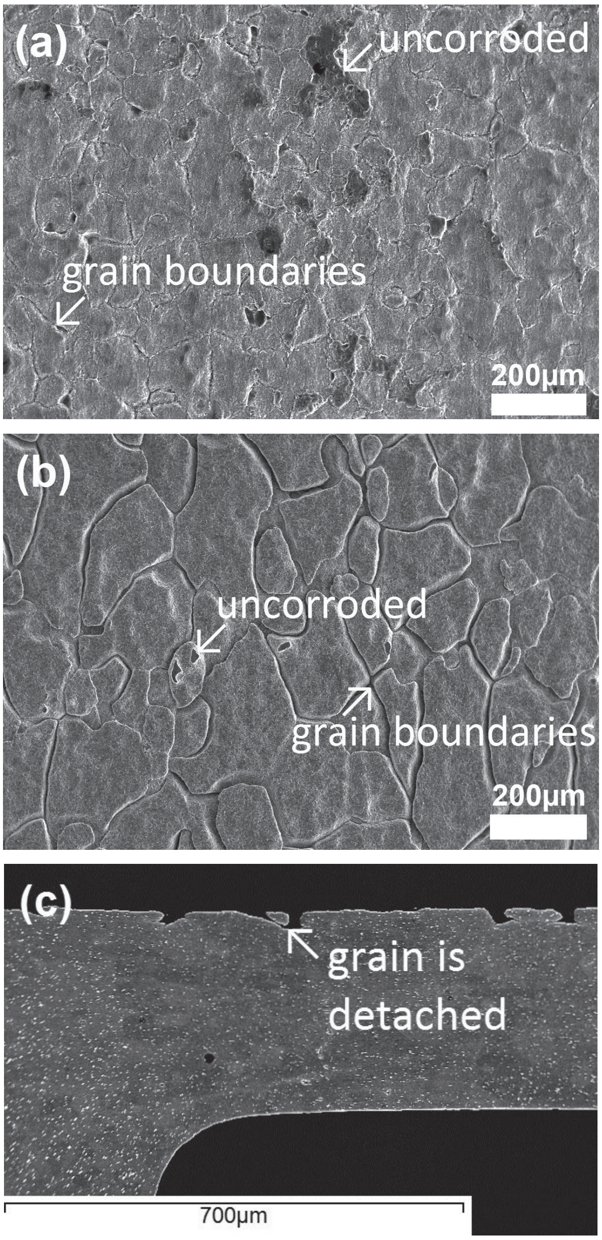

FIGURE 6.6: Corrosion morphology of AlMn alloy MPE tube sample, coated with 8 g/m^2 of Zn and heat-treated for 2 hours at 350 °C, after immersion in the test solution for a) 10 hours and b) 4 days in plain view and c) 4 days in cross section in the backscattered electron mode.

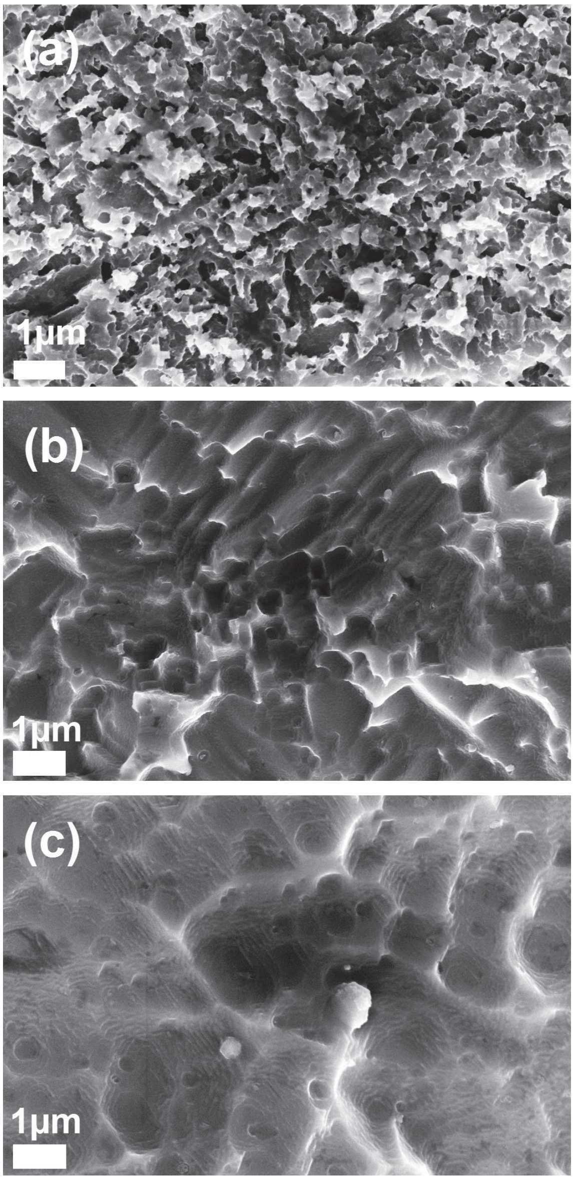

FIGURE 6.7: High magnification SEM micrographs of corrosion morphology on AlMn alloy, coated with 8 g/m^2 of Zn and heat treated for 2 hours at 350 °C, after immersion in the test solution for a) 18 hours, b) 4 days and c) 11 days.

Development of corrosion morphology on high Zn load samples, heat treated for 2 hours at 390 °C was quite similar to that described above for samples heat treated for 2 hours at 350 °C, with the exception, that the lateral propagation of corrosion was delayed in the case of heat treatment for 2 hours at 390 °C. About half of the surface was corroded after 10 hours of immersion, while the other half, which was Zn-lean, remained uncorroded. After immersion for 18 hours, the attacked area increased significantly and the surface resembled the one shown in figure 6.5 for the sample heat threated for 2 hours at 350 °C. After immersion for 4 days, corrosion spread to almost entire surface, as in the case of the samples heat threated for 2 hours at 350 °C.

Corrosion morphology of the sample heat treated 2 hours at 390 °C resembled, after 18 hours of immersion, the morphology shown in figure 6.7a for the sample heat treated for 2 hours at 350 °C after the same immersion period. The attack morphology on the sample heat treated for 2 hours at 390 °C became coarser after 4 days of immersion, yet still with significant porosity (figure 6.8), compared to the sample heat treated for 2 hours at 350 °C (figure 6.7b). 11 days of immersion lead to a notably coarser structure with crystallographic features, similar to the sample heat treated for 2 hours at 350 °C after the same period of immersion (figure 6.7c). No porosity was observed.

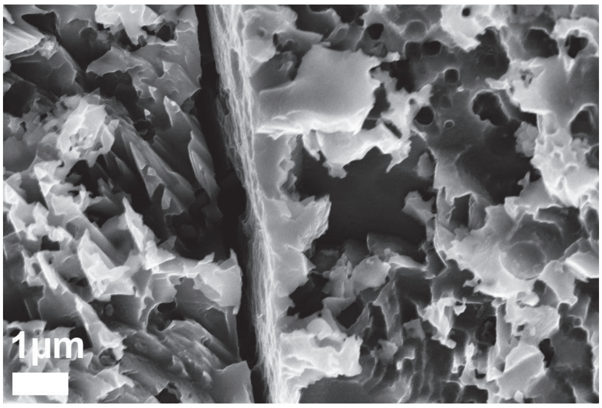

FIGURE 6.8: High magnification SEM micrograph of corrosion morphology on AlMn alloy coated with 8 g/m^2 of Zn and heat-treated for 2 hours at 390 °C after immersion in the test solution for 4 days.

Figure 6.9 shows macrographs of localized corrosion initiation and spreading of the localized attack into a more uniform etching type of corrosion as a function of immersion time for samples heat treated for 4 hours at 430 °C. Somewhat similar to the sample types previously described, corrosion initiated locally only on a small part of the surface after 10 hours of immersion, as visualized by the dark contrast areas (figure 6.9a). Immersion for

18 hours lead to spreading of corrosion to approximately half of the surface area (figure 6.9b). After 11 days of immersion (figure 6.9c) most of the surface was corroded except for limited number of regions near the bottom edge of the sample in light contrast.

Changes in the spreading of corrosion on this type of sample were also observed at higher magnification on SEM, as shown in figure 6.10. After immersion for 10 hours less than half of the surface was corroded (figure 6.10a). After 18 hours of immersion about half of the surface was attacked, as shown in figure 6.10b. A limited amount of uncorroded regions remained after 11 days of immersion (figure 6.10c). No significant corrosion at the grain boundaries was visible. This is expected since this type of sample showed no visible enrichment of Zn at the grain boundaries according to figure 3.15c. Corrosion morphology on these samples at higher magnification, after 18 hours and 4 days of immersion, was similar to the morphology of the samples heat treated for 2 hours at 390 °C, with the difference that a smaller area fraction corroded for a given time of immersion. Surface with fine porous structure after 4 days of immersion developed into a coarser porous structure with crystallographic features after 11 days of immersion, as shown in figure 6.11. In comparison, a coarser structure was observed for the sample heat treated for 2 hours at 350 °C and 390 °C after immersion for the same period, and no porosity was observed (figure 6.7c).

Heat treated low Zn load samples. The macroscopic appearance of corrosion propagation on the low Zn load sample (2.7 g/m^2 of Zn), heat treated for 4 hours at 430 °C, was quite similar to the cases discussed above. Figure 6.12 shows SEM micrographs of a low Zn load sample, heat treated for 4 hours at 430 °C, after 11 days of immersion in the test solution. The lower magnification image in figure 6.12a shows that most of the surface was corroded. Slight grain-boundary attack visible occurred during hot chromic phosphoric treatment before heat treatment, as was shown earlier in chapter 3 (figure 3.16a). It is assumed that no further grain boundary attack occurred during immersion after heat treatment. Higher magnification of the image, shown in figure 6.12b, reveals quite porous morphology with crystallographic features.

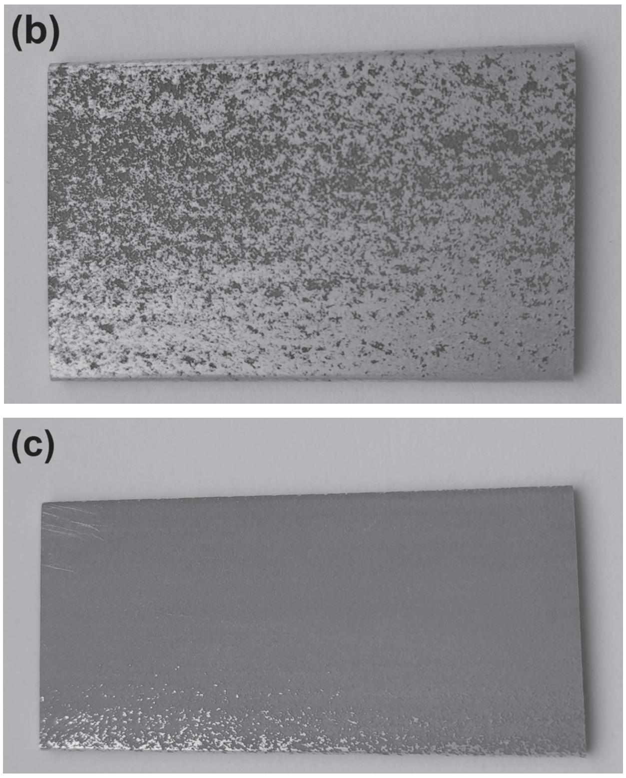

FIGURE 6.9: AlMn alloy, coated with 8 g/m^2 of Zn and heat treated for 4 hours at 430 °C, after immersion in the test solution for a) 10 hours, b) 18 hours and c) 11 days. Dark contrast areas are corroded. Tube lengths were 4.6, 4.2 and 5.5 cm, respectively. Tube width was 2.6 cm for all samples.

Most of the surface of the low Zn load sample, heat treated for 4 hours at 510 °C, remained uncorroded after 3 days of immersion, as shown in figure 6.13a. Corroded regions (dark contrast) were concentrated near the top one edge of the tube. The same pattern was observed after 11 days of immersion (figure 6.13b). The corroded area increased slightly and was still concentrated near the same edge of the tube. High magnification SEM image of such area (figure 6.14a) showed grain boundary attack, which occurred during hot chromic phosphoric treatment before heat treatment. Further magnification (figure 6.14b) revealed slightly coarser and non-porous corrosion morphology compared to the low Zn load sample heat treated for 4 hours at 430 °C (figure 6.12b).

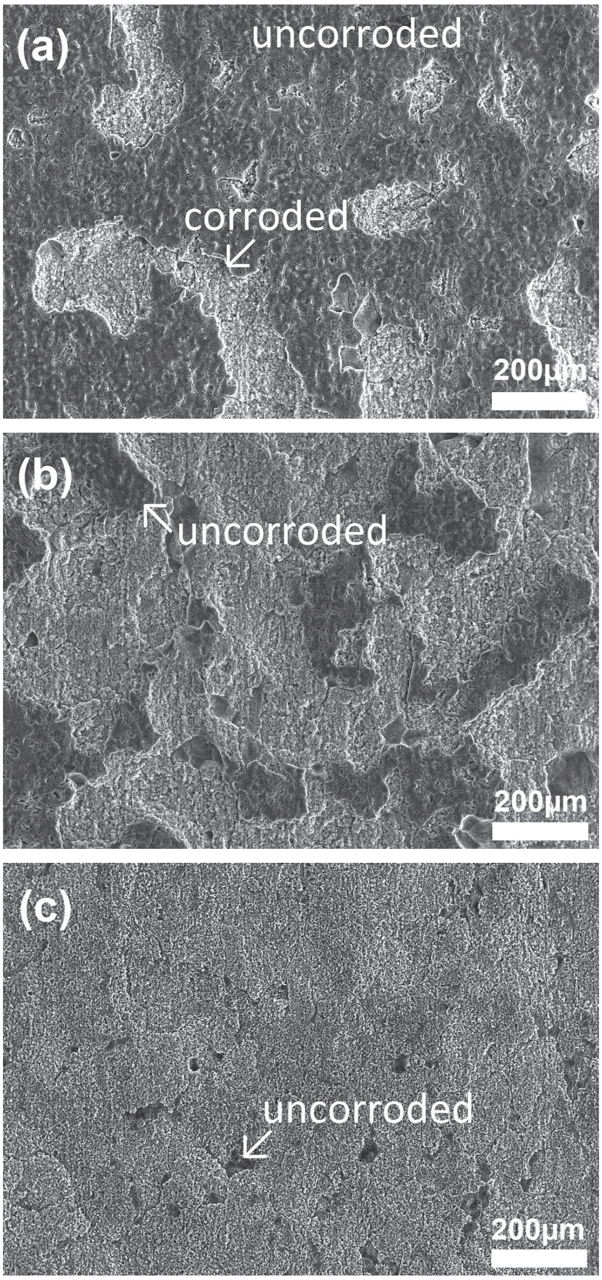

FIGURE 6.10: Corrosion morphology of AlMn alloy, coated with 8 g/m^2 of Zn and heat treated for 4 hours at 430 °C, after immersion in the test solution for a) 10 hours, b) 18 hours and c) 11 days. Dark areas are uncorroded.

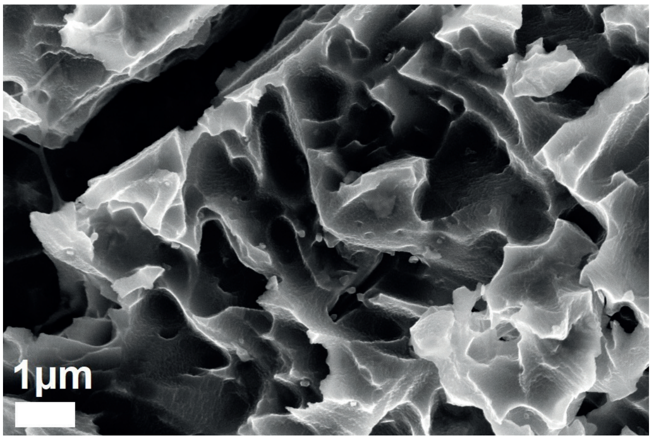

FIGURE 6.11: High magnification SEM micrograph of corrosion morphology on AlMn alloy, coated with 8 g/m^2 Zn and heat treated for 4 hours at 430 °C, after immersion in the test solution for 11 days.

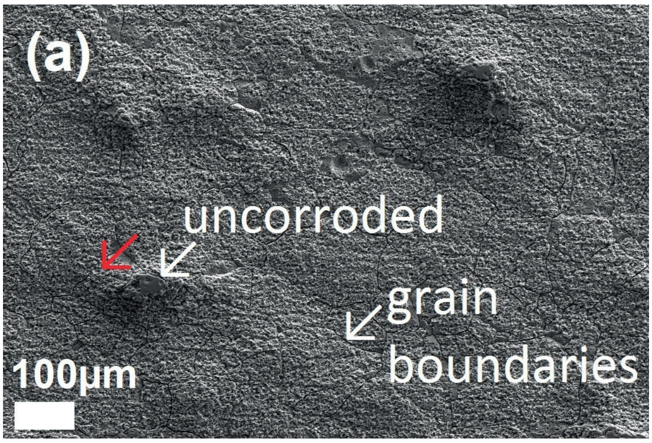

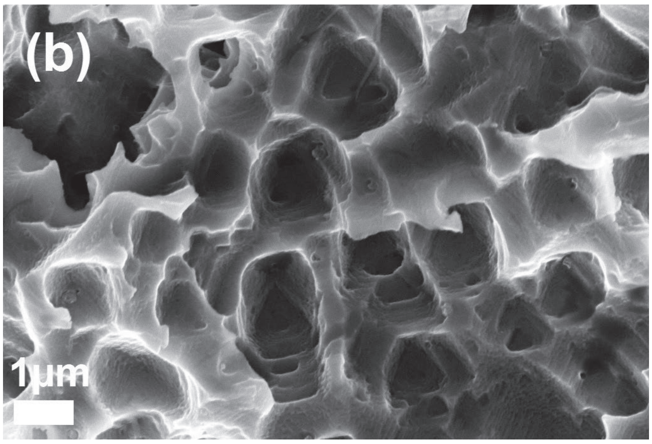

FIGURE 6.12: Corrosion morphology of AlMn alloy, coated with 2.7 g/m^2 of Zn and heat treated for 4 hours at 430 °C, after immersion in the test solution for 11 days. (b) is a higher magnification image from the site marked by a red arrow in (a).

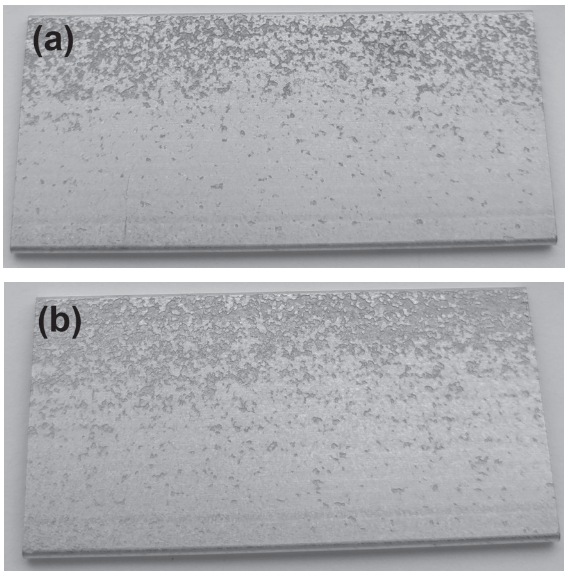

FIGURE 6.13: AlMn alloy coated with 2.7 g/m^2 of Zn and heat treated for 4 hours at 510 °C after immersion in the test solution for a) 3 days and b) 11 days. Areas with dark contrast are corroded, while the regions with lighter contrast are uncorroded. The length of samples were 5.7 and 5.1 cm, respectively. Tube width was 2.6 cm for all samples.

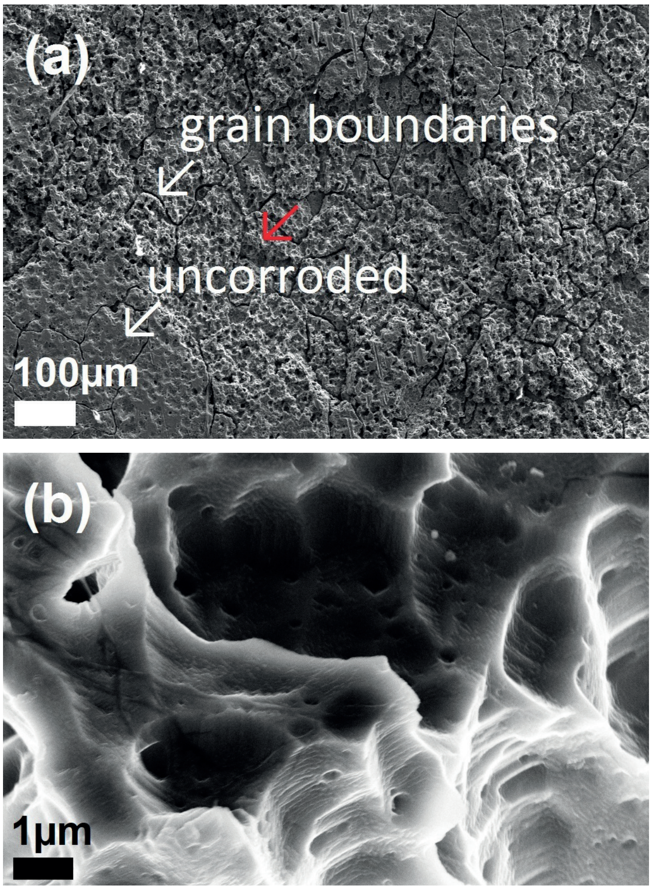

FIGURE 6.14: Corrosion morphology of AlMn alloy, coated with 2.7 g/m^2 of Zn and heat treated for 4 hours at 510 °C after immersion in the test solution for 11 days. (b) is a higher magnification image of the site marked by a red arrow in (a).

6.3.2 Local elemental analysis after immersion test

Corroded areas. EDS analysis of the corroded areas, performed as described in section 6.2, on as coated and heat treated high-Zn load samples are shown in figure 6.15 for the elements Zn, Al, O, Mn and Fe. Concentrations at the surface before immersion test reported in table 3.11 are included at time equal to zero.

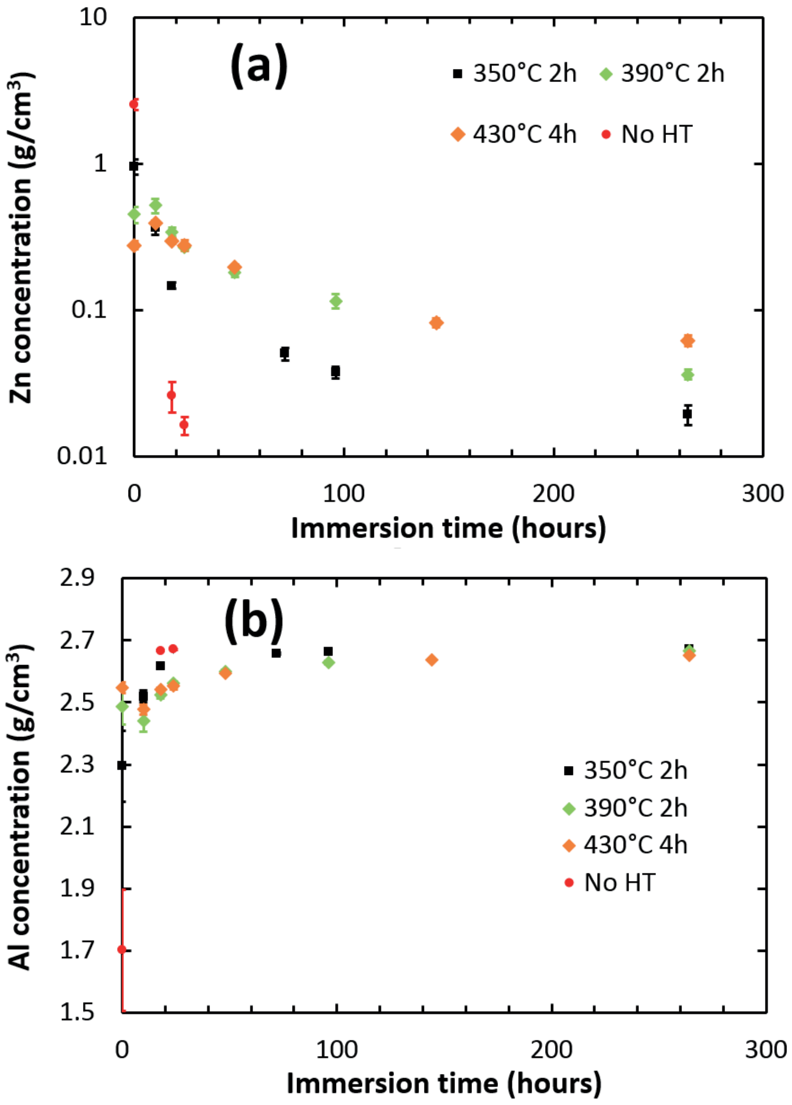

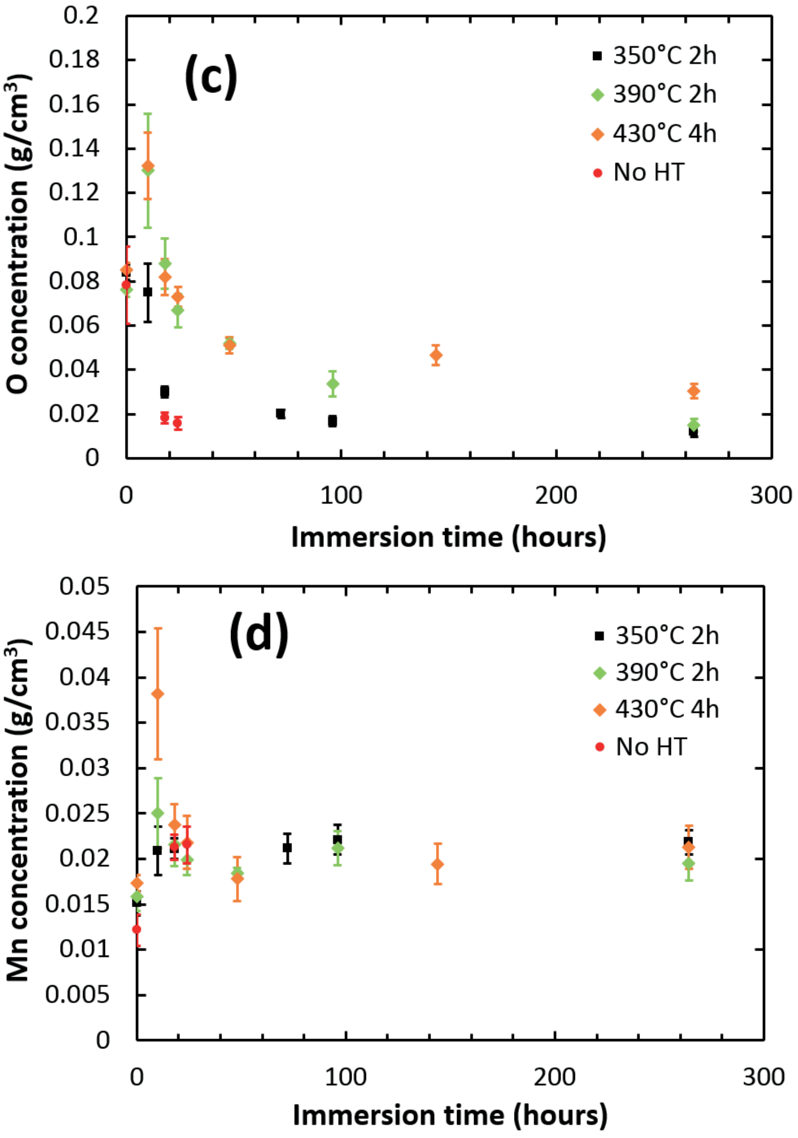
(c)
O concentration (g/cm³)
0.2
0.18
0.16
0.14
0.12
0.1
0.08
0.06
0.04
0.02
0
0
100
200
300
Immersion time (hours)
350°C 2h
390°C 2h
430°C 4h
No HT
(d)
Mn concentration (g/cm³)
0.05
0.045
0.04
0.035
0.03
0.025
0.02
0.015
0.01
0.005
0
0
100
200
300
Immersion time (hours)
350°C 2h
390°C 2h
430°C 4h
No HT

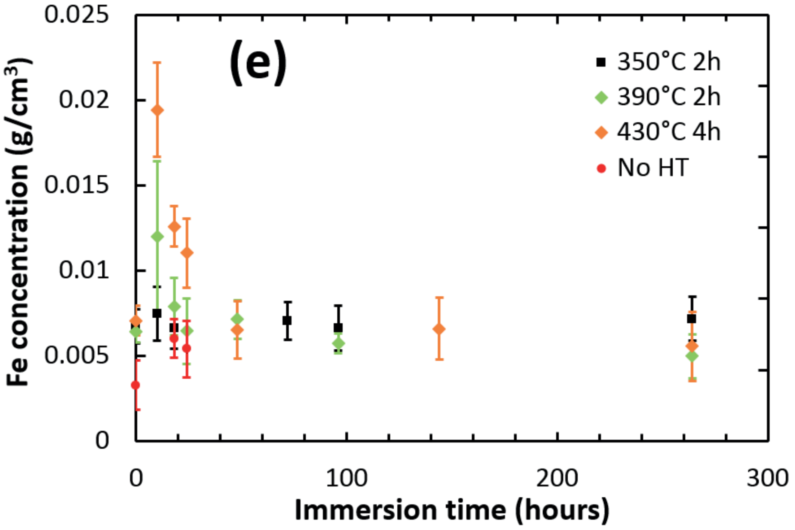

FIGURE 6.15: Effect of immersion in the test solution on composition measured by EDS for Zn coated AlMn alloy MPE tube samples with 8 g/m^2 of Zn, as coated and heat treated. a) Zn, b) Al, c) O, d) Mn, e) Fe.

Figure 6.15a shows the change in mass concentration of the corroded regions, $\rho_{Zn(corr)}$, as a function of immersion time in the test solution. $\rho_{Zn(corr)}$ decreased monotonically for the as coated (non-heat-treated) sample and sample heat treated for 2 hours at 350 °C. After 10 hours of immersion, $\rho_{Zn(corr)}$ for samples treated for 2 hours at 390 °C and 4 hours at 430 °C increased relative to their values before immersion. After these maxima, $\rho_{Zn(corr)}$ for these cases decreased monotonically with immersion time. After 11 days of immersion $\rho_{Zn(corr)}$ for the higher degrees of heat treatment exceeded that for the lower degrees.

Al concentration (figure 6.15b) for the untreated sample and the sample treated for 2 hours at 350 °C (low degree treatment) increased monotonically during immersion and reached values close to the bulk level sooner than for higher degrees of heat treatment, as expected. The Al concentration for samples treated for 2 hours at 390 °C and 4 hours at 430 °C showed minima relative to their pre-immersion values after 10 hours of immersion before increasing monotonically to their bulk values.

O concentration shown in figure 6.15c dropped significantly for non-heat-treated and heat treated for 2 hours at 350 °C samples after 18 hours of immersion and continued to decrease slowly. In the case of samples heat treatment for 2 hours at 390 °C and 4 hours at 430 °C, O concentration increased after 10 hours of immersion and then decreased monotonically. After 4 days of immersion O concentration of the heat treated samples was higher for higher degrees of heat treatment.

The concentration profiles for Mn and Fe, shown in figures 6.15d and e, respectively, showed similar behaviour with one another. Mn and Fe concentration of the non-heat-treated sample and samples heat treated for 2 hours at 350 °C increased to their bulk levels monotonically within the first 18 hours of immersion. For samples heat treated for 2 hours at 390 °C and 4 hours at 430 °C, concentrations of these elements increased to maxima after 10 hours of immersion. The values for the latter treatment were the highest among all samples for both Mn and Fe at this point. After their respective maxima Mn and Fe concentrations decreased and stabilized at their bulk levels after about two days of immersion.

Uncorroded areas. On all of the samples analysed by EDS, Zn concentration of uncorroded regions, $\rho_{Zn(uncorr)}$, varied significantly and was lower than average $\rho_{Zn(corr)}$. This is illustrated by the backscattered electron SEM image in figure 6.16 for high Zn load sample heat treated for 2 hours at 390 °C and immersed in acidified artificial sea water solution for 10 hours. ρ_{Zn} of several regions on the SEM image measured by EDS is reported in the figure caption with scatter limits based on standard deviation of the measurement. $\rho_{Zn(uncorr)}$ in regions B, C and D varied significantly and was lower than $\rho_{Zn(corr)}$ in region A. $\rho_{Zn(corr)}$ showed smaller scatter than $\rho_{Zn(uncorr)}$ on all samples, as can be seen from the scatter limits indicated in figure 6.15a.

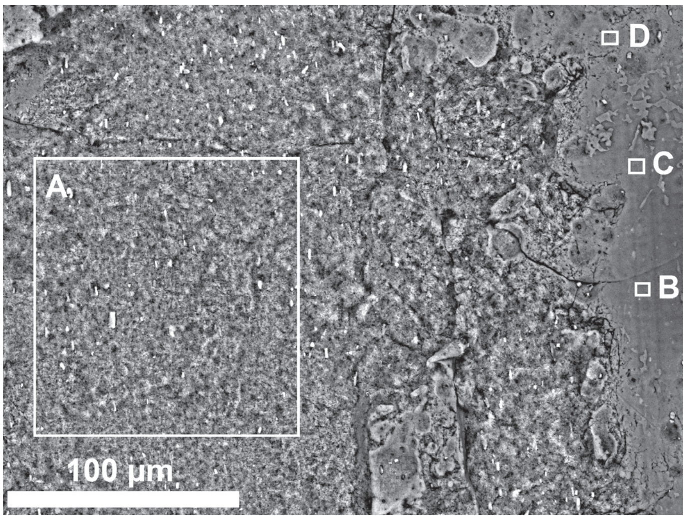

FIGURE 6.16: Backscattered SEM image of corrosion morphology on Zn coated AlMn alloy MPE tube sample with 8 g/m^2 of Zn heat treated for 2 hours at 390 °C after immersion in the test solution for 10 hours. Zn concentration of the marked regions measured by EDS analysis: (A) 15.2 ± 0.3 wt%, (B) 2.7 ± 0.1 wt%, (C) 7.4 ± 0.2 wt% and (D) 9.8 ± 0.2 wt%.

6.3.3 Correlation between corrosion potential and Zn concentration

Figure 6.17 compares corrosion potential, a) measured on samples immersed in large volume of test solution, as a function of Zn concentration at localized corroded areas, $\rho_{Zn(corr)}$, measured by EDS, as reported in the previous section (red points) and b) average concentration for sputtered craters, measured by GD-OES, and corrosion potential measured in a drop of test solution in the crater, as reported in section 5.3.5 (blue points). The scatter in the EDS data for Zn concentration is based on replicate measurements at different locations on the same specimen, while the GD-OES data are based on potential measurements in replicate craters, also on the same specimen. Zn concentration is presented in wt% to compare the correlation with data from references [10, 11] for high purity AlZn alloys which agree fairly well with the present EDS results.

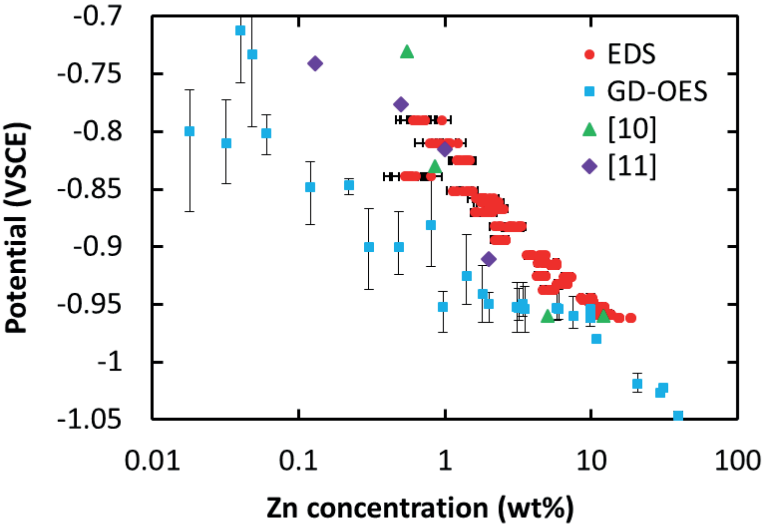

FIGURE 6.17: Effect of Zn concentration on corrosion potential of Zn-rich layers on AlMn alloy samples with 8 g/m^2 of Zn load. Zn concentration after immersion in acidified artificial sea water solution was measured by EDS (red symbols) at different locations for each sample. Analogous correlation from figure 5.16 based on measurements in GD-OES craters (blue symbols) and literature data for high purity AlZn binary alloys are included for comparison. The literature data were measured in synthetic sea water [10] (green symbols) and deaerated 0.5 M NaCl solution [11] (purple symbols).

For a given corrosion potential in figure 6.17, $\rho_{Zn(corr)}$ measured by EDS was higher than the average Zn concentration $\rho_{Zn(av)}$, measured by GD-OES in craters. As was discussed in chapter 5, Zn concentration measured by GD-OES is the average for 4-mm diameter area. This concentration does not correspond to the concentration of the localized corroding areas, owing to the fact that the composition of the Zn-rich layers (discussed in chapter 3) and their corrosion rate (discussed in section 6.3.1) are non-uniform laterally. Potential measured in a drop (small volume) of electrolyte can also be affected by rapidly changing chemistry of the solution due to corrosion and reduction processes. In contrast, EDS measurements were performed on corroded regions of the samples after full immersion of a larger area sample in a large volume of electrolyte. Therefore, correlation of the corrosion potential in this manner and Zn concentration measured by EDS on locally corroded areas is considered to be reasonable.

The data shown in figure 6.17 was fitted to a sum of two exponential functions by least squares regression analysis in the form of

$$\rho_{Zn(corr)} = Aexp(-aE_{corr}) + Bexp(-bE_{corr}) \tag{6.1}$$

as shown in figure 6.18, with fitting parameters A = 4.3 × 10^{-54}, B = 125.8, C = 5.3 × 10^{-9}, D = 18.6. The coefficient of determination, R^2, was 0.95. This relationship was used to convert the corrosion potential measured during immersion into $\rho_{Zn(corr)}$ – immersion time curves. The results were similar to the ones reported in 6.3.2 and therefore not shown. The fitted curve in figure 6.18 indicates that in order to maintain corrosion potential below the repassivation potential of -0.85 V_{SCE} Zn concentration should be higher than 0.040 ± 0.002 g/m^3.

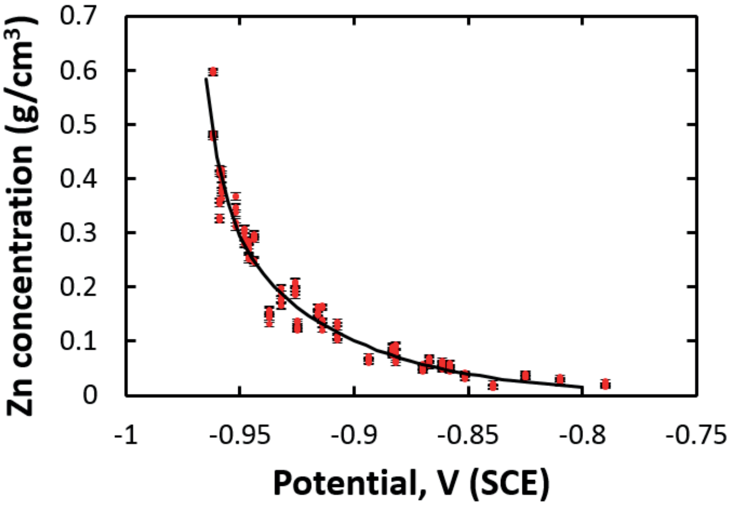

FIGURE 6.18: Zn concentration of corroding regions in Zn coating and Zn-rich layers in AlMn alloy MPE tubes with 8.0 g/m^2 of Zn as a function of corrosion potential in acidified artificial sea water solution. Red circles represent experimental data, black line is the fitted curve.

6.3.4 Correlation between corrosion rate and Zn concentration

In chapter 5 corrosion rate was estimated as increase of reduction in thickness between two subsequent measurements divided by the corresponding time interval. Reduction in thickness, in turn, was calculated based on weight loss measurements after continuous immersion tests with varied duration in acidified artificial sea water solution. Figures 5.12 and 5.14 in chapter 5 showed corrosion rate change with time for Zn-rich layers on AlMn alloy MPE tube samples with Zn loads of 8 g/m^2 (high Zn load) and 2.7 g/m^2 (low Zn load), respectively. In order to correlate Zn concentration of the corroded regions $\rho_{Zn(corr)}$ with corrosion rate, the following procedure was used:

1. The mean corrosion potential E_{corr} for each time interval (two adjacent points of measurement on the time axis) in figures 5.12 and 5.14 was calculated.
2. $\rho_{Zn(corr)}$ was estimated based on E_{corr}, using correlation $\rho_{Zn(corr)} = f(E_{corr})$ shown in figure 6.18.
3. Corrosion rate calculated in chapter 5, as summarized above, was correlated with $\rho_{Zn(corr)}$ on log-log scale, as shown in figure 6.19.

Use of figures 6.18 and 6.19 allows estimation of the concentration of Zn at the corroding areas from simple corrosion potential measurements within the error limits of the correlations. The upper limit for the corrosion potential in these correlations is -0.79 V$_{\mathrm{SCE}}$ because of the limitation of the analytical methods used in determining Zn concentrations. Corrosion rates corresponding to the first time interval of the tests (first 10 hours for high Zn load and 3 days for low Zn load) are not shown because of apparent effect of the intermetallic particles precipitated during heat treatment on corrosion rate for short times of immersion, as was discussed in section 5.3.3.

Figure 6.19 shows that corrosion rate decreases significantly with decreasing Zn concentration. The data on a log-log scale appears to fit a straight line. The data was fitted to a straight line by least squares regression analysis. The fitted line with coefficient of determination $R^2 = 0.75$ is also shown in figure 6.19. Based on this fitted curve, corrosion rate is 1 ± 0.25 µm/day for the minimum Zn concentration required (0.04 g/cm^3, as determined in the previous section) for lowering the corrosion potential below repassivation potential of -0.85 V$_{\mathrm{SCE}}$.

6.3.5 Comparative summary of corrosion morphology and chemistry of Zn-rich layers

Table 6.1 summarizes and compares corrosion morphology, Zn concentration and corrosion potential, E_{corr}, after immersion in acidified artificial sea

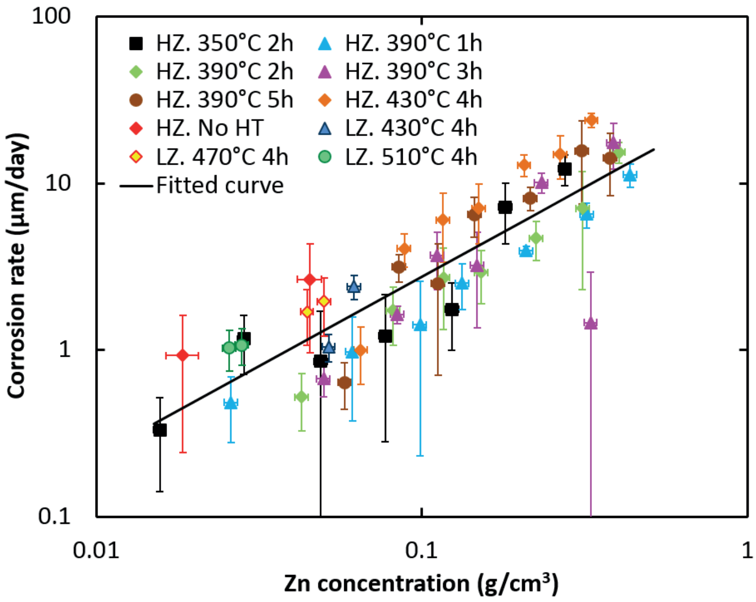

FIGURE 6.19: Effect of Zn concentration of the corroded regions, $\rho_{Zn(corr)}$, on Zn coated and heat treated AlMn alloy MPE tubes, with 8 g/m^2 (HZ) and 2.7 g/m^2 (LZ) of Zn, on corrosion rate in acidified artificial sea water solution. $\rho_{Zn(corr)}$ was calculated based on the relationship between corrosion potential and $\rho_{Zn(corr)}$ shown in figure 6.18. Corrosion rate was taken from figures 5.12 and 5.14 for HZ and LZ, respectively. Data for non-heat-treated high HZ sample is included.

water solution for the Zn-rich layers obtained by heat treatment of AlMn alloy coated with 8 g/m^2 (high Zn load) and 2.7 g/m^2 (low Zn load) of Zn. Corrosion morphology was reported in section 6.3.1. Area of corrosion attack was roughly estimated based on the macrographs of the corroded samples. Morphology structure and porosity were based on high magnification SEM micrographs. Zn concentration of the corroded areas, $\rho_{Zn(corr)}$, was calculated based on measured E_{corr}, using the correlation between E_{corr} and $\rho_{Zn(corr)}$, as described in section 6.3.3. Average Zn concentration, $\rho_{Zn(av)}$ was estimated by correlation of reduction in thickness after immersion test and simulated GD-OES profiles, as described in section 5.2. Concentration estimated in this way is an average value for the exposed sample surface and does not take into account the local non-uniformity of corrosion, including the presence of uncorroded regions and preferential attack at the grain boundaries. E_{corr} measured on samples during immersion test, reported in section 5.3.2, is also included. Significance of E_{corr} is discussed in the next chapter.

TABLE 6.1: Comparison of corrosion morphology, attack at the grain boundaries (GB), Zn concentration of the corroded areas, $\rho_{Zn(corr)}$, average Zn concentration, $\rho_{Zn(av)}$, and corrosion potential, E_{corr}, after immersion in the test solution for different durations (t) of the Zn-rich layers obtained by heat treatment of Zn coated AlMn alloy with different Zn load (ZL).

ZL (g/m^2)	**HT**	t	**Area attacked**	**Morphology structure**	**Porosity magnitude**	**GB attack**	$\rho_{Zn(av)}$ **(g/cm^3)**	$\rho_{Zn(corr)}$ **(g/cm^3)**	E_{corr} **(V$_{SCE}$)**
8	350°C 2h	10 h	80%				0.39 ± 0.02	0.38 ± 0.05	-0.96
		18 h	80%	very fine	0.1 μm, deep	small	0.17 ± 0.02	0.22 ± 0.01	-0.94
		2 d	90%				0.08 ± 0.01	0.10 ± 0.01	-0.90
		4 d	90%	coarse	1 μm, not deep	very deep	0.055 ± 0.008	0.040 ± 0.002	-0.85
		11 d	100%	very coarse	no porosity	very deep	0.028 ± 0.004	0.012 ± 0.001	-0.78
	390°C 2h	10 h	50%				0.42 ± 0.01	0.50 ± 0.02	-0.96
		18 h	70%	very fine	0.1 μm, deep	no	0.33 ± 0.01	0.34 ± 0.02	-0.95
		2 d	80%				0.19 ± 0.02	0.18 ± 0.01	-0.93
		4 d	90%	coarse	1 μm, deep	small	0.10 ± 0.02	0.11 ± 0.01	-0.90
		11 d	100%	very coarse	no porosity	deep	0.044 ± 0.005	0.029 ± 0.001	-0.83
	430°C 4h	10 h	10%				0.20 ± 0.01	0.40 ± 0.02	-0.96
		18 h	50%	very fine	0.1 μm, deep	no	0.19 ± 0.01	0.28 ± 0.01	-0.95
		2 d	70%				0.15 ± 0.01	0.17 ± 0.01	-0.93
		4 d	80%	fine	0.5 μm, deep	small	0.10 ± 0.01	0.11 ± 0.01	-0.90
		11 d	90%	coarse	2 μm, deep	small	0.056 ± 0.004	0.056 ± 0.003	-0.87

ZL (g/m^2)	**HT**	t	**Area attacked**	**Morphology structure**	**Porosity magnitude**	**GB attack**	$\rho_{Zn(av)}$ **(g/cm^3)**	$\rho_{Zn(corr)}$ **(g/cm^3)**	E_{corr} **(V_{SCE})**
2.7	430°C 4h	3 d	70%				0.058 ± 0.001	0.066 ± 0.003	-0.88
		11 d	80%	coarse	1 μm, deep	small	0.038 ± 0.001	0.046 ± 0.002	-0.86
	510°C 4h	3 d	10%				0.029 ± 0.001	0.029 ± 0.001	-0.83
		11 d	20%	very coarse	no porosity	small	0.030 ± 0.001	0.024 ± 0.001	-0.82

$\rho_{Zn(av)}$, estimated from the weight loss measurements using GD-OES depth profiles, was higher than $\rho_{Zn(corr)}$, obtained by EDS analysis of the corroded areas, for high Zn load sample heat treated for 2 hours at 350 °C for immersion time of 4 days and longer. The reason must be Zn diffusion along the grain boundaries (figure 3.15b), which increased average concentration, measured by GD-OES. During immersion localized attack of these Zn-rich grain boundaries was observed, which resulted in overestimation of $\rho_{Zn(av)}$, while $\rho_{Zn(corr)}$ was not influenced by grain boundaries, as it was measured on the grains themselves. For shorter immersion times, the sets of data for local and average concentrations for this type of samples agree well, as well as for all immersion intervals for the high Zn load samples heat treated for 2 hours at 390 °C. The exception is immersion for 11 days, where $\rho_{Zn(av)}$ was larger than $\rho_{Zn(corr)}$. This difference originates also from the grain boundary attack, discussed above. For heat treatment for 4 hours at 430 °C, $\rho_{Zn(av)}$ for high and low Zn load was lower than $\rho_{Zn(corr)}$ during the first 2 and 3 days of immersion, respectively. The reason in this case must be localization of the attack on high Zn areas, also reported in table 6.1, which was discussed in section 6.3.2, while average concentration of the surface was smaller.

Corrosion attack spread over the sample surface slower for higher degrees of heat treatments and lower Zn concentrations. Corrosion morphology was very fine for corroded areas with high $\rho_{Zn(corr)}$, and became coarser with decreasing $\rho_{Zn(corr)}$. The same trend was observed for porosity.

6.3.6 GD-OES of corroded surfaces

Figures 6.20a-e show depth profiles for Zn, Al, O, H and Cl, respectively, for AlMn alloy coated with 8 g/m^2 of Zn and heat treated for 2 hours at 390 °C, after immersion in the test solution for 2 days. The figures include profiles of two samples subjected to different treatments after immersion in the test solution. The first sample was cleaned with distilled water and dried for 3 hours at 90 °C, while the other was subjected to the chromic-phosphoric treatment for removal of corrosion products according to the procedures described in chapter 5, in addition to rinsing and drying mentioned above.

Zn (figure 6.20a) was slightly enriched at the outermost surface, and its concentration decreased logarithmically with depth above 50 nm. During first 50 nm Zn concentration in the sample untreated by Cr-P acid was slightly higher than Zn concentration in the sample after Cr-P acid treatment. Al depth profile (figure 6.20b) showed reciprocally opposite behaviour to the Zn profile. Depletion of Al was observed up to larger depths than enrichment of Zn. The sample after Cr-P acid treatment had smaller depletion in Al than the sample without such treatment. Concentration of O, and H and Cl signals (figures 6.20c, d and e, respectively) had their maximum at the surface, decreasing to negligible bulk values with depth, as expected. The profiles of these elements were higher for the untreated surfaces as compared to their respective CrP-treated surfaces. Cl signal on the Cr-P-treated surface was nearly at the noise level.

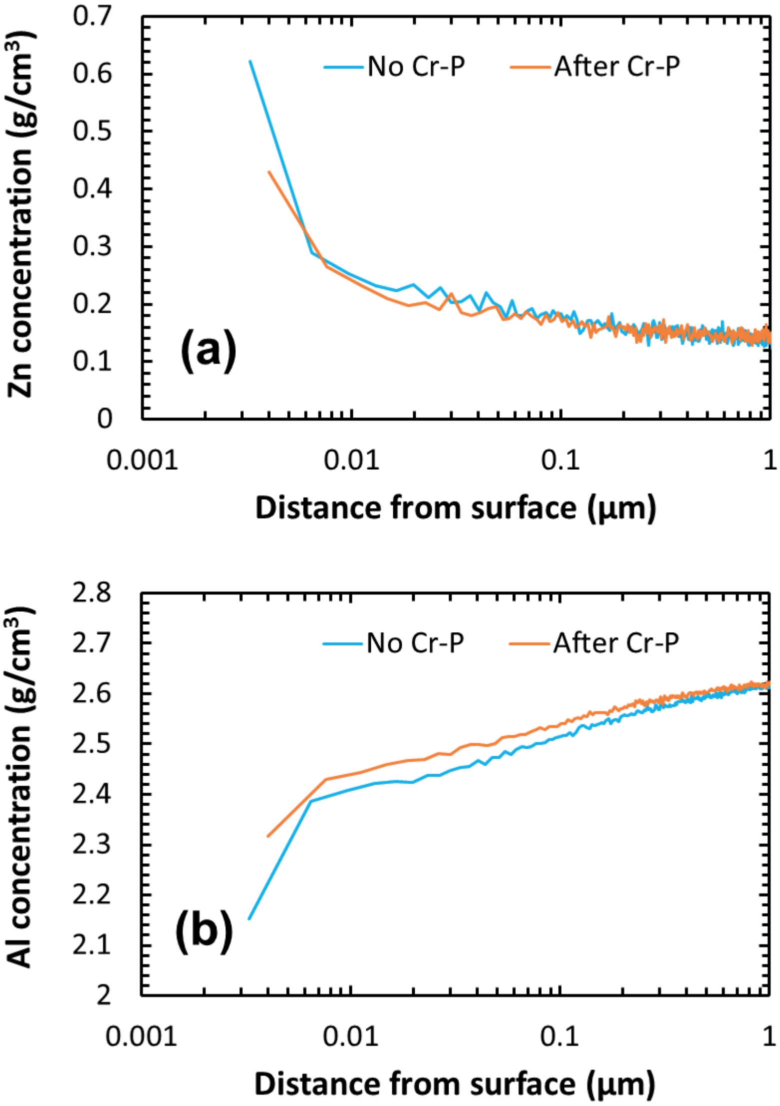

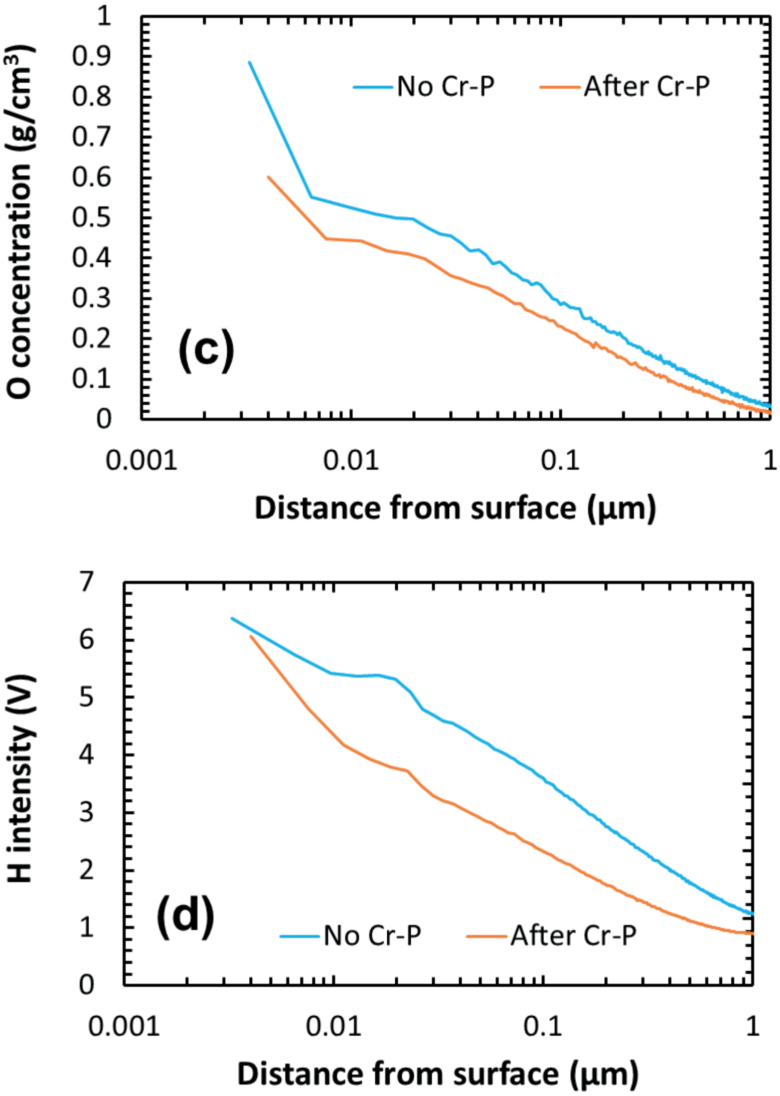
(c)
O concentration (g/cm³)
1
0.9
0.8
0.7
0.6
0.5
0.4
0.3
0.2
0.1
0
No Cr-P
After Cr-P
0.001
0.01
0.1
1
Distance from surface (µm)
(d)
H intensity (V)
7
6
5
4
3
2
1
0
No Cr-P
After Cr-P
0.001
0.01
0.1
1
Distance from surface (µm)

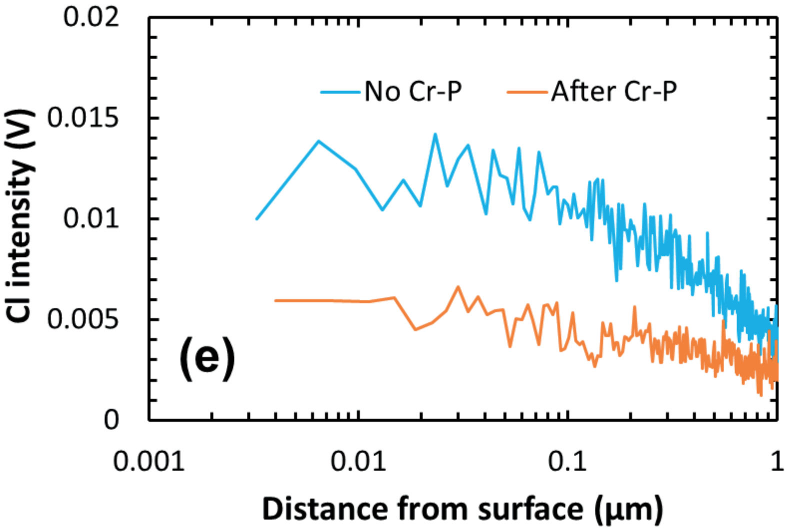

FIGURE 6.20: EGD-OES depth profiles of AlMn alloy coated with 8 g/m^2 of Zn and heat treated for 2 hours at 390 °C, after immersion in the test solution for 2 days: a) Zn, b) Al, c) O, d) H, e) Cl.

GD-OES profiles shown in figure 6.20 suggest that corrosion products in the form of Zn and Al oxides, hydroxides and chlorides were present on the surface of the corroded samples. Part of the corrosion products seem to be removed by the Cr-P acid treatment. No evidence for enrichment and depletion of either Al or Zn was observed.

6.4 Discussion

Lateral and in-depth non-uniformity of Zn-rich layers on AlMn alloy MPE tube samples obtained by heat treatment of Zn thermal-arc sprayed coating resulted in significant non-uniformity of corrosion. Zn concentration of the corroded regions, $\rho_{Zn(corr)}$, did not vary notably on a given sample (figure 6.15a). On the contrary, Zn concentration of the uncorroded regions, $\rho_{Zn(uncorr)}$, varied considerably, as shown in figure 6.16. The SEM and EDS analysis of corroded surfaces confirmed the assumption made in chapter 5 that corrosion attack was localized at regions with higher Zn concentration, ρ_{Zn}. As was discussed in chapter 5, non-uniformity of potential distribution is impossible in the present work due to high conductivity of both solution and sample. Corrosion potential, E_{corr}, appeared to be determined by $\rho_{Zn(corr)}$, which was roughly the same at all corroding locations, where it was measured on a given sample. The uncorroding areas with large differences in the measured $\rho_{Zn(uncorr)}$ were probably passive and did not contribute significantly to the oxidation and reduction processes on the surface. With increasing time of immersion and propagation of corrosion attack, $\rho_{Zn(corr)}$ decreased and corrosion attack spread over a larger surface area with similar ρ_{Zn}, as shown by the present results. The assumption that $\rho_{Zn(corr)}$ was roughly the same at all corroding locations is supported by low standard deviation of the correlation between $\rho_{Zn(corr)}$ and E_{corr}, shown in section 6.3.3. In view of the forgoing, the correlations in the literature between the concentration of a critical alloying element (Zn in the present case) and the corrosion potential should therefore be viewed with care.

Since E_{corr} is a mixed potential, the types of reduction reaction and their rates have to be taken into consideration along with the oxidation processes in order to understand its significance. It was shown in section 5.3.1, that hydrogen evolution is the dominating reduction reaction, which can occur on the locally corroding sites as well as on the noble intermetallic particles. There is a reason to believe that hydrogen evolution, which is activation controlled, will dominate over the diffusion controlled oxygen reduction on microscopic sites [12]. This will further be enhanced by MgO (and/or $Mg(OH)_2$) deposition on these sites [13]. If the oxidation reaction is further controlled by a pitting-type of mechanism, then E_{corr} will be equal to the pitting potential independent of the type and rate of the reduction process, as in section 5.3.1. For such cases, it is possible to postulate that E_{corr} is a function of $\rho_{Zn(corr)}$ at the surface, which can be quite different from ρ_{Zn} in the bulk. Despite other complications to be discussed, this work showed that a certain empirical correlation between the corrosion rate and $\rho_{Zn(corr)}$ (figure 6.19) is viable for AlZn alloys.

A complicating factor in the measurement of $\rho_{Zn(corr)}$ is the need to determine the surface concentration of metallic Zn. It has to be analytically distinguished from its oxide. Determination of the surface concentration of metallic Zn on a localized corroded area is not an easy task. Poor depth resolution of the EDS method used in this chapter, selected in consideration of its advantage over GD-OES in lateral resolution, can also be questioned. Neither of these methods can determine the oxidation state of Zn. Use of other advanced characterization techniques, such as Auger electron spectroscopy or X-ray photoelectron spectroscopy (XPS), was not possible due to the roughness and porosity of the corroded surfaces and due to poor lateral resolution in the case of XPS.

An important factor determining the surface concentrations of Zn and Al, which in turn determine the electrochemical and corrosion behaviour, is dealloying. The difficulty in determining the surface concentration of these elements at the localized corrosion sites has impeded a detailed investigation of the role of dealloying in the present work. The literature study (section 6.1) suggested that nanoporosity of the corroded surface can possibly be used as an indirect indication of dealloying. Corrosion morphology of Zn-rich layers with relatively high $\rho_{Zn(corr)}$ ($\geq$ 10 wt%) is significantly porous. Corrosion morphology in figures 6.7a and 6.8 resembles results of dealloying of Zn from AlZn alloys at an applied potential shown in reference [8].

However, the same study was restricted to ρ_{Zn} > 30 wt%, while ρ_{Zn} of the corroded regions investigated in this work was < 12 wt%. GD-OES profiles of Zn and Al in figure 6.20 a and b, respectively, on corroded surfaces did not indicate enrichment of either Al or Zn. Therefore, no definite conclusions about dealloying can be drawn from the results reported in this work.

Concentration maxima for Fe and Mn near the surface, which were appreciably higher than the respective bulk and surface concentrations, observed after immersion for 10 hours of the samples heat treated for 2 hours at 390 °C and 4 hours at 430 °C, can be attributed to enrichment of intermetallic particles near the surface. Particles of type Al(Fe,Mn)Si precipitated close to the surface due to heat treatment of the AlMn alloy MPE tube, which was originally contaminated with Fe from the extrusion dye, as was discussed in section 3.4.2. Such enrichment was presumably also due to exposure of the intermetallic particles by preferential corrosion of the solid-solution alloy around the particles, which acted as the local cathodes. High density of intermetallic particles could lead to high corrosion rate for higher level heat treatments, as reported in chapter 5, figure 5.12. Corrosion rate was highest for the samples with highest heat treatment, which had the lowest surface ρ_{Zn} (figure 5.12), as well as the highest surface enrichment of intermetallic particles.

SEM of uncoated AlMn alloy MPE tube sample after 11 days of immersion in acidified artificial sea water solution showed slight crystallographic etching of the surface with micropits and no macropits were found. Nevertheless, corrosion of AlMn alloy is of pitting type, as was discussed in chapter 5 based on potentiodynamic polarisation curve in figure 5.5. Pourbaix diagram for a commercial Al alloy in chloride solution [14] shows that both pitting and general attack can occur at pH = 3. No micro- or macropits were found on Zn coated and heat treated samples, although the attack observed on a macroscopic scale is highly localized, which can be interpreted as pits. However, these localized attacks, which are nearly two-dimensional pits, propagate laterally following the Zn-rich layer, as documented by several macro-images in section 6.3.1. They spread over most of the surface within a few days of exposure to the test solution, producing as a result superficial etching-type of morphology. Based on the potentiodynamic polarization data in figure 5.5, corrosion of Zn-rich layers also appear to suggest characteristic pitting type of mechanism. The spread of corrosion attack laterally instead of deeper pitting can also suggest that Zn concentration gradient is restricting corrosion to propagate deeper instead of two-dimensional attack. Due to non-uniformity of the Zn-rich layer and influence of Fe-rich intermetallic particles on corrosion rate, discussed in section 5.3.3, influence of Zn concentration gradient on corrosion rate could not be estimated.

Immersion of untreated Zn thermal-arc sprayed coating in acidified chloride solution lead to undermining of the coating due to poor adhesion and non-uniformity of the Zn coating, which was observed in figure 3.15a. Therefore, this confirms the conclusion made in chapter 5, that the untreated Zn coating produced by themal-arc spraying cannot provide sufficiently long protection of the substrate against pitting. Certain heat treatment is necessary to obtain a Zn-rich layer (a solid-solution alloy) or minimal metallurgical bonding by diffusion of the Zn into the substrate. Minimal heat treatment required to achieve this, which was outside the present scope, is worth investigating in future work.

Lateral non-uniformity of corrosion due to non-uniformity of the Zn-rich coating makes it challenging to find optimal coating properties for minimizing the self-corrosion rate of the coating, while preventing the pitting of the AlMn substrate. Despite the non-uniformities, we showed in chapter 4 that a fairly reliable theoretical method can be developed for estimating the Zn concentration profiles as a function of depth. In the previous and present chapters, we investigated whether the surface concentration of Zn could be correlated with the corrosion rate of the Zn-rich coating. With appreciable scatter limits, this appeared to be possible if the correlation was based on the concentration of the locally corroding sites on a sample. The present approach assumes that the entire exposed specimen area corrodes uniformly, which is far from reality for short immersion times. This assumption is the largest source of error on the scatter limits in the correlation discussed, especially for higher heat treatments and small immersion times, as discussed in section 6.3.5. At large times of exposure, the decreasing self-corrosion rate is expected to become more uniform as the decreasing Zn concentration becomes increasingly more uniform with depth, as shown in figure 6.9. With increasing immersion time, $\rho_{Zn(corr)}$ approached the average Zn concentration estimated based on weight loss measurements, as was reported in table 6.1.

Combination of the prediction of depth profiles for Zn, described in chapter 4, with the correlation of corrosion rate with $\rho_{Zn(corr)}$, as shown in figure 6.19, can allow prediction of corrosion rate for any Zn concentration profile in the present test environment. Similar correlations will have to be developed for corrosion in different environments. Measurement of the corrosion potential, if possible during corrosion test, should also indicate the Zn concentration of the corroding sites. Optimal Zn load and heat treatment conditions can be selected based on these considerations. However, the scatter in the data in figure 6.19 suggests that such calculations will at best be limited to rough estimates. Further validation of the suggested methodology and investigation of the restrictions imposed by the empiricism involved were unfortunately outside the present scope.

For the present corrosion data in acidified artificial sea water at 25 °C, the minimum ρ_{Zn} required for protection of the substrate against pitting, considering a maximum potential limit of -0.85 V_{SCE}, was estimated as 0.04 g/cm^3 from the correlation of corrosion potential and $\rho_{Zn(corr)}$ in figure 6.18. Optimal Zn depth profile should give the lowest ρ_{Zn} , while at the same time ρ_{Zn} should be maintained above 0.04 g/cm^3 as long as possible. Among the Zn-rich layers studied in this work and simulated Zn depth profiles shown in section 4.5, the optimal depth profile appears by inspection to correspond to the Zn coating with 3.5 g/m^2 load, heat treated for 3 or 4 hours at 470 °C.

For these cases, ρ_{Zn} at the surface is 0.07 and 0.06 g/cm^3, decreasing to 0.04 g/cm^3 at depths 47.5 and 47 µm, respectively. The corresponding corrosion rates at the surface are 1.9 ± 0.5 and 1.6 ± 0.4 µm/day, respectively, according to the correlation in figure 6.19. As expected, corrosion rates for the two heat treatments are quite similar. Shorter heat treatment time should be chosen as it is more beneficial from technological point of view and would lead to smaller precipitation of the Fe-rich intermetallic particles during heat treatment, attributed to contamination from the extrusion die, as discussed in section 5.3.3. If, on the other hand, maintaining the corrosion potential below the critical pitting potential of Al alloy is sufficient for protection against pitting, then high Zn load sample heat treated for 2 hours at 350 °C would be optimal, as discussed in section 5.4.

As a final note, it is interesting to mention, that the corrosion rate corresponding to the minimum Zn concentration (0.04 g/cm^3) required for the Zn-rich layer to maintain the corrosion potential above -0.85 V_{SCE} for protection of the AlMn alloy against pitting, is 5 times larger than the self-corrosion rate of the AlMn substrate in the environment of interest. Such result does not make sense for cathodic protection, but it is possible if one accepts the fact that the protection method in question is in principle anodic protection. Nevertheless, the example suggests that the use of pure Zn coating for the protection of an Al alloy is not the best choice. Alloying the AlMn substrate with 1.5% Zn may be considered a more practical solution, but this would increase the self-corrosion of the entire thickness of the heat-exchanger tube wall by a factor of 5. Seeking coatings of metallic alloys of type AlZnIn, with much lower self-corrosion than pure Zn may be a better choice.

6.5 Conclusions

- The lateral non-uniformity of Zn depth profile in the Zn-rich layer causes non-uniform self-corrosion. This restricts the development of models to predict corrosion rate as a function of Zn depth profile and thereby optimize the effective lifetime of Zn-rich layers in protection against pitting.
- The relationship between the corrosion potential of AlZn alloys and surface concentration of Zn, ρ_{Zn}, was verified and extended over a wide concentration range. In localized corrosion, the corrosion potential is controlled by the electrochemical processes at the active sites and ρ_{Zn} at these sites, which may be quite different from the bulk concentration.
- Relationship between the corrosion rate of Zn-rich layers in chloride solution and ρ_{Zn} was established within the restrictions specified above. Combined with the previous conclusion, correlation between the corrosion potential and corrosion rate may be possible.

- ρ_{Zn} as low as 0.04 g/cm^3 (1.5 wt% Zn) in Al appears to be the minimum value sufficient to protect the alloy against pitting by maintaining the corrosion potential below -0.85 V_{SCE} at room temperature in chloride solution. Corrosion rate at this concentration was estimated to be 5 times higher than the corrosion rate of the AlMn alloy itself.
- The following conditions for production of optimal Zn-rich layer were suggested for protection against pitting by maintaining the corrosion potential below -0.85 V_{SCE} in the specified environment: Zn load of 3.5 g/m^2, heat treatment for 3 hours at 470 °C.

References

1. H. W. Pickering, *Corrosion Science*, **23**, 1107–1120 (1983).
2. J. Erlebacher, M. J. Aziz, A. Karma, N. Dimitrov, K. Sieradzki, *Nature*, **410**, 450–453 (2001).
3. J. Erlebacher, K. Sieradzki, *Scripta Materialia*, **49**, 991–996 (2003).
4. J. Erlebacher, *Journal of the Electrochemical Society*, **151**, C614–C626 (2004).
5. H. N. McMurray, *Corrosion*, **57**, 313–322 (2001).
6. X. Zhang, T. N. Vu, P. Volovitch, C. Leygraf, K. Ogle, I. O. Wallinder, *Applied Surface Science*, **258**, 4351–4359 (2012).
7. T. N. Vu, P. Volovitch, K. Ogle, *Corrosion Science*, **67**, 42–49 (2013).
8. O. M. Suarez, E. G. Estremera, R. Soler, A. Declet, A. J. Hernandez-Maldonado, *Advances in Materials Science and Engineering*, **2014**, Article ID 963042, 6 pages (2014).
9. H. Ikeda, *Aluminium*, **58**, 467–471 (1982).
10. J. T. Reding, J. J. Newport, *Materials Protection*, **5**, 15–18 (1966).
11. F. Sato, R. C. Newman, *Corrosion*, **55**, 3–9 (1999).
12. R. Gundersen, K. Nisancioglu, *Corrosion*, **46**, 279–285 (1990).
13. S. H. Salleh, S. Thomas, J. A. Yuwono, K. Venkatesan, N. Birbilis, *Electrochimica Acta*, **161**, 144–152 (2015).
14. P. Gimenez, J. J. Rameau, M. C. Reboul, *Corrosion*, **37**, 673–682 (1981).

Chapter 7

Discussion

This chapter aims to summarize the important results of the thesis, discuss their overall significance in improving the understanding of the relevant phenomena, their possible practical significance, the extent to which the objectives (chapters 1 and 2) have been satisfied, and propose further work for further improvement of the experimental approach and understanding of the mechanisms.

7.1 Anodic protection of Al by Zn

The results verify and support some of the earlier work that about 1 wt% of Zn in solid solution or as an alloying element is sufficient to protect the metal against pitting in chloride solution at the expense of a significant increase in the self-corrosion of the layer or alloy. The increase in self-corrosion for such low level of Zn was estimated to be about a factor of 5. The obvious question to raise is the need to deposit a significant amount of Zn (8 g/m^2). It is of course based on current industrial practice (chapters 1 and 2) and the cost and convenience of using thermal spray (although a significant amount of Zn is wasted), in relation, e.g., to the zincating process, in view of the fact that conventional galvanizing (as for steel) does not work for aluminium (chapter 1).

Clearly, possible methods for lowering the Zn level used should be investigated for conserving the Zn metal. Alloying the entire component with Zn is not desirable since the component becomes susceptible to high rate of self-corrosion instead of limiting this process to an essentially sacrificial surface layer. The aqueous zincating processes should certainly be investigated. Electrolytic deposition is an option for better control of the amount of Zn deposited. Other possibilities, such as using alternatives to pure Zn as the coating material will further be discussed later in this chapter.

The mechanism of high self-corrosion imparted by Zn is not clarified despite the long practical experience with Zn as a common alloying element for certain classes of Al alloys. As discussed in chapter 2, the hydrogen overpotential of Zn metal in aqueous solution is high (the rate of hydrogen evolution is low) in relation to comparable elements, such as Al and Mg [1].

This is an important factor in depressing the corrosion potential of Zn in the negative direction. It appears that the presence of Zn in solid solution with Al, even at small concentrations, also imparts a significant depression of the corrosion potential. The mechanistic cause of this is not clear in the available literature other than the higher electrochemical activity of Zn as an empirical fact. Based on the difference in the corrosion potential, Zn is expected to be more active than aluminium under the conditions of present interest. Therefore, selective corrosion of Zn would be expected for the Zn-rich layer in aqueous chloride media, causing enrichment of the Al component. As a result, the surface would be expected to passivate faster than that normally observed in contrast to the present results and literature data for AlZn alloys (section 2.3).

Detailed study of this phenomenon has not been within the scope of the present thesis. However, this chapter allows further speculation of possible causes. Based on the results and discussion in chapter 6, selective dissolution of Zn does not seem to occur on Zn-rich Al if the Zn concentration is less than 30 wt%, which is supposed to lie around the parting limit for dealloying of Zn on AlZn alloys. The present study showed that the amount of Zn remaining in the Zn-rich layer, after the pure Zn areas corrode away, is smaller than this limit for most cases. Since the Zn level does not become reduced by dealloying, the presence of Zn on the surface down to 1 wt% appears to have a significant effect on the surface properties on the Zn-rich layer, such as passivity, self-corrosion, cathodic behaviour and corrosion potential.

High self-corrosion due to Zn is synonymous with poor passivity of the Zn containing Al-alloy surface. It is a chemical process controlled by the dissolution of the passivating oxide [2]. Therefore, self-corrosion cannot be controlled by electrochemical means. If its rate is as high as the case for Zn, it may become as important as pitting, *i.e.*, protection provided for pitting, which is an electrochemical process, may not be sufficient if self-corrosion leads to significant thinning. Therefore, successful protection against pitting at the expense of significant self-corrosion of a Zn-rich layer may not be acceptable. The Zn-rich layer will ultimately become consumed, probably locally. Remnants of the Zn-rich layer will probably continue to protect the areas, where the aluminium alloy substrate is exposed, against pitting. At these areas, self-corrosion will be decreased significantly because of superior passivity of the exposed Zn-free Al alloy. In this regard, the present practice of Zn-rich coatings, based on thermal spray of Zn followed with heat treatment can be regarded as an effective protection method against pitting for thin-walled AlMn heat exchangers. However, the ability of these layers to provide sufficiently long service life has to be investigated further.

Insofar as design criteria are concerned, reduction of Al potential below its repassivation potential, E_{rp} = -0.85 V_{SCE}, below which the existing pits cannot propagate, has been considered as the condition for protection of Al against pitting in this work, based on the references [3, 4]. However, this condition may be too conservative, if pits do not initiate as long as the potential does not exceed the critical pit initiation potential E_c, such that maintaining the potential below E_c ccan be regarded as sufficient for the present purpose [5]. The present work could not clarify which of the potential requirements is more relevant since no pitting was observed on any of the specimens investigated in the immersion tests used in acidified artificial sea water solution. Uncoated AlMn alloy showed slight non-uniform etching with crystallographic micropits. However, unpolarizability of the surface above the critical potential indicated pitting-type of kinetics for both AlMn alloy and Zn-rich layers 5.3.1 as was observed also for binary AlZn alloys in neutral chloride solution in earlier work [1].Acidified chloride solution and immersion conditions resulted in the formation of large amount of small pits, which gave the appearance of uniform etching, rather than formation of easily visible deep pits [6].

In the development of aluminium heat exchangers in practice, the sea water acidified accelerated test (SWAAT) (ASTM G85), is often used for quality control for the corrosion resistance of the materials used. During this test the samples are subjected to consecutive cycles of spray with acidified artificial sea water for 30 minutes and soaking in 98% humidity for 90 minutes. While the spray solution in this test is the same as was in the immersion test used in this work, the test temperature (49 °C) is significantly higher than the present 25 °C. Correlation of the results between these two tests would be difficult since temperature is an important parameter determining the properties of the materials used. Aluminium becomes more active with increasing temperature [7], while corrosion potential of Zn is almost independent of temperature [8]. However, the corrosion rate of Zn is believed to decrease with increasing temperature due to accumulation of corrosion products on the surface [9]. Continuous immersion testing according to the same procedure, as in this work, but at 49 °C, would possibly be able to help to correlate the results of this work with the corrosion test performed in practice and give a better perspective on the behaviour of the materials in real life applications, although the validity of SWAAT for the present purpose can also be questioned. The suggestion is, therefore, purely empirical for practical application because of the following.

In reference [10], as sprayed Zn coating on AlMn substrate formed pits deeper than 200 μm after two weeks of exposure in SWAAT, while no deep pits were observed on the Zn-rich layers obtained by heat treatment of this coating, *i.e.*, qualitatively similar to the present results. Immersion testing gave higher corrosion rates, i.e., more accelerated than the SWAAT, despite the lower temperature.

7.2 Characterisation of Zn-rich layers on Al

Data base and methodology needed for calibration for the use of elemental depth profiling of Zn-rich layers on Al alloys by glow discharge optical emission spectroscopy (GD-OES) was developed in chapter 3. Calibration of Al and Zn, as well as secondary alloying elements and oxygen, allowed concentration profiling of Zn coating and Zn-rich layers obtained by heat treatment of the coating on AlMn alloys with high depth resolution. The method was validated by showing that the bulk compositions of the alloying and trace elements in the AlMn samples measured by GD-OES agreed well with the values determined by other techniques, such as spark optical emission spectroscopy and X-ray energy dispersive spectroscopy (EDS). The coating load specified for the coated multi-port extruded (MPE) specimens was verified from the measured depth profiles for Zn. Enrichment of Si and Mn close to the surface due to inward diffusion of Zn into the AlMn tube was detected. Enrichment of Fe close to the surface on the uncoated and non-heat treated AlMn MPE tube was attributed to the contamination by the extrusion die. Precipitation of AlMnFeSi intermetallic particles during heat treatment and possible depletion of the surrounding matrix with the Mn and Si resulted in increase of area of cathodic sites, which lead to activation of the AlZn matrix, as will be discussed in the following sections. These findings must have practical significance in the production and thermomechanical processing of the heat-exchanger tubes.

Scanning electron microscopy (SEM) characterisation of the as sprayed and as heat treated coatings revealed their non-uniformity both laterally and in depth, which could not be detected by GD-OES, since it characterised 4-mm diameter areas and did not have the necessary lateral resolution. EDS analysis allowed much better lateral resolution in the detection of high Zn and low Zn areas, as well as Zn-free areas. Such non-uniformity introduced a certain averaging error in the concentration profiles obtained by GD-OES. However, EDS lacked the depth resolution necessary for surface characterisation of these areas. Nevertheless, combination of GD-OES profiling and EDS analysis is believed to complement one another in providing sufficiently complete characterisation of Zn-rich layers for present purposes. More information about the differences in the oxide thickness and composition, and enrichment of the alloying elements on these areas can be obtained by advanced surface characterisation techniques, such as Auger and X-ray photoelectron spectroscopy, although the surface roughness could make it a challenging task. Such study was outside the scope of this thesis.

7.3 Modelling of corrosion of Zn-rich layers

A methodology for prediction of Zn concentration profiles of Zn-rich layers on commercial Al alloys, obtained by heat treatment, using a solution of Fick's second law for binary diffusion from a coating into a semi-infinite region, with certain simplifications for the initial condition in the formulation, was developed in chapter 4. The lateral non-uniformity of the Zn concentration was successfully incorporated into an effective diffusion coefficient, as it is common, e.g., in modelling diffusion of reactants and products in the pores of a catalyst in chemical reaction engineering [11]. This methodology can be used for selection of the Zn coating load and heat treatment parameters necessary to obtain desired Zn concentration profiles. The effective diffusion coefficients calculated from the GD-OES depth profiles of samples subjected to different heat treatments obeyed the Arrhenius law for the temperature dependence. As a result, the lateral average of the depth profiles for Zn could be satisfactorily predicted for the present specimens and heat-treatment conditions, which was a promising conclusion for predicting these profiles without laborious experimental determination for the present specimens and heat treatment conditions. The same approach can be used for predicting the Zn-depth profiles for any other type of samples, for which a temperature correlation of the effective diffusion coefficient for Zn can be obtained.

Due to non-uniformity of the Zn-rich layers, obtained by heat treatment of thermal-arc sprayed coatings, laterally and in depth, corrosion was localized at regions with higher Zn concentration, ρ_{Zn}, which was roughly the same on all corroded regions on the same sample. Regions with lower ρ_{Zn} remained passive until ρ_{Zn} of the corroded regions decreased with increasing reduction in thickness to the lower ρ_{Zn} level, and the attack spread to a wider area with similar ρ_{Zn}. It was shown that the corrosion potential was determined by the ρ_{Zn} of the corroding areas (chapter 6). ρ_{Zn} of the corroding areas approached average ρ_{Zn} on the surface with increasing immersion time, as corrosion spread over the surface and became more uniform.

The well known relationship between the corrosion potential of AlZn alloys in chloride solution and ρ_{Zn}, which is normally based on the ρ_{Zn} of the bulk alloy composition (figure 2.2) was improved and extended over a wider concentration range by using the EDS data for the Zn concentration on the localized corroding areas instead of the bulk Zn concentration. Based on this correlation the measured corrosion potential can be correlated with the ρ_{Zn} of the corroding sites. Similarly, the minimum ρ_{Zn} required for maintaining the corrosion potential of Al at a certain critical level, can be estimated. If, for example, the repassivation potential of Al alloys is used, the relationship gives ρ_{Zn} of 0.040 ± 0.002 g/cm^2 (1.5 wt%).

Moreover, in chapter 6, corrosion rate calculated based on weight loss measurements, was correlated with ρ_{Zn} of the attacked regions. The obtained relationship can give a rough estimate of the corrosion rate of the Zn-rich layer based on its concentration profile. The approach used for calculation of the corrosion rate assumed that the corrosion was uniform, which is far from reality and an important source of error. Such error is common in the use of electrochemical measurement and quantification of localized corrosion.

Based on the modelling procedure for simulation of Zn diffusion in Al alloys substrate and the relationship obtained for corrosion rate vs. ρ_{Zn}, an empirical methodology for modelling of corrosion of Zn-rich layers in acidified artificial sea water is developed. The procedure is the following:

1. Zn concentration profile can be calculated, as was described in chapter 4, based on the Zn coating parameters (Zn load, coating thickness, Zn concentration in the coating) and heat treatment conditions (temperature and time).
2. Corrosion rate can be estimated for a given Zn concentration in the profile using the correlation shown in chapter 6 (figure 6.19).
3. Reduction in thickness during a certain (small) period of immersion time can be calculated based on the corrosion rate.
4. Zn concentration of the corroded surface after that period of immersion can be estimated using the Zn concentration profile calculated in step 1 and calculated reduction in thickness from step 3, as was described in section 5.2.
5. Points (1)-(4) can then be repeated to obtain the reduction in thickness and corrosion rate as a function of immersion time in the test solution.

Corrosion rate of the Zn-rich layer during immersion in acidified artificial sea water solution can also be estimated from its corrosion potential, which can be measured easily during the immersion test. The procedure is to estimate first ρ_{Zn} by using the relationship between the corrosion potential and Zn concentration shown in chapter 6 (figure 6.18). Corrosion rate can then be estimated based on ρ_{Zn} using the correlation in figure 6.19.

The methodology developed can be used for optimisation of the Zn concentration profile and thickness of the Zn-rich layer. Given a maximum allowable corrosion depth during immersion, an optimal Zn concentration profile can be selected using the procedure described above. The expected variation in the corrosion potential can then be estimated from figure 6.18, to determine the immersion time or extent of corrosion required before exceeding a critical protection potential for the alloy.

Due to non-uniformity of the Zn-rich layers causing non-uniform distribution of corrosion at the surface and other possible complicating factors, such as the contamination of the surface with Fe by the extrusion die, only rough estimates of the corrosion rate can be made. Zn thermal-arc sprayed coating, although useful for many practical applications, appeared not to be well suited as a model system to study the influence of Zn on corrosion of Zn-rich layers obtained by heat treatment of the coating.

7.4 Improvement of protection of Al alloys

The results presented throughout this work show that Al alloys can be protected against pitting by alloying with Zn. The properties of the Zn-rich layer can be modified to a certain degree by using the procedure described in the previous section for improved corrosion protection and extended service life. The effect of Zn gradient in the Zn-rich layer, which was suggested to be beneficial for protection against pitting [12], could not be verified in the present work due high scatter of corrosion rate originating from non-uniformity of the layers.

An important, frequently mentioned challenge is that self-corrosion of the Zn-rich layers is too high. While the layer may be successful in preventing pitting corrosion, it introduces the challenge of self-corrosion. Self-corrosion occurs non-uniformly because of the non-uniformity of the Zn coating and may become a challenge comparable to pitting in causing local thinning of already thin heat-exchanger walls, leading to failure. A coating material with lower self-corrosion rate may be a better choice. The use of AlZnIn coatings can be suggested by analogy to the sacrificial anodes used for the protection of offshore steel structures. Zn anodes were used earlier for this purpose. These were replaced with the AlZnIn anodes later for weight reduction and better current efficiency due to much smaller self-corrosion [13, 14]. Zn anodes were found to passivate and cause polarity reversal between Zn and steel at certain conditions, such as temperature higher than 65 °C [15]. The passivation was suggested to be promoted by formation of Zn carbonates. If such polarity reversal occurs on AlZn alloys, the Al substrate will no more be protected against pitting. In case of sacrificial anodes, this problem was solved by the introduction of indium as an activator [14]. Similar solution can be suggested for heat exchange applications. However, spraying of an AlZn(In) coating on an Al alloy may pose a new challenge if the temperature needed for thermal spraying has to be increased.

Another way of improvement can be application of a more uniform AlZn coating with low Zn concentration, for example, 2 wt%, and using a low level of heat treatment, sufficient for creation of Zn gradient, and, at the same time, maintaining Zn concentration at the level necessary for protection of Al against pitting [12]. In this case, corrosion rate of the Zn-rich layer will be minimized and non-uniformity of the attack will be reduced. Such coatings can be developed by using electroplating or metal cladding. Hot dip galvanizing in AlZn alloy melt with low Zn content is another possibility to investigate.

7.5 Suggestions for future work

The results of this work are believed to shed light on mechanism of corrosion protection of Al alloy substrate by Zn-rich layers and its optimisation. However, further work is required in order to achieve deeper understanding of these effects and their practical significance. The suggestions for future work are the following:

- ***Electrochemical characterisation and corrosion testing of AlZn alloys.***

  Potentiodynamic polarisation measurements and corrosion behaviour of model AlZn alloys with low Zn concentrations (0.5 - 10 wt% Zn) can improve understanding of mechanism of Al activation by Zn further. Comparison of the results with the behaviour of the Zn-rich layers with the same Zn concentration can give insight to the effect of Zn concentration gradient on the corrosion properties of the Zn-rich layers [12]. This type of investigation was not possible in the present work due to non-uniformity of corrosion, which introduced a high scatter to calculated corrosion rate. Testing of commercial alloys with varying Zn content can help to evaluate influence of the minor alloying elements on the corrosion properties. Another possibility to obtain better understanding of the processes in the Zn-rich layer is to perform linear polarisation measurements to obtain instantaneous corrosion rate during immersion test of these layers at exposure times corresponding to sufficiently uniform corrosion.

- ***Measurement of non-uniformity of corrosion.***

  An attempt to correlate non-uniformity of the Zn-rich layers with non-uniformity of corrosion can be made. Estimation of non-uniformity of corrosion can help to obtain better correlation between corrosion rate and Zn concentration. Propagation of corrosion can be filmed in situ during immersion test. Ex situ interferometry can provide information about roughness of corroded samples and be correlated with concentration maps, obtained by EDS.

- ***Testing at 49 °C.***

  In order to try to correlate results of this work with the SWAAT test, electrochemical and corrosion experiments at 49 °C are required. Potentiodynamic polarisation and immersion testing of bare Al alloys, pure Zn and Zn-rich layers at 49 °C will give insight into changes of their behaviour due to temperature increase and provide information necessary for such correlation. Alternatively, SWAAT test, modified to allow measurement of corrosion potential can be done.

- ***Testing in NaCl solution.***

  In order to study the effect of corrosion products and calcareous deposits formed in sea water on corrosion rate and passivation of Zn-rich layers on Al, testing in other solutions, such as NaCl, has to be performed.

- ***Zn coating improvement.***

  A more uniform coating produced for laboratory experiments will allow to exclude errors originating from the change in the attacked area during immersion tests and, subsequently, give a more reliable correlation between corrosion rate and Zn concentration. Modelling of corrosion of Zn-rich layers obtained by heat treatment of a more uniform coating using the methodology described in section 7.3 will be more reliable. Deposition of such coating can be done by electroplating on a laboratory scale. The coating can then be applied on an alloy sample free of contamination with Fe. In this way influence of Fe-rich intermetallic particles on the corrosion rate of Zn-rich layers can also be investigated.

- ***AlZnIn spray coating.***

  Minimization of self-corrosion rate of Zn-rich layers on Al alloy can probably be achieved by using other types of metallic coatings, such as AlZnIn. Electrochemical and corrosion testing of such coatings and effect of heat treatment on these has to be studied.

References

1. I. L. Muller, J. R. Galvele, *Corrosion Science*, **17**, 995–1007 (1977).
2. D. D. Macdonald, *Electrochimica Acta*, **56**, 1761–1772, sp. Iss. SI 729lp Times Cited:148 Cited References Count:74 (2011).
3. K. Nisancioglu, H. Holtan, *Corrosion Science*, **18**, 1011–1023 (1978).
4. K. Nisancioglu, Corrosion and protection of aluminium alloys in seawater, in D. Féron, Corrosion Behaviour and Protection of Copper and Aluminium Alloys in Seawater, pp. 145–155, Woodhead Publishing Limited, Cambridge, England (2007).
5. K. Nisancioglu, H. Holtan, *Corrosion Science*, **18**, 835–849 (1978).
6. O. Lunder, K. Nisancioglu, Electrochemical and Surface-Structural Aspects of the Corrosion of AlMn Alloys, pp. 706–709, Aluminium–Verlag, Düsseldorf (1988).
7. B. N. Stirrup, N. A. Hampson, I. S. Midgley, *Journal of Applied Electrochemistry*, **5**, 229–235 (1975).
8. X. G. Zhang, Corrosion and electrochemistry of zinc, pp. 140–141, Plenum Press, New York (1996).
9. E. D. Mor, A. M. Beccaria, *Corrosion*, **31**, 275–279 (1975).
10. O. Lunder, J. Nordlien, J. Lein, Proceedings of the 230th Meeting of the Electrochemical Society, 2016, Honolulu, USA, p. 1354 (2016).
11. R. B. Bird, W. E. Stewart, E. N. Lightfoot, Transport phenomena, J. Wiley, New York, 2nd ed. (2002).
12. H. Ikeda, *Aluminium*, **58**, 467–471 (1982).
13. S. L. Wolfson, *Materials Performance*, **33**, 22–28 (1994).
14. A. G. Munoz, S. B. Saidman, J. B. Bessone, *Corrosion Science*, **44**, 2171–2182 (2002).
15. G. K. Glass, V. Ashworth, *Corrosion Science*, **25**, 971–983 (1985).

Chapter 8

Conclusions

- Zn-rich layers, formed by thermal-arc spraying and subsequent heat treatment for diffusing Zn into the surface of AlMn alloy multi-port extruded tubes in a controlled manner, provide protection of Al against pitting by maintaining the corrosion potential below the pitting potential, at the expense of increased self-corrosion. Poor passivity of the Zn containing Al alloy surface can lead to general corrosion, which may become more important than pitting in acidified synthetic sea water.
- Zn-rich layers formed with Zn load smaller than possible by Zn thermal-arc spraying (5-8 g/m^2) and heat treated at high levels, such as 4 hours at 430 °C, which lead to small Zn concentrations in the layer, can maintain the corrosion potential of Al below its repassivation potential against pitting, -0.85 V_{SCE}, longer than the test duration (11 days) used in continuous immersion in acidified sea water of pH 3. At Zn concentration of 1.5 wt%, which is sufficient to reduce Al potential to -0.85 V_{SCE}, self-corrosion rate of the layer is 5 times larger than the corrosion rate of the uncoated AlMn alloy itself.
- Use of more positive potentials than the conservative level specified above, with the premise that pitting does not initiate if the critical pitting potential, -0.73 V_{SCE}, is not exceeded, allows relaxation of the restrictions imposed on the thermal processing of the Zn-rich layers in the previous conclusion. Low level heat treatment, such as 2 hours at 350 °C of 8 g/m^2 Zn coating, can be sufficient for protection of Al against pitting and providing lowest total reduction in thickness during the test period.
- Alloying of Al with Zn even in small amounts activates Al electrochemically by reducing its corrosion potential. Al component transforms uniform corrosion kinetics of pure Zn to pitting-type of kinetics in the acidified chloride solution. Two-dimensional pits are formed, which propagate laterally following the Zn-rich layer. During this process, the underlying AlMn substrate is protected.
- Dealloying of Zn, expected from the difference in the corrosion potentials of Al and Zn, was not observed. Further studies are necessary for development of improved understanding of the mechanism of activation of Al with Zn.

- Non-uniformity of the Zn-rich layer causes non-uniform self-corrosion, where areas with higher Zn concentrations corrode first, while the areas with lower Zn concentrations are protected. The corrosion potential is controlled by the electrochemical processes at the active sites and their Zn concentration. This restricts the development of a model to predict the corrosion rate and reduction in thickness as a function of Zn concentration.
- With the restrictions in mind, the existing relationships between the corrosion potential of AlZn alloys and surface concentration of Zn in chloride solutions were verified and extended over a wide concentration range. An approximate relationship between the corrosion rate of Zn-rich layers in chloride solution and Zn concentration was also established, using which a rough estimate of corrosion rate based on Zn concentration profile can be obtained. Combination of the relationships mentioned can in principle allow modelling of corrosion of Zn-rich layers and thereby optimize the properties of the Zn-rich layer for longer service life.
- Glow discharge optical emission spectroscopy is well suited to measure concentration profiles of major and minor alloying elements, as well as oxygen, in the Zn-rich surfaces in depth, in which the sputtering rates of major components, such as Al and Zn, vary widely. Coating load can also be estimated.
- A methodology was developed for predicting Zn concentration profiles of Zn-rich layers obtained by heat treatment of Zn coatings on Al commercial alloys using solution of Fick's second law for binary diffusion from layer with fixed thickness and concentration into a semi-infinite region. The lateral non-uniformity of the Zn concentration was successfully incorporated into an effective binary diffusion coefficient, for the system. Values of activation energy and pre-exponential factor were determined as 103 kJ/mol and 2×10^{-6} m^2/s, respectively, based on the temperature dependence of the effective diffusion coefficient and the Arrhenius law. The method was incorporated into the modelling work above in predicting the necessary Zn depth for given Zn load and heat-treatment conditions.
- Enrichment of Fe on the bare AlMn substrate occurred during extrusion due to contamination from the extrusion die. Fe-rich intermetallic particles precipitated close to the surface due to exposure to heat during thermal-arc spraying and subsequent heat treatment, which caused also enrichment of Si and Mn, which was attributed to inward diffusion of Zn into the AlMn substrate. Precipitation of AlMnFeSi intermetallic particles lead to increase of the area of cathodic sites and corresponding increase of corrosion rate of the surface layer.